3D attribute analysis and classification to interpret ground-penetrating radar (GPR) data collected across sedimentary environments:

Synthetic studies and field examples

Doctoral Thesis of
Philipp Koyan

Universität Potsdam

Universität Potsdam | Mathematisch-Naturwissenschaftliche Fakultät
Institut für Geowissenschaften

Kumulative Dissertation mit dem Titel

3D attribute analysis and classification to interpret ground-penetrating radar (GPR) data collected across sedimentary environments: Synthetic studies and field examples

zur Erlangung des akademischen Grades
"doctor rerum naturalium"
(Dr. rer. nat.)
in der Wissenschaftsdisziplin
"Angewandte Geophysik"
eingereicht von

Philipp Koyan, M.Sc.

Potsdam, Dezember 2023

Datum der Disputation: 17.05.2024

Principal supervisor:

Prof. Dr. Jens Tronicke, Universität Potsdam, Germany

Second Supervisor:

Dr. Niklas Allroggen, DB Engineering & Consulting GmbH, Bremen
& Universität Potsdam (until May 2023), Germany

Reviewers:

Prof. Dr. Jens Tronicke, Universität Potsdam, Germany

Dr. Craig Warren, Assistant Professor, Northumbria University,
Newcastle upon Tyne, United Kingdom

Emanuele Forte, PhD., Associate Professor,
Università degli studi di Trieste, Italy

Examining committee:

Prof. Dr. Max Wilke, Universität Potsdam, Germany

apl. Prof. Dr. Martin H. Trauth, Universität Potsdam, Germany

Prof. Dr. Eva Eibl, Universität Potsdam, Germany

Published online on the
Publication Server of the University of Potsdam:
https://doi.org/10.25932/publishup-63948
https://nbn-resolving.org/urn:nbn:de:kobv:517-opus4-639488

Erklärung der Eigenständigkeit

Ich erkläre hiermit, dass ich die vorliegende Arbeit selbständig und ohne Benutzung anderer als der angegebenen Quellen und Hilfsmittel verfasst habe. Wörtlich zitierte Sätze oder Satzteile sind als solche gekennzeichnet; sonstige Bezüge sind durch vollständige Angabe der betreffenden Publikationen gekennzeichnet. Diese Arbeit wurde in gleicher oder ähnlicher Form noch bei keiner Prüfungsstelle eingereicht. Ferner erkläre ich, dass die eingereichten schriftlichen (gebundenen) Exemplare der vorliegenden Arbeit und die eingereichte digitale Version inhaltlich übereinstimmen.

Potsdam, Dezember 2023 .....

Philipp Koyan

Für Franzi, Mama und Papa

Allgemeinverständliche Zusammenfassung

Die Untersuchung des oberflächennahen Untergrundes erfolgt heutzutage bei Fragestellungen aus den Bereichen des Bauwesens, der Archäologie oder der Geologie und Hydrologie oft mittels zerstörungsfreier beziehungsweise zerstörungsarmer Methoden der angewandten Geophysik. Ein Bereich, der eine immer zentralere Rolle in Forschung und Ingenieurwesen einnimmt, ist die Untersuchung von sedimentären Umgebungen, zum Beispiel zur Charakterisierung oberflächennaher Grundwassersysteme. Ein in diesem Kontext häufig eingesetztes Verfahren ist das des Georadars (oftmals GPR - aus dem Englischen Ground-Penetrating Radar). Dabei werden kurze elektromagnetische Impulse von einer Antenne in den Untergrund ausgesendet, welche dort wiederum an Kontrasten der elektromagnetischen Eigenschaften (wie zum Beispiel an der Grundwasseroberfläche) reflektiert, gebrochen oder gestreut werden. Eine Empfangsantenne zeichnet diese Signale in Form derer Amplituden und Laufzeiten auf. Eine Analyse dieser aufgezeichneten Signale ermöglicht Aussagen über den Untergrund, beispielsweise über die Tiefenlage der Grundwasseroberfläche oder die Lagerung und Charakteristika oberflächennaher Sedimentschichten. Dank des hohen Auflösungsvermögens der GPR-Methode sowie stetiger technologischer Entwicklungen erfolgt heutzutage die Aufzeichnung von GPR-Daten immer häufiger in 3D.

Trotz des hohen zeitlichen und technischen Aufwandes für die Datenakquisition und -bearbeitung werden die resultierenden 3D-Datensätze, welche den Untergrund hochauflösend abbilden, typischerweise von Hand interpretiert. Dies ist in der Regel ein äußerst zeitaufwendiger Analyseschritt. Daher werden oft repräsentative 2D-Schnitte aus dem 3D-Datensatz gewählt, in denen markante Reflektionsstrukuren markiert werden. Aus diesen Strukturen werden dann sich ähnelnde Bereiche im Untergrund als so genannte Radar-Fazies zusammengefasst. Die anhand von 2D-Schnitten erlangten Resultate werden dann als repräsentativ für die gesamte untersuchte Fläche angesehen. In dieser Form durchgeführte Interpretationen sind folglich oft unvollständig sowie zudem in hohem Maße von der Expertise der Interpretierenden abhängig und daher in der Regel nicht reproduzierbar.

Eine vielversprechende Alternative beziehungsweise Ergänzung zur manuellen Interpretation ist die Verwendung von so genannten GPR-Attributen. Dabei werden nicht die aufgezeichneten Daten selbst, sondern daraus abgeleitete Größen, welche die markanten Reflexionsstrukturen in 3D charakterisieren, zur Interpretation herangezogen. In dieser Arbeit wird anhand verschiedener Feld- und Modelldatensätze untersucht, welche Attribute sich dafür insbesondere eignen. Zudem zeigt diese Arbeit, wie ausgewählte Attribute mittels spezieller Bearbeitungs- und Klassifizierungsmethoden zur Erstellung von 3D-Faziesmodellen genutzt werden können. Dank der Möglichkeit der Erstellung so genannter attributbasierter 3D-GPR-Faziesmodelle können zukünftige Interpretationen zu gewissen Teilen automatisiert und somit effizienter durchgeführt werden. Weiterhin beschreiben die so erhaltenen Resultate den untersuchten Untergrund in reproduzierbarer Art und Weise sowie umfänglicher als es bisher mittels manueller Interpretationsmethoden typischerweise möglich war.

General Summary

Today, near-surface investigations are frequently conducted using non-destructive or minimally invasive methods of applied geophysics, particularly in the fields of civil engineering, archaeology, geology, and hydrology. One field that plays an increasingly central role in research and engineering is the examination of sedimentary environments, for example, for characterizing near-surface groundwater systems. A commonly employed method in this context is ground-penetrating radar (GPR). In this technique, short electromagnetic pulses are emitted into the subsurface by an antenna, which are then reflected, refracted, or scattered at contrasts in electromagnetic properties (such as the water table). A receiving antenna records these signals in terms of their amplitudes and travel times. Analysis of the recorded signals allows for inferences about the subsurface, such as the depth of the groundwater table or the composition and characteristics of near-surface sediment layers. Due to the high resolution of the GPR method and continuous technological advancements, GPR data acquisition is increasingly performed in three-dimensional (3D) fashion today.

Despite the considerable temporal and technical efforts involved in data acquisition and processing, the resulting 3D data sets (providing high-resolution images of the subsurface) are typically interpreted manually. This is generally an extremely time-consuming analysis step. Therefore, representative 2D sections highlighting distinctive reflection structures are often selected from the 3D data set. Regions showing similar structures are then grouped into so-called radar facies. The results obtained from 2D sections are considered representative of the entire investigated area. Interpretations conducted in this manner are often incomplete and highly dependent on the expertise of the interpreters, making them generally non-reproducible.

A promising alternative or complement to manual interpretation is the use of GPR attributes. Instead of using the recorded data directly, derived quantities characterizing distinctive reflection structures in 3D are applied for interpretation. Using various field and synthetic data sets, this thesis investigates which attributes are particularly suitable for this purpose. Additionally, the study demonstrates how selected attributes can be utilized through specific processing and classification methods to create 3D facies models. The ability to generate attribute-based 3D GPR facies models allows for partially automated and more efficient interpretations in the future. Furthermore, the results obtained in this manner describe the subsurface in a reproducible and more comprehensive manner than what has typically been achievable through manual interpretation methods.

Scientific Abstract

Ground-penetrating radar (GPR) is a widely recognized tool for imaging the near-surface across diverse fields, including engineering, archaeology, geology, and sedimentology. Recent advancements in GPR system design, processing tools, and analysis techniques have led to an increased adoption of 3D GPR. The collected 3D GPR data sets typically exhibit superior resolution compared to other near-surface geophysical methods, establishing GPR as a standard for imaging complex near-surface sedimentary environments.

Despite technological progress in GPR, the development of techniques for interpreting 3D GPR data sets has not kept pace with the growing level of detail in imaged sedimentary structures. Typically, 3D GPR data sets collected across sedimentary systems are interpreted manually and, thus, results are frequently considered subjective and non-reproducible. Furthermore, manual approaches are time-consuming and, hence, interpretations tend to focus on selected 2D slices assumed to be representative of the entire 3D data set. To address these challenges and advance towards a more objective, reproducible, and comprehensive approach for interpreting 3D GPR data sets imaging sedimentary environments, this thesis reports on the development, evaluation, and application of attribute analysis and attribute classification to produce classified GPR facies models.

In contemporary geophysical applications, assessing novel processing, analysis, and interpretation approaches often involves utilizing subsurface models and corresponding synthetic geophysical data sets. The first part of this thesis presents a modeling study resulting in a publicly available 3D GPR data set and model. This model is generated using outcrop observations and field measurements resulting in a realistic 3D distribution of electromagnetic properties in a gravel pit. This model is then used to simulate densely sampled 3D GPR reflection data sets employing commonly used source frequencies.

This thesis focuses on the use of attribute analyses and classifications to structure the subsurface, employing two prominent multi-trace attribute families: structure and texture attributes. The second part of this thesis introduces the 3D gradient structure tensor (GST) approach to calculate GPR structure attributes. It outlines the basic ideas behind the GST approach, and detailed parameter testing is conducted using synthetic data sets and models from the first part. The GST approach is subsequently applied to two GPR field data sets, showcasing its potential for analyzing 3D GPR data sets imaging diverse sedimentary structures.

In the third part, a set of structure and texture attributes is employed to develop an attribute-based classification approach in 3D. This methodology is applied to generate a classified 3D GPR facies model, accurately delineating sandy deposits observed in 3D GPR data collected on a dune island. The results emphasize the potential of attribute analysis and attribute classification for deciphering complex sedimentary systems using 3D GPR. Furthermore, the adaptability of this methodology is evident in its successful application to multi-frequency GPR data, as demonstrated through its application to synthetic data sets, resulting in detailed 3D multi-scale facies models. While fully realizing the potential of 3D attribute-based facies classification requires further investigation, the methods and results presented in this thesis not only contribute to a more efficient, reproducible, and comprehensive interpretation of 3D GPR data sets but also lay the scientific basis for future advancements in sedimentary imaging.

Contents

List of Figures

List of Tables

Preface

This thesis comprises the work of my past years in the working group of Applied Geophysics at the Institute of Geosciences at the University of Potsdam. This work has been financially supported by the Deutsche Forschungsgemeinschaft (DFG), Germany, under grant no. 374920008 entitled "Analyzing and classifying attributes to generate 2D/3D GPR facies models of sedimentary systems". This thesis is a cumulative work and comprises four peer-reviewed journal articles (three of which were written by the candidate as the first author) and five reviewed expanded abstracts (four of which were written by the candidate as the first author). During my work, I made substantial use of the open-source electromagnetic modeling software gprMax and I want to thank the development team for their excellent support and constant further improvement of a unique 3D modeling framework for GPR. A second software tool that helped me during my work was DIPlib, a well-established open-source C++ library that is under constant further development, and, hence, I want to thank the DIPlib development team for their excellent software.

Ein ganz besonderer Dank gilt Jens Tronicke, da ich mir sowohl auf wissenschaftlicher als auch auf persönlicher Ebene keinen geeigneteren Doktorvater vorstellen kann und ohne dessen Engagement und Verständnis diese Arbeit in dieser Art und Weise heute nicht vorliegen würde. Ich möchte zudem Niklas Allroggen besonders danken, der seit meinem Masterstudium durch unzählige Gespräche sowie durch viele Feldeinsätze maßgeblich zu meiner wissenschaftlichen Entwicklung beigetragen hat. Weiterhin danke ich meinen KollegInnen in der Arbeitsgruppe Angewandte Geophysik, allen voran Marko für seine Zuverlässigkeit und seinen Einsatz in der Planung und Vorbereitung der Feldeinsätze sowie Sophie, Erika, Julien, Mauricio und Tim für die tollen Jahre der Zusammenarbeit.

Ein unendlicher Dank geht an meine wundervollen Eltern, Susann und Frank, sowie an meine Verlobte Franzi, ohne die ich heute nicht dort wäre, wo ich bin, und nicht der wäre, der ich bin. Sowohl mein Studium als auch meine Zeit an dieser Arbeit wären ohne meine Freundinnen und Freunde undenkbar gewesen und dafür möchte ich euch danken: Henning, Malte, Paula, Basti, Roland, Marten, Robert, Toni, Carl, ...

1. Introduction

In the last decades, ground-penetrating radar (GPR) has become a well-established, non-invasive near-surface geophysical tool (Davis and Annan, 1989; Mellett, 1995; Olhoeft, 2000; Annan, 2002; Daniels, 2004; Annan, 2005a,b; Jol, 2009). GPR has been routinely employed in various applications ranging from archeological (Vaughan, 1986; Leckebusch, 2003; Manataki et al., 2021; Forte et al., 2021a; Conyers, 2023), engineering (Benedetto and Pajewski, 2015; Lai et al., 2018; Elseicy et al., 2022), environmental (Peters et al., 1994; Hubbard et al., 2005), geological (Beres and Haeni, 1991; Neal and Roberts, 2000; Forte et al., 2021b) to extraterrestrial studies (Fang et al., 2014; Xing et al., 2017; Giannakis et al., 2024). The increasing use of two-dimensional (2D), and especially 3D, GPR can be attributed to steady developments in data acquisition (Grasmueck, 1996; Slob et al., 2010; Forte and Pipan, 2017) including the use of multi-antenna arrays (Sato et al., 2004; Leckebusch, 2005; Trinks et al., 2010; Goodman and Piro, 2013) and coupling with GPS or TTS for kinematic surveying (Böniger and Tronicke, 2010c), novel processing and analysis techniques including efficient visualization, migration or filtering techniques (Grandjean and Gourry, 1996; Nuzzo et al., 2002; Grasmueck et al., 2005; Allroggen et al., 2015; Roncoroni et al., 2023), or the ability to model and invert complex GPR data sets using state-of-the-art software solutions (Warren et al., 2016; Giannakis et al., 2016; Warren et al., 2018; van der Kruk et al., 2018). Especially in 3D surveys, the spatial resolution of GPR is usually unsurpassed compared to all near-surface geophysical methods and, thus, GPR has become a standard method to image complex near-surface sedimentary environments, for example, in view of mapping subsurface architecture including the reconstruction of past depositional environments, to reveal the nature of sedimentary processes or to aid hydrogeological observations (Beres et al., 1995; Huisman et al., 2003; Bristow and Jol, 2003; Neal, 2004; Kostic and Aigner, 2007; Burke et al., 2010; Lang et al., 2017; Switzer et al., 2020). The technical developments in GPR instrumentation and the ever-increasing computing power result in ever-growing data sets comprising several 100000 traces imaging near-surface sedimentary structures in 3D. In contrast, developments of interpretation techniques have not kept pace with the resulting increase in details and complexity of the imaged sedimentary structures, because interpreting typical GPR data sets is still widely employed in a manual and, thus, time-consuming, inefficient, non-reproducible, subjective, and often incomplete fashion.

In general, interpreting GPR data relies on the assumption that, after the application of a structural imaging processing sequence including interpolation, spatial and frequency filters, amplitude scaling, and migration, the imaged reflection patterns are directly related to the buried structures. When interpreting GPR data acquired across sedimentary environments, the most prominent interpretation technique relies on the concept of GPR facies (Van Overmeeren, 1998). In detail, following the original ideas of seismic

facies analysis (Payton, 1977; Vail et al., 1977; Roksandić, 1978), GPR facies are units composed of characteristic reflection patterns in terms of reflection amplitude, continuity, geometry, and internal configuration. Typically focusing on the GPR amplitude image, interpretations are carried out with the help of GPR facies charts (Figure 1.1) often complemented by previous or subsequent reflection picking and horizon analysis to delineate the mapped facies (Schmelzbach et al., 2011).

To illustrate this, Figure 1.2a shows a selected 2D slice of a processed 3D GPR data set imaging sandy Holocene deposits on the island of Spiekeroog (Northern Germany) across an area of approximately 100 m x 60 m. Figure 1.2b shows the same 2D slice and additionally highlights different characteristics across the reflection amplitudes and corresponding spatial patterns (such as continuity, absolute values, contrast, dip angle, dip direction) which we typically focus on when interpreting such a data set in terms of GPR facies. Based on these observations and reflection picking, a data set can be interpreted and delineated into different GPR facies which are then correlated to typical depositional environments using GPR facies charts (e.g., as indicated in Figure 1.1). Without a more detailed interpretation of the result, Figure 1.2c illustrates a typical outcome obtained using such an interpretation procedure for the GPR data shown in Figure 1.2a and b after Delock (2013). Then, the distinguished facies are interpreted in terms of sedimentary and depositional processes (McMechan et al., 1997; Corbeanu et al., 2001; Szerbiak et al., 2001; Lee et al., 2007a,b; Garrison et al., 2010) and, in view of an integrated geological and geophysical analysis, can be correlated with electro-, hydro-, and lithofacies (e.g., Heinz and Aigner, 2003; Lang et al., 2017; Winsemann et al., 2018). Although these largely manual concepts are routinely applied today, the interpretation results always depend on the interpreter's expertise. Hence, interpretations are typically not reproducible and, especially in complex 3D settings, are a time-consuming task. Thus, interpretations typically focus on a few selected 2D slices of the 3D data set (i.e., 2D amplitude images as illustrated in Figure 1.2), and, then, the results are regarded as representative of the entire surveyed area. Especially in complex 3D sedimentary environments, these simplifications often cannot justify the effort previously invested in recording and processing the underlying data sets and such approaches bear the potential of misinterpretations. To address these limitations, this thesis strives towards developing efficient and more objective tools based on attributes derived from 3D GPR amplitude data sets to aid and concise typical interpretation processes such that future GPR studies result in a more complete and comprehensive understanding of the investigated environments.

1.1. Attribute analysis and classification

In general, we understand attributes as "any measure calculated or extracted from the data that helps to enhance or quantify features of interpretation interest" (Chopra and Marfurt, 2007). Here, the term *data* in general refers to the (processed) 2D and 3D amplitude images (e.g., Figure 1.2a). When processing, analyzing, and interpreting GPR data, we often rely on the analogy between GPR and post-stack seismic reflection data.

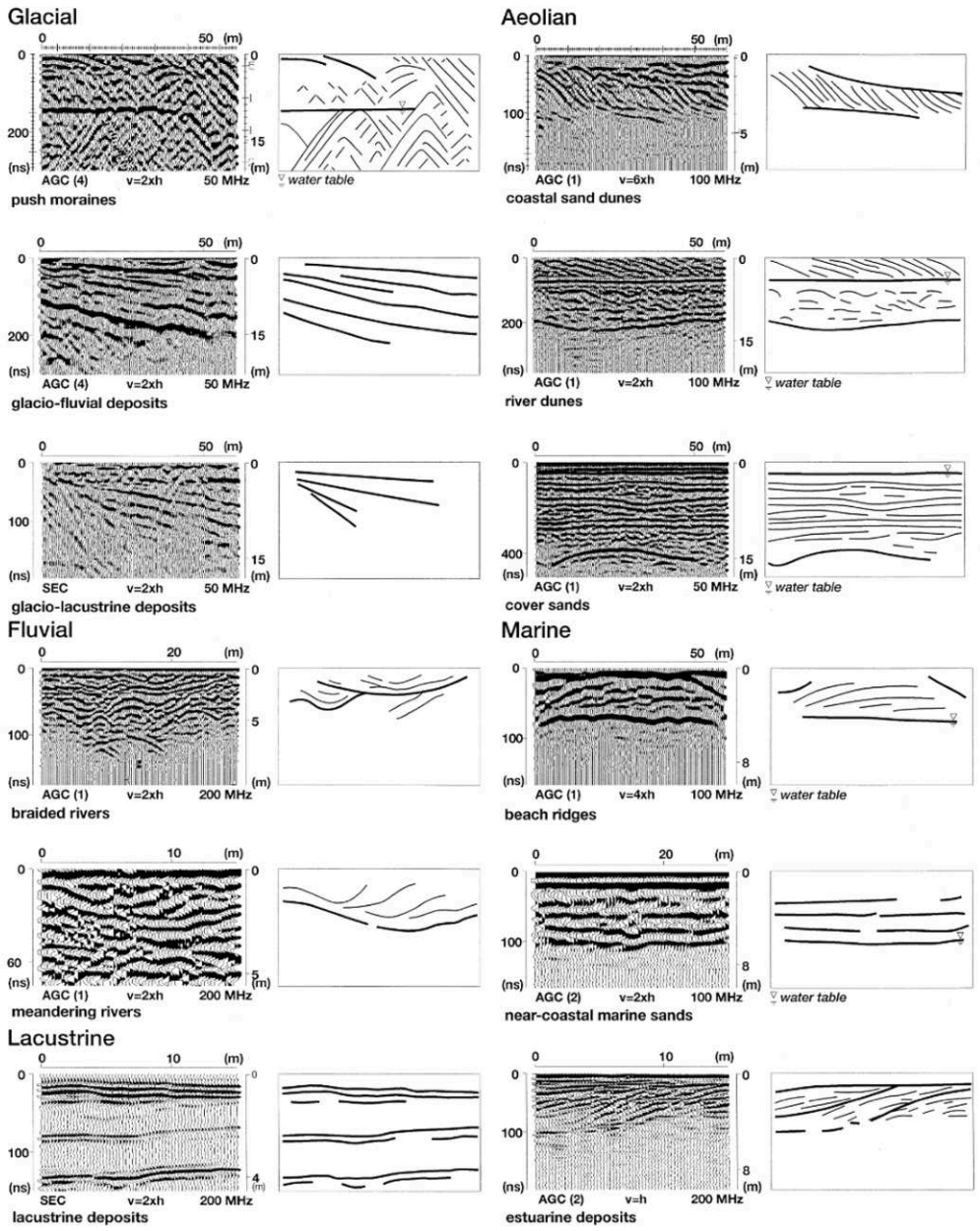

Figure 1.1.: GPR facies chart compiled by Van Overmeeren (1998) characterizing the most frequent facies signatures found across the Netherlands.

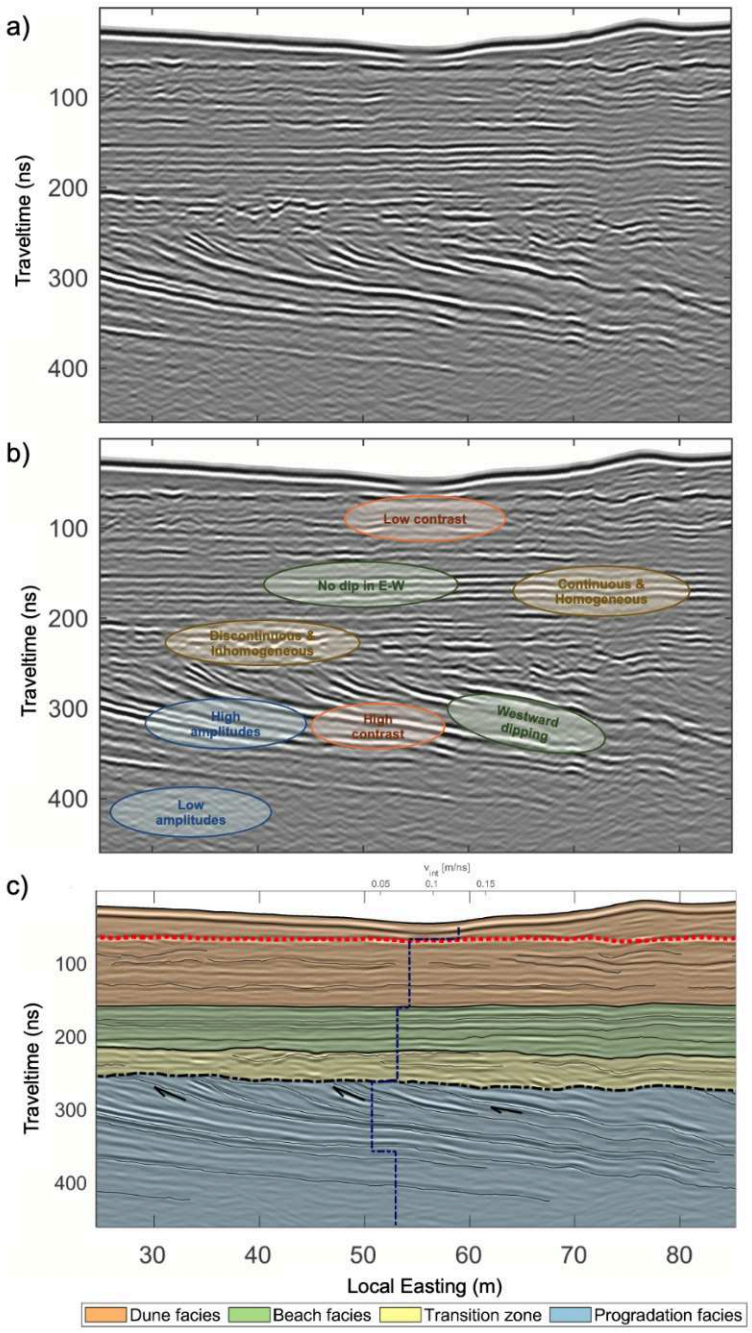

Figure 1.2.: (a) 2D slice of a 3D processed GPR data set imaging sandy deposits on the island of Spiekeroog (Germany). (b) same as (a) but highlighting characteristic reflection patterns typically focused on in a manual GPR facies interpretation. (c) same as (a) but showing the result of a manual GPR facies interpretation as transparent overlay.

Since the middle of the last century, seismic reflection data are produced in an industrial fashion, and attributes and attribute-based interpretation strategies are routinely used to analyze and interpret these data sets. The development of seismic attributes (whose only constraint often was the availability of computing power) has always been based on the constantly growing demand for hydrocarbons and the resulting need for efficient and reproducible strategies to manage the ever-growing size and amount of data sets imaging diverse geological structures. Starting from single-trace attributes (such as complex trace or instantaneous attributes; Taner and Sheriff, 1977; Robertson and Nogami, 1984; Robertson and Fisher, 1988; White, 1991), modern industry-standard data sets are analyzed using 2D, 3D, and 4D geometrical multi-trace attributes characterizing spatial, temporal, and spatiotemporal variations in the data (Chopra and Marfurt, 2005, 2006, 2007; Barnes, 2016).

From the application point of view, specific attributes (or attribute families) are typically used for addressing different tasks of interpretation. One famous attribute family incorporates multi-trace structure attributes, that highlight spatial and geometrical variations in seismic volumes or along (previously interpreted) horizons in terms of seismic reflection amplitude, continuity, dip angle, dip azimuth, or curvature (Marfurt et al., 1999; Barnes, 2000; Marfurt and Kirlin, 2000; Barnes, 2001; Al-Dossary and Marfurt, 2006; Marfurt, 2006). Up to today, structure attributes are routinely applied to delineate and characterize seismic facies or to map and analyze discontinuities because, in general, structure attributes show a physical meaning and, thus, characterize the underlying data sets plausibly. In general, structure attributes base on the calculation of 2D and 3D reflection dip in terms of angle and direction (azimuth). To calculate reflection dip, various approaches (depending on characteristics of the input data, the output data requirements, and available computational power and time) have been suggested including principal component analysis (PCA), Fourier transform, or amplitude and phase-gradient techniques such as gradient structure tensors (Bakker, 2002; Tingdahl and Hemstra, 2003; Marfurt, 2006; dGB Earth Sciences, 2023). Such structure tensors, for example, include amplitude gradients in all spatial directions and have proven to be a computationally efficient tool to characterize and quantify structure in 2D and 3D amplitude images.

A second prominent attribute family incorporates multi-trace texture attributes, where texture is defined by the spatial arrangement of neighboring amplitudes and "refers to a characteristic pattern defined by the magnitude and variation of neighboring amplitude samples at a given location in an image space" (Gao, 2011). Although their actual physical meaning is often debated, texture attributes are a field of active research as they are a reliable tool to describe and delineate amplitude variations and patterns in a defined neighborhood and have shown to be promising means to delineate complex geological features or to quantify subsurface property distributions (Vinther et al., 1995; Gao, 2003, 2004; Yenugu et al., 2010; de Matos et al., 2011; Eichkitz et al., 2013, 2015; Eichkitz and Amtmann, 2018; Long et al., 2018). To characterize and calculate texture and related attributes, the approach based on the gray-level cooccurrence matrix (GLCM) has become a standard technique, and several GLCM texture attributes have been proposed

in the past (Haralick et al., 1973; Soh and Tsatsoulis, 1999; Eichkitz et al., 2013, 2015; Eichkitz and Amtmann, 2018).

In the last decades, it has been shown that seismic attributes (including structure and texture attributes) are promising input measures when aiming for the production of classified seismic facies models to further automatize interpretation tasks. In general, there are two options to delineate the input attributes into a finite number of classes or facies, namely unsupervised techniques such as k-means, self-organizing maps, or fuzzy c-means (Barnes, 2000; West et al., 2002), and supervised methods such as artificial neural networks, Gaussian mixture models or support vector machines that also incorporate (but at the same time critically depend on) geological or geophysical a-priori information (Coléou et al., 2003; Zhao et al., 2015, 2017; Wrona et al., 2018; Alaudah et al., 2019; Kaur et al., 2023; Narayan et al., 2023).

Despite the above-mentioned analogy between post-stack reflection seismic and GPR data, attribute-based analysis in general, and attribute-based classification in particular, are far from being a standard tool in GPR interpretation workflows. More precisely, only a limited number of studies indicates the potential of 2D and 3D GPR attribute analysis in geological (Grasmueck, 1996; Young et al., 1997; Sénéchal et al., 2000; Corbeanu et al., 2004; Tronicke et al., 2006; McClymont et al., 2008; Tronicke and Böniger, 2013; Zhao et al., 2018; Forte et al., 2021b; Svendsen et al., 2023) or archaeological applications (Böniger and Tronicke, 2010a; Zhao et al., 2013, 2016; Trinks and Hinterleitner, 2020; Forte et al., 2021a). Moreover, at the start of this thesis, only four studies reported the general applicability of attribute-based classification approaches to produce sedimentary or geological GPR facies models in 2D (Moysey et al., 2006; Forte et al., 2012; Tronicke and Allroggen, 2015; Bowling et al., 2018).

In addition to differences in industrial interest, one major reason is that (despite the far-reaching similarities of elastic and electromagnetic wave propagation; Ursin, 1983) characteristics of resulting reflection seismic and GPR amplitude images typically differ. For example, when used to image sedimentary structures, the resulting images differ in terms of the number and continuity of imaged reflections. This is mainly based on differences in employed source types, wavelets, wavelengths, and different spatial scales of investigation addressed by reflection seismics and GPR. Hence, a typical reflection seismic image shows one to two orders of magnitude more reflections than a typical GPR image. This indicates that a one-to-one adaption of seismic attribute-based workflows, even for similar targets, is limited and we need to develop GPR-specific workflows based on their seismic archetypes. Thus working out an appropriate set of attributes and applying a proper workflow that reveals the full potential of GPR attribute analysis and classification is still a challenging task that this thesis wants to further improve.

Following the basic ideas of Tronicke and Allroggen (2015) and considering the imaging potential of different attribute families for facies characterization mentioned above (compare also to Figure 1.2b), this thesis focuses on the use of texture and structure attributes in 3D to evaluate and develop attribute-based analysis and classification approaches in a systematic fashion (Figure 1.3). To illustrate the potential of the proposed workflow, but without analyzing the results in more detail, Figure 1.4b anticipates one key

outcome of this study. That is, Figure 1.4a compares the results of a manual interpretation approach (Figure 1.2c) to the same 2D slice extracted from a full 3D GPR facies model (b) that has been produced by classification of texture and structure attributes following the workflow illustrated in Figure 1.3. However, when attempting to formulate novel approaches in processing, analysis, and interpretation, it has become good practice to evaluate and reference novelties using subsurface models and the corresponding synthetic geophysical data sets.

1.2. 3D GPR modeling

Synthetic subsurface models and resulting geophysical data sets are of great interest throughout the geophysical community to perform feasibility studies, plan and optimize acquisition campaigns, perform data inversion routines or reference novel processing, analysis and interpretation routines. For example, the seismic community has been using standardized 2D and 3D reference models and resulting data sets for numerous geological settings for decades such as the famous 2D Marmousi model (Figure 1.5a) and its 3D variants or the SEG salt and overthrust models (Versteeg, 1994; Aminzadeh et al., 1997). Today, testing and evaluating novel processing and analysis routines using such reference models and data sets has become good practice.

Synthetic GPR data and models in geological and sedimentary applications have been used for several years, for example, to understand the physical phenomena governing electromagnetic wave propagation (Xu and McMechan, 1997; Holliger and Bergmann, 2002; Cassidy and Millington, 2009) or to reference and develop novel data processing, analysis, and interpretation routines (Cassidy, 2007; Paasche and Tronicke, 2007; Cassidy, 2009; Klotzsche et al., 2010; van der Kruk et al., 2018). Though, up to the beginning of this thesis, the use of synthetic GPR data to characterize sedimentary environments commonly focused on application-specific 1D/2D scenarios (Cassidy, 2008; Bricheva et al., 2021; Schennen et al., 2022), and the corresponding data and models hence were not made publicly available. Although the physical and numerical principles of modeling electromagnetic wave propagation using the finite-difference time-domain (FDTD) method have been well understood and applied for decades (Yee, 1966; Cassidy and Murdie, 2000; Taflove et al., 2005; Adams et al., 2007; Cassidy, 2007; Millington and Cassidy,

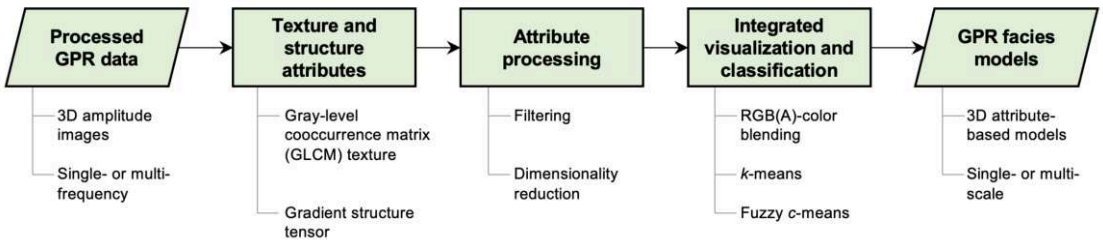

Figure 1.3.: Flowchart diagram presenting the main workflow of this thesis.

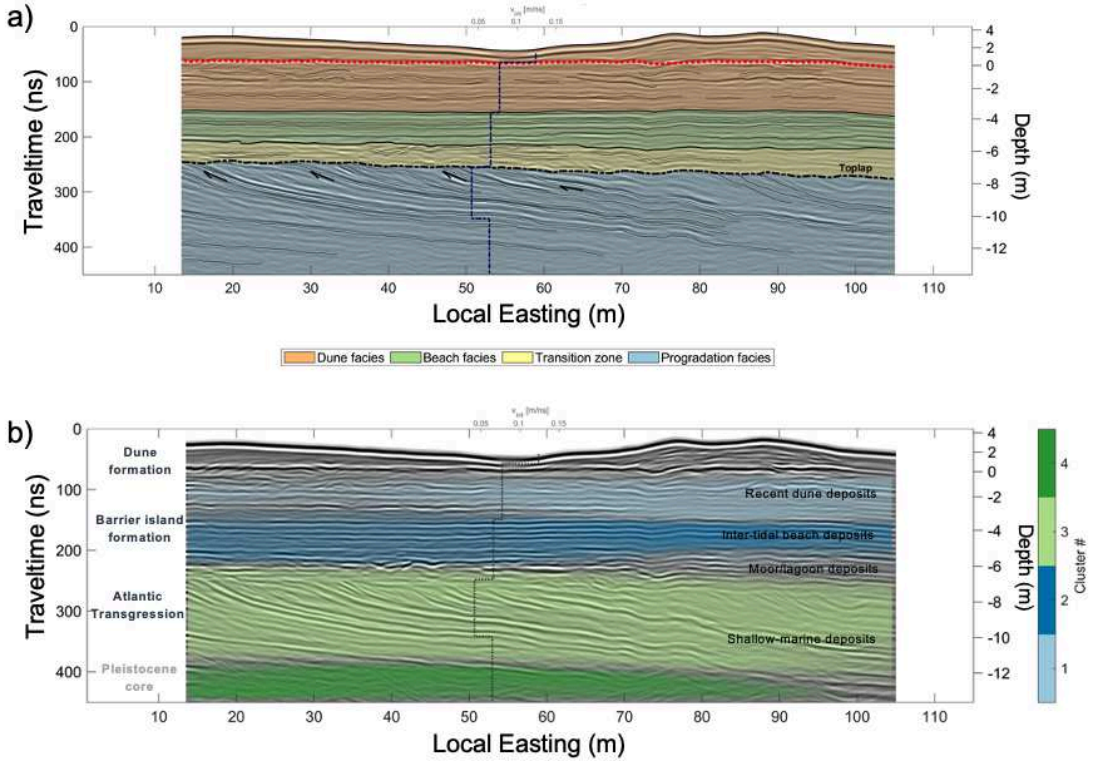

Figure 1.4.: a) Result of a typical manual 2D GPR facies interpretation approach for the Spiekeroog data set (Figure 1.2c) compared to (b) a 3D GPR facies model resulting from an attribute-based classification approach.

2010), only modern developments in personal computing power and the availability of open-source well-maintained software solutions have made possible the production of realistic and complex 3D GPR data sets (Warren et al., 2016). More precisely, taking advantage of recent developments in GPU-based modeling, gprMax, the most widely used modeling software in the GPR community today, drastically accelerated 3D GPR modeling. The resulting speed-up in the order of one to two magnitudes compared to parallelized CPU computing first enabled GPR users to produce complex 3D data sets without the need for expensive high-performance computing resources (Warren et al., 2018). However, modeling realistic 3D GPR data sets in general (and those characterizing sedimentary or geological scenarios in particular) marks an area of research that was largely unexplored both at the beginning of this work and today. Hence, to reveal the potential of the computational novelties and to develop, reference, and evaluate the proposed workflow and future analysis, processing, and interpretation techniques, one part of this thesis reports on the production of a realistic 3D GPR data set. This is freely available to the community in order to act as a first benchmarking and reference data set for 3D GPR as the Marmousi model did three decades ago for the seismic community (Figure 1.5b).

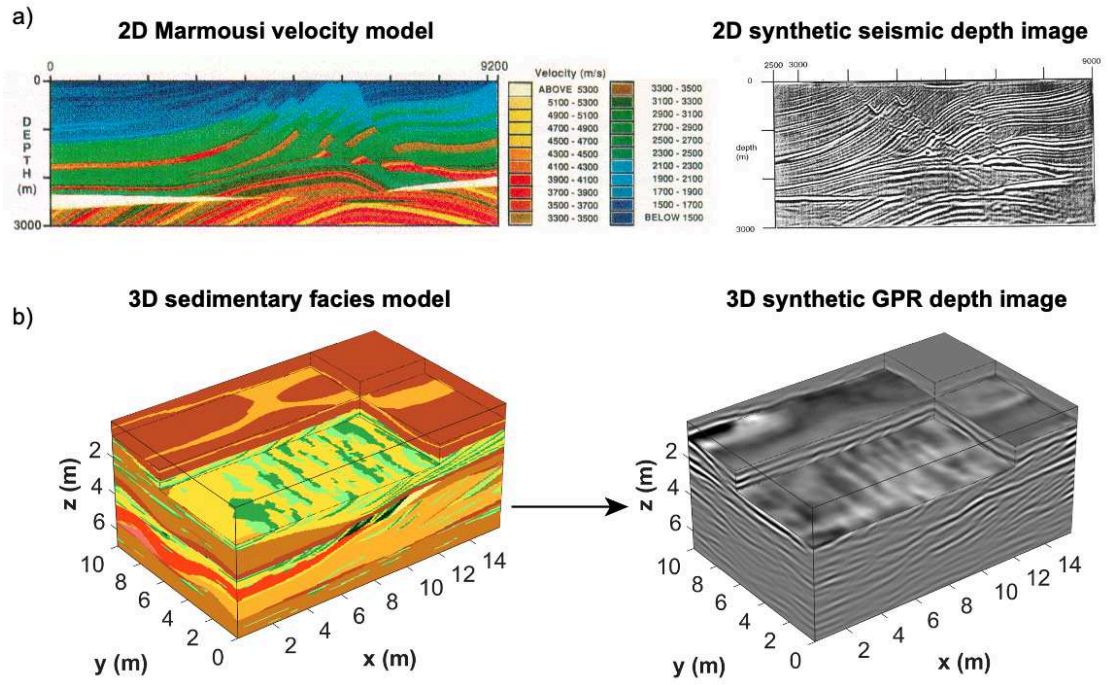

Figure 1.5.: (a) 2D Marmousi model and corresponding synthetic 2D seismic depth image after Versteeg (1994). (b) 3D model of a gravel pit and corresponding synthetic 3D GPR depth image.

1.3. Objective and outline of this thesis

This thesis is a cumulative work and comprises four peer-reviewed journal articles (three of which were written by the candidate as the first author) and five reviewed expanded abstracts (four of which were written by the candidate as the first author) that are included as chapters in this thesis. This section provides a general overview of the structure of this thesis centered around Figure 1.3. For a detailed list of contributions and information on further work performed in this project, I refer to Appendix E.

Chapter 2 presents a modeling study resulting in a publicly available 3D GPR data set and model, respectively. I show, how outcrop observations and field measurements can be used to produce a realistic 3D model of the electromagnetic properties within a gravel pit. Developing and using an efficient modeling strategy and novel GPU acceleration in gprMax, I generate a densely sampled 100 MHz GPR data set. The modeling results are compared to the input parameter distributions illustrating the feasibility and potential of the presented study. The publicly available model and data set have been featured on the gprMax website (www.gprmax.com/projects.shtml) and were well received by the community which is reflected in >500 downloads and

>3300 views since the data set has been hosted on Mendeley Data in June 2019 (data.mendeley.com/datasets/by3yh79hx4/1).

A major advantage of GPR is its flexibility in terms of source frequencies. Using the model from Chapter 2, in Chapter 3, I augment the synthetic database with two more 3D GPR data sets using further source frequencies (50 and 200 MHz) typically employed to record GPR data in sedimentological applications. Considering frequency-dependent model discretization requirements and resulting model sizes (i.e., higher frequencies require finer model discretization leading to increased model sizes), I present a customized modeling strategy that enables the calculation of a 200 MHz data set across the whole 3D input model. These modeling studies have also been presented in the course of an invited talk at the *1st Online Workshop on Ground-Penetrating Radar Modelling Using gprMax* in 2020 (www.youtube.com/watch?v=sw5zncmyKU0). Appendix A provides an example of how these synthetic data sets can be used to evaluate novel processing techniques. The chapter presents the development, evaluation, and application of a 1D/2D/3D scale-based filtering technique relying on the redundant wavelet transform.

Typically, GPR data recorded across sedimentary systems are interpreted manually, for example, relying on picking distinct reflection patterns and horizons to structure the near-surface. An example of such a typical interpretation approach employed to characterize, delineate, and map the stratigraphy of a complex peat structure in 3D is presented in Appendix B. However, in this thesis, I focus on the use of attribute analyses and classifications to structure the subsurface using two prominent attribute families that have been identified in Chapter 1.1, namely structure and texture attributes. Chapter 4 presents the 3D gradient structure tensor (GST) approach to calculate GPR structure attributes. I show the basic ideas behind the GST approach and, using the synthetic data from Chapters 2 and 3, perform parameter testing to analyze the influence of different filter sizes and types on the resulting structure attributes. The GST approach is applied to two GPR data sets imaging different sedimentary scenarios. The first example images sandy deposits on the Island of Spiekeroog, Northern Germany (see also Figures 1.2 and 1.4). Here, the GST approach is successfully used to characterize and quantify the diverse facies as imaged by the GPR data. The second example images fault strands in volcanic and lacustrine sediments on the North Island of New Zealand. Here, the GST approach is applied to characterize and quantify the 3D geometry of the fault strands. Results of structure attribute analysis of both field examples are compared to previous interpretation results illustrating the potential of structure attributes in general, and the GST approach in particular, for the analysis of 3D GPR data.

Although this thesis mainly focuses on GPR data acquired across sedimentary deposits, Appendix C shows how structure attributes can be used to analyze GPR data imaging near-surface archaeological remains. Here, in addition to the typically used GPR amplitude images, I calculate selected GST-based structure attributes in a so-called chained fashion, this is, these attributes are also calculated across selected attribute images (here, reflection energy). Comparing the GPR amplitude image and a typical reflection energy image to

the corresponding structure attributes indicates the potential of structure attributes to detect and highlight archaeological remains in 3D GPR data.

In Chapter 5 (which includes a paper that is also featured in the *Geophysics Bright Spots* section of SEG's The Leading Edge magazine in January 2022), a set of structure and texture attributes is used to develop and apply an attribute-based classification approach. I present and evaluate scale-based filtering and structuring strategies resulting in an attribute database characterizing the GPR data set in terms of GPR facies. Then, this attribute database is analyzed using integrated visualization and classification that is applied to obtain a classified 3D GPR facies model precisely delineating the sandy deposits in the Spiekeroog data set. As already anticipated in Figure 1.4, this study indicates the potential of attribute-based analysis and classification to characterize complex sedimentary environments in 3D using GPR.

The flexibility of GPR in terms of source frequencies enables the characterization of sedimentary systems at multiple resolutions and spatial scales. In Chapter 6, the synthetic 50 MHz and 200 MHz data sets presented in Chapter 3 are used to further develop the attribute-based interpretation approach in view of an integrated classification of multi-frequency GPR data to obtain multi-scale classified 3D GPR facies models. This study illustrates that the attribute-based interpretation workflow developed in this thesis poses a flexible and reliable tool to characterize sedimentary systems at one or multiple spatial scales using single- or multi-frequency GPR data sets.

Appendix D (which includes a paper that has been awarded by the SEG with *Honorable Mention* in the selection of *the Best Paper in Geophysics in 2022*) presents a field study on Spitsbergen/Svalbard (Norway) in which a comparable workflow based on texture and structure attributes is applied to delineate structures in a different geological situation compared to the ones presented above. Here, an attribute-based classification approach is employed to distinguish faulted and brecciated areas in a paleokarst breccia pipe from the surrounding (undisturbed) regions. The resulting facies model is compared to results obtained by a typical horizon-based interpretation approach thus highlighting the potential of attribute-based analysis and classification to make interpretations of complex 3D GPR data sets acquired across diverse sedimentary systems a more efficient, reproducible, and comprehensive task.

2. 3D modeling of ground-penetrating radar data across a realistic sedimentary model

Philipp Koyan and Jens Tronicke*

2.1. Abstract

Ground-penetrating radar (GPR) is an established geophysical tool to explore a wide range of near-surface environments. Today, the use of synthetic GPR data is largely limited to 2D because 3D modeling is computationally more expensive. In fact, only recent developments of modeling tools and powerful hardware allow for a time-efficient computation of extensive 3D data sets. Thus, 3D subsurface models and resulting GPR data sets, which are of great interest to develop and evaluate novel approaches in data analysis and interpretation, have not been made publicly available up to now.

We use a published hydrofacies data set of an aquifer-analog study within fluvio-glacial deposits to infer a realistic 3D porosity model showing heterogeneities at multiple spatial scales. Assuming fresh-water saturated sediments, we generate synthetic 3D GPR data across this model using novel GPU-acceleration included in the open-source software gprMax. We present a numerical approach to examine 3D wave-propagation effects in modeled GPR data. Using the results of this examination study, we conduct a spatial model decomposition to enable a computationally efficient 3D simulation of a typical GPR reflection data set across the entire model surface. We process the resulting GPR data set using a standard 3D structural imaging sequence and compare the results to selected input data to demonstrate the feasibility and potential of the presented modeling studies. We conclude on conceivable applications of our 3D GPR reflection data set and the underlying porosity model, which are both publicly available and, thus, can support future methodological developments in GPR and other near-surface geophysical techniques.

*A peer-reviewed journal article of the same title is published as Koyan and Tronicke (2020a) in Computers and Geosciences 137, article no. 104422. Supplementary material for this article can be found in an online repository hosted at Mendeley Data (doi:10.17632/by3yh79hx4.1) and is published as Koyan and Tronicke (2019).

2.2. Introduction

Ground-penetrating radar (GPR) is a standard geophysical tool increasingly employed in various archaeological, engineering, environmental, and geological applications (Knight, 2001; Bristow and Jol, 2003; Daniels, 2004; Lai et al., 2018). Within the field of GPR, synthetic data sets and the underlying models play an important role as they can serve, for example, to formulate suitable target-specific acquisition strategies (e.g., Samet et al., 2017; Liu et al., 2018), to reference novel data processing and analysis routines including data inversion (e.g., Paasche and Tronicke, 2007; Klotzsche et al., 2010), or to study GPR response to different saturation scenarios within sedimentary deposits (e.g., Kowalsky et al., 2001). In the seismic community, 3D models and resulting synthetic data sets are widely used; for example, the famous Marmousi model and its variants or the SEG/EAGE 3D salt and overthrust models (Versteeg, 1994; Aminzadeh et al., 1997) are an actively utilized reference to test and evaluate novel methodological ideas (e.g., Yang et al., 2014; Boehm et al., 2016; Métivier et al., 2016). However, up to now there are no publicly available reference models and data sets for GPR.

To simulate GPR data, numerous implementations typically relying on the Finite-Difference Time-Domain (FDTD) method have been proposed and continuously developed throughout the past decades (e.g., Bergmann et al., 1998; Irving and Knight, 2006; Millington and Cassidy, 2010). The open-source software gprMax (Warren et al., 2016) is a well-established and well-maintained tool, which delivers a highly flexible FDTD scheme to model GPR data. The computational effort to tackle FDTD modeling problems in a 3D fashion is highly demanding (especially regarding calculation time). Thus, the most recent development within gprMax can be considered as a quantum leap, because the software now features a GPU modeling engine (Warren et al., 2018). For the first time, the resulting speed-up allows time-efficient modeling of 3D GPR reflection data sets with typical constant-offset geometries (commonly consisting of thousands of single source positions) across 3D models comprising several millions of cells without the need of high-performance computing resources.

In sedimentary environments, high-resolution 3D GPR images facilitate a deeper understanding of depositional processes, tectonic activity or the hydrogeological settings at a field site (e.g., Neal, 2004). However, throughout the whole range of sedimentological applications, the use of 3D GPR modeling (e.g., to improve near-surface characterization strategies) has not kept pace with the steady development of modeling tools and technologies. Hence, the publicly available hydrofacies data set resulting from an aquifer-analog study within a gravel quarry near the village of Herten in SW-Germany (Bayer et al., 2011; Comunian et al., 2011) poses an ideal basis to perform 3D GPR modeling across a realistic sedimentary environment. This data set comprises hydrogeological data (including porosity and hydraulic conductivity) and facies models, respectively, which describe heterogeneities within a volume of 16 x 10 x 7 m (length x width x depth) dominated by sandy and gravelly fluvio-glacial deposits.

In this study, we make use of the novel GPU engine in gprMax to generate extensive 3D GPR data across a realistic 3D sedimentary model. Therefore, we use the Herten

data set to derive a porosity model showing realistic variations down to the sub-facies scale. Assuming fresh-water saturated sediments, this porosity model then is translated into a model comprising fundamental electrical subsurface parameters. After introducing our modeling setup, we propose an approach to examine 3D effects in synthetic GPR data. Considering the results of this examination study, we conduct a spatial model decomposition in order to perform a computationally efficient 3D modeling of a typical GPR reflection data set across the entire model surface. To analyze this data set, we apply a standard 3D GPR processing sequence including the analysis of a synthetic common-midpoint experiment and evaluate our results by a direct comparison to the input model. Finally, we present our conclusions and discuss the further use of our synthetic GPR reflection data set and our porosity model, which are both publicly available (Koyan and Tronicke, 2019).

2.3. Database and model preparation

In this section, we introduce and present the Herten data set. Furthermore, we outline the derivation of our porosity model and its transformation into the electrical parameter models which are used as input for modeling 3D GPR data.

2.3.1. Hydrofacies and porosity model

As starting point, we use a high-resolution 3D hydrofacies data set resulting from an aquifer-analog study within fluvio-glacial deposits. Here, we only give a brief overview of the steps performed to obtain this data set and summarize the most striking sedimentary features therein. For a detailed description of the underlying field work, the mapping procedure, and the sedimentological interpretation, we refer to Bayer et al. (2011). A precise portrayal of the applied 3D geostatistical modeling is presented by Comunian et al. (2011).

The 3D data set comprises hydrogeological properties and their spatial distributions within a well-described gravel quarry near the village of Herten (SW-Germany). There, mainly poorly to well-sorted sand and gravel sequences formed in a braided-river regime characterize the subsurface. The data set originates from six parallel digitized outcrop images with a lateral distance of 2 m between individual images. Supported by sedimentary mapping performed during excavation (Bayer, 2000), these images are interpreted in terms of lithological facies resulting in six 16 m wide rasterized 2D facies sections. These sections cover a depth range of 7 m and show a resolution of 0.05 m. Laboratory measurements of facies-specific hydrogeological properties including porosity Φ and hydraulic conductivity K lead to a subdivision of the mapped lithological facies into 10 different variants, termed hydrofacies. Comunian et al. (2011) use these 2D hydrofacies sections to perform geostatistical modeling resulting in 3D realizations of the local subsurface architecture with a resolution of 0.05 m in all spatial dimensions which these authors provide as supplementary material.

In Figure 2.1, we visualize the 3D hydrofacies model used in this work ("Realization 1" of Comunian et al., 2011) and also introduce our coordinate system. The hydrofacies code is based on a convention from Bayer et al. (2011) compiled from Keller (1996) and Heinz and Aigner (2003). In Table 2.1, we support the understanding of this model by a brief description of the different hydrofacies including their representative porosity values and the associated porosity ranges as compiled by Bayer et al. (2011). Combining the representative porosity values and the 3D hydrofacies model yields a representative 3D porosity model for the Herten site of which we show a typical 2D slice at $y = 6$ m in Figure 2.2a. Figures 2.1 and 2.2a illustrate that the local subsurface exhibits a highly heterogeneous 3D architecture showing numerous sedimentary features on the cm- to m-scale including corresponding porosity variations.

Referring to Figures 2.1 and 2.2a, we discuss the most prominent sedimentary features and the associated porosity variations. The model is capped by typical accretionary structures down to a depth of ~1 - 2 m. These structures are formed by a thin, continuous gravel layer with a sand-rich matrix (sGcm) showing the overall smallest porosity values embedded in a minimally less condensed facies with a cobble-rich matrix (cGcm). Directly underneath, we identify cut-and-fill sequences showing an alteration of highly porous, gently dipping open-framework gravels (Gcg,o and sGcg,o) and less porous sand-gravel mixtures (mainly sGcm,b). A comparable depositional structure can be found at depths around 4 m (up to $x \approx 12$ m) where it overlays an up to 1 m thick body accommodating the globally most porous well-sorted gravels and sands (GS-x and S-x). In the deeper parts

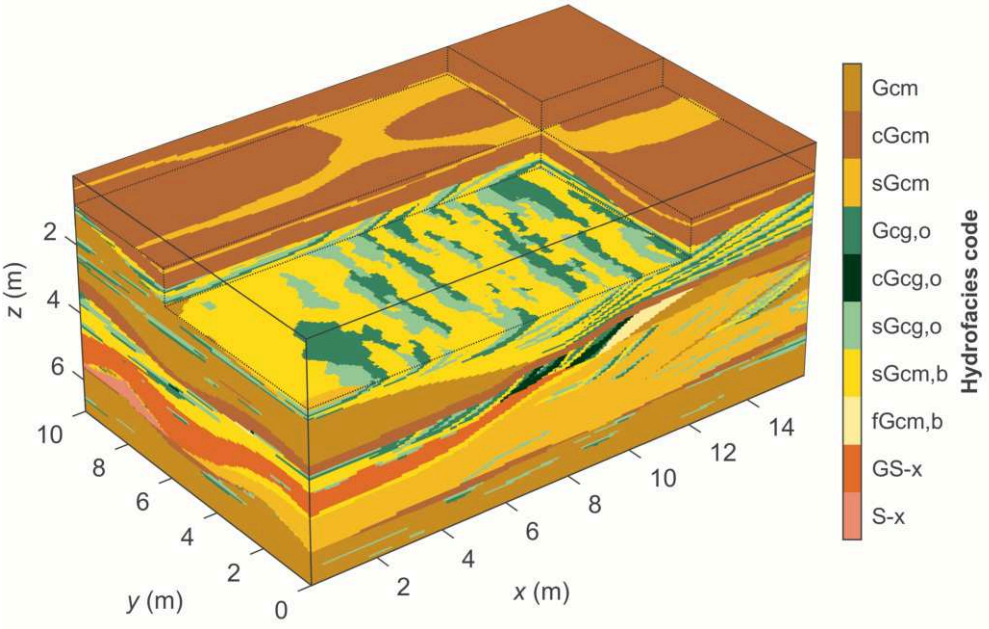

Figure 2.1.: 3D view across the Herten hydrofacies model used as starting point in this work ("Realization 1" of Comunian et al., 2011). Details on the hydrofacies code are provided in Table 2.1.

Table 2.1.: Description of hydrofacies code used in Figure 2.1 as well as representative porosity values and associated ranges (Bayer et al., 2011). Porosity ranges marked by * assumed for this work (no data provided).

Hydrofacies code	**Description** (details)	**Porosity** Φ (range)
Gcm	Poorly sorted, matrix-supported gravel (normal)	0.17 (± 0.07)
cGcm	Poorly sorted, matrix-supported gravel (cobble-rich)	0.15 (± 0.01)
sGcm	Poorly sorted, matrix-supported gravel (sand-rich)	0.13 (± 0.04)
Gcg,o	Alternating gravel (matrix-free, clast-supported open framework, coarse-fine pebbles)	0.26 (± 0.02)
cGcg,o	Alternating gravel (cobbles-coarse pebbles, open framework)	0.26 (± 0.02)
sGcg,o	Alternating gravel (granules/sand, open framework)	0.23 (± 0.01)*
sGcm,b	Alternating gravel (bimodal basal sub-unit with sand matrix)	0.22 (± 0.01)*
fGcm,b	Alternating gravel (bimodal basal sub-unit with silt/clay matrix)	0.20 (± 0.01)*
GS-x	Well sorted gravel (and coarse sand)	0.27 (± 0.07)
S-x	Pure, well sorted sand	0.36 (± 0.04)

of the model, beneath the well-sorted sand-gravel body and the cut-and-fill sequences, the model again exhibits typical accretionary structures dominated by the least porous, matrix-supported gravels (Gcm and its variants). In this context, we observe thin, partially discontinuous and (sub)-horizontal to gently dipping layers which locally exhibit a sequentially graded bedding. These layers include highly porous open-framework gravels (Gcg,o and its variants) as well as small portions of the most porous, well-sorted sands (S-x). This results in local high-wavenumber, high-magnitude porosity variations in the lowermost parts of the model.

The representative porosity model in Figure 2.2a shows considerable multi-scale and multi-magnitude variations. However, up to now we assume that each hydrofacies shows uniform properties throughout the entire model and therefore is characterized by a single representative porosity value. To generate a more realistic porosity distribution in view of modeling realistic GPR data, we upgrade the representative porosity model (Figure 2.2a) by introducing heterogeneities at the sub-facies scale. As no deterministic information on the spatial distribution and correlation of heterogeneities within each hydrofacies are

available, we take advantage of the fact that a wide range of petrophysical properties within sedimentary deposits shows fractal characteristics (e.g., Walden and Hosken, 1985; Desbarats and Bachu, 1994). To consider this, we use the popular exponential covariance model characterized by a commonly observed ratio between vertical and horizontal correlation length of 1:10 (e.g., Gelhar, 1993) to simulate an independent, spatially correlated 3D random field with a Gaussian probability density function for each of the 10 hydrofacies. We perform the numerical realization utilizing the turning bands algorithm of Emery and Lantuéjoul (2006) allowing for an efficient calculation of such random fields. We scale the 10 resulting 3D random fields using the porosity ranges listed in Table 2.1 and add the results to the representative porosity model (Figure 2.2a) considering the spatial appearance of the respective hydrofacies. In the following, we limit the precision of this porosity model to three decimal places. Thus, we restrict the number of different porosity values in the model and therefore the amount of different property values in the resulting electrical parameter models which is a prerequisite for an efficient GPR modeling procedure (Section 2.4). In Figure 2.2b, we visualize our resulting porosity model at the same 2D slice as in Figure 2.2a. Figure 2.3 illustrates the associated porosity distribution for the entire 3D model as hydrofacies-specific histogram plots. These plots are normalized to the total number of porosity values and give an impression of the relative portions of the individual hydrofacies found in the model. Analyzing Figures 2.2b and 2.3 illustrates that the porosity values within each hydrofacies now exhibit a commonly observed spatial correlation structure, and are also characterized by a Gaussian distribution whose mean value, standard deviation, and minimum/maximum values depend on the associated representative porosity value and range as listed in Table 2.1.

2.3.2. Electrical parameter models and discretization

Fundamental electrical properties affecting the propagation of electromagnetic waves are (1) the dielectric permittivity $\varepsilon = \varepsilon_r \varepsilon_0$, where ε_r is the material dependent dielectric constant and ε_0 the dielectric permittivity of free space, (2) the electrical resistivity ρ, (3) the magnetic loss σ^*, and (4) the magnetic permeability $\mu = \mu_r \mu_0$, where μ_r and μ_0 are the material dependent relative magnetic permeability and the magnetic permeability of free space, respectively. Due to the absence of magnetic materials in our model, we fix the magnetic permeability to the value of free space (i.e., $\mu_r = 1$) and assume no magnetic loss (i.e., $\sigma^* = 0$). For this modeling study being a first attempt toward modeling extensive 3D GPR data, we use first-order realistic media; i.e., we basically assume frequency-independent electrical parameters. Furthermore, we only consider fresh-water saturated sediments. This allows us to use standard two-component mixture models without any further assumptions on the material characteristics (not available for the Herten field site) to translate our porosity model (Figure 2.2b) into ε_r and σ, respectively (e.g., Tronicke and Holliger, 2005). More specifically, we obtain a

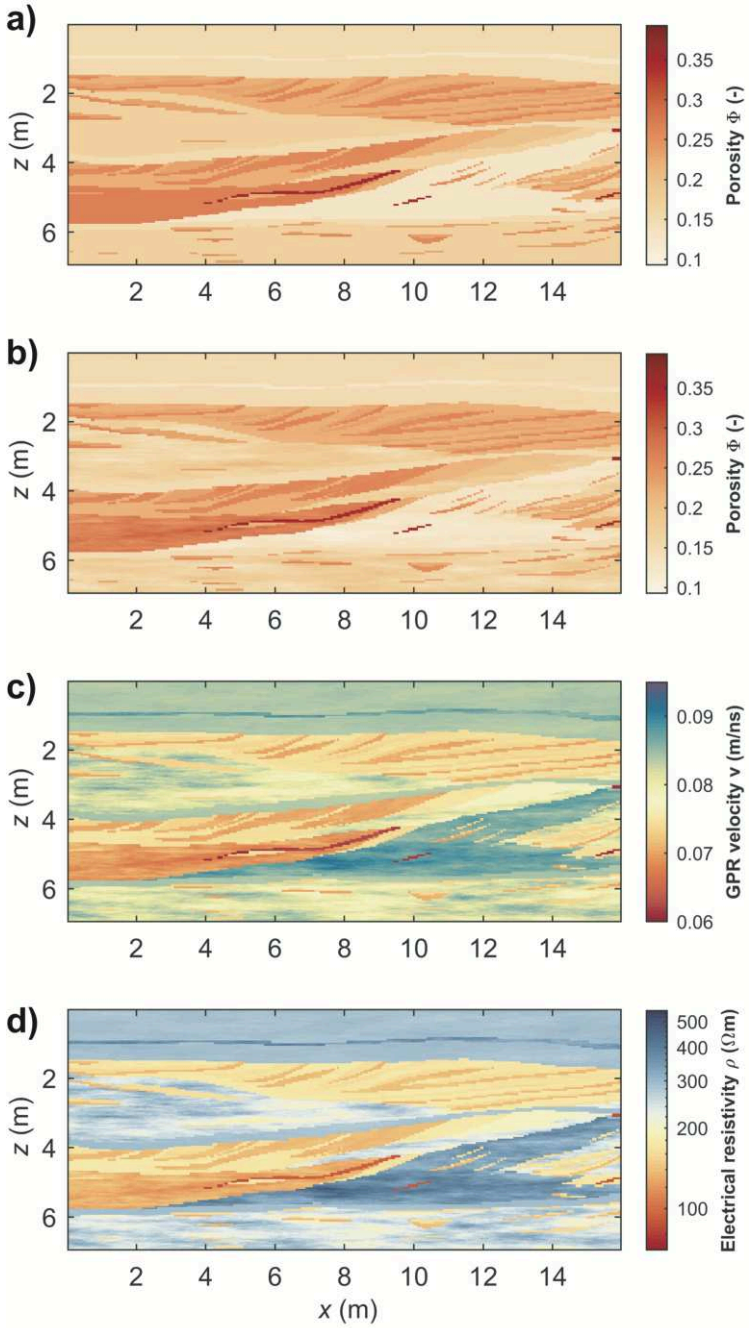

Figure 2.2.: Typical 2D profile slices at $y = 6$ m of (a) porosity model with representative values from Table 2.1, (b) our porosity model including spatially correlated heterogeneities at the sub-facies scale, (c) GPR velocity model derived from (b) assuming fresh-water saturated sediments, and (d) electrical resistivity model derived from (b) assuming fresh-water saturated sediments.

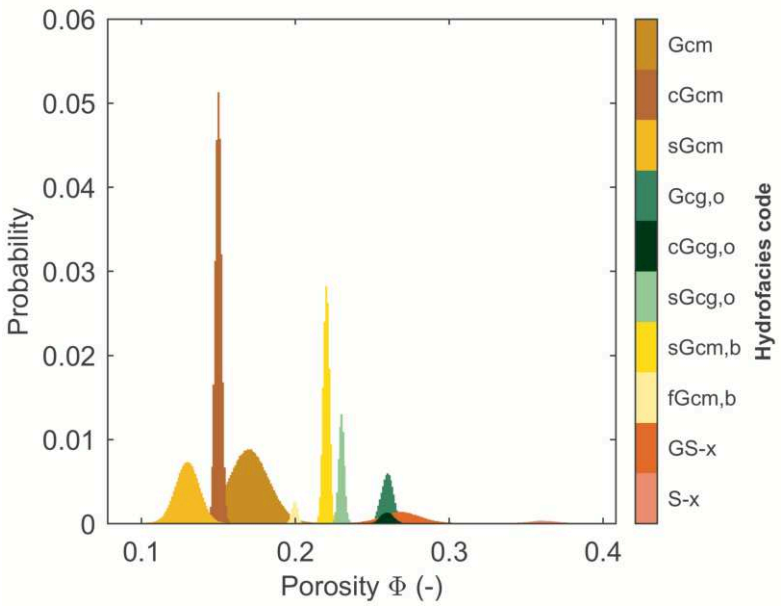

Figure 2.3.: Hydrofacies-specific porosity values as histogram plots illustrating the porosity distribution for the entire 3D model after adding spatially correlated heterogeneities at the sub-facies scale. Plots are normalized to the total number of porosity values in our model.

model of ε_r using the two-component formulation of the complex refractive index model (CRIM; e.g., Roth et al., 1990; Zakri et al., 1998):

$$\varepsilon_r = \left((1-\Phi)\sqrt{\varepsilon_{r,m}} + \Phi\sqrt{\varepsilon_{r,w}}\right)^2 . \tag{2.1}$$

Here, $\varepsilon_{r,m}$ is the dielectric constant of the dry matrix and $\varepsilon_{r,w}$ that of fresh water, which we set to typical values of 6.9 and 80, respectively (e.g., Kowalsky et al., 2001). To obtain a model of ρ, we use a formulation of the well-known Archie's equation for fresh-water saturated media (Archie, 1942):

$$\rho = \rho_w \left(\frac{a}{\Phi^m}\right) . \tag{2.2}$$

Here, we set the electrical resistivity of the fresh water ρ_w to a typically observed value of 25 Ωm, and use for the empirical parameters a and m average values for unconsolidated sand of 0.88 and 1.37, respectively (Schön, 1998). For a better hands-on interpretation in terms of GPR wave propagation, we translate ε_r into GPR velocity v using $v = {c_0}/{\sqrt{\varepsilon_r}}$ with c_0 being the speed of light in vacuum. In Figure 2.2c, we show a selected 2D slice of the resulting 3D GPR velocity model. In Figure 2.2d, we visualize the same 2D slice in terms of electrical resistivity as calculated using Equation 2.2. The electrical parameter distributions predominantly show GPR velocity values between 0.07 and 0.085 ${}^{\mathrm{m}}/_{\mathrm{ns}}$ and

electrical resistivity values between 150 and 350 Ωm. Within the most porous well-sorted sands and gravels (S-x, GS-x) and the least porous matrix-supported gravels (Gcm and its variants), we observe extreme values down to $v \approx 0.06$ $^{m}/_{ns}$ and $\rho \approx 80$ Ωm and up to $v \approx 0.095$ $^{m}/_{ns}$ and $\rho \approx 500$ Ωm, respectively. Comparable values and associated variations of electrical properties are commonly observed in similar fresh-water saturated environments (e.g., Klotzsche et al., 2010; Hamann and Tronicke, 2014) and thus, we consider that our electrical parameter models closely resemble a typical sedimentary subsurface scenario.

The model discretization is a fundamental property of input models for FDTD GPR modeling. A rule-of-thumb typically applied to obtain adequate modeling results is that the discretization should be around ten times smaller than the smallest wavelength of the propagating electromagnetic wave field (Kunz and Luebbers, 1993). This wavelength depends on the minimum GPR velocity and the maximum frequency of the propagating waves, which is approximately 2-3 times as high as the nominal center frequency f_c of a typical broad-band GPR signal. For the chosen saturation scenario, we observe GPR velocities down to ~0.06 $^{m}/_{ns}$ (compare Figure 2.2c). For our modeling study, we choose a nominal center frequency $f_c = 100$ MHz typically employed in comparable sedimentological field applications (e.g., Beres et al., 1995). Thus, we determined a discretization of 0.025 m in all spatial dimensions for the given modeling situation, which has been realized in every model presented in this work (starting with a nearest neighbor interpolated version of the hydrofacies model as shown in Figure 2.1).

2.4. 3D GPR modeling

In this section, we briefly introduce the modeling tool gprMax as well as the key input parameters for 3D GPR modeling based on the subsurface scenario described in Subsection 2.3.2. Furthermore, we discuss a numerical approach to examine 3D effects within modeled GPR data and present the modeling strategy used to produce our synthetic 3D GPR reflection data set.

2.4.1. Modeling software and basic parameters

gprMax is open-source software to simulate the propagation of electromagnetic waves using the Finite-Difference Time-Domain (FDTD) method (Warren et al., 2016). This software is employed in a diverse range of applications; for example, to study GPR wave propagation in lossy environments (Loewer and Igel, 2016), to investigate the potential of GPR for landmine detection (Giannakis et al., 2016), or as a forward solver to inverse problems like full-waveform inversion of cross-hole GPR data (van der Kruk et al., 2018). Due to the nature of FDTD modeling schemes, especially 3D simulations require extensive computational resources in terms of processing time. A recent development within gprMax tackles this problem as the software now offers the possibility to model on graphics processing units (GPUs) within NVIDIA's CUDA-framework. As a result, calculations are now performed up to 30 times faster compared to a multi-core desktop

CPU using OpenMP parallelization (Warren et al., 2018). For the first time, this allows to model large and thus complex 3D GPR data sets consisting of thousands of single traces based on 3D subsurface models with millions of cells on a well-equipped work station without the need of costly high-performance computing resources. Here, we exploit this GPU-acceleration using gprMax v.3.1.4 to perform extensive 3D GPR modeling using our realistic model of subsurface sedimentary heterogeneities.

In the following, we introduce the key modeling parameters used in this work, whereas study-specific parameters are introduced where applied. As input, we set up a 3D model comprising the distributions of ε_r and the electrical conductivity $\sigma = 1/\rho$ associated with the distributions of v and ρ shown in Figures 2.2c-d. As discussed in Subsection 2.3.2, our model shows a discretization of 0.025 m and we assume $\sigma^* = 0$ and $\mu_r = 1$. Above the subsurface model, we insert an air layer (i.e., a material with $\varepsilon_r = 1$, $\sigma = 0$, $\sigma^* = 0$, and $\mu_r = 1$) with a thickness of 0.5 m. The thickness of the Perfectly Matched Layers (PMLs), which realize the absorbing boundary conditions, is set to 0.25 m in all spatial dimensions.

Up to now, no realistic antenna model with our desired nominal center frequency (i.e., $f_c = 100$ MHz) is available in gprMax. Hence, we assume a Hertzian dipole source, polarized perpendicular to the inline (x) direction, emitting a Ricker wavelet with unit amplitude. Considering both, our GPR velocity distribution (Figure 2.2c) and the maximum depth of the model, we infer a time window of $t = 200$ ns. The sampling interval $\Delta t \approx 0.048$ ns directly results from the model discretization considering the 3D stability condition for the FDTD method. We place all GPR sources/receivers on the air-subsurface boundary. For modeling GPR profiles, we realize a constant-offset GPR reflection geometry commonly employed in sedimentological applications, with a source-receiver offset of 0.5 m and an inline trace spacing of 0.05 m.

2.4.2. Examination of 3D effects

Having at hand both, a realistic 3D model of sedimentary heterogeneities and a modeling software allowing for efficient calculation of 3D electromagnetic wave fields, offers an up to now unique possibility to study 3D effects. Here, the term 3D effects comprises any phenomena related to energy originating from out-of-plane of a GPR profile acquired with a typical 2D constant-offset geometry. The following numerical approach allows us to assess and evaluate such 3D effects.

First, we select three locations in our model at $x/y = 5/5$, $8/6$, $10/4$ m around which we extract 3D sub-cuboids from the model with a size of 8 x 8 x 7 m (x, y, z). In the center of each sub-cuboid, we place a GPR profile with a length of 1 m (i.e., 21 traces), which is oriented along the x direction (Figure 2.4). This results in a minimum distance of 4 m in y direction between any GPR source/receiver and the boundary of the model domain enclosing each sub-cuboid. We start with modeling GPR data across these sub-cuboids fully containing 3D structures over a distance of $\Delta y_{3D} = 4$ m in y direction. Then, we iteratively decrease the extent of 3D structures to each side of the GPR profile (i.e., Δy_{3D}) by steps of 0.25 m while keeping each model domain at constant size of 8 x 8 x 7 m. For each step, we fill the remaining cells using replicates of the

respective outermost 2D (x-z) planes where 3D structures are found. This is repeated for each sub-cuboid until reaching the 2.5D case ($\Delta y_{3D} = 0$); i.e., a 3D model domain only comprising the 2D subsurface structures found directly beneath the GPR profile. In Figure 2.4, we illustrate this procedure by showcasing the modeling setup for the sub-cuboid around the study location $x/y = 5/5$ m for $\Delta y_{3D} = 2$ m; i.e., the case in which 3D structures, here shown in terms of GPR velocity, extend 2 m on each side of the GPR profile (air layer and PMLs not shown for simplicity).

To assess 3D effects in the modeled GPR profiles, we evaluate root mean square (rms) amplitudes. At each of the three locations and for every Δy_{3D}, we calculate the rms amplitude of each trace in a 170 ns time window (starting at 30 ns to suppress any effects related to high-energy direct arrivals), and average the resulting 21 rms values of each GPR profile. Figure 2.5 shows these averaged rms values calculated for each simulated GPR profile as a function of Δy_{3D} at every of the three locations. To ease the interpretation, the mean rms values are normalized to the according value calculated for $\Delta y_{3D} = 4$ m at each study location (i.e., the associated sub-cuboid completely contains 3D structures).

When analyzing Figure 2.5, we see that our modeled GPR data exhibit 3D effects. At each study location, this becomes clear as for Δy_{3D} larger than ~1.5 m, the normalized mean rms values show a high stability (i.e., no significant deviations compared to the case

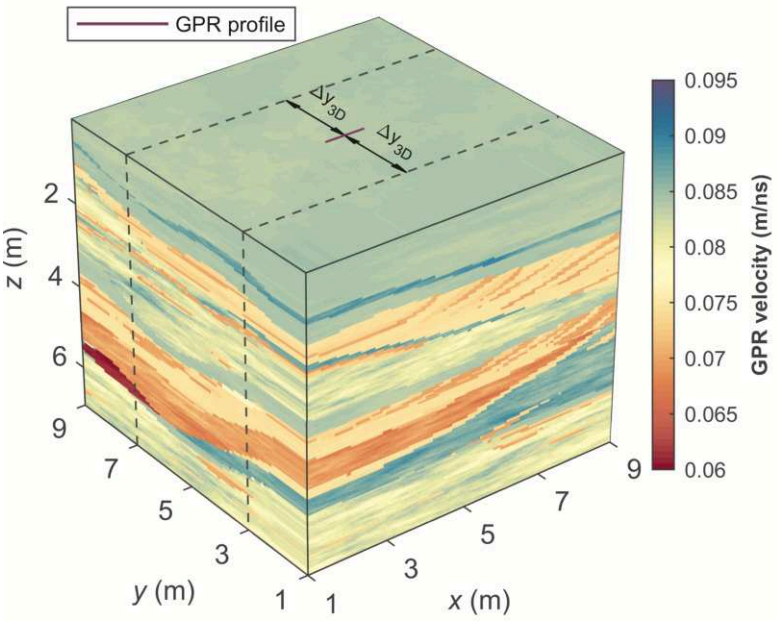

Figure 2.4.: Modeling setup used to examine 3D effects in our simulated GPR data. Here, we display the case $\Delta y_{3D} = 2$ m at the study location $x/y = 5/5$ m in terms of GPR velocity; i.e., 3D structures extend 2 m in y direction to each side of a GPR profile located in the center part of the model sub-cuboid. Air layer and PMLs not shown for simplicity.

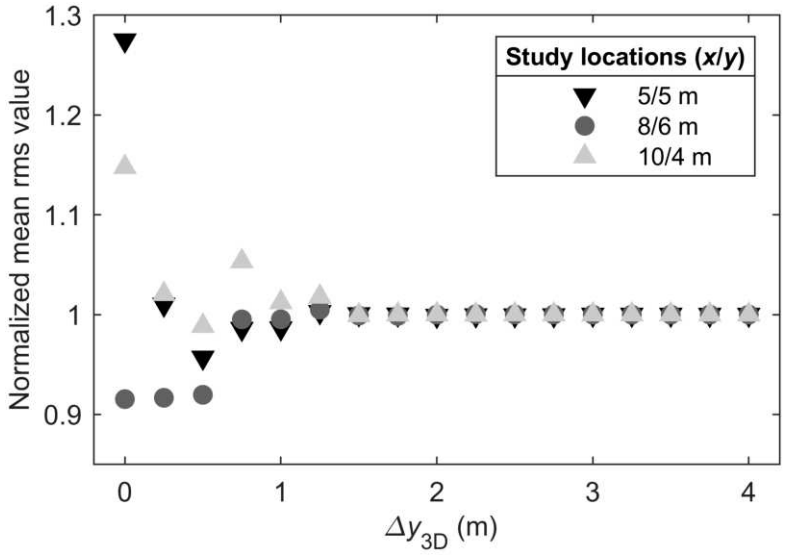

Figure 2.5.: Examination of 3D effects at three study locations. Mean rms amplitude values of each GPR profile as a function of Δy_{3D}. Values are normalized to the according rms value observed for $\Delta y_{3D} = 4$ m at each study location.

$\Delta y_{3D} = 4$ m), whereas with decreasing Δy_{3D} these values show a considerable scatter with deviations up to ~25 % related to 3D effects absent in the underlying GPR data. Hence, for the given subsurface model and GPR parameter configuration we conclude that (1) simulating GPR data in a 3D fashion is indispensable to fully capture 3D wave-propagation phenomena, and (2) the major source of reflected energy present in the GPR data extends ~1.5 m in crossline direction of a GPR profile.

2.4.3. Modeling strategy

To formulate a suitable strategy for modeling our extensive 3D GPR reflection data set, we consider the findings from Subsection 2.4.2 as well as the required RAM (commonly a limiting factor on GPUs) and calculation time, which both depend on the number of cells in a model domain. Accordingly, we decompose the full 3D model into three separate, equally sized sub-cuboids. These include the full x and z dimensions of the model and range from $y = 0$ - 6 m, 2 - 8 m and 4 - 10 m; i.e., the sub-cuboids show an overlap of 4 m in y direction. Using these sub-cuboids, we model a total of 51 GPR profiles along the full x dimension and with a crossline trace spacing of 0.2 m from $y = 0$ - 4 m, between $y = 4$ - 6 m, and from $y = 6$ - 10 m, respectively. Thus, we assure a minimum distance of 2 m in y direction between the GPR profiles and the border of 3D structures within each sub-cuboid wherever applicable. Consequently, considering the analyses of Figure 2.5, we assume that our modeled GPR data show a maximum of 3D character though using three separate model sub-cuboids. To assure that each GPR source/receiver is located at an adequate distance from every domain border, we additionally pad the sub-cuboids in

the horizontal directions by 0.5 m (where necessary) using replicates of the outermost 2D (x-z and y-z) planes.

A result of this modeling strategy is the uni-dimensional reduction in model domain size which, in turn, linearly decreases the calculation time. Moreover, our strategy ensures that each of the three sub-cuboids fits onto a single GPU RAM and enables us to use three NVIDIA GPUs (1x GeForce GTX1070, 2x Tesla K80, hosted by different workstations) to split the calculation tasks (i.e., one model sub-cuboid per GPU). The simultaneous use of three GPUs again decreases the overall calculation time significantly. Consequently, the complete simulation task comprising a total of 15810 traces has been performed within approximately one month. In Table 2.2, we sum up the key parameters characterizing our 3D GPR reflection data set, which we obtain by merging the three data sets individually simulated across the model sub-cuboids.

Common field practice is to complement constant-offset GPR data sets by performing experiments with a common-midpoint (CMP) geometry at selected locations. An analysis of GPR reflections observed within a CMP gather yields an estimate of the subsurface GPR velocity model which then, for example, can be used for migration of the corresponding constant-offset GPR reflection data set. Thus, we simulate a CMP gather with a center location at $x/y = 8/8$ m across the according 3D model sub-cuboid ranging from $y = 4$ - 10 m. This CMP gather is modeled along the x direction with a trace interval of 0.05 m and shows a maximum source-receiver offset of 5 m.

2.5. Results and interpretation

In this section, we present and interpret the results of our 3D GPR modeling exercise based on a realistic sedimentary subsurface scenario (Figures 2.2c-d) and discuss some of many conceivable applications when having at hand both, a realistic 3D subsurface model and the corresponding modeled GPR reflection data.

In Figure 2.6a, we show a representative 2D slice of the unprocessed 3D GPR data (along the same profile shown in Figure 2.2). This modeling result reveals that the multi-scale and multi-magnitude heterogeneities within the underlying electrical parameter

Table 2.2.: Key parameters describing our simulated 3D GPR reflection data set, which comprises a total of 15810 traces (51 profiles, 310 traces each).

Parameter	**Value**
Input model size (x, y, z)	16 x 10 x 7 m
Input model discretization	0.025 m
Sampling interval	~0.048 ns
Time window	200 ns
Nominal center frequency	100 MHz
Source-receiver offset	0.50 m
Inline trace spacing	0.05 m
Crossline trace spacing	0.20 m

fields result in GPR data with a realistic appearance and character. Beyond the high-energetic direct arrivals dominating travel times up to ~30 ns, we notice a large variety of commonly observed reflection patterns ranging from (semi-)continuous reflection structures to complex diffraction and interference phenomena.

To provide a typical GPR depth image (as expected in a corresponding field study), we apply a standard 3D GPR processing sequence including time zero correction, removal of direct arrivals, frequency filtering, 3D Kirchhoff migration and amplitude scaling (e.g., Allroggen et al., 2015; Schennen et al., 2016). As an example for the further use of our 3D model and following common field practice, we generated a CMP gather (Subsection 2.4.3) to estimate a subsurface GPR velocity model for our Kirchhoff migration. Figures 2.7a-b illustrate the result of a reflection-based spectral velocity analysis and the underlying modeled CMP gather, respectively. Hence, considering typical uncertainties of such analyses (e.g., Hamann et al., 2013), we conclude that a constant GPR velocity of 0.085 $^{m}/_{ns}$ characterizes the subsurface velocity field. This is in well agreement with the GPR velocities present in the model (compare Figure 2.2c) and thus, this constant velocity is used to perform the 3D Kirchhoff migration and the time-to-depth conversion of our data.

From the resulting 3D GPR depth image we extract the same profile shown in Figure 2.6a and present it in Figure 2.6b. To emphasize the 3D character of the GPR depth image, we visualize it in Figure 2.8 using the same perspective display chosen for the hydrofacies model shown in Figure 2.1. Comparing unprocessed and processed data reveals that diffracted energy (visible as hyperbolic events in Figure 2.6a) has been collapsed and spatial positions of reflections have been corrected in the course of 3D migration. In the GPR depth image, we clearly recognize sedimentary structures such as the shallow accretionary elements (hydrofacies sGcm embedded within Gcm) imaged by a slightly undulating reflection, or the cut-and-fill sequences in the central part of the model (shown in yellow and green colors in Figure 2.1) marked by gently dipping reflection patterns striking in y direction. Although a detailed interpretation of these results is beyond the scope of this work, we highlight the unique possibility to obtain a deeper understanding on the relations between subsurface structures within a realistic sedimentary scenario and the resultant reflection patterns in GPR images. To demonstrate this, we show in Figure 2.6c the GPR depth slice of Figure 2.6b together with the input GPR velocity model (equivalent to Figure 2.2c) as transparent overlay. Figure 2.6c emphasizes that (1) our GPR data are in good agreement with the input model, and (2) especially shallow, large-scale features like (semi-)horizontal interfaces as well as dipping structures (e.g., above, within, and beneath the cut-and-fill sequences) have been accurately imaged according to their depth, shape, dip, and spatial extend (compare Figures 2.1 and 2.8). Though, (3) we also notice effects of decreasing resolution with increasing depth inherent for the GPR method. This can be observed at features whose extend is beyond local GPR resolution; for example, in regions where small-scale GPR velocity variations evoked by high-wavenumber, high-magnitude porosity variations (Subsection 2.3.1) occur. Those features are repeatedly found in the deeper parts of the

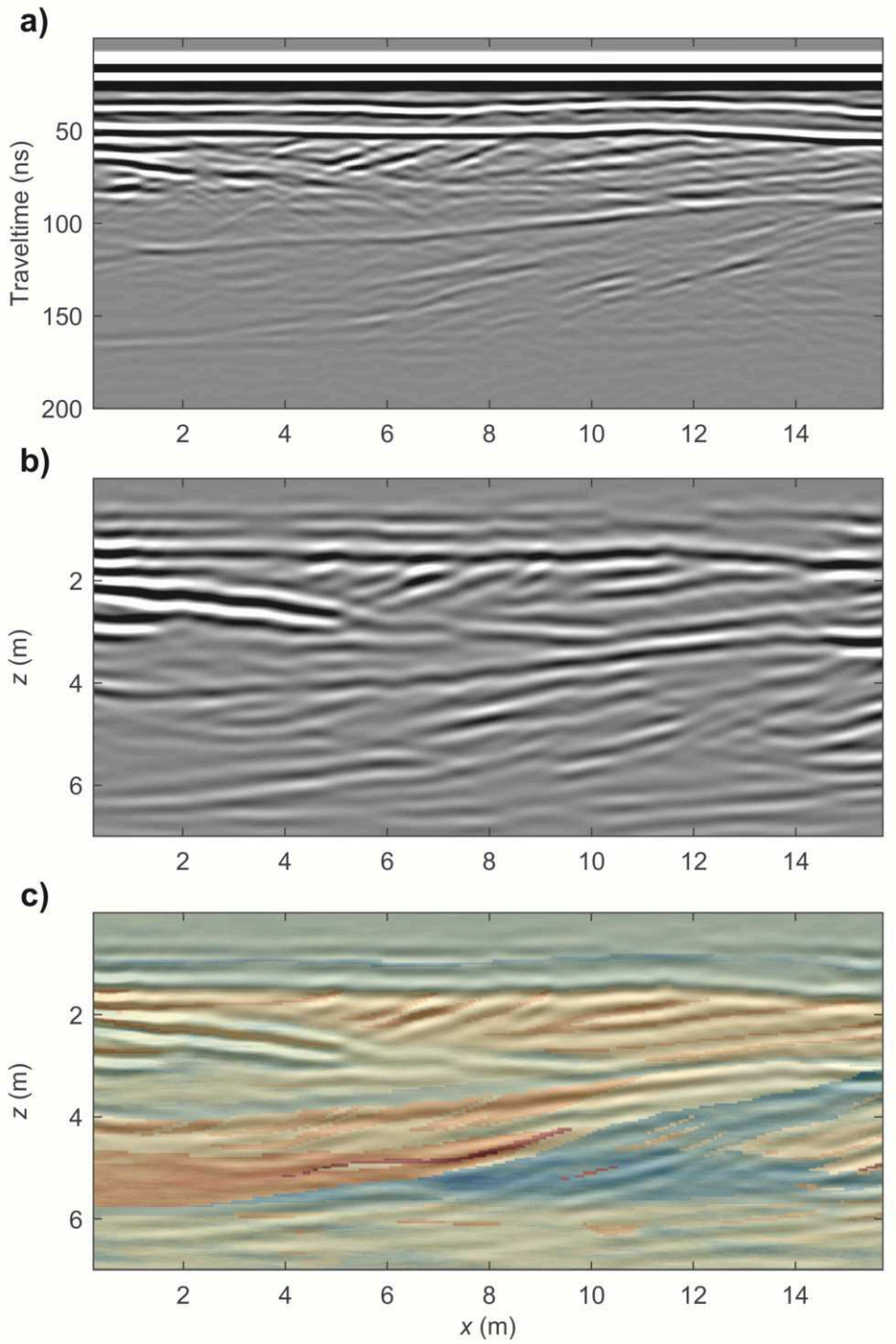

Figure 2.6.: Typical 2D profile slices at $y = 6$ m of (a) unprocessed 3D GPR reflection data set, (b) 3D processed GPR depth image, and (c) same as (b) with GPR velocity model (Figure 2.2c) as transparent overlay.

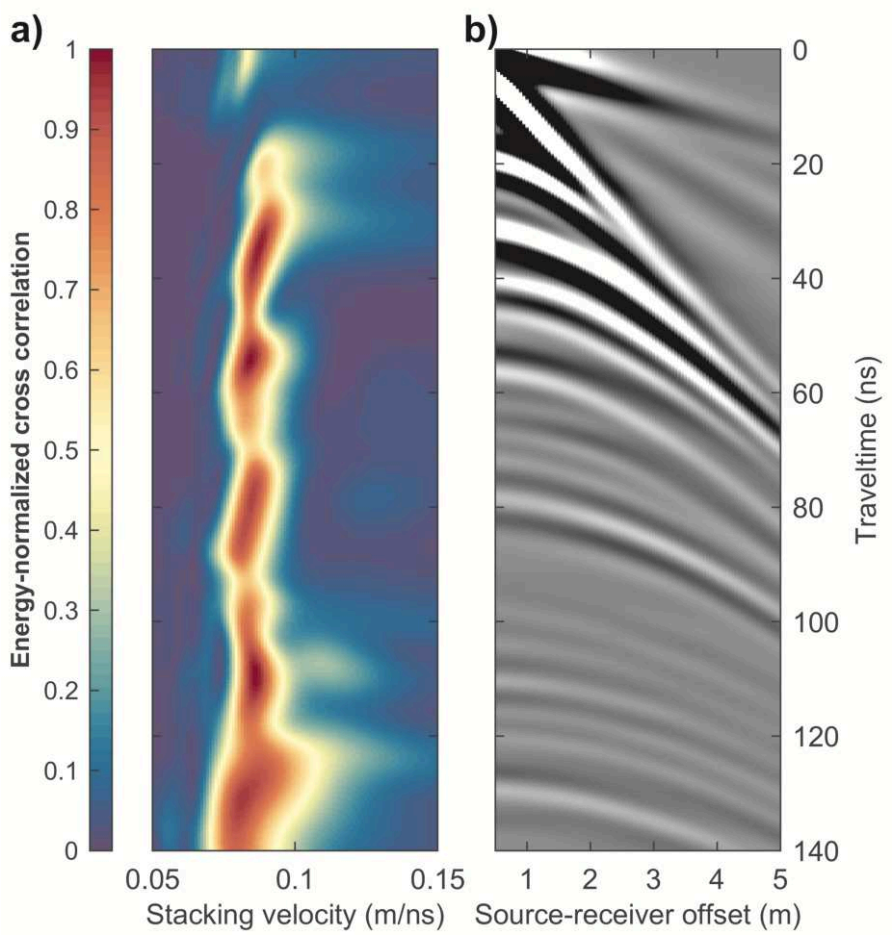

Figure 2.7.: (a) Result of a reflection-based spectral velocity analysis of (b) synthetic 3D CMP gather with a center location at $x/y = 8/8$ m modeled along the x direction.

model and produce complex interference phenomena which, in turn, entail fragmentary reflection patterns, and thus complicate a standard reflection-based interpretation.

2.6. Conclusions

We have demonstrated the viability of modeling extensive 3D GPR data based on a realistic sedimentary subsurface scenario. We used publicly available hydrofacies data from an aquifer-analog study to infer a realistic, high-resolution 3D porosity model, which exhibits heterogeneities down to the sub-facies scale. Recent developments within open-source electromagnetic modeling software gprMax (now including time-efficient GPU-accelerated solvers) allowed us to extensively model 3D GPR data across such a large and realistic sedimentary model for the first time. We have proposed a numerical approach to obtain a deeper understanding of 3D effects in modeled GPR data. The

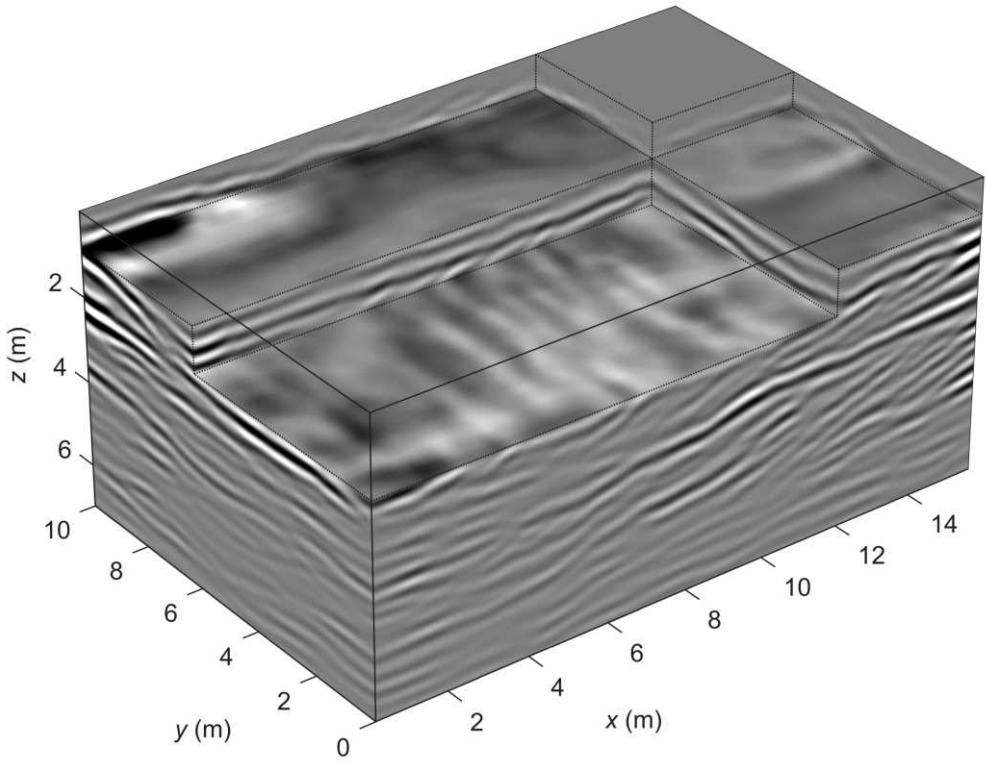

Figure 2.8.: A 3D view across processed GPR depth image. For comparability, we use the same perspective display chosen for the hydrofacies model in Figure 2.1.

results of this study have been considered when performing a spatial decomposition of the model in order to enable a computationally efficient 3D modeling of an extensive GPR reflection data set. The application of a standard 3D GPR processing sequence including the analysis of a 3D modeled common-midpoint experiment provided a realistic, high-resolution structural depth image. Our results are in good agreement with the input model thus demonstrating the feasibility and the potential of our modeling studies.

The subsurface model exhibits a large variety of realistic sedimentary features at different spatial scales. This includes thin, quasi-continuous interfaces as well as dipping layer sequences showing subtle to strong electrical parameter contrasts. Especially at greater depths, the resulting GPR reflection data show numerous fragmented reflection elements and interference patterns which make them, together with the model, a challenging and thus ideal target and reference to test and evaluate novel (3D) GPR processing and interpretation methods. For example, this may include the evaluation of amplitude scaling strategies, filtering, migration, or deconvolution algorithms as well as benchmarking innovative techniques aiming at a quantitative amplitude interpretation (e.g., to infer geophysical subsurface parameters), or the investigation of different interpretation approaches of structural GPR images. The provided porosity model can form a basis to generate complementary data sets using different GPR frequencies

and source types, acquisition geometries (as indicated by our CMP example), and/or using additional geophysical exploration methods (electrical resistivity tomography, electromagnetic induction etc.) to formulate and reference approaches of an integrated geophysical interpretation. Moreover, this subsurface model can be adjusted and perturbed in a study-specific manner; for example, to explore different saturation scenarios (e.g., when combined with realistic subsurface flow models), to investigate effects of higher-order realistic media (e.g., by incorporating frequency-dependent properties using a Debye relaxation model), or to study the detectability of objects such as unexploded ordnance (UXO) or utility pipes buried within a realistic sedimentary background. In conclusion, we expect our 3D modeling studies as well as our publicly available GPR reflection data set and porosity model to pose a beneficial input to the research community.

2.7. Data and computer code availability

Data associated with this article as well as basic MATLAB and python code to read and visualize these data can be found at doi:10.17632/by3yh79hx4.1, an open-source online data repository hosted at Mendeley Data (Koyan and Tronicke, 2019). The 3D GPR modeling presented in this work has been performed using gprMax v.3.1.4, an open-source electromagnetic modeling software (Warren et al., 2016, 2018) which can be found at https://github.com/gprmax/gprMax.

3. Analyzing 3D multi-frequency ground-penetrating radar (GPR) data simulated across a realistic sedimentary model

Philipp Koyan and Jens Tronicke*

3.1. Introduction

Ground-penetrating radar (GPR) is an established geophysical tool to image and characterize near-surface sedimentary environments (Neal, 2004). A major benefit of GPR is its flexibility in terms of selecting the source frequency, which controls the wavelength of the propagating signal and, thus, the vertical and horizontal resolution capabilities of the data affecting the level of detail in the resulting structural images or petrophysical parameter models. Synthetic 2D GPR data including the underlying petrophysical parameter models are frequently used to evaluate, develop, and reference novel data processing, analysis, and interpretation techniques (e.g., Bitri and Grandjean, 1998; Ernst et al., 2007; Allroggen and Tronicke, 2016). Today, novel GPU-acceleration featured in the open-source electromagnetic modeling software gprMax (Warren et al., 2016, 2018) and the steady progress in computer hardware enable a time-efficient simulation of densely sampled 3D GPR data sets. Koyan and Tronicke (2020a) exploit these novelties and use a realistic sedimentary model to simulate, for the first time, a publicly available constant offset (CO) 3D GPR data set (100 MHz). In this study, we use this model to generate complementary CO GPR data sets with source frequencies of 50 MHz and 200 MHz, which are also typically employed in sedimentary field applications. Furthermore, we simulate multi-frequency common midpoint (CMP) data. As an exemplary use of this multi-frequency GPR database, we apply a standard processing flow as typically used to analyze CO and CMP GPR data collected in sedimentological applications. We evaluate and compare our results and conclude on possible benefits of multi- frequency GPR data acquisition in sedimentological field campaigns.

*A reviewed expanded abstract of the same title is published as Koyan and Tronicke (2020b) in the proceedings of 18th International Conference on Ground Penetrating Radar, SEG, Global Meeting Abstracts, 275–278.

3.2. Model setup and modeling strategy

As input for simulating multi-frequency GPR data, we use a realistic 3D electrical parameter model as generated by Koyan and Tronicke (2020a), which we show in Figure 3.1 in terms of GPR velocity. This model bases on a publicly available hydrofacies data set, which has been derived from sedimentological outcrop mapping, direct sampling, and geostatistical simulation of an aquifer-analog at the Herten gravel pit (SW Germany; Bayer et al., 2011; Comunian et al., 2011). Using available porosity data (Bayer et al., 2011) and assuming fresh-water saturated sediments, Koyan and Tronicke (2020a) generate a 3D electrical property model of this field site comprising GPR velocity and electrical resistivity. Within a volume of 16 x 10 x 7 m, the model shows a large variety of typical sedimentary features on multiple spatial scales. We follow Bayer et al. (2011) to characterize the main genetic units I-VI highlighted in Figure 3.1. Units I, II and IV show medium to high velocities related to accretionary elements consisting of sand-rich gravels. These units include small patches of partially cross-bedded open-framework gravels resulting in local low-velocity zones. Units III and V show overall low velocities and comprise cut-and-fill elements marked by sequences of alternating bimodal and open-framework gravels. Unit VI marks a near-surface high-velocity zone and is formed by accretionary elements consisting of continuous, (sub-)horizontally stratified gravel sheets. Taking advantage of a novel GPU engine featured in gprMax, Koyan and Tronicke (2020a) use the model presented in Figure 3.1 to simulate a publicly available 100 MHz CO GPR data set across the entire model surface. In this study, we complement this data set by modeling comparable CO data sets with a source frequency of 50 and 200 MHz. To model GPR data, we use a Hertzian dipole source polarized perpendicular to the inline (x) direction, add an air layer with a thickness of 0.5 m above the surface, and place all sources and receivers directly onto the air- subsurface boundary. In Table 3.1, we sum up the basic modeling parameters used to simulate the 3D CO data sets.

For the first time, GPU-based modeling facilitates a time- efficient simulation of extensive 3D GPR data sets typically comprising thousands of single source positions. However, the available RAM of even modern GPUs might become a limiting factor

Table 3.1.: Modeling parameters used to simulate 3D GPR constant offset data sets, each comprising a total of 51 profiles.

Parameter	**Value**
Source frequency	50/100/200 MHz
Model discretization	0.05/0.025/0.0125 m
Model size	9.6/77/614 MCells
Time Window	250/200/200 ns
Source-receiver offset	0.8/0.5/0.5 m
Inline trace spacing	0.1/0.05/0.05 m
Crossline trace spacing	0.2 m
Number of traces	7752/15810/15810

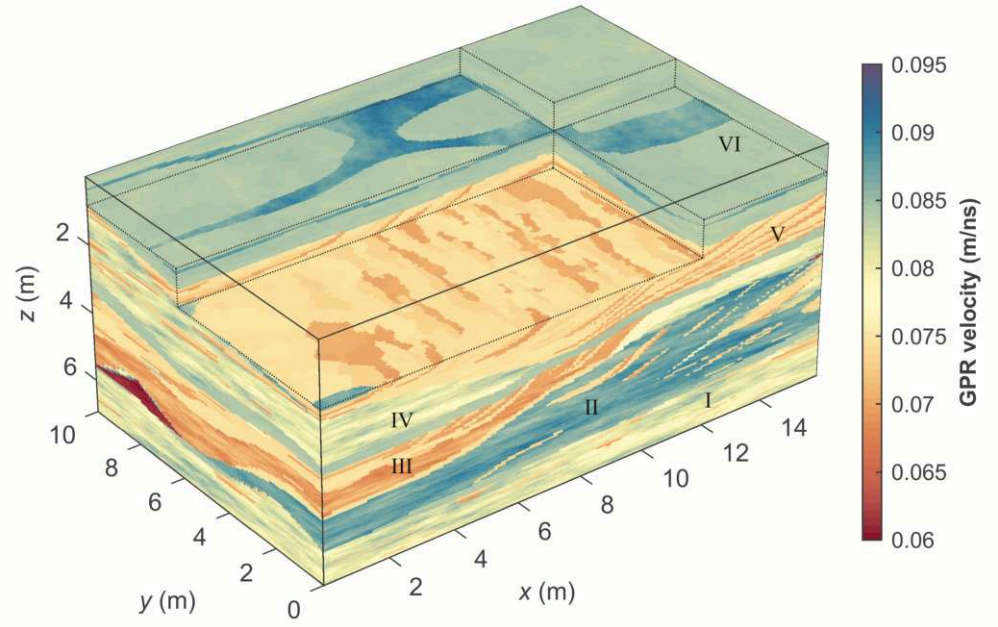

Figure 3.1.: Model of the Herten field site in terms of GPR velocity used as input for modeling GPR data. The main genetic units are labeled from I to VI (for details see text).

for generating such 3D data sets. To perform the modeling procedure as efficient as possible, we adjust the input model discretization and, thus, the number of cells in the model considering the velocity distribution (Figure 3.1) and the source frequency content. Nevertheless, only the input model with a discretization of 0.05 m fits onto a modern GPU RAM and, thus, solely the 50 MHz CO data set can be modeled in a single run within approximately one week. To simulate the 200 MHz CO data set, we follow Koyan and Tronicke (2020a) and perform a model decomposition taking into consideration the results of an examination of 3D effects in modeled 200 MHz CO data. Accordingly, we iteratively decompose the full model into sub-cuboids with a size of 4.5 x 4 x 7.5 m (x, y, z), whose central x and y positions resemble the trace locations of the corresponding 100 MHz CO data set (Koyan and Tronicke, 2020a). For each iteration, we simulate a single GPR trace in the center of the according model sub-cuboid. Thus, we (1) assure that each sub-cuboid fits onto a single GPU RAM and (2) preserve the 3D character in the resulting 200 MHz CO data set, which has been modeled within approximately 10 weeks using two modern GPUs simultaneously. Sedimentological GPR field campaigns typically include CMP surveys at selected representative locations; for example, to obtain a GPR velocity model for migration and time-to-depth conversion of the corresponding CO data. Thus, we also model CMP data using source frequencies of 50, 100, and 200 MHz across the corresponding input models (Table 1). The three CMP gathers are oriented along the x direction, and are modeled around a center position at $x/y = 8/5$ m using a maximum source-receiver offset of 5 m, and a trace spacing of 0.05 m.

3.3. Modeling results and interpretation

As a result of our 3D modeling exercises, we obtain a 50 MHz and 200 MHz CO data set across the entire model surface, of which we show in Figure 3.2 typical 2D time sections at $y = 6$ m together with the 100 MHz data from Koyan and Tronicke (2020a). In general, all synthetic GPR data show a realistic appearance and exhibit a large variety of typical sedimentary reflection patterns including (semi-) continuous horizontal to dipping reflections, diffraction events, and interference phenomena. With increasing source frequency both the vertical and the horizontal resolution in the GPR time sections increase. This becomes also evident in the according CMP data, which we show in Figure 3.3 together with the corresponding velocity spectra resulting from standard reflection-based spectral velocity analyses. In general, these spectra exhibit comparable rms- velocity functions as indicated by maximum coherence values around 0.085 m/ns. With increasing frequency, the spectral resolution in both velocity and time dimension increases, and we observe significantly sharper maxima indicating better defined velocity and traveltime values at the corresponding coherence maxima. The 50 MHz CMP data show well-separated reflections resulting in five distinct peaks in the corresponding spectrum highlighting the architecture of the main genetic units (Figure 3.1). In the 100 MHz and 200 MHz gathers, we observe additional reflections providing more in-depth information on layer- internal structures. However, a more detailed analysis reveals that with increasing frequency the according spectra, especially for the 200 MHz data, are increasingly contaminated by energy resulting from interference phenomena (e.g., around traveltimes of 160 ns in Figure 3.3c. This complicates an interpretation in terms of meaningful subsurface velocity variations and, without any prior knowledge on the subsurface architecture (e.g., as obtained from the 50 MHz CMP data), could lead to erroneous picks in the spectra which, in turn, result in erroneous rms velocity functions.

As an application example for the simulated CO data sets, we employ a typical structural imaging processing flow including 3D migration to obtain 3D GPR depth images as they could have been expected in an according sedimentological field campaign. Based on our CMP results, we use a constant rms velocity of 0.085 m/ns to perform the migration and time-to-depth conversion of our CO data sets. In Figure 3.4, we present on top the same 2D slice shown in Figure 3.2 and an example depth slice at $z = 2.4$ m (bottom) of the GPR velocity model in Figure 3.4a and the corresponding GPR depth images in Figure 3.4b-figure 3.4d. In general, the processing results are in well agreement with the input model as they realistically image the subsurface and, thus, illustrate a reasonable modeling and processing procedure. The depth images accentuate the frequency-related resolution capabilities and interference phenomena already discussed for the CMP data. Regarding a structural imaging, the 50 MHz and 100 MHz depth images highlight the main subsurface architecture by well-pronounced, quasi-continuous reflections. However, the limits of resolution of the 50 MHz data become evident when comparing the imaging of the interface between units IV and V in Figure 3.4b-figure 3.4d, especially in the presented depth slices. In contrast, the 200 MHz data provide the highest resolution showing numerous small-scale internal structures but also exhibit a

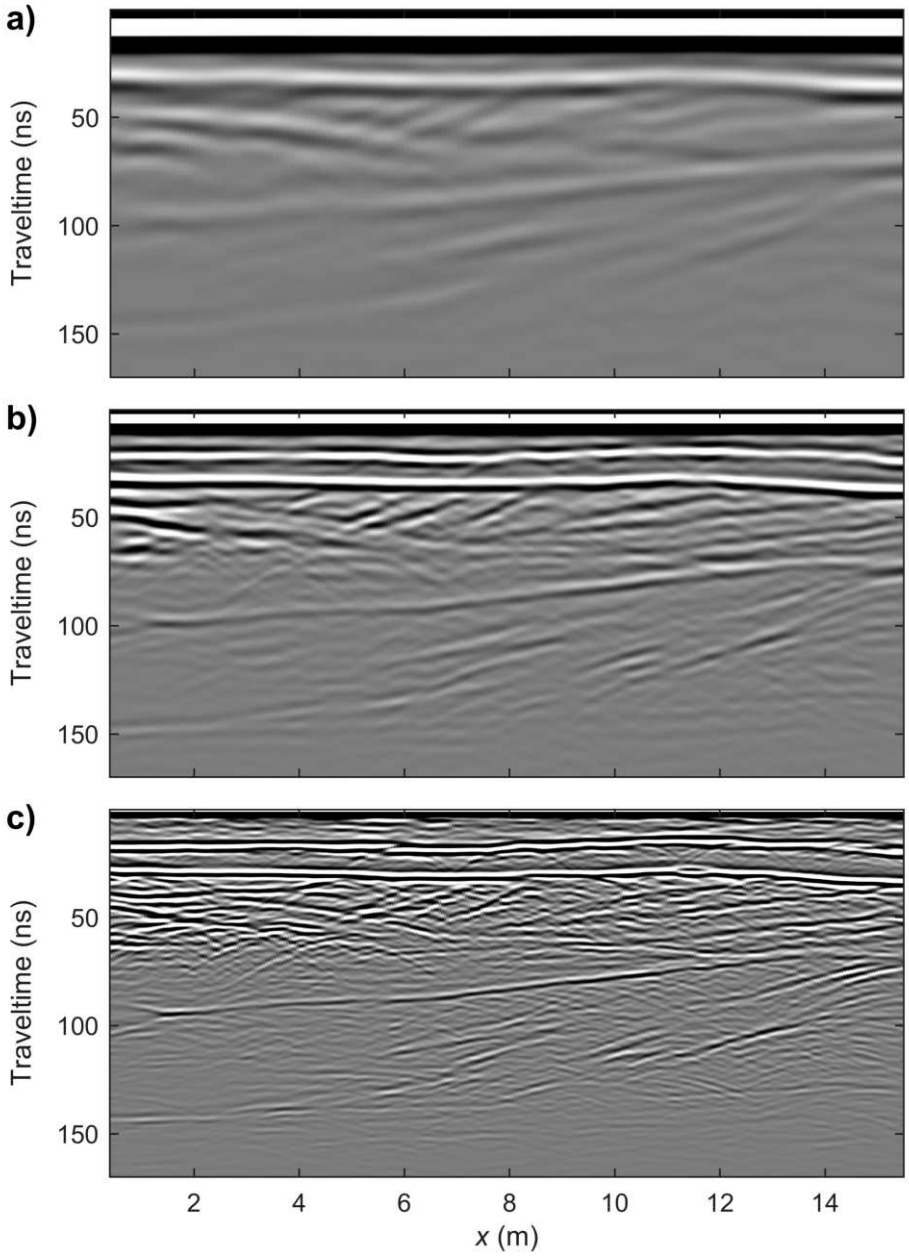

Figure 3.2.: Typical 2D time sections at $y = 6$ m of unprocessed GPR data with a source frequency of (a) 50 MHz, (b) 100 MHz (Koyan and Tronicke, 2020a), and (c) 200 MHz. For comparability in terms of traveltime, we show the data after time-zero correction.

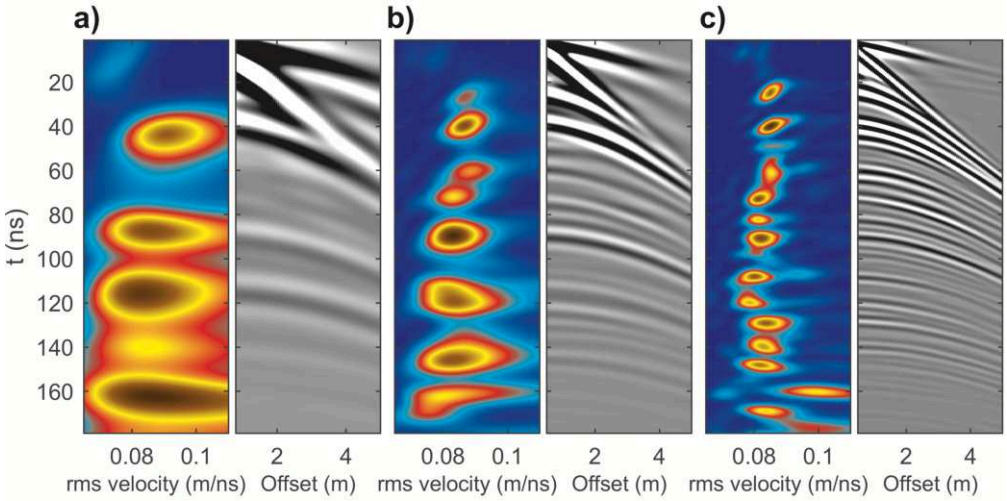

Figure 3.3.: Synthetic CMP data sets centered at $(x/y) = 8/5$ m with a source frequency of (a) 50 MHz, (b) 100 MHz, and (c) 200 MHz. To the left of the CMP gathers, we show the velocity spectra resulting from a reflection-based spectral velocity analysis (yellowish-brown values indicate high coherence values).

large variety of complex interference patterns. Especially the latter might complicate a structural interpretation in terms of separating main sedimentological units without any further information on the subsurface architecture (e.g., as obtained by analyzing the 50 MHz or 100 MHz GPR data).

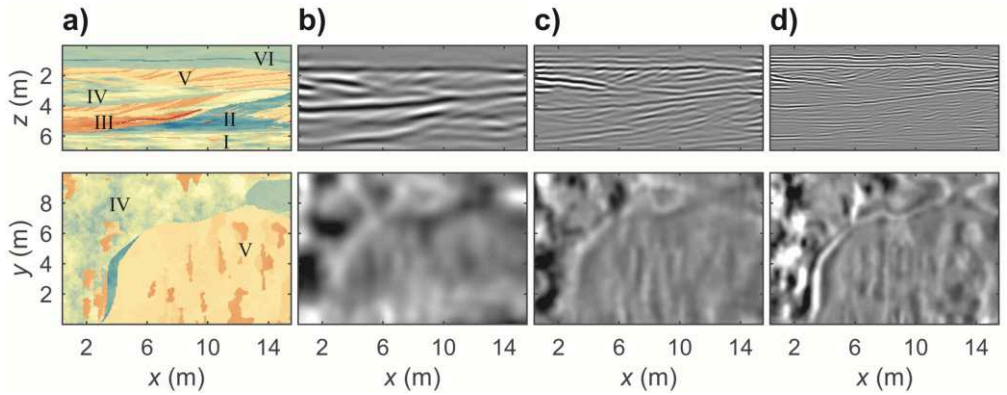

Figure 3.4.: Typical 2D profile slices at $y = 6$ m (top) and depth slices at $z = 2.4$ m (bottom) of (a) GPR velocity model (same color scaling as used in Figure 3.1), and GPR depth images obtained from the data simulated with a source frequency of (b) 50 MHz, (c) 100 MHz, and (d) 200 MHz.

3.4. Conclusions

In this study, we have demonstrated the viability of modeling densely sampled 3D multi-frequency GPR data using a realistic sedimentary model. Typical analyses of synthetic constant offset and common midpoint GPR data sets show that, especially in such highly heterogeneous sedimentary environments, using only a high source frequency does not always yield the most meaningful results. On the contrary, our synthetic case study illustrates that the results obtained by analyzing multi-frequency GPR data complement each other as both 50 MHz and 100 MHz data primarily highlight the main interfaces and roughly indicate internal structures. Analyzing these data sets provides fundamental information about the large-scale subsurface architecture which, then, eases and facilitates a reliable interpretation of the 200 MHz data. These data show a significantly higher degree of detail more accentuating internal structures and, thus, might be best suitable for advanced interpretation techniques such as GPR facies (e.g., Van Overmeeren, 1998) or attribute-based analyses. Hence, we conclude that it is desirable to acquire and analyze multi-frequency GPR data (e.g., using modern multi-channel instruments) in comparable sedimentological field studies. Using such a strategy may prevent possible misinterpretations, facilitates a data interpretation from large to small scales and, thus, provides a comprehensive understanding of the investigated sedimentary system. To support future geophysical and GPR developments, the input model and the 100 MHz CO data set (in HDF5 and VTK data format) including MATLAB and python scripts to read and visualize these data can be found at http://dx.doi.org/10.17632/by3yh79hx4.1, a publicly available data set hosted at Mendeley Data (Koyan and Tronicke, 2019).

4. 3D ground-penetrating radar data analysis and interpretation using attributes based on the gradient structure tensor

Philipp Koyan and Jens Tronicke*

4.1. Abstract

In near-surface geophysics, ground-penetrating radar (GPR) surveys are routinely employed in a variety of applications including those from archaeology, civil engineering, hydrology, and soil science. Thanks to recent technical developments in GPR instrumentation and antenna design, 3D surveys comprising several 100.000 traces can be performed daily. Especially in complex environments such as sedimentary systems, analyzing and interpreting the resulting GPR volumes is a time-consuming and laborious task that is still largely performed manually. In the last decades, several data attributes have been proposed to guide and improve such tasks and assure a higher degree of reproducibility in the resulting interpretations. Many of these attributes have been developed in image processing or computer vision and are routinely used, for example, in reflection seismic data interpretation.

Especially in sedimentary systems, variations in the subsurface are accompanied by variations of GPR reflections in terms of amplitudes, continuity, and geometry in view of dip angle and direction. A promising tool to analyze such structural features is known as the gradient structure tensor (GST). Up to today, the application of the GST approach is limited to a few 2D GPR examples. Thus, we take up the basic idea of GST analysis and introduce and evaluate the corresponding attributes to analyze 3D GPR data. We apply the proposed GST approach to one synthetic and two field data sets imaging diverse sedimentary structures. Our results demonstrate that the proposed set of GST-based attributes can be efficiently computed in 3D and that these attributes represent versatile measures to address different typical interpretation tasks and, thus, help for an efficient, reproducible, and more objective interpretation of 3D GPR data.

*A journal article of the same title has been submitted as Koyan and Tronicke (2023a) to Geophysics on November 7, 2023.

4.2. Introduction

In various applications, ground-penetrating radar (GPR) is a well-established geophysical tool to image near-surface structures (e.g., Daniels, 2004; Annan, 2005b). Typical subsurface target structures include natural geological features such as soil horizons, sedimentary layering, or faults and fracture systems (e.g., Knight, 2001; Bristow and Jol, 2003; Neal, 2004; Jol, 2009). If a detailed and accurate three-dimensional (3D) image is required, 3D GPR surveying is increasingly used. Today, 3D GPR data acquisition relies on kinematic surveying strategies that combine a single- or multi-channel GPR instrument with modern surveying technology such as global positioning systems (GPS; Aaltonen and Nissen, 2002) or tracking total stations (TTS; Böniger and Tronicke, 2010b). In practice, most 3D data sets are recorded using common-offset antenna configurations moved along numerous approximately parallel lines with dense in- and cross-line trace spacing to avoid spatial aliasing (Lehmann and Green, 1999; Grasmueck et al., 2005).

Processing 3D GPR data sets aims at maximizing the information content (in terms of resolution and signal-to-noise ratio) and the quality of the final 3D structural image (in terms of reflector positioning and geometry), as needed to derive a detailed subsurface model. Thus, a typical 3D processing sequence includes standard trace-based processing steps such as zero-time correction, frequency domain band-pass filtering, and amplitude scaling (e.g., Annan, 2005b; Cassidy, 2009). For kinematic data sets, the recorded irregularly spaced traces have to be interpolated to a regular grid after correcting the GPS/TTS positioning data for latencies (i.e., the time delay between the positional measurement and its availability to the geophysical instrument; Böniger and Tronicke, 2010b). Furthermore, if the data are collected in areas of rugged topography, we also have to correct for the position of the GPS receiver (or TTS prism) in relation to the midpoint of the antenna pair to obtain accurate trace coordinates (Lehmann and Green, 1999). After gridding the data, the application of a 3D migration scheme is necessary to move dipping reflections to their correct position, unravel crossing events, and collapse diffractions (Yılmaz, 2001). Because topographic variations can be easily in the order of the target depths and GPR velocities often vary by more than a factor of two within near-surface environments, 3D migration schemes explicitly considering surface topography and subsurface velocity variations are commonly recommended (Allroggen et al., 2015). For specific processing tasks, the outlined basic processing flow is often complemented by additional pre- and post-migration processing steps that, for example, aim at enhancing the data frequency content (e.g., Irving and Knight, 2003; Belina et al., 2009; Economou and Vafidis, 2012) or at suppressing coherent source-generated noise (e.g., Grasmueck, 1996; Nuzzo and Quarta, 2004; Kim et al., 2007; Wang and Liu, 2017).

The interpretation of processed 3D GPR data is similar to the basic concepts used for interpreting reflection seismic data; i.e., after 3D migration, we assume that the data volume represents a reliable image of subsurface impedance contrasts (reflecting bounding surfaces and other heterogeneities) from which a subsurface model can be derived (Yılmaz, 2001). Today, this strategy is largely supported by (interactive) 3D visualizations also using software solutions originally developed for analyzing 3D seismic

data. Depending on the application, the actual structural interpretation relies on three different strategies including (1) reflector selection and tracking (e.g., to outline target geological horizons; Schmelzbach et al., 2011), (2) identifying and isolating abrupt changes along reflectors (e.g., to highlight edges of buried objects; Trinks and Hinterleitner, 2020), and (3) delineating units of characteristic reflection patterns (e.g., to identify GPR facies in sedimentary environments; Corbeanu et al., 2004). Today, these concepts are often supported by selected attributes (Tronicke and Böniger, 2013; Manataki et al., 2021); i.e., measures calculated or extracted from the data that help to enhance or quantify features of interpretation interest (Chopra and Marfurt, 2007). In the seismic literature, a variety of attributes have been proposed for analyzing post-stack seismic data (Barnes, 2016) and some of these measures have also been successfully used to aid GPR data interpretation. For example, Dossi et al. (2015) use the cosine of the instantaneous phase as an attribute to pick locally continuous reflection events in an automated fashion, while Böniger and Tronicke (2010a) use similarity as a multi-trace attribute to highlight discontinuities and, thus, to improve the interpretation of buried archaeologically relevant objects. Furthermore, Koyan et al. (2021) use a set of geometrical and textural attributes to identify and classify GPR facies in Holocene sediments deposited in a coastal environment.

Although the three basic GPR interpretation strategies outlined above are conceptionally different and typically address different kinds of subsurface targets and structures, respectively, they all rely on analyzing the continuity (or discontinuity) and the spatial arrangement of reflector elements and amplitudes, respectively. This indicates that a set of geometrical attributes characterizing the local structure would represent a proper starting point for different interpretation tasks. Under the basic assumption that a processed and migrated GPR data volume images subsurface structures, we propose a set of attributes calculated from a 3D gradient structure tensor (GST) that comprises amplitude gradients in all spatial dimensions. For decades, gradient structure tensors have been known in the fields of image processing and computer vision and used for estimating local orientation and characterizing local image structures such as lines, edges, and corners (Kass and Witkin, 1987; Harris and Stephens, 1988; Knutsson, 1989; van Vliet and Verbeek, 1995). Today, they can be regarded as popular tools for analyzing 2D and 3D images in various applications including 3D medical imaging and video processing (e.g., Westin et al., 1997, 2001; Hladuvka and Gröller, 2001; Wright and Pless, 2005; Khan et al., 2015). Published geophysical applications mainly focus on analyzing 2D and 3D reflection seismic images including the formulation of structure-oriented filter procedures (Bakker, 2002; Fehmers and Höcker, 2003; Faraklioti and Petrou, 2005; Hale, 2009; Wu, 2017). For analyzing GPR data, the usage of GST is limited, and published studies focus on the analysis of 2D data sets; for example, Bowling et al. (2018) apply a 2D GST to identify GPR facies in 2D data collected across carbonate platforms, while Zhu et al. (2021) use such a tensor to aid the extraction of horizons from 2D GPR data sets.

In the following, we present the methodological basics which include the definition of the used 3D gradient structure tensor and its decomposition into a set of eigenvalues and eigenvectors. From this eigendecomposition, we derive a set of GST-based attributes

to characterize local structures in 3D GPR data sets. Then, we use these attributes to analyze various synthetic and field data examples addressing different typical applications of GPR surveying to evaluate the potential of the proposed attributes.

4.3. Methodology

4.3.1. 3D Gradient Structure Tensor

The basic idea of structure tensors is to comprise the information of partial derivatives in a local neighborhood (e.g., Knutsson, 1989; van Vliet and Verbeek, 1995; Bakker, 2002; Faraklioti and Petrou, 2005). Focusing on first-order derivatives and 3D data, the gradient structure tensor $\mathbf{N}$ can be defined as

$$\mathbf{N} = \begin{pmatrix} \langle I_x^2 \rangle & \langle I_x I_y \rangle & \langle I_x I_z \rangle \\ \langle I_y I_x \rangle & \langle I_y^2 \rangle & \langle I_y I_z \rangle \\ \langle I_z I_x \rangle & \langle I_z I_y \rangle & \langle I_z^2 \rangle \end{pmatrix}, \tag{4.1}$$

where I_x, I_y, and I_z represent the partial derivatives of the data I in x-, y-, and z-direction, respectively. The operator $\langle \cdot \rangle$ indicates a smoothing operation to stabilize the results for noisy input data. If we use a Gaussian function with a standard deviation σ as a smoothing kernel, σ can also be considered as a scale parameter specifying the integration scale; i.e., the local scale at which we calculate the gradients. In practice, we may implement Equation 4.1 by a one-step convolution filter procedure using Gaussian derivatives as filter kernels. Because of the well-known separability property of such filter kernels, the components of $\mathbf{N}$ can be efficiently computed also when analyzing rather large 3D data volumes consisting of more than 1,000,000 individual data points.

If we want to analyze local structures at specific or multiple spatial scales (e.g., following linear scale-space theory; Lindeberg, 1993), the implementation of Equation 4.1 often explicitly considers two individual spatial scales implemented using two separated Gaussian filter operations (e.g., Bakker, 2002; Faraklioti and Petrou, 2005). The first scale is known as the smoothing or gradient scale and aims at stabilizing the differentiation process (using a Gaussian filter kernel with a standard deviation σ_G), while the second scale represents the integration, tensor, or target scale that is related to the size of the structures to be analyzed (using a Gaussian kernel with a standard deviation $\sigma_T > \sigma_G$). Here, for analyzing our 3D GPR data examples, we follow this strategy and specify σ_G considering the signal-to-noise ratio and the resolution capabilities of our data as needed for a stable estimation of the individual components of $\mathbf{N}$ (typically in the order of $\sigma_G \approx 0.1$ m). Then, we specify σ_T depending on the scale of the target structures (typically $3\sigma_G \lesssim \sigma_T \lesssim 10\sigma_G$). Because GPR data volumes are often characterized by different spatial sampling intervals in x-, y-, and z-direction and, furthermore, we may intend to use anisotropic kernels (e.g., in view of emphasizing horizontal directions when analyzing stratified structures in our GPR reflection images), we explicitly consider anisotropic Gaussian kernels defined by $\sigma_{G|T,x}$, $\sigma_{G|T,y}$, and $\sigma_{G|T,z}$. For computing $\mathbf{N}$

in such a way as well as for performing the following decomposition of the tensor, we use the computationally efficient implementations as provided by DIPlib, which is an open-source C++ library steadily developed for more than two decades and licensed under the Apache 2.0 license (for details see www.diplib.org and www.github.com/DIPlib).

4.3.2. Tensor Decomposition and Interpretation

Characterizing local structures using the 3D gradient structure tensor $\mathbf{N}$ (Equation 4.1) typically relies on an eigendecomposition fulfilling the characteristic equation

$$\mathbf{N} = \lambda_1 \mathbf{e_1} \mathbf{e_1}^T + \lambda_2 \mathbf{e_2} \mathbf{e_2}^T + \lambda_3 \mathbf{e_3} \mathbf{e_3}^T, \tag{4.2}$$

where λ_i are the eigenvalues (with $\lambda_1 \geq \lambda_2 \geq \lambda_3 \geq 0$), $\mathbf{e}_i$ the eigenvectors of $\mathbf{N}$, and the superscript T denotes the transpose of a vector. The given ordering of λ_i indicates that $\mathbf{e}_1$ identifies the direction of maximum variation. This decomposition can be visualized as an ellipsoid where the vectors $\mathbf{e}_i$ define a 3D rectangular Cartesian coordinate system while the eigenvalues λ_i values characterize the semi-lengths of the ellipsoidal shape (as illustrated by the example sketched in Figure 4.1). Comparing the magnitudes of every λ_i to each other allows for identifying different local structures such as planes, lines, or uniform (isotropic) structures (Table 4.1). For example, in case $\lambda_1 \gg \lambda_2 \approx \lambda_3 \approx 0$, e_1 is the normal vector of a plane P_1 (Figure 4.1) that locally describes the orientation of the underlying plane-like structure.

In the literature, different λ_i-based measures have been proposed to summarize the results of the given tensor decomposition (Equation 4.2) and to identify specific structures. For example, the trace of the tensor calculated by

$$E_g = \sum_i \lambda_i, \tag{4.3}$$

represents the total GST energy E_g and, thus, might be used to highlight intensity and amplitude variations as well as to normalize individual eigenvalues or further measures and attributes, respectively (Bakker, 2002). To quantify the similarity of a local 3D structure to a plane and a line, respectively, the two contrast-independent measures C_{plane} and C_{line} have been introduced by van Kempen et al. (1999):

$$C_{plane} = \frac{\lambda_1 - \lambda_2}{\lambda_1 + \lambda_2} \tag{4.4a}$$

and

$$C_{line} = \frac{\lambda_2 - \lambda_3}{\lambda_2 + \lambda_3}. \tag{4.4b}$$

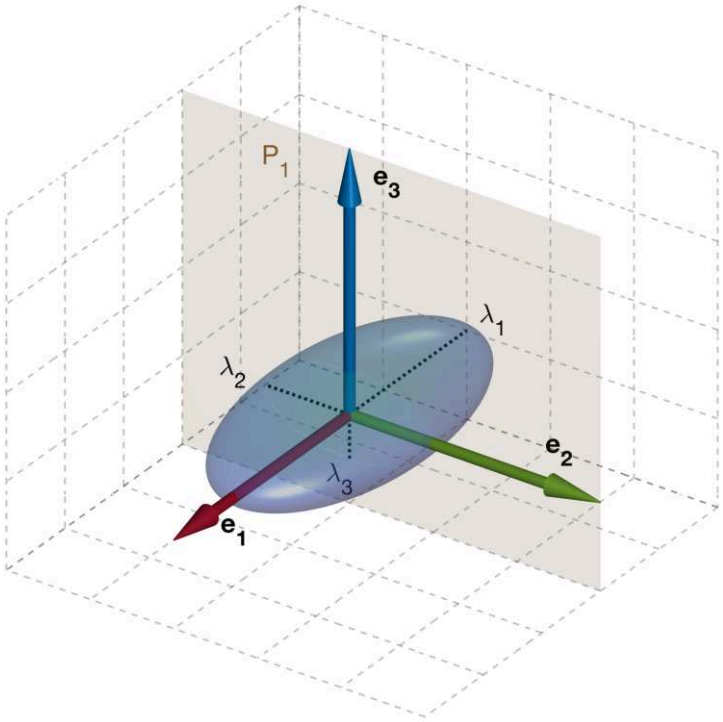

Figure 4.1.: Visualizing a 3D structure tensor $\mathbf{N}$ using its eigenvalues λ_i and eigenvectors $\mathbf{e}_i$ obtained by tensor eigendecomposition. While $\mathbf{e}_i$ define the orientation of the sketched ellipsoid, the shape is defined by λ_i representing the semi-lengths of the major axes of the ellipsoid. For the sketched case $\lambda_1 = 2\lambda_2 = 4\lambda_3$, $\mathbf{e_1}$ is the normal vector of plane P_1 locally describing the orientation of the underlying plane-like structure.

With this definition, both C_{plane} and C_{line} vary between 0 and 1 and, thus, can be used to identify corresponding local structures (see also Table 4.1). In addition, the orthogonal vectors $\mathbf{e}_i$ can be used to quantify the orientation of local structures. While $\mathbf{e}_1$ points toward the maximum gradient, $\mathbf{e}_3$ identifies the orientation of the smallest intensity variations. For example, for a plane-like structure ($C_{plane} \approx 1$), the orientation of $\mathbf{e}_1$ is normal to the plane P_1 (Figure 4.1) and, then, we can estimate the angles of structural dip ϕ and azimuth θ (see also Figure 4.2) defined as

$$\phi = \cos^{-1}\left(\frac{z}{\sqrt{x^2+y^2+z^2}}\right) \tag{4.5a}$$

and

$$\theta = \cos^{-1}\frac{x}{\sqrt{x^2+y^2}}. \tag{4.5b}$$

Table 4.1.: Selected 3D local structures as they can be identified by the eigenvalues λ_i of the 3D gradient structure tensor and the two confidence measures C_{plane} and C_{line}.

Local structure	Eigenvalues	C_{plane}	C_{line}
Plane	$\lambda_1 \gg \lambda_2 \approx \lambda_3 \approx 0$	~1	~0
Line	$\lambda_1 \approx \lambda_2 \gg \lambda_3 \approx 0$	~0	~1
Uniform	$\lambda_1 \approx \lambda_2 \approx \lambda_3$	~0	~0

In summary, interpreting the eigenvalues and the eigenvectors of the gradient structure tensor allows us to characterize local structures in a 3D image or data set. In view of interpreting 3D GPR data sets, such an analysis provides a set of 3D structural attributes to describe local amplitude continuity and variations (λ_i, E_g), to characterize structural shape (C_{plane}, C_{line}), and to quantify the local orientation (ϕ, θ). In the following, we will evaluate the potential of these attributes to analyze synthetic and field data examples representing different typical applications of 3D GPR surveying.

4.4. Synthetic example

4.4.1. Model and GPR data

To illustrate the basic ideas and the applicability of the proposed methodology to 3D GPR data, we use a 200 MHz synthetic data set simulated across a realistic sedimentary model (Koyan and Tronicke, 2020a,b). In Figure 4.3a, we show the input model in terms of GPR velocities along selected in- and crossline slices. This model is considered to represent a realistic sedimentary environment because the underlying structures and parameters have been derived from a 3D outcrop analog study (Bayer et al., 2011; Comunian et al., 2011). We follow these authors to label the main genetic units I-VI in the model. In general, these genetic units are characterized by multi-scale stratigraphic structural variations. On the large scale (several meters), we observe continuous accretionary elements showing

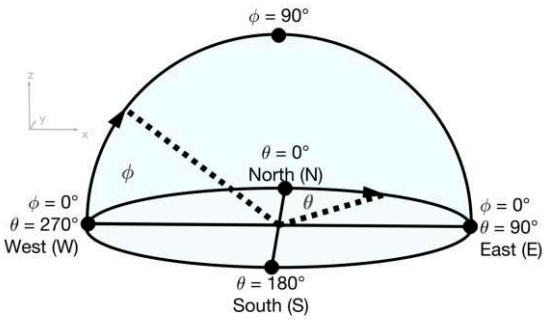

Figure 4.2.: Definition of structural dip ϕ and azimuth θ to quantify the orientation of local structures as used in this study.

low to medium dip angles and varying dip azimuth (units I, II, IV, and VI). On the medium scale (several decimeters to some meters), the stratigraphic structures are mostly continuous, westward-dipping cut-and-fill elements showing the globally highest dip angles (units III and V). On the small scale (centimeters to some decimeters), we find discontinuous cross-bedded patches with varying dip angles and azimuth (within units I, II, and IV).

Using this model, a 200 MHz source wavelet, and in- and crossline trace spacings of 0.05 m and 0.2 m, respectively, Koyan and Tronicke (2020b) model a 3D GPR data set using open-source software gprMax (Warren et al., 2016, 2018). In Figure 4.3b, we visualize the modeled GPR data volume along the same in- and crossline slices as shown in Figure 4.3a after applying a standard processing sequence including 3D migration and time-to-depth conversion.

4.4.2. GST-based analysis

As given by Equation 4.1 and the corresponding explanations above, the user-specified parameters to compute and analyze a gradient structure tensor are the gradient and the target scale σ_G and σ_T, respectively. Here, we fix $\sigma_T = 3\sigma_G$ for all experiments thus reducing the number of user-specified parameters to one (either σ_G or σ_T). Having at hand both the input model and the corresponding GPR data set (Figure 4.3a,b) allows us to study how gradient structure tensors and, consequently, the derived GST attributes (1) are affected by isotropic (i.e., $\sigma_{T,x} = \sigma_{T,y} = \sigma_{T,z}$) or anisotropic Gaussian filter kernels (e.g., $\sigma_{T,x} = \sigma_{T,y} > \sigma_{T,z}$), and (2) are influenced by different spatial filter scales (in the following defined by the target scale σ_T).

In this work, we refer to any GST attributes using the respective Gaussian filter kernels and target scales incorporated in the calculation of the corresponding GST. In Figure 4.3c-f, we show GST energy E_g (Equation 4.3) calculated using different Gaussian filter kernels and target scales as transparent overlays on the processed GPR data as shown in Figure 4.3b. For the result shown in Figure 4.3c, we use an isotropic Gaussian filter kernel (i.e., $\sigma_{T,x} = \sigma_{T,y} = \sigma_{T,z}$) and a target scale corresponding to a dominant signal wavelength λ_d of approximately 0.45 m (considering both the subsurface velocity distribution and the frequency content of the GPR data). Figure 4.3c illustrates that, in general, high E_g values highlight regions of high reflection amplitudes and, in turn, regions of high contrasts in electromagnetic properties (compare Figure 4.3a to 4.3c). However, to consider and emphasize the stratified nature of the subsurface in the resulting attribute images, we also consider an anisotropic Gaussian filter kernel characterized by a ratio between vertical and horizontal scales of 1:5 (i.e., $\sigma_{T,z} = 0.09$ m and $\sigma_{T,xy} = 0.45$ m) and show the result for E_g in Figure 4.3d. Comparing Figure 4.3c and 4.3d illustrates that by decreasing $\sigma_{T,z}$, the attribute adapts to the stratigraphic layering. More precisely, layers and interfaces characterized by high, medium, and low reflection amplitudes in the GPR data can be precisely related to high, medium, and low values of E_g (compare Figure 4.3b and 4.3d).

In the next step, we fix the ratio between $\sigma_{T,z}$ and $\sigma_{T,xy}$ to 1:5 and evaluate the influence of different target scales representatively on the E_g values. For this, we calculate E_g

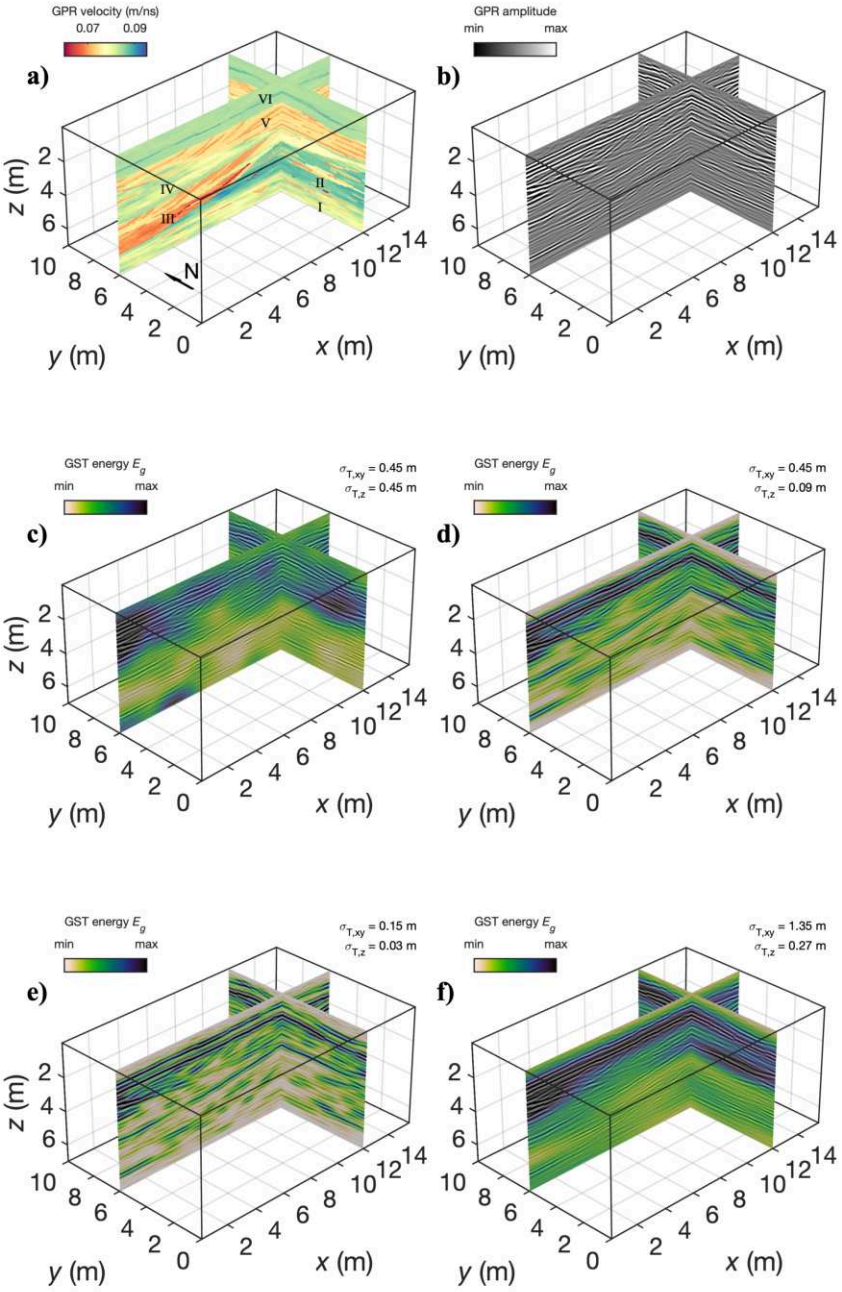

Figure 4.3.: 3D synthetic data example illustrating results of a parameter test for GST-based analysis. We show selected inline and crossline slices of (a) the input model in terms of GPR velocities, (b) the processed GPR amplitude data volume, and (c-f) the volume from (b) with GST energy E_g as transparent overlay calculated using different Gaussian filter kernels as indicated by the different target scales $\sigma_{T,xyz}$.

using $\sigma_{T,xy} = 0.15\,\text{m} \approx \frac{\lambda_d}{3}$ and $\sigma_{T,xy} = 1.35\,\text{m} \approx 3\lambda_d$ and show the results in Figure 4.3e and 4.3f, respectively. Using target scales sized by a fraction of λ_d yields GST attributes showing a high degree of structural detail (Figure 4.3e) whereas using target scales sized by a multiple of λ_d produces GST attributes emphasizing corresponding large-scale structural variations (Figure 4.3f).

The parameter test outlined in Figure 4.3 illustrates the advantage of using anisotropic Gaussian filter kernels to analyze GPR data sets if a layered subsurface is expected and a reasonable guess on the ratio between horizontal and vertical correlation lengths is available. Furthermore, small values of σ_T (i.e., $\sigma_T < \lambda_d$) result in a high degree of structural detail (Figure 4.3e) and might preferably be used as input for advanced processing and filtering procedures such as dip-steered filters (e.g., Luo et al., 1996). In contrast, attributes calculated using larger values of σ_T (i.e., in the order of one to several dominant wavelengths) are better suited to interpret GPR reflection patterns and facies (e.g., in view of attribute-based classification procedures as developed by Koyan et al., 2021).

To further analyze our synthetic data example and calculate further GST-based attributes, we use $\sigma_{T,xy} = 5\sigma_{T,z} = 0.45\,\text{m}$ as shown in Figure 4.3d, because we consider this parameter combination to be a reasonable compromise to analyze large, medium, and small-scale structural features in GST attributes. In Figure 4.4, we show further selected attributes derived by decomposing the GST into its eigenvectors and eigenvalues (Equation 4.2) as transparent overlays on the GPR data along selected in- and crossline slices.

In Figure 4.4a, we show C_{plane} calculated using Equation 4.4a. As indicated by the color scale, C_{plane} has a defined range between 0 and 1 (Table 4.1). In this example, we observe values for C_{plane} between approximately 0.4 ($\lambda_1 \approx 2.5\lambda_2$, i.e., a ratio in the order of the one illustrated in Figure 4.1) and 0.9 ($\lambda_1 \approx 20\lambda_2$). In general, C_{plane} specifies to which extent the local structure resembles a plane. Therefore, C_{plane} can be interpreted as a measure of how confident the absolute values derived from the corresponding eigenvectors can be interpreted in terms of structural dip angle and azimuth because the measures resulting from Equation 4.5a and Equation 4.5b are only well-defined in the presence of plane-like structures. Here, the observed C_{plane} values allow us to analyze and interpret the eigenvectors (Figure 4.4b) as well as the derived dip attributes in terms of the dip angle ϕ (Figure 4.4c) and dip azimuth θ (Figure 4.4d) with a high level of confidence.

In Figure 4.4b, we show the eigenvector $\mathbf{e}_1$ at selected locations along the selected in- and crossline slices. To ease the interpretation, we add the corresponding plane P_1 (see Figure 4.1) that locally describes the orientation of the plane-like structure and, thus, the orientation of the reflections as imaged by the GPR data. Comparing $\mathbf{e}_1$ and P_1 to the underlying GPR reflections (Figure 4.4b) indicates the potential of the GST eigenvector-based attributes for describing structural features in terms of dip angle ϕ and azimuth θ (Equation 4.5a and Equation 4.5b). This is emphasized by analyzing Figure 4.4c and 4.4d in terms of absolute values of ϕ and θ considering the stratigraphic features present in the input model (Figure 4.3a). In general, we observe an overall high level of agreement between stratigraphic structures, GPR reflections, and the

corresponding GST eigenvector-based attributes. For example, the cut-and-fill structures as found in unit III (Figure 4.3a) are precisely characterized in terms of dip angles (showing the globally highest values up to 10°) and west-to-west-northwest-dominated azimuthal directions. Moreover, analyzing the accretionary elements (unit VI) in more detail highlights the importance of 3D GPR processing and 3D GST-based analysis in the presence of such complex subsurface structures. This is, although the showcased inline slice at $y = 6$ m creates the impression of a largely (sub)-horizontal near-surface interface, Figure 4.4b-d indicates a southward-dipping structure with dip angles up to 5°. Overall, these observations are in good agreement with the actual structures observed in the input model (see Figure 4.3a). In conclusion, we regard this synthetic study as an important step to demonstrate that GPR interpretation tasks will undoubtedly benefit from GST-based techniques as these provide a comprehensive and complete understanding of structural interrelationships, especially in complex 3D settings.

4.5. Field examples

Analyzing a synthetic GPR data set and model allowed us to study the influence of different parameters used for calculating gradient structure tensors on the resulting GST-based measures and attributes. We now use the obtained knowledge to analyze 3D GPR field data sets with the GST method. Although the selected data sets both image complex sedimentary structures, they fundamentally differ in terms of reflection patterns and the corresponding target scales.

4.5.1. Example 1 - Facies characterization in sandy deposits

Field site and GPR data

The study area is located on the island of Spiekeroog, one of the seven inhabited East Frisian Islands located a few kilometers off the coast of Lower Saxony (Germany). Spiekeroog is a dune island actively growing towards the north-east whose near-surface geology (i.e., the first 15-20 m below mean sea level) is mainly characterized by (from top to bottom) recently and actively accumulated dunes, intertidal beach deposits as well as shallow marine deposits. These Holocene sand deposits are saturated up to depths of 20-30 m below mean sea level by a freshwater lens which is of vital hydrological importance as it acts as the island's main freshwater reservoir (further details in Tronicke et al., 1999; Röper et al., 2012).

The field site crosses a northwest-southeast striking dune valley in the central part of the island. Here, Koyan et al. (2021) collected 200 MHz GPR data including a high-resolution 3D data set covering an area of approximately 5000 m^2 with an inline and crossline spacing of approximately 0.08 and 0.25 m, respectively. These authors produce a GPR data volume by applying a 3D structural imaging processing approach including 3D topographic migration (using a CMP-based velocity model), time-to-depth conversion, and topographic correction. In Figure 4.5, we display this data set within the freshwater-saturated zone set along selected inline (x-direction), crossline (y-direction),

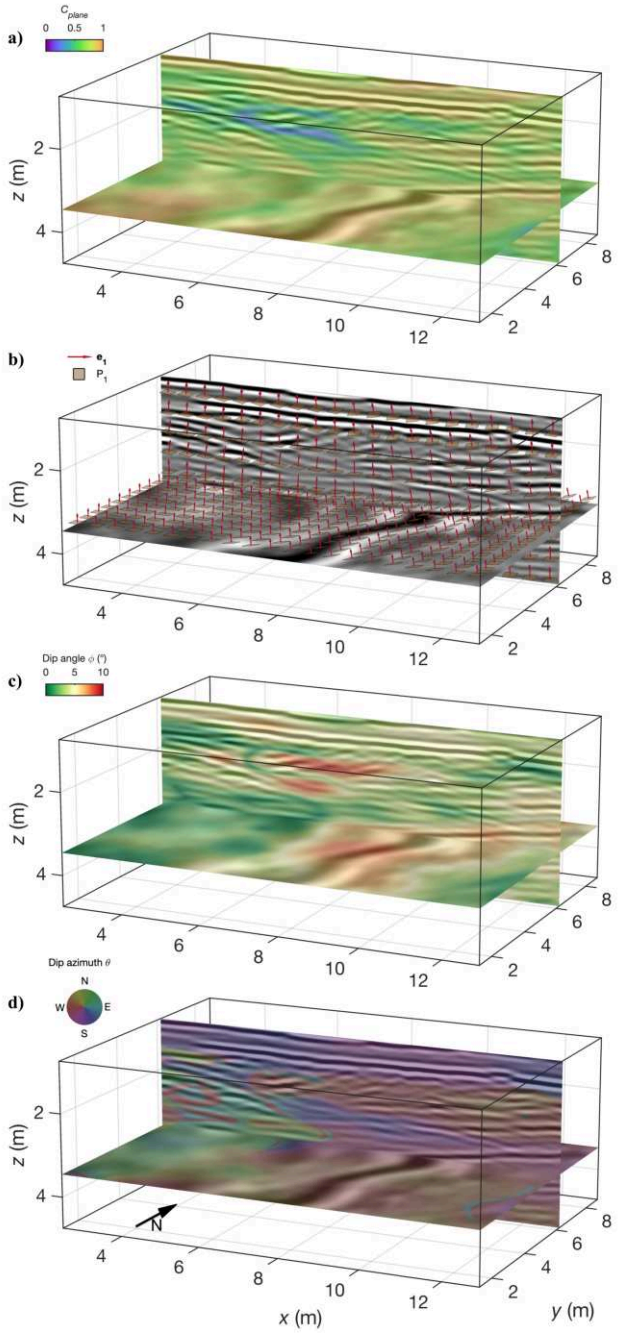

Figure 4.4.: Further GST attributes and measures calculated using $\sigma_{T,xy} = 5\sigma_{T,z} = 0.45\,\mathrm{m}$ (Figure 4.3d) and Equations 4.2, 4.4a, 4.5a, and 4.5b as transparent overlay across selected in- and crossline slices of the processed synthetic 3D GPR data volume: (a) C_{plane}, (b) $\mathbf{e_1}$ and corresponding plane P_1 at selected locations, (c) dip angle ϕ, and (d) dip azimuth θ.

and depth slices (z-direction). The shown data set images sandy depositional structures of varying internal stratification within the saturated zone. These regions significantly vary, for example, in terms of reflection amplitude, continuity, or dip angle and direction. This makes this data set a suitable target to apply and further explore the potential and limitations of the proposed GST method to analyze 3D GPR in terms of sedimentary structures GPR facies.

GST-based analysis

Using the processed 3D GPR data set (Figure 4.5), we calculate the GST and the corresponding attributes for the Spiekeroog data set. Based on our geological background, the layered nature of the data set, and the observations from our synthetic example, we use target scales of $\sigma_{T,xy} = 5\sigma_{T,z} = 0.6$ m such that $\sigma_{T,xy}$ corresponds to one dominant wavelength λ_d (considering the velocity distribution and frequency content observed by Koyan et al., 2021). In Figure 4.6, we show selected GST-based attributes (E_g, C_{plane}, ϕ, and θ) as transparent overlays along selected inline, crossline, and depth slices of the processed GPR data set.

In general, comparing the GST-based attributes and the GPR data set reveals that the GST approach produces meaningful attribute volumes for E_g, C_{plane}, ϕ, and θ characterized by a high level of agreement with the underlying GPR reflection patterns. We generally observe C_{plane} values of 0.4 or higher which means that the eigenvector-based attributes can be interpreted with a high level of confidence throughout the entire volume. Analyzing the attribute volumes in more detail shows that variations of these attributes with depth indicate a zonation summarized in Table 4.2.

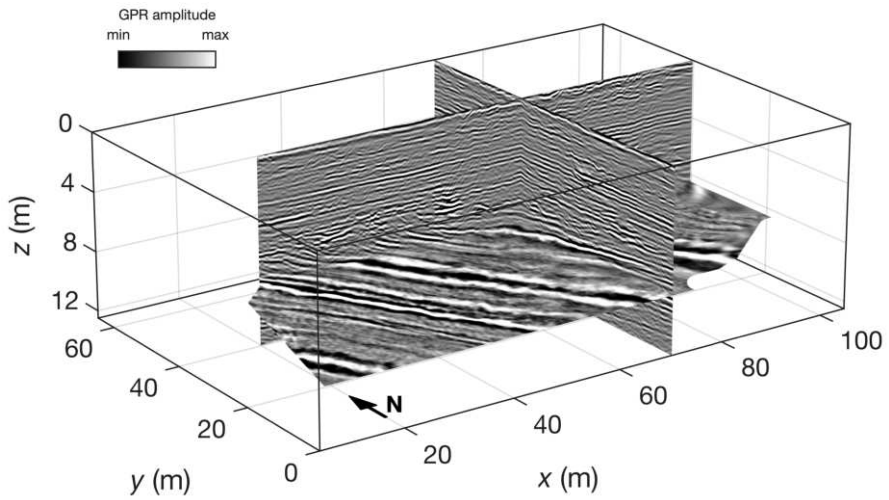

Figure 4.5.: 3D processed GPR data set imaging sandy structures in various depositional environments on the dune island of Spiekeroog (Germany). Depth z refers to the depth below water table corresponding to the top of a local freshwater lens.

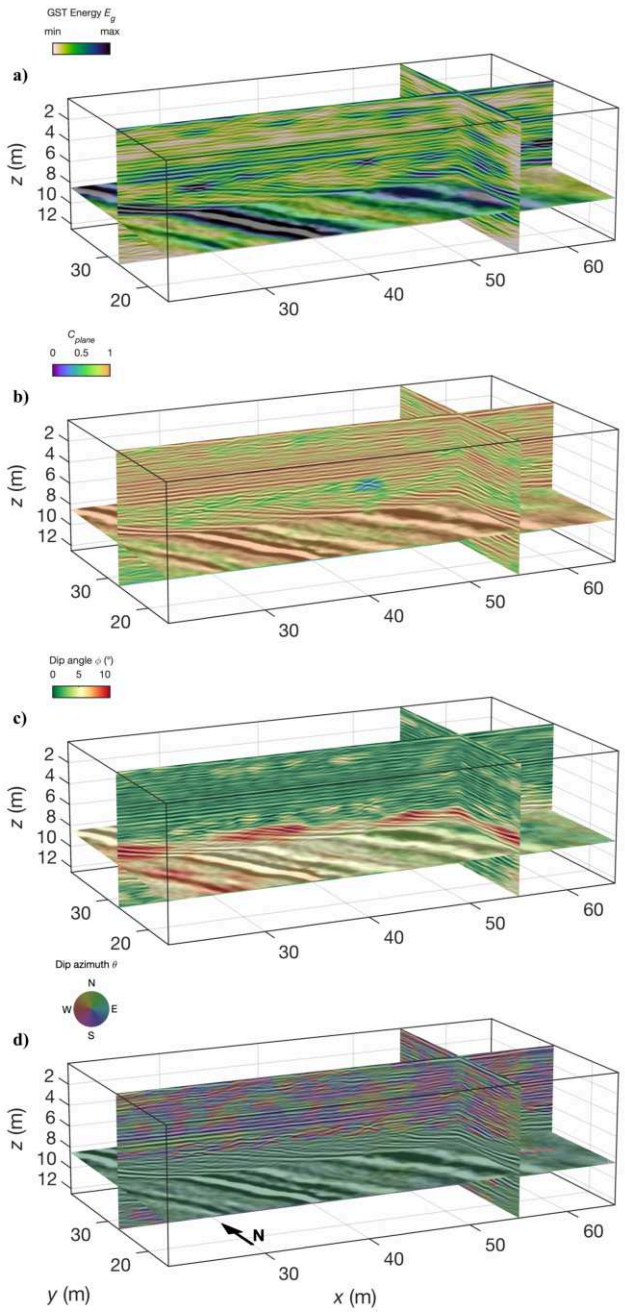

Figure 4.6.: GST attributes calculated using $\sigma_{T,xy} = 5\sigma_{T,z} = 0.6\,\mathrm{m}$ as transparent overlay across selected in- and crossline slices of a subset of the processed Spiekeroog 3D GPR data volume (Figure 4.5): (a) GST energy E_g, (b) C_{plane}, (c) dip angle ϕ, and (d) dip azimuth θ. Depth z refers to the depth below water table corresponding to the top of a local freshwater lens.

In detail, at depths up to $z \approx 5\,\mathrm{m}$, we observe low values for E_g, C_{plane}, and ϕ. However, these are locally disturbed by decreased C_{plane} values, increased ϕ values, highly varying θ values, and/or E_g values. This illustrates locally higher reflection amplitudes (high E_g values), and discontinuous features (low C_{plane} values) with anisotropic dip azimuth as well as a considerable dip angle.

At depths of $z \approx 5 - 7$ m, we observe uniformly high C_{plane} and E_g values along with minor ϕ values and, in turn, varying (non-interpretable) θ values. This characterizes a highly continuous, horizontally layered unit with uniformly high reflection amplitudes. At depths of $z \approx 7 - 8$ m, we observe spot-like features showing the globally highest E_g values coupled with comparably high C_{plane} and ϕ values. This illustrates local anomalies characterized by discontinuous, high-amplitude reflection patterns. At depths of $z \gtrsim 8\,\mathrm{m}$, we notice frequently alternating high and low E_g values. Here, C_{plane} shows uniformly high values and we observe the globally highest dip angles (showing values of more than 10°) as well as stable dip azimuth values. This characterizes largely continuous, uniformly northeast dipping layers with reflection amplitudes varying between low and high values.

The GST-based attributes show a high level of agreement with the underlying GPR data (Figure 4.5) thus illustrating that the GST approach can highlight and distinguish sedimentary facies in a meaningful manner. In addition, the zonation outlined by the GST-based attributes is in agreement with Koyan et al. (2021) who present a GPR facies model for this field site mainly relying on texture attributes. In general, this model

Table 4.2.: Attribute variations with depth as outlined by the GST-based attribute volumes in Figure 4.6 and geological interpretation following Koyan et al., 2021.

Depth	**GST Energy E_g**	C_{plane}	**Dip angle ϕ**	**Dip azimuth θ**	**Geological Interpretation**
≤5 m	generally low, locally increased values	generally high, locally decreased values	generally low, locally increased values up to 5°	varying	recent and actively accumulated dunes
5-7 m	uniformly high	uniformly high	insignificant	non-interpretable	intertidal beach deposits
7-8 m	spots with globally highest values	spots with globally lowest values	spots with values up to 5°	varying	mud lenses, moor/lagoon deposits
≥8 m	frequently alternating between low and high	uniformly high	globally highest values of >10°	uniformly towards northeast	shallow marine deposits

describes (from top to bottom) recently and actively accumulated dunes ($z \lesssim 5$ m), intertidal beach deposits ($z \approx 5 - 7$ m), local moor and lagoon deposits comprising mud and clay lenses ($z \approx 7 - 8$ m), and shallow marine deposits ($z \gtrsim 8$ m). Moreover, not only do the general trends of the presented GST-based attributes confirm previous studies but, using GST analysis, we can also access physically valuable values for dip angle and azimuth to deepen the understanding of such complex sedimentary systems. As a more detailed geological and sedimentological interpretation is beyond the scope of this work, we refer to previous studies that further describe the depositional environments at this field site (Koyan et al., 2021) and on a more regional scale (Tronicke et al., 1999; Röper et al., 2012).

4.5.2. Example 2 - Fault characterization in volcanic and lacustrine deposits

Field site and GPR data

The study area is located within the Taupo Volcanic Zone (TVZ), the dominant region of active volcanism on the North Island of New Zealand where the Pacific Plate subducts westward beneath the Australian Plate. A specific region of the TVZ is known as the Maleme Fault Zone (MFZ; Villamor and Berryman, 2001) that forms the central axis of the Ngakuru Graben comprising faults active over the last approximately 20 ka. The near-surface at the MFZ comprises volcanic and lacustrine deposits that have been displaced along several fault strands over the last 20 ka. As the TVZ as well as the entire North Island is subject to frequent shallow earthquakes, an understanding of the morphology, geometry, and variability of fault zones is crucial here. Although rough estimates on the location and vertical displacement of fault strands at MFZ can be inferred from morphological variations, GPR is a promising tool to provide a more detailed image of the fault geometry.

The field site is located southeast of the actual graben axis at MFZ. Across an area of approximately 1200 m^2 perpendicular to the southwest-northeast striking graben axis, Tronicke et al. (2006) acquire 100 MHz GPR data including a 3D data set using an inline and crossline spacing of approximately 0.1 and 0.5 m, respectively. These authors produce a GPR data volume by applying a 3D structural imaging processing approach including 3D topographic migration (using a CMP-based velocity model), time-to-depth conversion, and topographic correction. In Figure 4.7a, we display the processed data set along selected inline (y-direction), crossline (x-direction) and depth slices (z-direction). Here, the local y-axis is perpendicular to the graben axis located at $y \approx$ -40 m. This data set images two parallel reflections that correspond to the upper boundaries of Late Pleistocene Tephra and lacustrine sediments. This characteristic reflection signature is locally interrupted and offset at individual fault strands. Tronicke et al. (2006) manually track these reflections in the GPR and derived attribute volumes. Analyzing the topography of these picked horizons allows us to locate the individual fault strands and characterize their geometry. In Figure 4.7b, we show one of these horizons and visualize three interpreted fault strands (lower transparency, labels A-C) dipping towards the northwest (i.e., towards the graben axis). Analyzing the reflection patterns

in detail reveals that individual fault strands significantly vary, especially in terms of continuity and dip angle, when compared to the remaining parts of the horizon. This makes this data set a suitable target to apply our GST approach to analyze GPR data in view of fault localization and fault characterization.

GST-based analysis

We calculate the GST and the corresponding attributes using the processed 3D GPR data set (Figure 4.7) considering both the horizontal nature of sedimentary layers and the more vertical nature of the faults. To accomplish this, we use target scales of $\sigma_{T,xy} = 2\sigma_{T,z} = 0.75\,\mathrm{m} \approx \lambda_d$ that enable a compromise between resolving horizontal

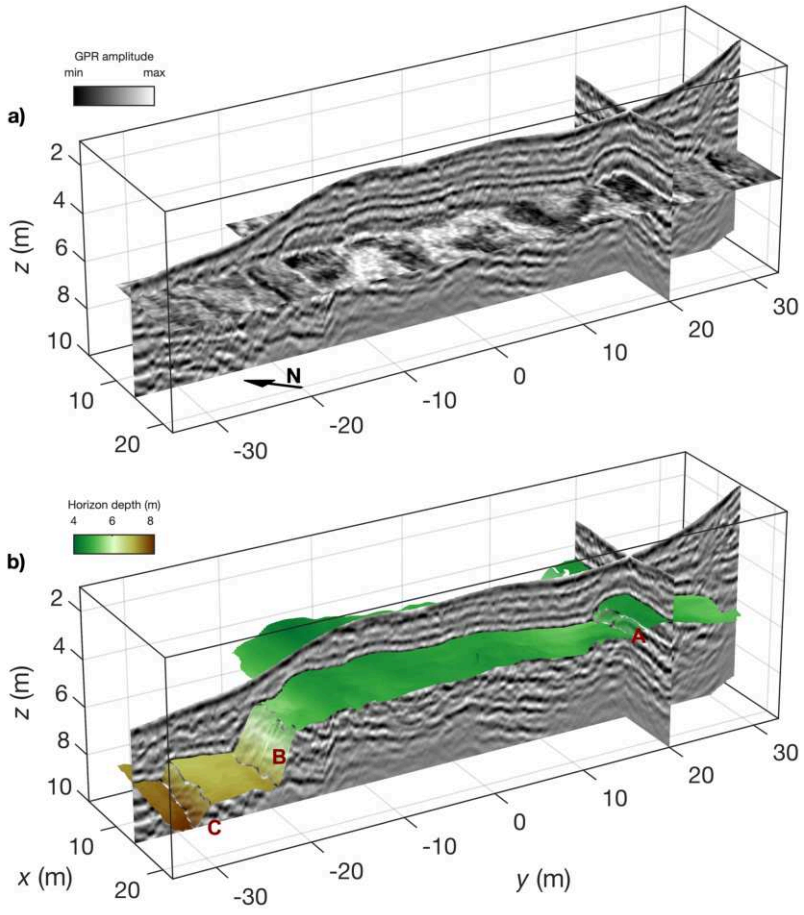

Figure 4.7.: (a) 3D processed GPR data set imaging fault strands within volcanic and lacustrine sediments at the Maleme Fault Zone (North Island, NZ). The local y-axis is perpendicular to the graben axis located at $y \approx$ -40 m. (b) Same as for (a) but with an interpreted GPR horizon. Here, lower horizon transparency marks three individual fault strands (labels A-C).

and more vertical vertical features in the resulting attribute volumes. In Figure 4.8, we display selected GST-based attributes (E_g, C_{plane} with interpreted fault strands, ϕ, and θ) as transparent overlays across the same inline, crossline, and depth slices of the GPR data shown in Figure 4.7a.

We observe a high level of agreement when comparing the shown attribute volumes to the corresponding GPR data (Figure 4.7 and Figure 4.8). Moreover, we observe C_{plane} values of 0.6 or more (except in regions labeled A, B, and D; Figure 4.8b) which allows us to interpret the absolute values of ϕ and θ with a high level of confidence. In general, the attribute volumes distinguish two fundamentally different regions in the data set. The larger one shows medium to high E_g values, high C_{plane} values, low ϕ values, and θ values frequently alternating between northeast and southwest. Here, the GST-based attributes highlight regions in which we can observe the undisturbed reflection signatures of the upper boundaries of Late Pleistocene Tephra and lacustrine sediments (Figure 4.7b).

In contrast, we locally observe four regions characterized by the globally lowest C_{plane} values, the highest ϕ values, and θ uniformly pointing towards the northeast. Here, the attribute volumes precisely differentiate the fault strands from undisturbed regions in the GPR data. The fault strand positioning coincides with the manual interpretation approach of Tronicke et al. (2006). To highlight this, we label these positions accordingly in Figure 4.8b and Figure 4.7b.

In the attribute volumes, we also can interpret an additional fault strand (D) that could not be mapped using a horizon-based interpretation approach. Analyzing Figure 4.8 in more detail and comparing it with, for example, Figure 4.7 or typical 2D GPR attributes (see Figure 7b-e in Tronicke et al., 2006) shows the potential of the GST approach to analyze fault environments. Thus, we conclude that GST-based attributes can provide comprehensive information on the 3D fault geometry including their vertical and lateral extent complemented by physically valuable information in the form of dip angle and dip azimuth. This information can be of immense value for further sedimentological analysis such as the determination of 3D fault displacement and the temporal development and variability in faulting regions.

4.6. Conclusion

In this work, we introduce and apply the 3D gradient structure tensor (GST) approach for analyzing GPR data acquired across sedimentary systems. We present our ideas using one synthetic and two field 3D GPR data sets exhibiting various reflection patterns at different spatial scales.

Based on our synthetic example, we introduce the fundamental parameters and their influence on both the GST calculation and the resulting attributes and measures. Using two fundamentally different field data sets, we highlight how the GST attribute database including measures of reflection amplitude, continuity, dip angle, and dip azimuth can be used to analyze, interpret, and characterize GPR data sets in a full 3D fashion to highlight structural similarities in terms of GPR facies and structural differences in terms of fault mapping, respectively.

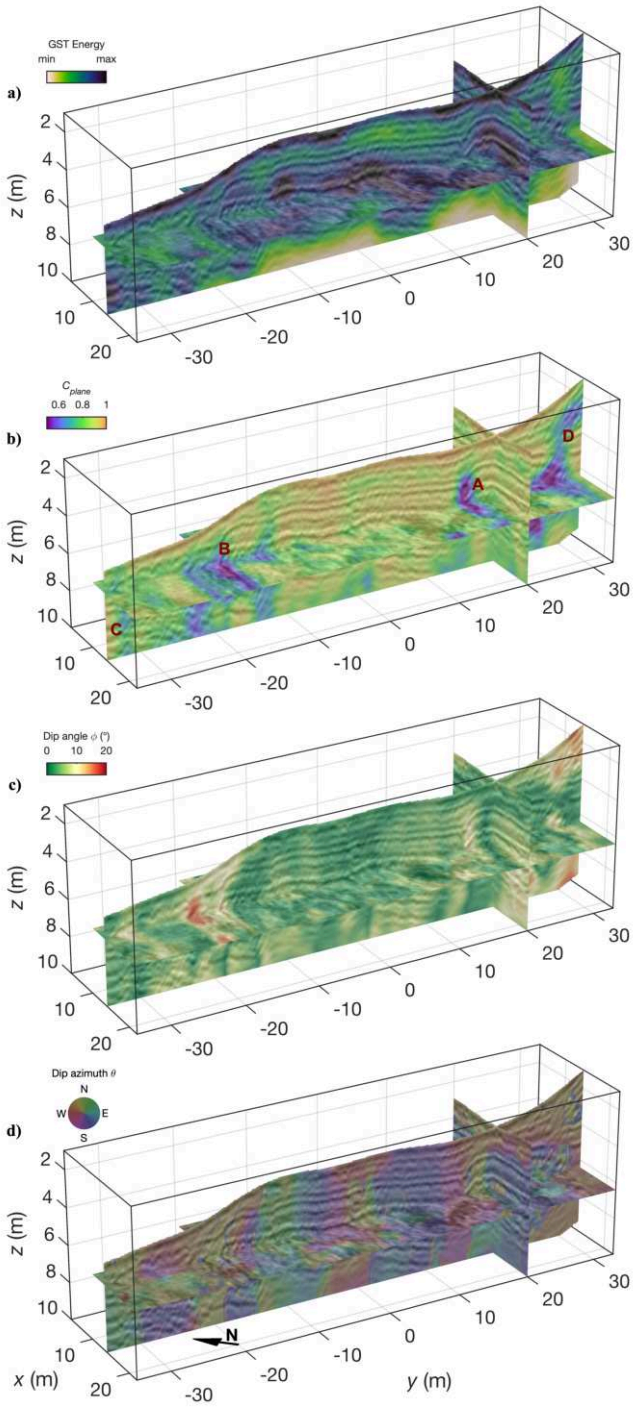

Figure 4.8.: GST attributes calculated using $\sigma_{T,xy} = 2\sigma_{T,z} = 0.75$ m as transparent overlay across selected inline, crossline, and depth slices of the processed MFZ 3D data set (Figure 4.7): (a) GST energy E_g, (b) C_{plane} with interpreted fault strands labeled A-D (compare Figure 4.7b), (c) dip angle ϕ, and (d) dip azimuth θ. Note the adjusted scaling of C_{plane} values in (b).

The proposed GST approach is computationally efficient, this is, a single run to calculate the GST is in the order of some seconds for the shown 3D examples. Then, from the GST we can derive a comprehensive attribute database as needed for further processing or interpretation tasks. This database includes eigenvalue-based attributes (e.g., C_{plane} and E_g) and eigenvector-based attributes (dip angle and dip azimuth) that have a plausible physical meaning. The latter allows us to analyze and characterize features identified in the GPR data or eigenvalue-based attributes in a more quantitive way thus providing a comprehensive picture of complex GPR data sets and environments, respectively.

The GST method only incorporates parameters with a clear physical meaning, namely $\sigma_{G,xyz}$ and $\sigma_{T,xyz}$ (i.e., the scales of Gaussian filter kernels used to calculate the GST). Our examples show that using, for example, a constant ratio between σ_G and σ_T, and a target scale σ_T in the order of a dominant wavelength produces reliable results. Additionally, we show that for typical sedimentary environments, an anisotropic formulation of the target scales (i.e., introducing a ratio between $\sigma_{T,xy}$ and $\sigma_{T,z}$) might be advantageous as the resulting attributes reflect the nature of typical GPR reflection signatures more precisely. All these choices might look like a drawback of the method, but can also be understood as an opportunity because the fast calculation times for the GST allow for extensive parameter testing and/or a multi-scale structure analysis of complex GPR data sets.

In this work, we focus on qualitative analysis and comparison of the GST attribute database to characterize stratigraphic similarities or differences in terms of amplitudes, continuity, and dip. Moreover, these attributes also form a promising database for integrated structural analysis, for example, in view of attribute-based classification procedures which could be the major focus of upcoming studies. In contrast to the presented sedimentological GPR data, GST-based attributes (also the ones not showcased here such as C_{line}) might also be a promising tool to analyze and interpret non-stratigraphic features, for instance, in the of field civil engineering where often more linear or cylindrical structures such as utility pipes represent the target objects. In conclusion, we believe that 3D GST-based analysis of GPR data is a promising approach to steer interpretation tasks in a more objective, quantitative, and reproducible direction.

Data and materials availability

The 3D synthetic input model including a 100 MHz 3D GPR data set are publicly available (Koyan and Tronicke, 2019). Structure tensor computation and analysis has been performed using the open-source library DIPlib (www.diplib.org and www.github.com/DIPlib).

5. 3D GPR attributes to generate classified facies models: A case study from a dune island

Philipp Koyan, Jens Tronicke and Niklas Allroggen*

5.1. Abstract

Ground-penetrating radar (GPR) is a standard geophysical technique used to image near-surface structures in sedimentary environments. In such environments, GPR data acquisition and processing are increasingly following 3D strategies. However, the processed GPR data volumes are typically still interpreted using selected 2D slices and manual concepts such as GPR facies analyses. In seismic volume interpretation, the application of (semi-)automated and reproducible approaches such as 3D attribute analyses as well as the production of attribute-based facies models are common practices today. In contrast, the field of 3D GPR attribute analyses and corresponding facies models is largely untapped. We have developed and applied a workflow to produce 3D attribute-based GPR facies models comprising the dominant sedimentary reflection patterns in a GPR volume which images complex sandy structures on the dune island of Spiekeroog (Northern Germany). After presenting our field site and details regarding our data acquisition and processing, we calculate and filter 3D texture attributes to generate a database comprising the dominant texture features of our GPR data. Then, we perform a dimensionality reduction of this database to obtain meta texture attributes, which we analyze and integrate using composite imaging and (also considering additional geometric information) fuzzy c-means cluster analysis resulting in a classified GPR facies model. Considering our facies model and a corresponding GPR facies chart, we interpret our GPR data set in terms of near-surface sedimentary units, the corresponding depositional environments, and the recent formation history at our field site. Thus, we demonstrate the potential of our workflow, which represents a novel and clear strategy to perform a more objective and consistent interpretation of 3D GPR data collected across different sedimentary environments.

*A peer-reviewed journal article of the same title is published as Koyan et al. (2021) in Geophysics 86(6), B335–B347. This article has also been featured in the *Geophysics Bright Spots* Section of SEG's The Leading Edge magazine in January 2022 (Behura, 2022).

5.2. Introduction

Ground-penetrating radar (GPR) is a well-established geophysical tool used to image and characterize near-surface structures and depositional environments across sedimentary systems (Neal, 2004). Thanks to recent technological developments including the availability of modern GPR array systems, the integration of differential global positioning systems or auto-tracking total stations for real-time kinematic surveying, the acquisition of high-accuracy high-resolution 3D data sets covering areas of thousands of square meters has become common practice (e.g., Grasmueck et al., 2004; Schennen et al., 2016). However, methods and developments in data interpretation have not kept pace with the increasing details and complexity of the sedimentary structures imaged by such densely sampled 3D GPR data. More specifically, processed 3D data sets, or only selected 2D subsets of them, are typically interpreted manually, often using concepts known as GPR facies analyses (e.g., Van Overmeeren, 1998; Kostic and Aigner, 2007; Pascucci et al., 2009; Burke et al., 2010; Lang et al., 2017). In general, GPR facies describe units composed of characteristic reflection patterns, and the related interpretation concepts can be regarded as laborious, especially, when applied to entire 3D data sets. Furthermore, the outcome of such an interpretation depends on the interpreter's knowledge and experience and is thus subjective and often difficult to reproduce.

In 3D seismics, techniques known as attribute-based analyses have been successfully applied to delineate characteristic reflection patterns and facies, respectively, in a semiautomated and reproducible manner for decades (Chopra and Marfurt, 2005). This includes the calculation of manifold attributes and the use of unsupervised classifications or the application of supervised techniques also considering independent ground-truth data such as borehole logs or sediment cores (e.g., Chopra and Marfurt, 2007, 2008; Eichkitz et al., 2013, 2015; Zhao et al., 2015; Eichkitz and Amtmann, 2018; Long et al., 2018). Moreover, recent developments in 3D seismics focus on the use of machine and deep learning to structure data sets based on reflection patterns, which represents a further step in seismic volume interpretation (e.g., Wrona et al., 2018; Alaudah et al., 2019). In contrast, for the interpretation of 3D GPR data sets collected across sedimentary environments attributes, in general, find only limited application up to now (e.g., McClymont et al., 2008; Forte et al., 2012; Zhao et al., 2013). The field of attribute-based 2D and 3D GPR facies models is largely untapped and only a few examples can be found in the literature (e.g., Moysey et al., 2006; Tronicke and Allroggen, 2015).

In this case study, we propose a workflow to obtain 3D attribute-based GPR facies models delineating the dominant structural variations in GPR data volumes and apply it to a 3D data set acquired across sedimentary structures on the dune island of Spiekeroog (Northern Germany). After introducing our field site, data acquisition, and processing, we calculate and filter 3D texture attributes to obtain a database comprising the major texture variations in our GPR data set. Then, we analyze and visualize meta texture attributes (obtained by dimensionality reduction of this database) using composite imaging and (also considering additional geometric information) fuzzy c-means cluster

analysis to generate a classified 3D GPR facies model. Finally, considering our facies model and a corresponding GPR facies chart, we interpret our data set in terms of the main sedimentary units, the related depositional environments, and the recent formation history at our field site.

5.3. Field data

5.3.1. Geologic setting and field site

Our field site is located on the island of Spiekeroog in Northern Germany. Spiekeroog is one of seven inhabited East Frisian Islands, an approximately 90 km long, east–west-oriented group of barrier islands situated in the Wadden Sea National Park a few kilometers off the coast of Lower Saxony (Germany) within the German Bight. Spiekeroog shows a maximum extension of 10 km in the east–west direction and 2 km in the north–south direction. As part of a dynamic system of tides, sea currents, and floods, the island's size and shape are in constant change; for example, nowadays the island actively grows toward the northeast caused by the prevailing westerly winds and coastal protection activities (Sindowski, 1973; Röper et al., 2012). To characterize near-surface structures and, thus, typical depositional environments at this dune island, we collected 3D GPR and topographic data and performed several common-midpoint (CMP) GPR experiments across a field site known as the "Eierscheeterplatz". This historical place is located in the central part of the island, east of Spiekeroog village, and south of the main dune area (53.771 N/7.713 E). Here, the near-surface geology (i.e., the uppermost 15–20 m below mean sea level) is mainly characterized by middle to coarse-grained Holocene sands deposited in typical coastal environments including shallow-marine sequences, intertidal beach deposits, and actively accumulated dune structures on top (further details can be found in Röper et al., 2012). These sands are saturated up to depths of 20–30 m below mean sea level by a freshwater lens (Tronicke et al., 1999); thus, the local subsurface is of vital hydrogeological importance because it represents the main freshwater reservoir of Spiekeroog.

Figure 5.1a shows a map of our field site including a digital topographic model (generated from the positioning data recorded during kinematic GPR data acquisition), the midpoints and orientations of CMP experiments, the location of our self-tracking total station (TTS), and the approximate view angle of a digital photograph of our field site shown in Figure 5.1b. The field site shows a size of approximately 110 x 65 m with topographic variations up to approximately 3 m associated with dune structures forming a prominent northwest–southeast-striking depression as well as some local minor hilly structures characterized by topographic variations up to approximately 1 m. The digital photograph in Figure 5.1b provides an impression of the local environmental conditions and the sparse vegetation predominantly consisting of grass, scattered bushes, and small trees.

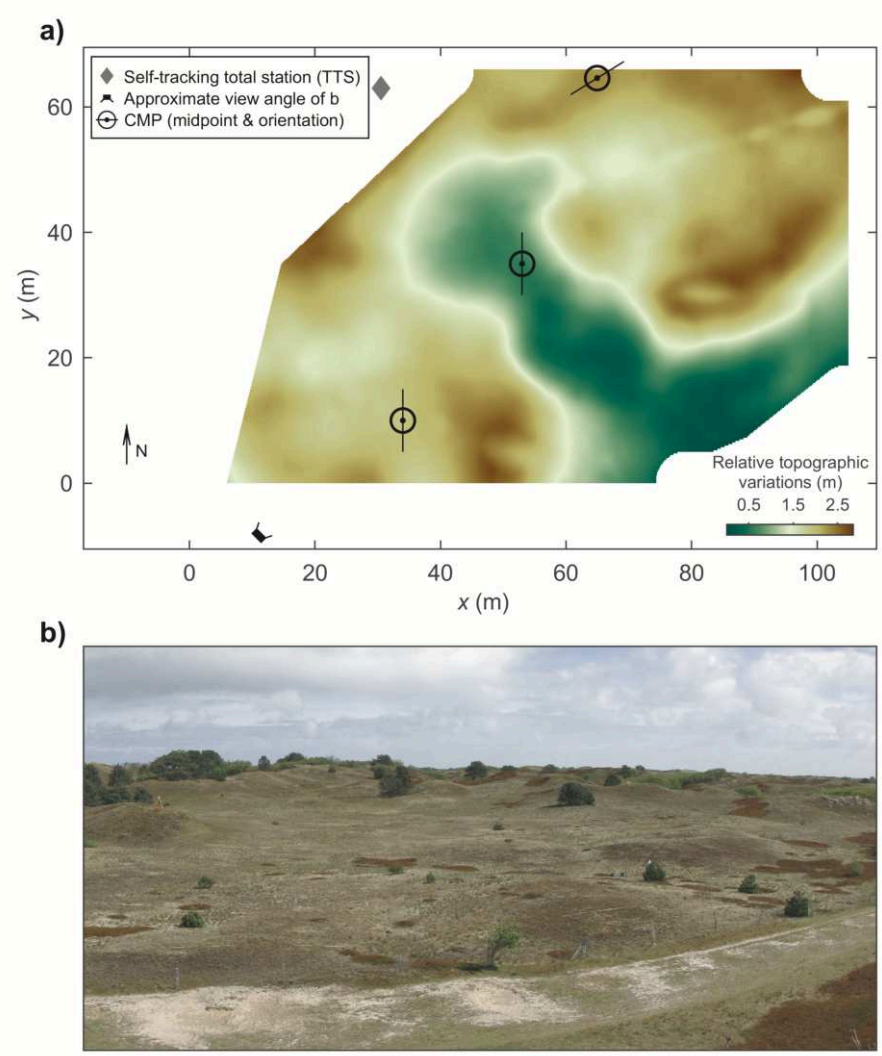

Figure 5.1.: (a) Map of our field site introducing the local coordinate system including a digital topographic model as obtained from our TTS-based surveying approach, the midpoints and orientations of CMP experiments (extent to scale), the location of the TTS, and the approximate view angle of (b) a digital photograph of our field site.

5.3.2. Data acquisition

In May 2012, 3D GPR data were collected along parallel lines in the east–west direction; that is, parallel to the x-direction of the local coordinate system (Figure 5.1a). Preliminary tests using different antenna frequencies revealed that, at this field site, the antennas with a nominal center frequency of 200 MHz offer an optimum compromise between penetration depth (more than 15 m) and resolution (decimeter scale). Thus, a pair of unshielded 200 MHz antennas combined with a PulseEKKO Pro GPR system was

mounted on a sled using a 1 m offset and a parallel broadside antenna orientation. To provide positioning accuracy in the centimeter range and a high-precision local digital elevation model as shown in Figure 5.1a, we used a TTS-based GPR surveying approach following Böniger and Tronicke (2010b,c). Therefore, we mounted a 360° prism on the sled that was automatically tracked by a TTS (Leica TPS1200) during the entire 3D GPR survey. Using this GPR surveying strategy, we recorded a total of approximately 218,000 GPR traces separated by an inline and crossline trace spacing of approximately 0.08 and 0.25 m, respectively, resulting in a dense data coverage indispensable for a sound and detailed 3D imaging of typical sedimentary structures (e.g., Bristow and Jol, 2003; Grasmueck et al., 2005). In Table 5.1, we summarize the acquisition parameters of this 3D GPR survey. To complement our 3D common-offset data by local velocity estimates, we performed CMP experiments with a maximum antenna offset of 10 m and antenna offset increments of 0.1 m using the same GPR and antenna system at three different locations across the survey site (Figure 5.1a).

Recording our densely sampled 3D data set across an approximately 5000 m^2 large survey area took three days during which we encountered stable weather and environmental conditions. To control GPR data quality, we additionally recorded 2D common-offset data along a 50 m long reference profile (using the parameters shown in Table 5.1) and CMP gathers at the center position of this 2D profile at $x/y = 65$ m/64.5 m (Figure 5.1a) on a daily basis. This allowed us to monitor and characterize possible diurnal variations in the common-offset and CMP data including the inferred velocity models. To illustrate this, we analyze selected CMP data and results in Figure 5.2. In Figure 5.2c, we show the CMP gather recorded at $x/y = 65$ m/64.5 m on the first day of the campaign (after applying some basic processing including band-pass filtering and amplitude scaling), and in Figure 5.2b we show the corresponding result of a typical reflection-based velocity analysis (using unnormalized crosscorrelation as a coherence measure). We observe numerous reflections in the CMP data resulting in well-separated coherence maxima in the velocity spectrum (the red colors in Figure 5.2b). From this spectrum, we derive an interval velocity model under the assumption of a horizontally layered medium (Dix, 1955), which is shown in red in Figure 5.2a. In terms of velocity variations, we can identify two main layers; that is, at approximately 45 ns, we recognize a decrease in interval velocity from approximately 0.135 to 0.07 m/ns corresponding to a largely horizontal

Parameter	**Value**
Nominal antenna frequency	200 MHz
Antenna offset	1 m
Time window	600 ns
Sampling interval	0.3 ns
Vertical stacking	16
Inline trace spacing	∼0.08 m
Crossline trace spacing	∼0.25 m

Table 5.1.: Acquisition parameters of the 3D common-offset GPR survey.

freshwater table at our field site (Tronicke et al., 1999). At larger traveltimes (>45 ns), we observe further well-pronounced and well-separated maxima in the velocity spectrum indicating four to five layers within the saturated zone. Reflections in the CMP data corresponding to spectral maxima found at traveltimes >320 ns originate from dipping reflectors and are therefore not considered to derive the 1D velocity model. For a daily comparison, we also show the interval velocity models derived from the CMP surveys at the same location performed on the two following days of the campaign (the blue and green models in Figure 5.2a). The daily variations in the shown velocity models range in the order of a few percent and can thus be regarded as insignificant considering typical uncertainties in CMP-based GPR velocity analysis (e.g., Hamann and Tronicke, 2014).

In addition, we calculate the mean trace amplitude spectra from our daily recorded CMP data sets, which we show in Figure 5.3 using the same color coding as in Figure 5.2a. These spectra exhibit a comparable shape regarding their global and local maxima and only show spectral amplitude variations in the order of a few percent. For each day, we observe the global maximum at a frequency of approximately 105 MHz illustrating a significant frequency downshift compared to the nominal antenna frequency of 200 MHz. A comparison of the daily velocity models (Figure 5.2a) and the daily mean amplitude spectra (Figure 5.3) demonstrates a near-perfect reproducibility of GPR data characteristics including temporal stability and frequency content throughout the three days of our survey.

5.3.3. Data processing

To obtain a high-resolution, ready-to-interpret 3D GPR data volume, we follow common practice in processing common-offset 3D GPR data sets (e.g., Böniger and Tronicke, 2010a; Schennen et al., 2016; Koyan and Tronicke, 2020a) and apply the structural imaging processing scheme illustrated in Figure 5.4. This includes typically applied temporal and spatial corrections and filters and a natural-neighbor gridding routine to interpolate the data onto an equidistant rectangular grid with an inline (x) and crossline (y) trace spacing of 0.125 and 0.25 m, respectively. Finally, we apply a 3D topographic migration (Allroggen et al., 2015), using a root-mean-square (rms) velocity model inferred from the CMP experiments (as indicated in Figure 5.2), followed by a topographic correction.

In Figure 5.5, we illustrate typical inline (Figure 5.5a and 5.5c), crossline (Figure 5.5b and 5.5d), and time (Figure 5.5e) slices extracted from our 3D GPR data volume after applying the processing sequence outlined in Figure 5.4. The depth is calculated using the same velocity model as used for migration and measured relative to the mean water table located at a traveltime of approximately 70 ns. In Figure 5.5, the example GPR slices demonstrate a uniform GPR data quality (despite being acquired on three different days) and a penetration depth of more than 12 m below the water table combined with a high spatial resolution in the order of a few decimeters. The inline and crossline slices in Figure 5.5a–5.5d provide high-quality images of the horizontal and dipping sedimentary structures in different directions, whereas the example time slice in Figure 5.5e highlights detailed imaging of more complex patterns such as (curvi-)linear bow structures or isolated lenticular features (exemplified by the blue color). Overall, we observe major

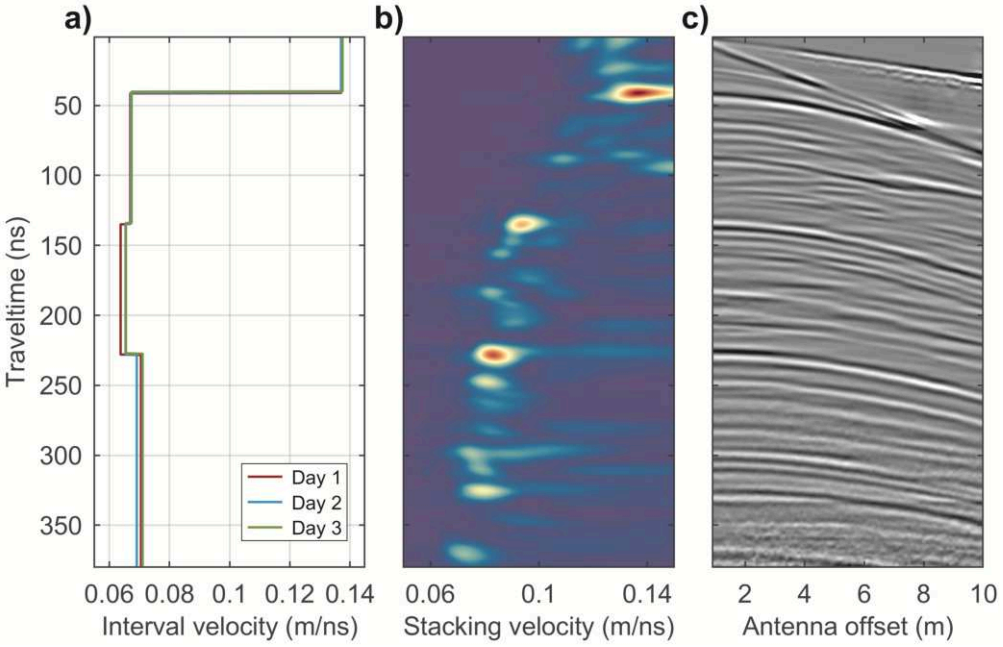

Figure 5.2.: (a) Interval velocity models derived from CMP gathers recorded on each day of the GPR survey with a center position at $x/y = 65$ m/64.5 m (Figure 5.1). The interval velocity model shown in red has been derived from (b) the result of a reflection-based spectral velocity analysis (the red colors indicate high spectral values) of (c) the CMP gather recorded on the first day of the survey.

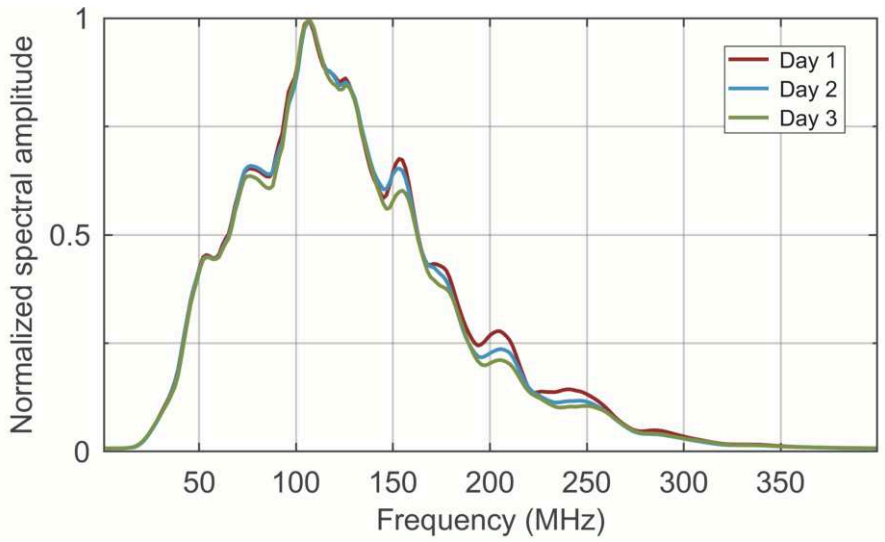

Figure 5.3.: Mean amplitude spectra derived from the CMP gathers recorded on each day of the GPR survey after the application of a typical band-pass filter with the same color code as used in Figure 5.2a.

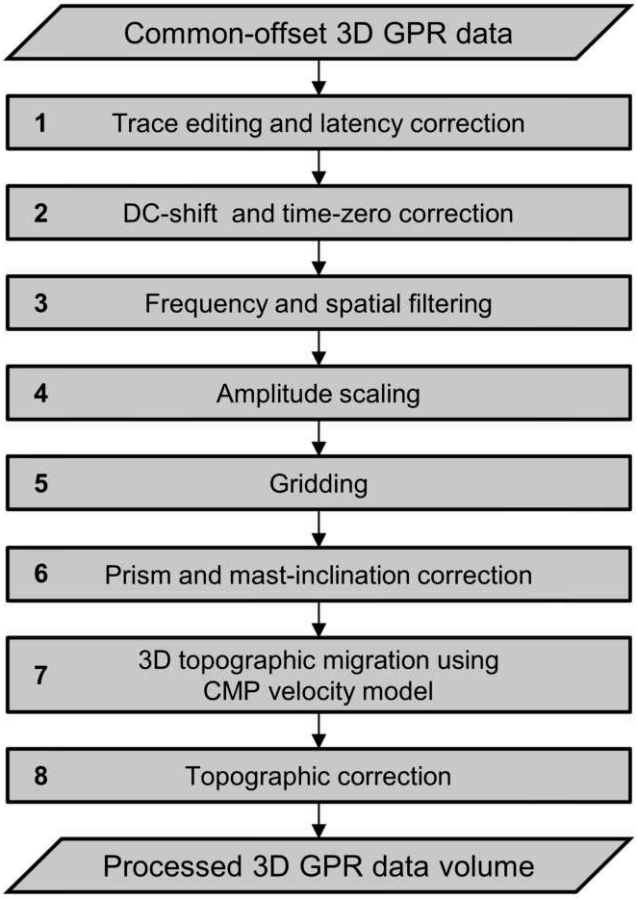

Figure 5.4.: Flow diagram illustrating the main processing steps applied to our 3D common-offset GPR data for structural imaging.

structural variations within the GPR reflection patterns at the scale of some meters in the depth direction and to tens of meters in the horizontal direction; thus, also considering the CMP velocity models, our processed 3D GPR data volume indicates zones of different internal stratification and, hence, diverse depositional environments. To interpret our data set in more detail and to separate the subsurface into different units and facies, respectively, we perform attribute-based analyses.

5.4. Attribute-based GPR facies models

In contrast to manual GPR facies analyses, attribute-based analyses of GPR data allow for characterization and delineation of structural patterns in a (semi-)automated, reproducible, and, thus, more objective manner. In general, an attribute can be defined as a measure calculated or extracted from data to enhance or even to quantify features of

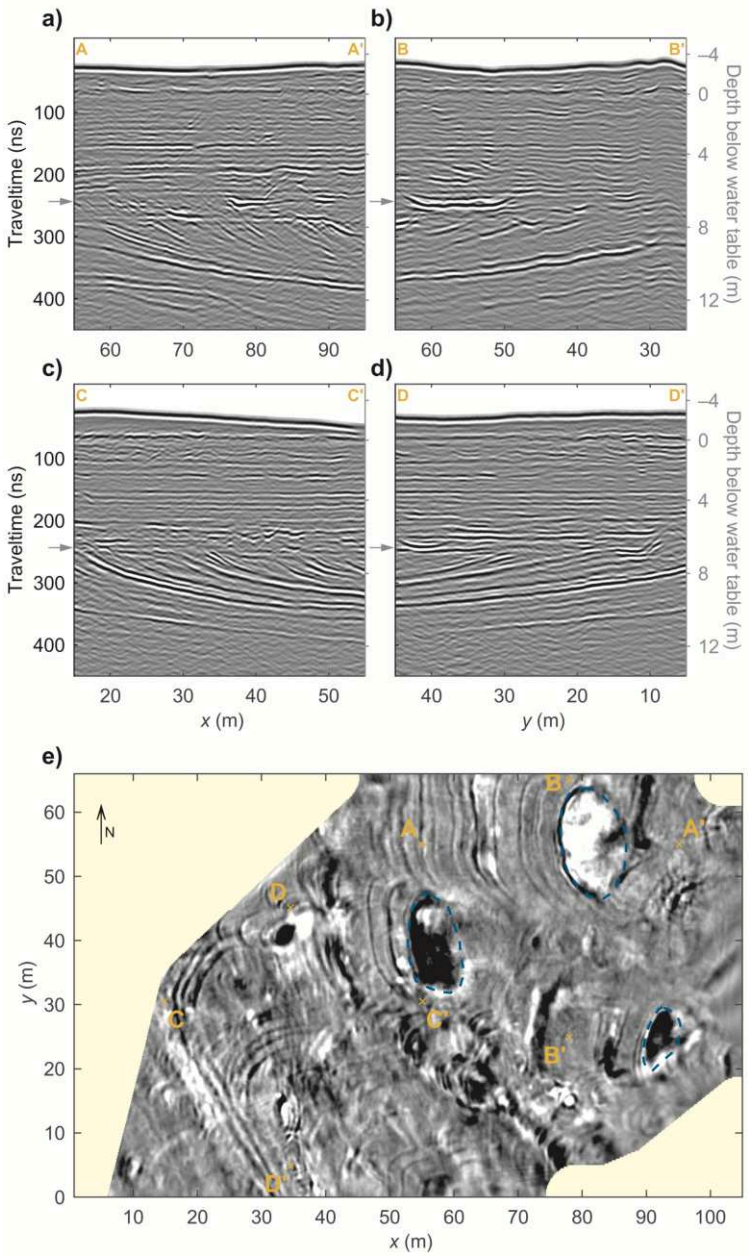

Figure 5.5.: Example slices extracted from our processed 3D GPR data volume along the (a and c) inline, (b and d) crossline, and (e) time direction. In (a-d), the gray arrows mark the location of the time slice as shown in (e), where the yellow crosses and labels indicate the start and endpoints of the inline and crossline slices as shown in (a-d). In (e), the blue colors mark example lenticular features forming local depression structures (a-b). Note, all GPR data images in this work are shown with the same amplitude color scaling, and (if not mentioned separately) the vertical exaggeration for inline and crossline slices is always two.

interpretation interest (Chopra and Marfurt, 2007). To perform GPR attribute analyses and to produce GPR facies models, we basically follow a workflow of Tronicke and Allroggen (2015), which these authors apply to delineate GPR facies in 2D GPR data recorded across horizontally stratified deposits. In comparison, our field site and our 3D GPR data set are characterized by more complex structures and reflection patterns, respectively. Taking this into consideration, we adopt, extend, and further develop their workflow to delineate our 3D data set into the main sedimentary units and GPR facies, respectively.

5.4.1. Gray-level cooccurrence matrix texture attributes

GPR facies can be distinguished based on their internal configuration imaged by characteristic reflection patterns in the GPR data. Texture attribute analysis is a popular approach to describe such patterns. In contrast to other geophysical attribute families, such as correlation- or semblance-based measures that are typically used to analyze and highlight differences and variations in the data including discontinuities, faults, and fractures (e.g., Barnes, 2016), texture attributes highlight zones of similar reflection characteristics. Thus, texture attributes are frequently used for advanced analysis and interpretation of 2D/3D seismic and 2D GPR data (e.g., de Matos et al., 2011; Zhao et al., 2016) whereas, up to now, the field of 3D GPR texture analysis has been largely untapped. Gao (2011) defines texture as a characteristic pattern defined by the magnitude and variation of neighboring amplitude samples in an image space. A popular statistical method to extract texture information is to calculate features from the gray-level cooccurrence matrix (GLCM) first introduced as an image processing tool by Haralick et al. (1973). In general, calculating GLCMs bases on 2D/3D images or data sets discretized into a specific number of gray levels n_g. In a 2D/3D window centered around an image pixel, different combinations of neighboring pixel values (cooccurrences) are counted and collected in an n_g x n_g matrix, the so-called GLCM. For interpretation of this 2D GLCM information, only a few application examples exist as it has been recognized to be quite counterintuitive. Thus, Haralick et al. (1973) and Soh and Tsatsoulis (1999) propose numerous features to condense the GLCM into point information known as GLCM attributes or features. Thus, if used in a moving-window approach, the GLCM-based method results in 2D attribute images or 3D attribute volumes comprising the texture around each pixel or geophysical datum, respectively. Despite the straightforward implementation of the GLCM method, the actual physical meaning of the derived attribute values is not clear; therefore, GLCM attribute images are primarily interpreted qualitatively.

To apply the GLCM method to our processed 3D GPR data volume (Figure 5.5), we focus on the saturated zone at traveltimes >70 ns where we encounter stable conditions in terms of subsurface velocity, signal frequency content, and signal wavelength, respectively. We use a typical value of $n_g = 16$ to calculate mean GLCMs and extract a total of 21 GLCM attributes in 3D including popular attributes such as autocorrelation, cluster shade, contrast, energy, entropy, and homogeneity (e.g., Chopra and Marfurt, 2007). The choice of the GLCM window is crucial in such analyses and finding an appropriate

size, such that the derived attributes highlight features at the scales of interpretation interest, is not a standardized procedure, and it often involves laborious parameter testing (especially when applied in three dimensions). In this study, we follow common practice and use a 3D window sized in the order of a dominant wavelength calculated using the dominant GPR signal frequency and the velocities in the saturated sediments (Figures 5.2 and 5.3) and, then, apply scale-based filtering in the next step of our workflow. To compromise the computational cost of the GLCM procedure and the temporospatial resolution in the resulting 3D attribute volumes, we extract GLCM features at every fourth time sample, every second inline sample, and every crossline sample. The resulting 21 attribute volumes comprise a total of 25M values each with a resolution of 0.25 m and 1.2 ns in the horizontal and vertical directions, respectively. In Figure 5.6a, we show the GLCM autocorrelation attribute as an example of the obtained 3D GLCM attribute database. In this visualization, GLCM autocorrelation is plotted as a transparent overlay on an inline slice extracted from our processed 3D GPR data volume at $y = 30.5$ m. As a typical example of a raw GLCM attribute, Figure 5.6a shows a noisy character with variations on multiple spatial and temporal scales. Especially at small scales (in the order of a few decimeters), we observe dominant scattered and isolated features as well as variations showing a wavelet-like character.

5.4.2. Scale-based attribute filtering

In the raw attributes (as exemplified in Figure 5.6a), multiple artifacts and noise components mask texture patterns at the target scale of several meters, that is, those of primary interest to characterize and delineate sedimentary structures using our GPR data set. Hence, an appropriate filtering strategy is needed, whose results highlight features at the scales of interpretation interest without introducing novel artifacts in the filtered attributes. Thus, we filter the 3D attribute volumes using an approach based on the discrete redundant wavelet transform (RWT) (Shensa, 1992), a well-established tool that has been successfully applied to 1D/2D/3D data sets including those from image processing, remote sensing, and geophysics (e.g., Leblanc, 2001; Prasad et al., 2012; Al-Dossary, 2015; Starck et al., 2015; Tronicke et al., 2020a) also including GPR data and attributes (Tronicke et al., 2020b). This RWT-based approach enables an undecimated rapid decomposition of a given data set into subsets comprising different temporal/spatial scales; that is, the decomposed data subsets show the same size as the input data set, which is advantageous for filtering typical geophysical data sets. Tronicke et al. (2020a) apply this method to archeogeophysical data and provide a comprehensive description of the two-step RWT-based filtering procedure used here. In the first step, a given data set is decomposed into a couple of wavelet planes w_n (scale levels) using a series of cubic-spline wavelet filters. Here, increasing n is related to increasing spatial and/or temporal scales in the data. In the second step, a filtered data set comprising the target scales is obtained by reconstruction. In this study, reconstruction is performed by summation of selected scale levels w_n. Due to its two-step implementation, this approach allows us to perform multiscale analyses; extract features at any scale of interest; and suppress artifacts, noise, and irrelevant features at any desired scale.

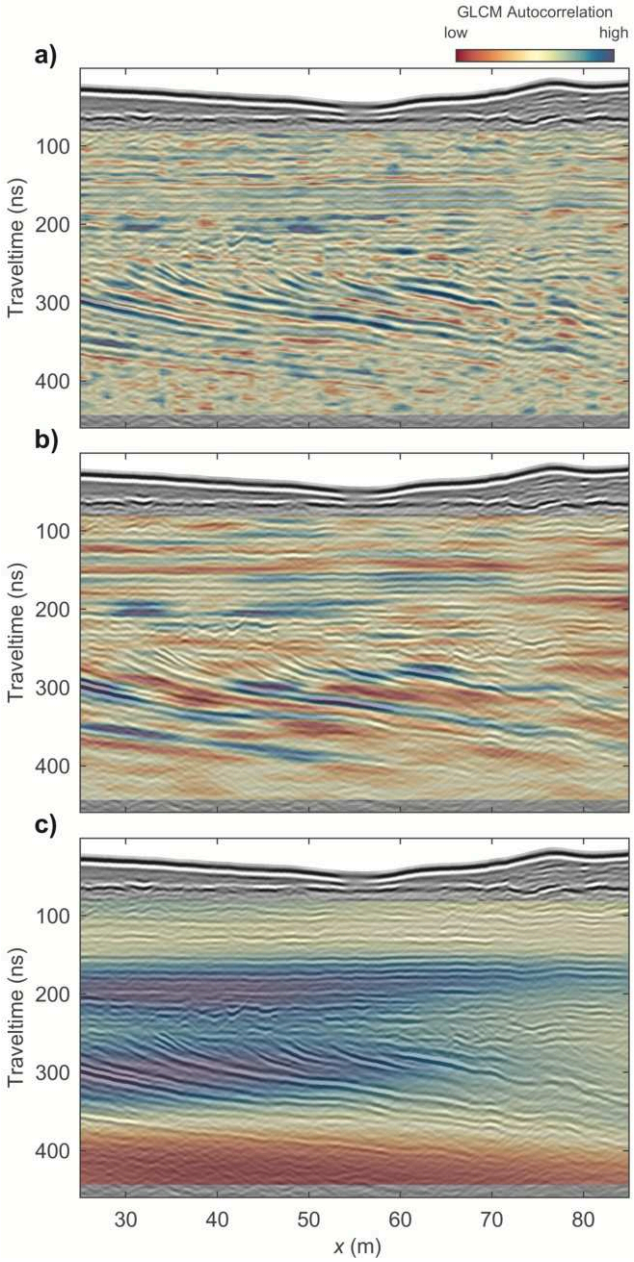

Figure 5.6.: Example inline slice at $y = 30.5$ m extracted from the processed 3D GPR data volume. As transparent overlays, we show three versions of 3D GLCM autocorrelation: (a) the raw (unfiltered) attribute as calculated directly from the GPR data, and (b) the detailed and (c) background attribute resulting from our scale-based filtering approach. All attribute images are normalized to their individual maximum value.

Using 3D RWT, we decompose our GLCM attribute volumes up to a scale level $n = 8$. In Figure 5.7, we show the rms values calculated for w_1 to w_8 obtained from the decomposition of the GLCM autocorrelation volume. In this representative example, the highest rms values are found at the two lowest scale levels, which confirms our observation of small-scale, high-amplitude noise components, and artifacts in the raw attribute (Figure 5.6a). To illustrate the filtering capabilities of this scale-based approach, we show in Figure 5.6b the reconstruction of GLCM autocorrelation using $\sum_{n=3}^{5} w_n$ for the slice shown in Figure 5.6a. In the following, we refer to these reconstructions as detailed attributes. A comparison of the raw and the detailed attribute images reveals that small-scale noise components and large-scale variations have been successfully suppressed. The detailed attribute image highlights texture patterns at small to intermediate scales and could be used, for example, to guide the visual interpretation of the underlying GPR data. Because a characterization of the main sedimentary units is the goal of this study, we also perform reconstructions using $\sum_{n=6}^{8} w_n$, which we term background attributes in the following; that is, they represent large-scale attribute variations at a scale of some meters in the vertical direction to tens of meters in the horizontal direction. In Figure 5.6c, we show the corresponding image of background GLCM autocorrelation for the slice selected in Figure 5.6a. In Figure 5.7, we highlight the wavelet planes used for the detailed and background attributes in blue and orange, respectively. Analyzing Figure 5.7 in more detail reveals, that the wavelet planes used for the background attribute show comparatively small rms values; hence, these attribute components are not visible in the raw (unfiltered) image. This representative example illustrates that applying the RWT approach to analyze and filter GLCM attributes helps to unveil texture features at the target scale for interpretation and represents an efficient and intuitive option to replace laborious parameter tests of GLCM window sizes.

To provide further insight into the background GLCM attribute database and to highlight its 3D character, we also show background GLCM correlation, energy, and entropy in Figure 5.8a–5.8c. Comparable to Figure 5.6, we visualize the attributes as transparent overlays in a 3D perspective view on a selected subvolume of our processed GPR data set. Without interpreting these results in detail, we see that the scale-based filtering approach yields attribute volumes with high continuity in the vertical and horizontal directions, which highlight areas of large-scale texture and structural variations in a meaningful way.

5.4.3. Meta texture attributes

Our background GLCM attribute database consists of 21 GLCM attribute volumes (as exemplified in Figure 5.8a–5.8c), which allow for a visual delineation of different large-scale GPR reflection patterns. However, comparing the GLCM correlation and energy (Figure 5.8a and 5.8b), especially at traveltimes >250 ns, reveals that different GLCM attributes might contain correlated information. Thus, we have to expect redundancy in our database that has to be eliminated because it might bias the results of the following classification procedure (which we intend to use for generating attribute-based GPR facies models in the next step of our workflow). Instead of manually eliminating correlated

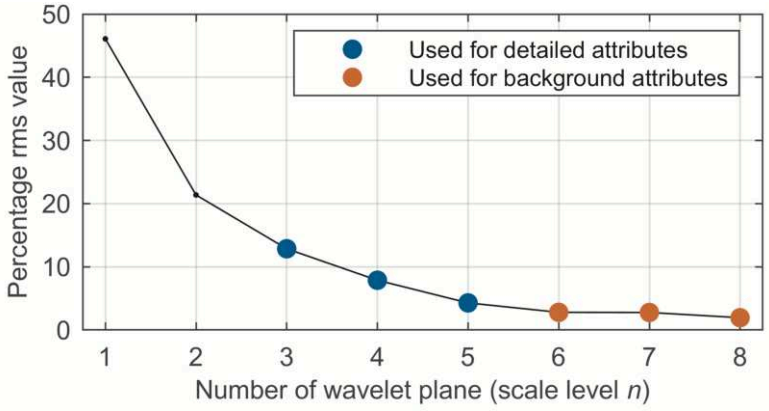

Figure 5.7.: Percentage rms values calculated for the wavelet planes resulting from the RWT-based decomposition of the 3D GLCM autocorrelation attribute volume. We use the scale levels $n = 3$, 4, and 5 (the blue dots) and $n = 6$, 7, and 8 (the orange dots) to reconstruct the detailed and background attribute volumes, respectively (Figure 5.6b–5.6c).

information (e.g., by visually selecting uncorrelated attributes from the background GLCM database), we use principal component analysis (PCA) to reduce the dimensionality of our database. PCA is a multivariate statistical tool that is typically used to structure, simplify, and visualize large databases and has been successfully used, for example, in seismic data and attribute analyses (e.g., Wang et al., 2015; Zhao et al., 2015). In general, PCA reduces the correlation between input variables by vector transformations and results in principal components (PCs) whose number equals the number of input variables. These PCs show less correlation than the input variables and are ordered by decreasing variance such that the first PC explains the largest amount of variance in the database. Selecting the first couple of PCs (i.e., the ones explaining most of the variance) for further analyses reduces the dimensionality of a database and eliminates redundant information from a database. In particular, the latter is crucial to obtain reliable and meaningful facies models from a high-dimensional attribute database using classification algorithms (Zhao et al., 2015).

In this study, we apply PCA to analyze and reduce our background GLCM attribute database. In Figure 5.9, we show the variance that is explained by the 21 resulting individual PCs as orange bars as well as the explained cumulative variance in blue. Our results show that the first three PCs explain more than 98% of the cumulative variance of the input database (74% by PC1, 18.5% by PC2, and 6% by PC3); thus, we select these PCs for further analyses. As PC1, PC2, and PC3 condense the main information of our background GLCM attributes, we call them meta texture attributes (Zhao et al., 2015) in the following and number them according to the underlying PCs (i.e., meta texture attribute 1, 2, and 3). In Figure 5.10, we show the meta texture attributes 1, 2, and 3 as transparent overlays on the same GPR data slice as analyzed in Figure 5.6. In general, Figure 5.10 demonstrates that our meta texture attributes highlight areas

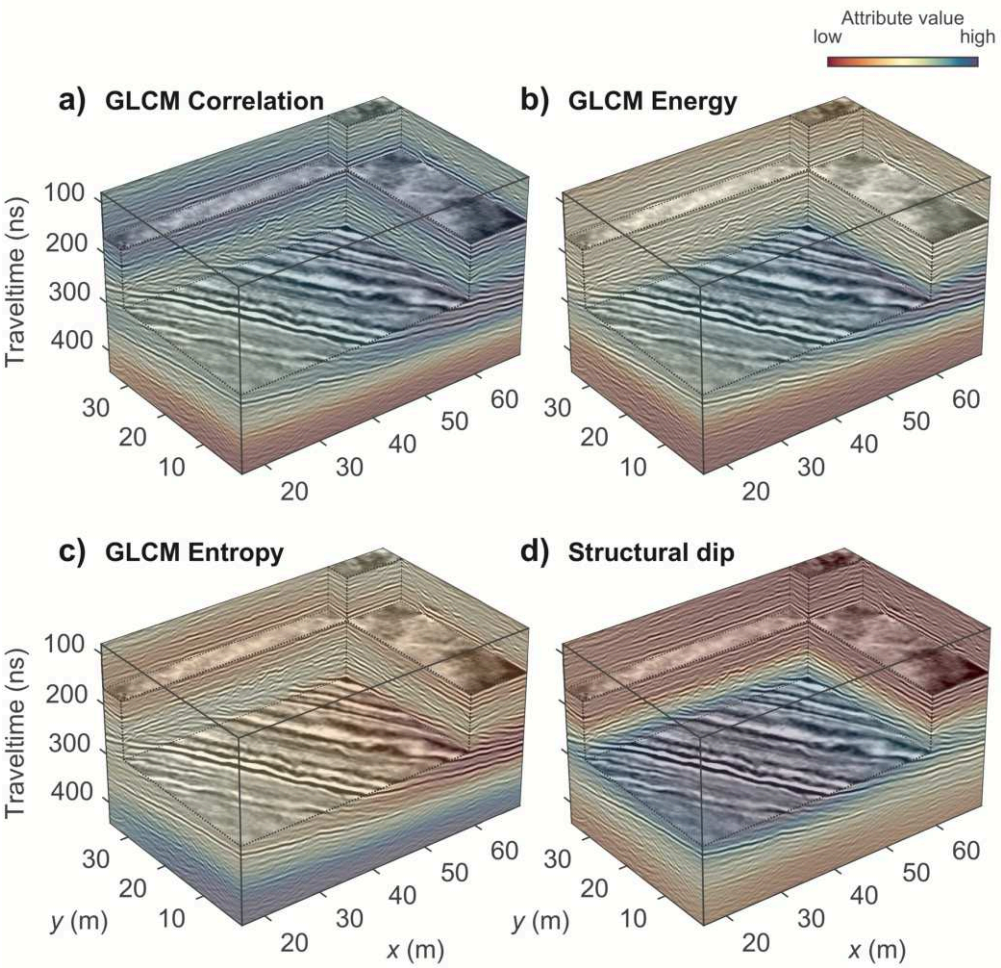

Figure 5.8.: A 3D perspective view across a selected subvolume of our processed 3D GPR data set. As transparent overlays, we show (a-c) selected background GLCM attributes and (d) the background structural dip, which result from our scale-based filtering approach. All attribute images are normalized to their individual maximum value.

of different large-scale structural variations in our GPR data, whereas each of the meta texture attributes shows different variations indicating three to five sedimentary units. Now, these meta texture attributes form the basis for further interpretation, that is, to generate GPR facies models characterizing the sedimentary settings at our field site.

5.4.4. Geometric attributes

As discussed previously, the sedimentary features imaged by our GPR data set show considerable differences regarding their structural dip (Figure 5.5), which is commonly regarded as a key feature when interpreting 3D seismic and GPR data. To better quantify and distinguish sedimentary structures and to complement our meta texture attributes with geometric and, thus, physically verifiable information, we include 3D structural dip as an additional attribute. To compute this attribute, we extract the inline and crossline dip from our GPR data set using a localized PCA approach (e.g., Tingdahl and Hemstra, 2003). Considering the same velocity model as used for migration, we then transform the inline and crossline dip into the structural dip (i.e., the true geologic dip). To analyze and use this attribute at the same spatial scales as the meta texture attributes, we apply the same scale-based filtering approach as used for the GLCM texture attributes (i.e., decomposition up to $n = 8$ and reconstruction using $\sum_{n=6}^{8} w_n$) resulting in a background structural dip attribute volume. In Figure 5.8d, we show this attribute as a transparent overlay on a subvolume of our processed 3D GPR data and compare it to selected GLCM background attributes (Figure 5.8a–5.8c). The structural dip shows minimum (the red

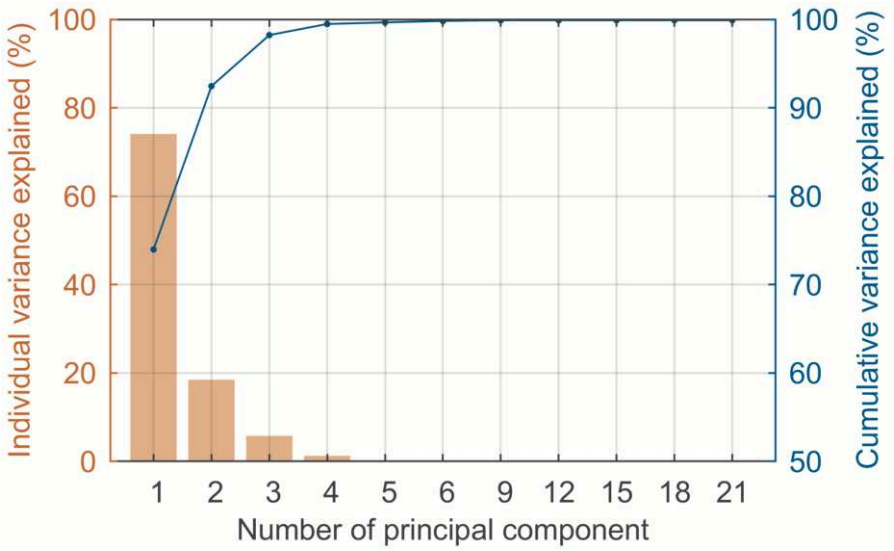

Figure 5.9.: Individual (the orange bars) and cumulative (the blue line) variance explained by the PCs resulting from PCA of the background GLCM attribute database. The PCs 1–3 (called meta texture attributes here) explain more than 98% of the cumulative variance in the database and are used for further analyses.

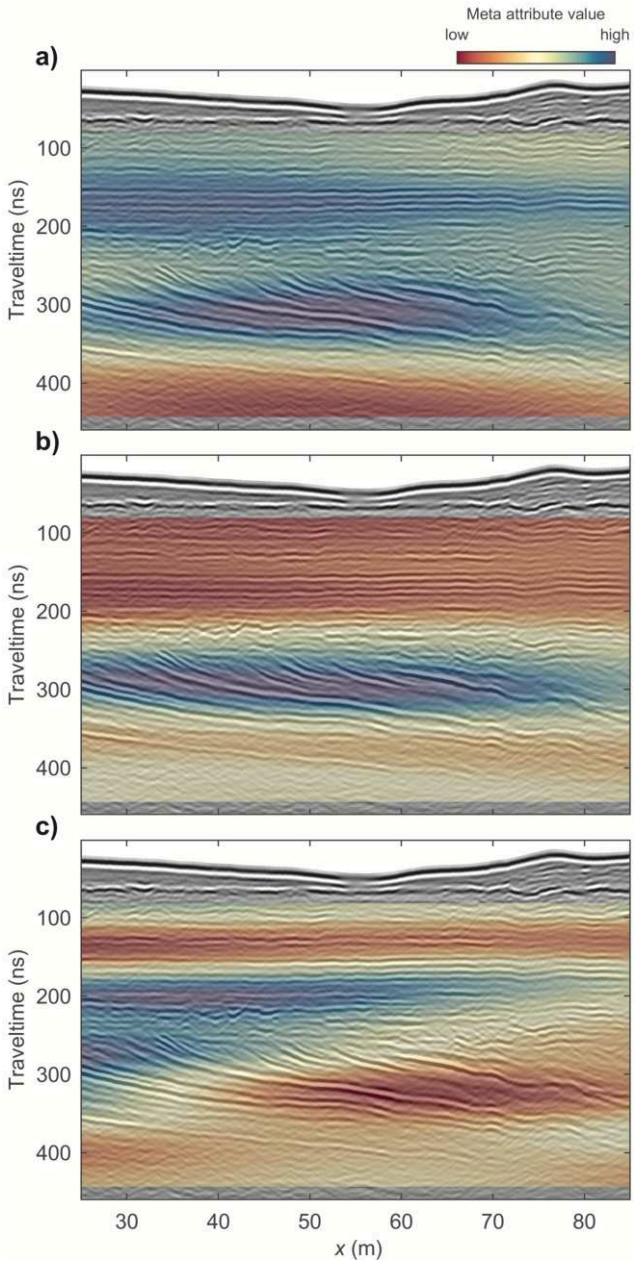

Figure 5.10.: Example GPR inline slice as shown in Figure 5.6. As transparent overlays, we show (a-c) the meta texture attributes 1, 2, and 3; that is, the first three PCs resulting from PCA of the background GLCM attribute database. All attribute images are normalized to their individual maximum value.

colors) and maximum (the blue colors) values of 0° and 12°, respectively, and it indicates three major units characterized by small/no dip at traveltimes up to approximately 250 ns, large dip between traveltimes of approximately 250 and 320 ns, and intermediate dip at traveltimes larger than approximately 320 ns.

5.4.5. Visualization and classification

Using PCA, we have reduced our background GLCM attribute database (as exemplified in Figure 5.8a–5.8c) to three meta texture attributes (Figure 5.10) highlighting the major textural and structural variations in the GPR data. In geophysical data analysis, a commonly applied composite imaging technique to produce integrated visualizations of three colocated data sets (such as our meta texture attributes) is known as color stacking or red-green-blue (RGB) blending (e.g., Henderson et al., 2008; Böniger and Tronicke, 2010b). In general, an RGB-blended image is generated by assigning each of the three data sets to one particular color channel. The resulting RGB composite image integrates the information of three different data sets and, thus, simplifies and aids comparative analyses of a database.

A further step in interpretation, which represents a more quantitative approach to analyze such databases, relies on unsupervised clustering approaches that are used to partition the input data into classified models. Among many others, the unsupervised fuzzy c-means algorithm has proven to be a robust classification method for largely unexplored data and has been successfully used in different geophysical applications (e.g., Paasche et al., 2006; Linder et al., 2010; Saraswat and Sen, 2012). In general, the fuzzy c-means algorithm partitions the input data into a (user-defined) number of clusters (classes) by iteratively minimizing a distance-based objective function to search for optimum cluster centers. In contrast to other relevant classification techniques such as the k-means algorithm, the fuzzy c-means algorithm includes partial memberships and, hence, provides individual membership information to each of the clusters for every classified datum. This, in turn, yields information on the integrity of the classified model and, hence, can be used to efficiently visualize a kind of probability that a datum belongs to the assigned class. Bezdek (1981) and Bezdek et al. (1984) provide a comprehensive description, a detailed derivation, and an implementation guide for the fuzzy c-means algorithm.

To qualitatively interpret the meta texture attributes in terms of GPR facies, we conduct RGB blending by assigning the meta texture attributes 1, 2, and 3 to the red, green, and blue color channels, respectively. In Figure 5.11a, we show the resulting composite GPR facies image as a transparent overlay on the same GPR data slice as analyzed in Figures 5.6 and 5.10. The major color variations in this composite image indicate four facies. For example, the yellow colors predominantly highlight continuous dipping beds whereas the purple colors between approximately 150 and 220 ns emphasize (sub-)horizontal strata. Because our field site is part of the Wadden Sea National Park, we lack independent information such as borehole-based logs for validating our GPR facies models. However, for comparison, we add the local interval velocity model (the black line) derived from a spectral velocity analysis of the CMP gather recorded at a

center position at $x/y = 53$ m/30.5 m which indicates a similar layering compared to the composite image. Thus, the composite GPR facies image visualizes major structural variations and now can guide further interpretations including the generation of classified GPR facies models.

To obtain a classified GPR facies model, we perform fuzzy c-means clustering. As discussed previously, the number of clusters is a user-defined parameter. The optimum number of clusters is typically established by statistical evaluation of the results obtained with varying numbers of clusters, or, if available, by considering a priori information. Based on the results of our CMP experiments (Figure 5.2), our observations in the processed GPR data volume (Figure 5.5) and the composite GPR facies image (Figure 5.11a), and considering the results of parameter tests using different numbers of clusters (not shown here), we present two versions of a four-class GPR facies model. In Figure 5.11b–5.11c, we show these models as transparent overlays on the same GPR data slice as illustrated in Figure 5.11a. The color saturation of the models shown in Figure 5.11b–5.11c reflects the degree of membership resulting from the fuzzy c-means clustering approach. For the model shown in Figure 5.11b, we only use the meta texture attributes (Figure 5.10) as input data; that is, this model can be considered as a pure texture-based facies model. For the model shown in Figure 5.11c, we use the meta texture attributes and the structural dip (Figure 5.8d) as input data; that is, this model can be considered as a dip-constrained texture-based facies model. Comparing these two models illustrates that the overall structures and facies class distributions show only minor differences. However, using the structural dip as additional input helps to refine and constrain the clustering process resulting in higher memberships and an overall sharper facies model. Thus, we regard the dip-constrained facies model (Figure 5.11c) as our final model and consider it for further interpretation. As already discussed for the composite facies image (Figure 5.11a), also our final GPR facies model is in good agreement with the interval velocity variations derived from our CMP data. To emphasize the 3D character of our final facies model, we show it in Figure 5.12 in 3D perspective view as a transparent overlay on the processed 3D GPR data volume. This illustrates that our four-class solution provides an overall sharp 3D delineation of the individual facies classes, which show a high spatial continuity in the horizontal and vertical directions. The final facies model (Figures 5.11c and 5.12) can now be used to interpret the individual facies classes also in view of depositional environments and history.

5.5. Facies interpretation

Using attribute-based analyses, we have produced a classified 3D GPR facies model (Figures 5.11c and 5.12) from our processed 3D GPR data volume (Figure 5.5), which delineates four facies classes based on their individual texture patterns (as measured by 3D GLCM attributes) and the structural dip attribute (Figure 5.8). Due to strict environmental protection rules in the Wadden Sea National Park, reference data (such as borehole-based logs, outcrop, and excavation data) are not available at our field site for a further geologic interpretation of our facies model (e.g., in terms of sediment composition).

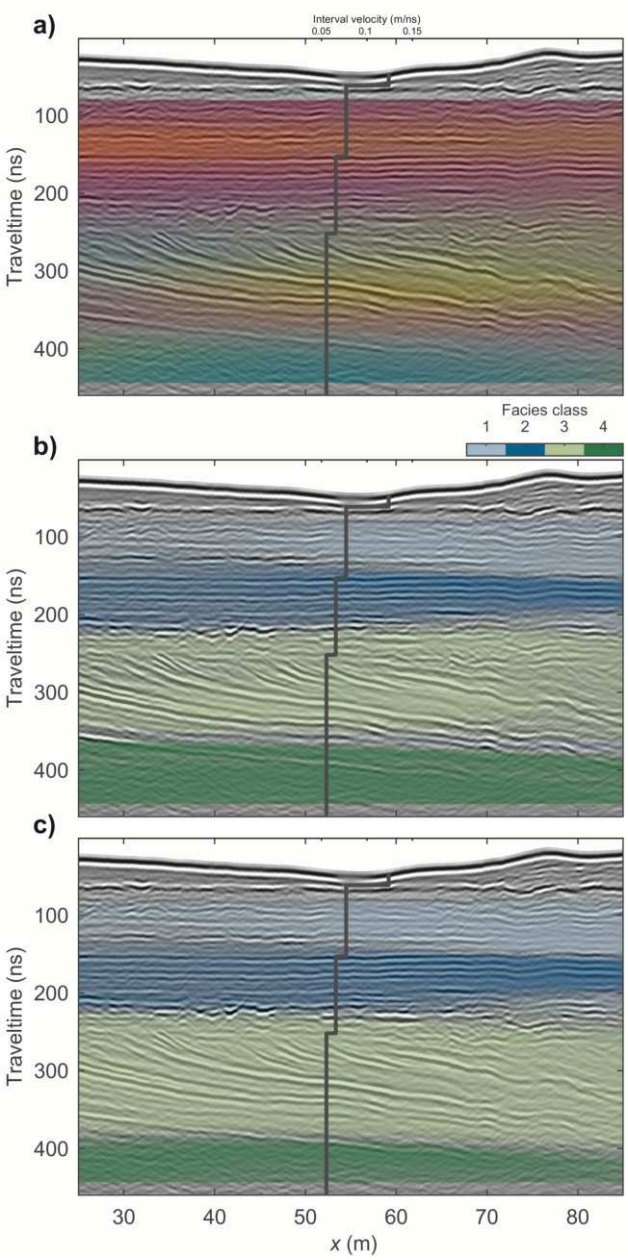

Figure 5.11.: Example GPR inline slice as shown in Figures 5.6 and 5.10 including an interval velocity model (the black line) as derived from our CMP data recorded at a center position at $x/y = 53$ m/30.5 m (Figure 5.1) using spectral velocity analysis. As transparent overlays, we show (a) the composite GPR facies image as obtained by RGB blending of the meta texture attributes as well as two four-class GPR facies models as obtained by fuzzy c-means clustering using as input (b) the meta texture attributes only and (c) the meta texture attributes and the structural dip. In (b-c), the color saturation reflects the degree of membership.

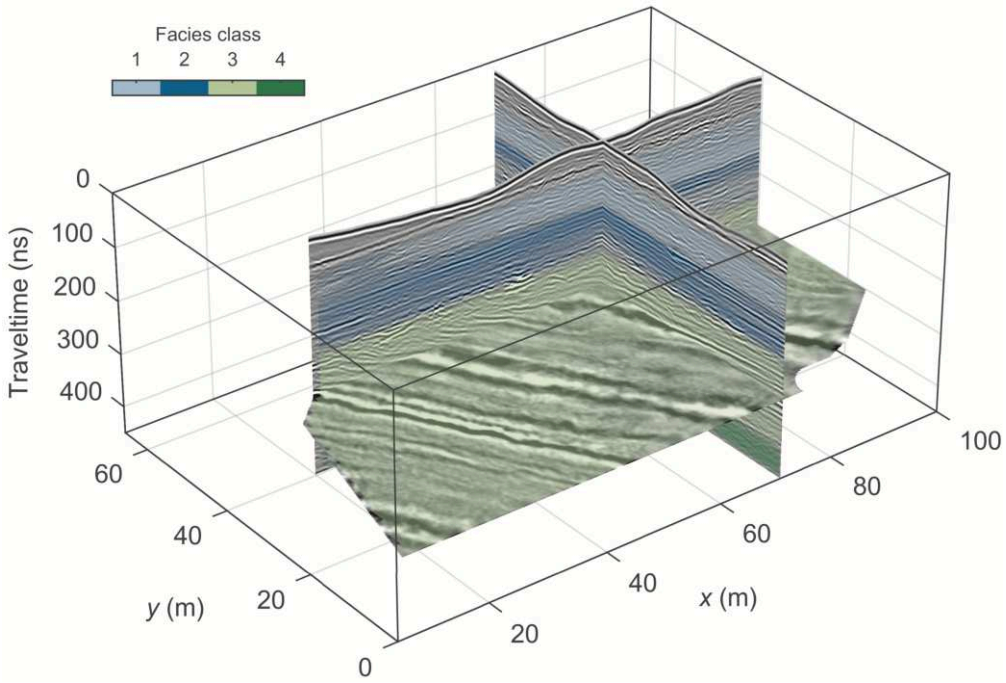

Figure 5.12.: A 3D perspective view across our processed 3D GPR data volume. As a transparent overlay, we show our final four-class GPR facies model as obtained by fuzzy c-means clustering using as input the meta texture attributes and the structural dip (Figure 5.11c). The color saturation reflects the degree of membership.

Thus, we follow common practice in such sedimentological GPR applications and construct a GPR facies chart by extracting the typical inline, crossline, and time/depth reflection patterns from our processed 3D GPR data volume for each of the four facies classes found in our final facies model. In Figure 5.13, we present this facies chart including a description of typical characteristics of the extracted reflection patterns (note that, considering our velocity models as shown in Figure 5.2, a traveltime of 100 ns corresponds to a depth of approximately 3.30 m in the saturated sediments).

Having at hand and referring to our processed GPR data volume (Figure 5.5), our final facies model (Figures 5.11c and 5.12), and the corresponding facies chart (Figure 5.13), we interpret our data in terms of the underlying depositional environments and the recent formation history of Spiekeroog island, which is extensively discussed by Streif (1990, 2002) and summarized by Röper et al. (2012). Facies class 4 identifies a thin area in the deepest parts of our GPR data set and shows the globally lowest amplitudes. The reflections found here exhibit an anisotropic character with discontinuous patterns in the inline direction and increased continuity in the crossline direction. However, the overall reflection characteristics of this facies class indicate that the maximum penetration depth of our GPR data is reached; thus, this facies is not analyzed in more detail. Facies class 3 starts at traveltimes of approximately 250 ns and generally extends over more than 100 ns. Here, we observe high-amplitude quasicontinuous beds with dip angles up to 12°

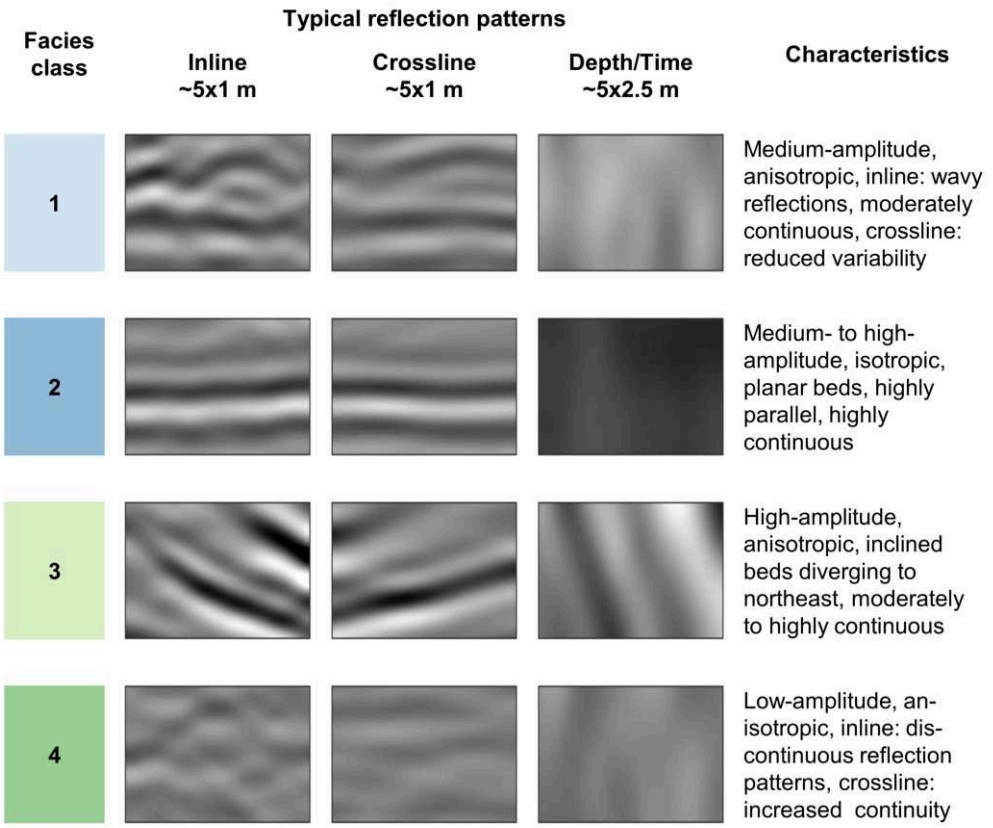

Figure 5.13.: GPR facies chart of the facies classes 1-4 from our final 3D GPR facies model (Figures 5.11c and 5.12) characterizing typical inline, crossline, and depth/time reflection patterns as extracted from our processed 3D GPR data volume (Figure 5.5). The individual facies classes identify typical near-surface depositional environments of a dune island (class 1, recent dunes; class 2, intertidal beach deposits; and classes 3 and 4, shallow-marine beds). The vertical exaggeration for the inline and crossline slices is 3.5.

inclined toward the northeast. The layering is dominated by a prograding pattern; that is, the layer thickness grows in the northeast direction, which is in good agreement with the overall northeast-oriented growth of the island. These features indicate deposition in a shallow-marine environment near a former shoreline close to the island's core. At the transition between facies classes 2 and 3 (at traveltimes from approximately 200 to 250 ns), we recognize small degrees of membership and observe high-amplitude reflections also forming local lenticular depression structures, which are also highlighted in blue in Figure 5.5e. We speculate that these structures are associated with clay or mud lenses reported for some parts of the island. Such moor and lagoon deposits on top of marine sediments are typically accumulated during the stage of a dune or barrier island formation in which the island slowly begins to emerge above the mean sea level (Streif, 1990). At greater depths (not imaged by our GPR data), more continuous clay/mud structures deposited during earlier stages of the island's formation create an aquitard constraining the structure of the local freshwater lens (Röper et al., 2012). Within facies class 2 (located at traveltimes between approximately 150 and 200 ns), we observe medium- to high-amplitude isotropic and continuous reflections forming an approximately 2 m thick horizontally layered unit. This sequence can be associated with intertidal beach deposits with individual layers accumulated by the steady turn of the tide. The uppermost facies class 1 extends up to traveltimes of approximately 150 ns and is characterized by medium-amplitude, anisotropic reflection patterns with a moderately continuous and wavy character in the inline direction showing increased continuity in the crossline direction. Here, moderately continuous patterns are locally interrupted by quasicontinuous reflection elements oriented parallel to the surface. These features indicate recently (and, on top, actively) accumulated dune sands deposited since the island's steady emergence above sea level. In summary, our attribute-based facies model reasonably delineates features as imaged by our 3D GPR data set into four facies classes, which particularly characterize the recent local depositional history in accordance with the findings of Streif (1990, 2002) and Röper et al. (2012); that is, from bottom to top we find shallow-marine sediments topped by clay/mud lenses, intertidal beach deposits, as well as recently and actively accumulated dune sands.

5.6. Conclusion

In this case study, we use state-of-the-art data acquisition, quality control, and processing to produce a 3D GPR data set that, in detail, images numerous near-surface sedimentary features and patterns at a field site on the dune island of Spiekeroog (Northern Germany). To analyze this data set beyond typical manual interpretation approaches, we developed and applied a workflow combining modern data analysis, filtering, and statistical techniques to calculate, process, and integrate 3D GLCM texture and geometric attributes to obtain attribute-based GPR facies models.

In general, the proposed workflow is a four-step approach to obtain 3D GPR facies models including attribute calculation, filtering, dimensionality reduction, and classification. Here, we calculate a set of GLCM texture and geometric attributes, and we

use an RWT-based filtering approach, PCA for dimensionality reduction, and a fuzzy c-means classification approach. Although this workflow has been successfully applied to our GPR data set, there are of course various methodologies for each of these four analysis steps, which might reproduce or even improve the presented results. However, a detailed discussion of such methodological variants is beyond the scope of this case study.

GLCM texture attributes are a powerful tool to characterize reflection patterns and, thus, pose an ideal basis to delineate GPR data into sedimentary facies. Features emphasized in unprocessed GLCM texture attributes critically depend on the size of the GLCM analysis window and are typically dominated by variations at small scales (in the order of some centimeters to a few decimeters in the presented data set) related, for example, to the wavelet character of GPR data. Thus, we implemented an approach to replace extensive parameter tests of GLCM window sizes and configurations with a 3D scale-based filtering procedure. We believe that this procedure is crucial to obtain the presented results because it allows for undecimated and rapid filtering to generate attribute volumes highlighting texture and geometric attribute features at the spatial scales of interpretation interest.

By integrating meta texture attributes (derived by PCA of our filtered texture attribute database) with composite imaging and fuzzy c-means clustering, we produced 3D GPR facies models characterizing the dominant, large-scale texture and structural variations in our GPR data set. In addition to texture attributes, geometric attributes are commonly used to describe facies in geophysical analyses of sedimentary systems. In contrast to GLCM texture attributes, geometric attributes provide quantitative information about reflection patterns and associated structures. Our results show that considering additional geometric information such as the structural dip in the classification step helps to refine and constrain pure GLCM texture attribute-based facies models. Our GPR facies models are in good agreement with velocity models derived from additional CMP measurements. Moreover, typical reflection patterns within the facies of our classified model show characteristic sedimentary features of relevant depositional environments including shallow-marine sequences, intertidal beach deposits, as well as recently and actively accumulated dune deposits. Accordingly, our facies model supports a basic understanding of the recent formation history of the island.

In this study, we focus on the large-scale information extracted from our attribute database (consisting of texture and geometric attributes) to generate GPR facies models delineating sedimentary units at a spatial scale of several meters. Therefore, we discard detailed texture and geometric features corresponding to intermediate scale levels (in the order of several decimeters to a few meters in the presented data set) in our scale-based analysis and filtering approach. Thus, a possible extension of our workflow (which we aim to address in future research) is to use this detailed information to improve and refine our facies models at the subfacies scale. However, the proposed workflow represents a novel and clear strategy to obtain GPR facies models in a semiautomated and reproducible way. Because our interpretation approach comprises only a few user-specified parameters (e.g., in the scale-based filtering approach), it eases the derivation of reliable facies models

from 3D GPR data sets and can thus help to perform a more objective and consistent interpretation of GPR data collected across different sedimentary environments.

6. 3D Classified GPR Facies Models from Multi-frequency Data Volumes: A Synthetic Study

Philipp Koyan and Jens Tronicke*

6.1. Introduction

Ground-penetrating radar (GPR) is a standard technique to image near-surface structures in sedimentary environments (Neal, 2004). The availability of modern multi-channel GPR systems enables the acquisition of densely sampled GPR data sets also using multiple antenna frequencies to image the subsurface at different spatial scales (Lu et al., 2020). However, today's interpretation techniques largely rely on single-frequency data sets typically interpreted in a manual and, thus, subjective and non-reproducible manner, for example, following concepts of GPR facies as described by Van Overmeeren (1998). More recently, attribute-based workflows have shown to be a more objective and reproducible approach to interpret individual 2D/3D GPR data sets and to generate classified facies models, for example, using unsupervised classification techniques (Tronicke and Allroggen, 2015; Koyan et al., 2021).

To investigate the potential of an integrated interpretation of multi-frequency data sets, we apply an attribute-based workflow introduced by Koyan et al. (2021) for single-frequency 3D GPR data in a hierarchical manner to analyze synthetic multi-frequency GPR volumes. The GPR volumes have been simulated using source frequencies of 50 and 200 MHz across a realistic sedimentary model (Figure 6.1a; Koyan and Tronicke, 2020a,b). The attribute-based workflow includes the calculation of an attribute database for each data volume comprising gray-level co-occurrence matrix (GLCM) texture attributes, a scale-based filtering approach, and the application of principal component analysis (PCA). The resulting meta texture attributes comprise the dominant information at the respective spatial scale and represent the input for fuzzy c-means classification. Classifying our 50 MHz meta attributes complemented by a structural dip attribute yields a facies model comprising the major structural zonation. To realize an hierarchical approach integrating data at different spatial scales, we then subdivide these major facies using the classification results of the corresponding 200 MHz attributes.

*A reviewed expanded abstract of the same title is published as Koyan and Tronicke (2022) in the proceedings of 19th International Conference on Ground Penetrating Radar, SEG, Global Meeting Abstracts, 139–142.

As a result, we obtain a multi-scale facies model; that is, a model comprising major structural variations as inferred from the 50 MHz data and also including structural details as resolved by the 200 MHz data. We compare this model to the input model to illustrate that our strategy results in a single facies model comprising subsurface heterogeneities at different spatial scales and represents an initial step towards a more objective and reproducible interpretation of multi-frequency GPR volumes.

6.2. Synthetic GPR data

As starting point, we use two synthetic GPR data volumes simulated with a source wavelet center frequency of 50 and 200 MHz (Koyan and Tronicke, 2020b). These GPR data have been generated using open-source electromagnetic modeling software gprMax (Warren et al., 2016) across a realistic sedimentary input model inferred from outcrop observations and geostatistical modeling (Bayer et al., 2011; Comunian et al., 2011; Koyan and Tronicke, 2020a). The model has a size of 16 x 10 x 7 m and shows diverse sedimentary variations on multiple spatial scales. In Figure 6.1a, we show the model in terms of GPR velocity with the main genetic units labeled from I to VI (and separated by white dotted lines) following Bayer et al. (2011). When comparing these units to each other, we observe structurally rather homogeneous, large-scale undulating, small-amplitude velocity variations (unit VI), more heterogeneous regions characterized by local small-scale, high-amplitude velocity variations partly dipping towards lower x values (Units I, II, and IV), and alternating sequences showing small-scale, medium-amplitude velocity variations dipping towards lower x values (Units III and V). Further details and background information can be found in Bayer et al. (2011), Comunian et al. (2011), and Koyan and Tronicke (2020a,b).

In this study, we use ready-to-interpret versions of the 50 and 200 MHz data sets (Figure 6.1b and 6.1c) resulting from a 3D GPR processing sequence including topographic migration (Koyan and Tronicke, 2020b). In general, the resolution and, thus, the degree of detail in the GPR volumes increases with increasing source frequency. The 50 MHz volume images large-scale structures and the major zonation. In contrast, the 200 MHz volume resolves structural details, for example, within the alternating sequences found in units III and V. Comparing Figure 6.1a-c also considering the average frequency content of both data volumes (i.e., peak frequencies of 55 and 181 MHz, and bandwidths of 40 and 126 MHz for the 50 and 200 MHz volume, respectively) reveals that the multi-frequency GPR volumes complement each other in terms of the imaged spatial scales. This already indicates that an integrated interpretation of these multi-frequency GPR data might be a suitable strategy to better understand such complex sedimentary settings.

6.3. GPR attribute databases

To calculate and analyze the attribute databases, we follow Koyan et al. (2021) who present a workflow to generate attribute-based facies models from a single-frequency GPR volume imaging structures across a dune island. For each processed GPR volume

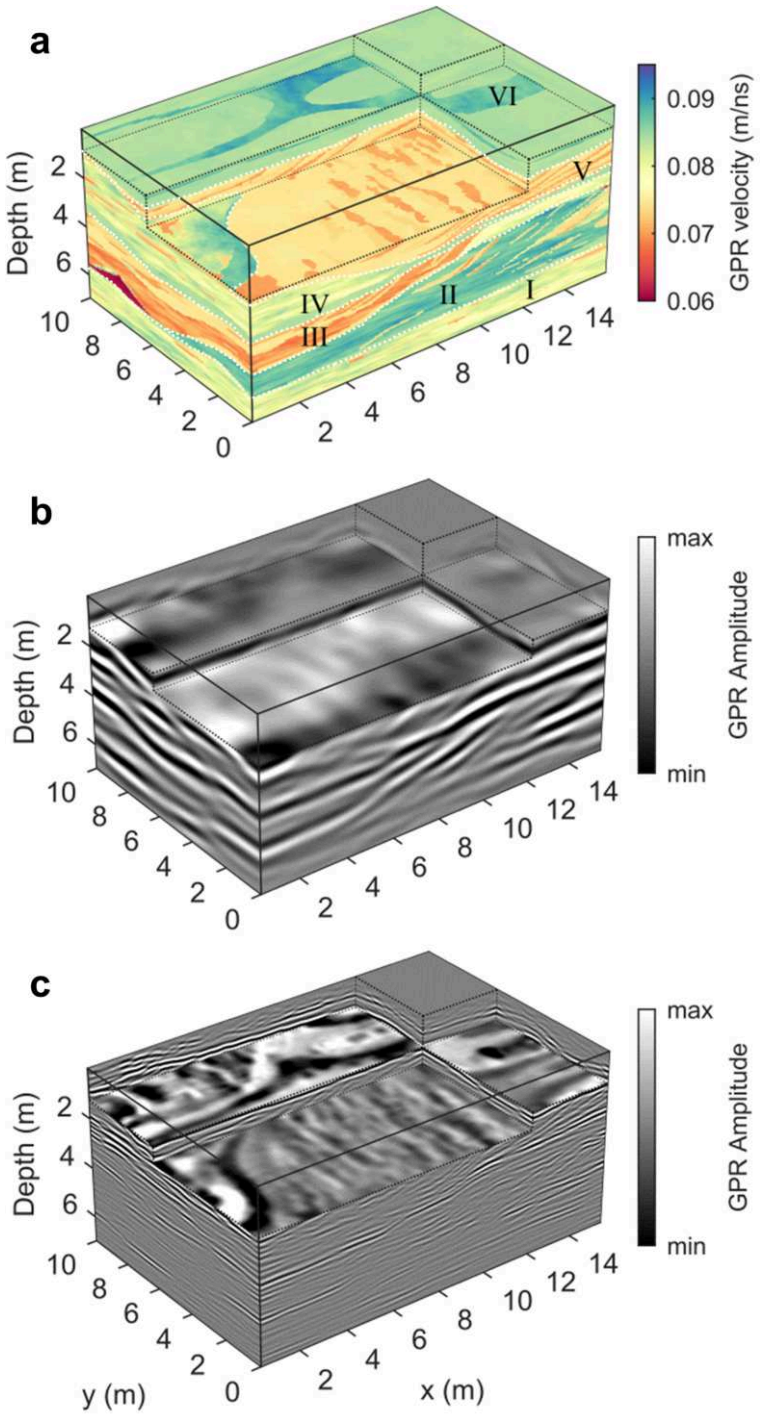

Figure 6.1.: 3D view across (a) the GPR velocity model used as input to model GPR volumes with a center frequency of (b) 50 MHz and (c) 200 MHz. In (a), the main genetic units are labeled from I to VI. GPR volumes in b and c are shown after 3D GPR processing.

(Figure 6.1b and 6.1c), we calculate a total of 17 texture attributes including contrast, energy, entropy, and homogeneity using the gray-level co-occurrence matrix (GLCM) technique (Haralick et al., 1973). To account for the different resolution of the GPR volumes, we adjust the 3D GLCM window size to the respective average wavelength (i.e., ~1.6 m and ~0.4 m in all directions for the 50 and 200 MHz data, respectively).

GLCM texture attributes typically show artifacts and noise (e.g., related to the wavelet character of the GPR data). To eliminate these patterns that might mask texture features at the target spatial scales (i.e., some decimeters to a few meters for the 200 and 50 MHz data, respectively), we filter both attribute databases using a scale-based strategy based on the redundant wavelet transform (RWT; Tronicke et al., 2020a,b).

Moreover, GLCM attributes are prone to contain correlated information resulting in redundancy in a typical GLCM attribute database which, in turn, biases further analyses such as unsupervised facies classification. To eliminate correlated information, we perform a dimensionality reduction of our GLCM databases by applying principal component analysis (PCA). For further analysis, we use the first three principal components (PCs) that explain more than 95% of the database variance, and term them meta texture attributes numbered with respect to the corresponding PC (i.e., meta texture attribute 1, 2, and 3).

Koyan et al. (2021) show that complementing texture attributes with a structural dip attribute (i.e., the geologic dip angle) for unsupervised classification helps to obtain sharper GPR facies models compared to results just relying on texture attributes. Thus, we calculate structural dip volumes for both GPR data sets and (to analyze all attributes at comparable spatial scales) filter them using the same scale-based approach as applied to the texture attribute databases. As a result, we obtain an attribute database for each frequency consisting of three meta texture attributes and a structural dip attribute comprising the dominant information at the respective spatial scale.

To provide insight into our attribute databases, we show as a transparent overlay on the corresponding GPR data volume the meta texture attribute 1 (Figure 6.2a and 6.2d) and the structural dip attribute (Figure 6.2b and 6.2e). Analyzing the databases in more detail reveals that the multi-frequency attributes complement each other in the same way as the corresponding GPR data volumes (Figure 6.1b and 6.1c). The 50 MHz attributes comprise information on the large-scale stratification. For example, the meta texture attribute 1 indicates three zones characterized by low, medium, and high values which are less evident in the corresponding 200 MHz attribute (compare Figure 6.2a and 6.2d). In contrast, the 200 MHz attributes reveal details that are not resolved by the 50 MHz data and attributes, respectively (compare Figure 6.2a and 6.2b with 6.2c and 6.2d).

6.4. Attribute classification and interpretation

To produce classified facies models, we rely on the fuzzy c-means classification algorithm that yields a degree of membership to each class for each classified datum. In contrast to other popular techniques such as k-means, this membership information allows analyzing the integrity of the classification result. Using the 50 MHz attribute database (the meta

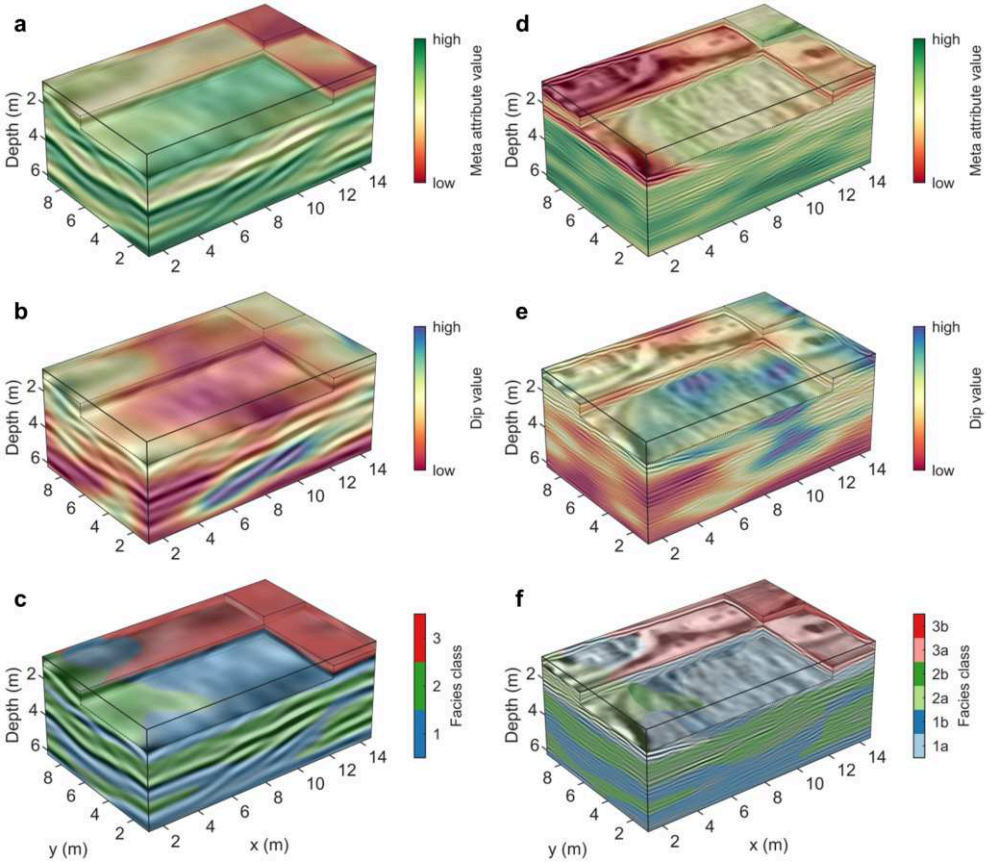

Figure 6.2.: 3D view across the synthetic (a-c) 50 MHz and (d-f) 200 MHz GPR volumes. As a transparent overlay, we show the meta attribute 1 calculated from the (a) 50 MHz and (d) 200 MHz texture attribute database, the structural dip across the (b) 50 MHz and (e) 200 MHz GPR volume, (c) a major facies model obtained by classification of the 50 MHz meta attributes and structural dip, and (f) a detailed facies model resulting from classification of the 200 MHz meta attributes and structural dip constrained by the major facies model as shown in c. Color saturation in (c) and (f) reflects the degree of membership as provided by fuzzy *c*-means cluster analysis.

attributes 1 to 3 and the structural dip) as input data and considering the observations from Figure 6.2a and 6.2b as well as results of tests with different numbers of classes (not shown here), we produce a three-class facies model as shown in Figure 6.2c as a transparent overlay on the 50 MHz GPR volume. Here, the color saturation of the model reflects the degree of membership to the assigned facies class for each datum.

Analyzing Figure 6.2c in more detail reveals that our approach results in a facies model sharply delineating three continuous facies characterized by overall high memberships. Comparing the classification result to the input model (Figure 6.1a) shows that the three-class model characterizes the major (large-scale) structural variations and zonation in a meaningful way. That is, facies class 3 mainly comprises the structurally most homogeneous part located at shallow depths (unit VI), facies class 2 predominantly characterizes regions showing localized small-scale structural heterogeneities (unit IV and more heterogeneous parts of unit II such as the one found at x >12 m and depths between 3 and 5 m), and facies class 1 includes zones with repeating small-scale variations found in the alternating sequences (units III and IV) as well as structurally less heterogeneous regions showing locally high dip values (major parts of units I and II).

In the next step, we integrate the small-scale structural details contained in the 200 MHz attribute database (Figure 6.2d and 6.2e) into the major facies model (Figure 6.2c). For this, we use the major facies model to constrain the classification of the 200 MHz attribute database; i.e., we classify the 200 MHz meta attributes and structural dip in the regions of facies classes 1, 2, and 3 separately to subdivide these regions into two detailed classes (a and b) each. To ease the interpretation and maintain comparability between the major facies model and the detailed facies model resulting from this hierarchical approach, we show it in Figure 6.2f as a transparent overlay on the 200 MHz volume with similar colors as used in Figure 6.2c.

The detailed facies model (Figure 6.2f) sharply delineates six classes that show an overall continuous character and high membership values. Comparing Figures 6.1a, 6.2c, and 6.2f illustrates that by integrating multi-frequency attributes through the application of our hierarchical approach, the major facies classes 1-3 are subdivided into detailed facies 1a-3b in a reasonable way. That is, facies class 3b characterizes the largely homogeneous parts of major facies class 3 (unit VI) whereas facies class 3a coincides with the region of an embedded undulating high-velocity layer. Facies class 2a includes regions characterized by only subtle heterogeneities (unit IV) compared to facies class 2b that comprises the more heterogeneous regions of major class 2 such as parts of unit II characterized by small-scale, high-amplitude velocity variations. Finally, facies class 1a distinguishes alternating dipping sequences (unit V) from facies class 1b that includes less heterogeneous parts of major facies class 1 (unit I and parts of units II and III).

6.5. Conclusions

Using attribute-based analysis, we present a multi-scale classified facies model based on 50 and 200 MHz GPR data volumes generated across a realistic sedimentary model. Having at hand both the input model and the classification results offers an up to now unique

possibility to (1) evaluate a recently developed workflow to generate attribute-based facies models and to (2) test a strategy to integrate multi-frequency/multi-scale GPR attributes by hierarchical application of this workflow.

Our results show that the facies model inferred from 50 MHz texture and structural attributes characterizes three large-scale zones of the input model in a meaningful way. Using this facies model as a constrain for the classification of 200 MHz attributes allows to further subdivide the three major facies classes into six detailed ones. The resulting multi-scale facies model is in good agreement with the sedimentary features, structures, and even sedimentary units found at multiple spatial scales of the input model.

Based on our results, we conclude that this attribute-based workflow poses an efficient and reliable tool to interpret both single- and multi-frequency GPR data and, thus, can either be an alternative or guide for typical manual interpretation approaches. Although further testing of this workflow is required in future studies (e.g., using multi-frequency and/or further single-frequency GPR field examples), we regard the presented synthetic study as an important step towards a more objective and reproducible analysis and interpretation of 3D GPR data acquired or modeled across complex sedimentary environments.

7. Conclusions and Perspectives

Typically, 3D GPR data sets acquired across sedimentary systems are interpreted manually, for example, using approaches known as GPR facies interpretation. The thus obtained interpretation results are often considered subjective (i.e., the results depend on the interpreter's expertise) and hence non-reproducible. Moreover, manual interpretation is often time-consuming, especially for complex 3D settings, and, thus, interpretations typically focus on selected 2D slices that are then interpreted representatively for the entire 3D data set. To provide a more objective, reproducible, and complete approach for interpreting 3D GPR data sets imaging sedimentary environments, this thesis reports on the development, evaluation, and application of attribute analysis and attribute-based classification to produce classified GPR facies models.

To develop, test, and evaluate the proposed workflow, I follow good practice by generating and using synthetic 3D GPR data sets and models that are as realistic as possible. Modeling GPR data is an active and ever-growing field of research and gprMax (the most widely used GPR modeling software today) is under constant further development. However, due to the nature of FDTD modeling schemes, the model size (which is a function of source frequency and velocity distribution) and the available storage capacity of even modern GPUs (needed for accelerated modeling) mark the bottleneck of modeling even more realistic 3D GPR data (Delf et al., 2017, 2021). This could be achieved, for example, by using realistic antenna models (rather than a point source) that are already available in the modeling framework of gprMax. Moreover, recent studies also try to increase the level of realism by combining a realistic subsurface with such an antenna model (Giannakis et al., 2016, 2019; Stadler and Igel, 2022; Patsia et al., 2023; Stadler et al., 2023) and by additionally incorporating characteristic system noise (Stephan et al., 2023). However, already the modeling studies presented in this thesis required the use of special modeling strategies to enable modeling in 3D using a point source. Moreover, using a realistic antenna model poses new demands that, in general, lead to a considerable increase in the model size. However, recent developments in gprMax (which are in the beta-testing phase at the moment) include the possibility of subgridding the model (Hartley et al., 2018). This will be an important step towards enabling the combination of complex and extensive 3D subsurface and antenna models which, in turn, will result in GPR data sets showing an even higher level of realism compared to the ones presented in this study.

Using the results of Tronicke and Allroggen (2015) as a starting point (Figure 7.1a), I develop a workflow to produce 3D GPR facies models that is applied to various synthetic and field GPR data sets in 3D (e.g., Figure 7.1b). This workflow is centered around the use of structure attributes (calculated using the gradient structure tensor [GST] approach) and texture attributes (calculated using the gray-level cooccurrence

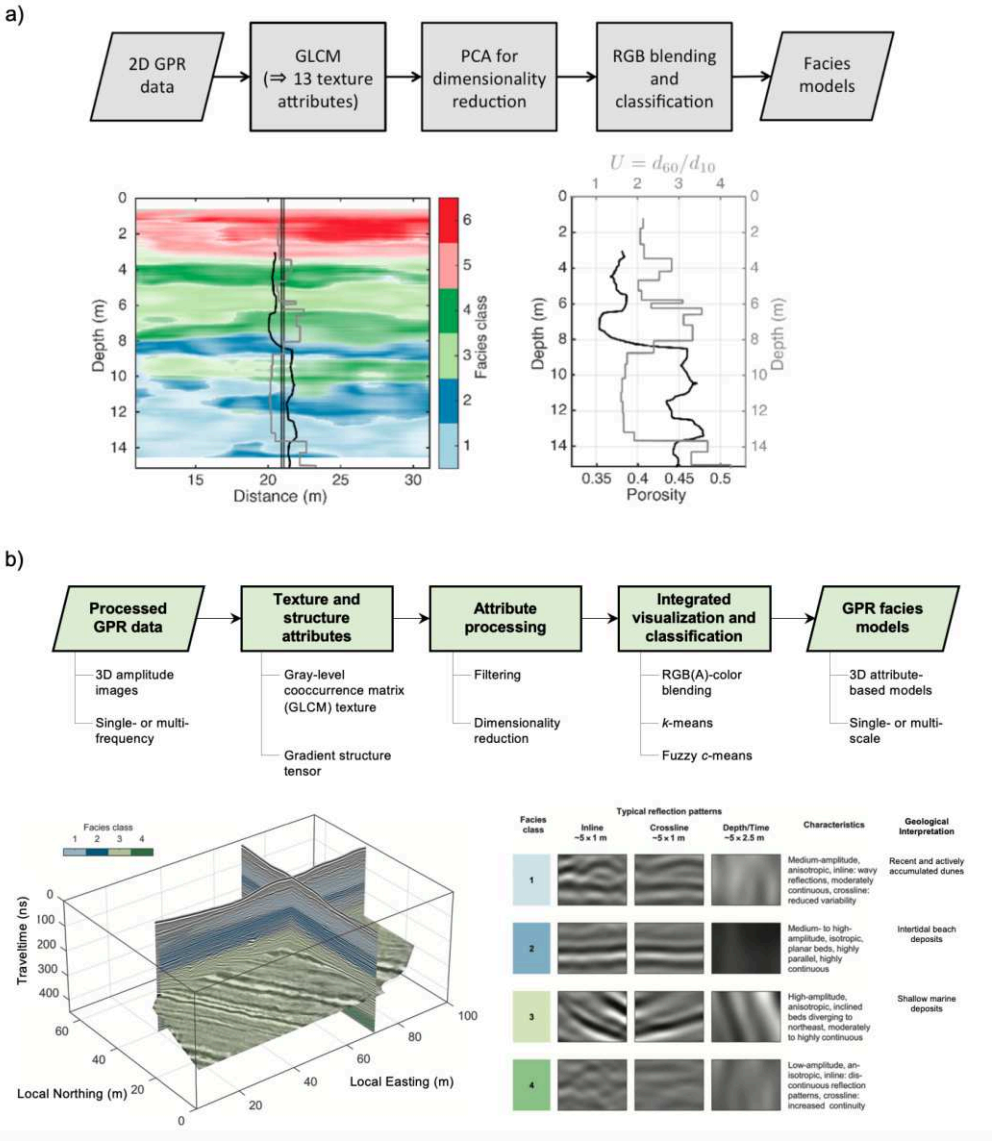

Figure 7.1.: (a) Workflow of Tronicke and Allroggen (2015) to produce texture attribute-based GPR facies models in 2D. The workflow is applied to GPR data imaging stratified glaciofluvial deposits and the results are evaluated using 1D borehole data characterizing grain size uniformity U and porosity. (b) Workflow developed in this thesis to generate texture and structure attribute-based GPR facies models in 3D. The workflow is applied to different synthetic and field GPR data including a field data set imaging complex sandy deposits on the island of Spiekeroog. In this study, the results are evaluated by integrated analysis of this facies model, the GPR data volume, and geological background information.

matrix [GLCM] approach). A comparison of these two multi-trace attribute families and included attributes shows that both carry representative and important information to characterize the corresponding GPR data. To illustrate the potential of 3D structure and texture attributes calculated across GPR data, Figure 7.2 shows four prominent structure attributes calculated using a 3D GST approach (left column) and four prominent texture attributes calculated using a 3D GLCM approach (right column) across the 3D GPR data set shown in Figure 7.1b. Although Figure 7.1b illustrates that these attributes can be used to produce classified GPR facies models in 3D, it is important to mention that these attributes alone are already excellent means to highlight specific characteristics in the GPR data volume, for example, to aid and guide manual analyses and interpretations or as a tool to map and characterize target structures and features in sedimentary, geological, archaeological, and many more applications. However, I recognized that structure and texture attributes as well as the corresponding calculation procedures based on the GST and GLCM approaches, respectively, show some fundamental differences. In general, these differences play an important role if these attributes are calculated across the entire data volumes (e.g., in view of a later 3D classification; Figure 7.1b) rather than along selected depth or profile slices (e.g., to be used as an interpretation guide or mapping tool; Figure 7.2).

For example, calculating a full set of 3D GLCM attributes is in the order of two to three magnitudes slower than calculating a set of 3D GST attributes considering the same input GPR data (i.e., calculation times in the order of some hours for GLCM attributes and in the order of a few seconds for the GST attributes). Moreover, my studies show that, typically, GLCM attributes are prone to show wavelet characteristics originating from the input GPR data. Thus, texture attributes are rather sensitive to the used 3D search window and resulting attributes have to be filtered (e.g., using scale-based filtering approaches) considering both the resolution capabilities of the input GPR data and the spatial scales of the target features such as the facies signatures. Additionally, a GLCM texture attribute database (typically including 10-20 different attributes) often carries redundant information which, in turn, requires further processing to reduce the database dimensionality (such as principal component analysis - PCA).

In general, structure attributes calculated using the GST approach depend on the shape and size of the employed Gaussian filter kernels. I show that using typical Gaussian filter shapes (e.g., anisotropic kernels in the presence of preferential directions such as stratification) and typical sizes (i.e., standard deviations of the filter kernels) in the order of a dominant wavelength or the target spatial scales produces valid results. Due to the smoothing (that is already applied in GST calculations by definition), the resulting attributes are typically not contaminated by noise originating from the wavelet character of the GPR data. Moreover, the resulting attribute database typically includes physically meaningful, largely uncorrelated, and verifiable information characterizing the GPR data in terms of amplitudes, continuity, or dip angle and azimuth. Hence, I conclude that, in the first instance, a standard attribute-based characterization and interpretation of 3D GPR data should focus on structure attributes that can be calculated comparably fast and stable. Additionally, the resulting database provides numerous attributes that

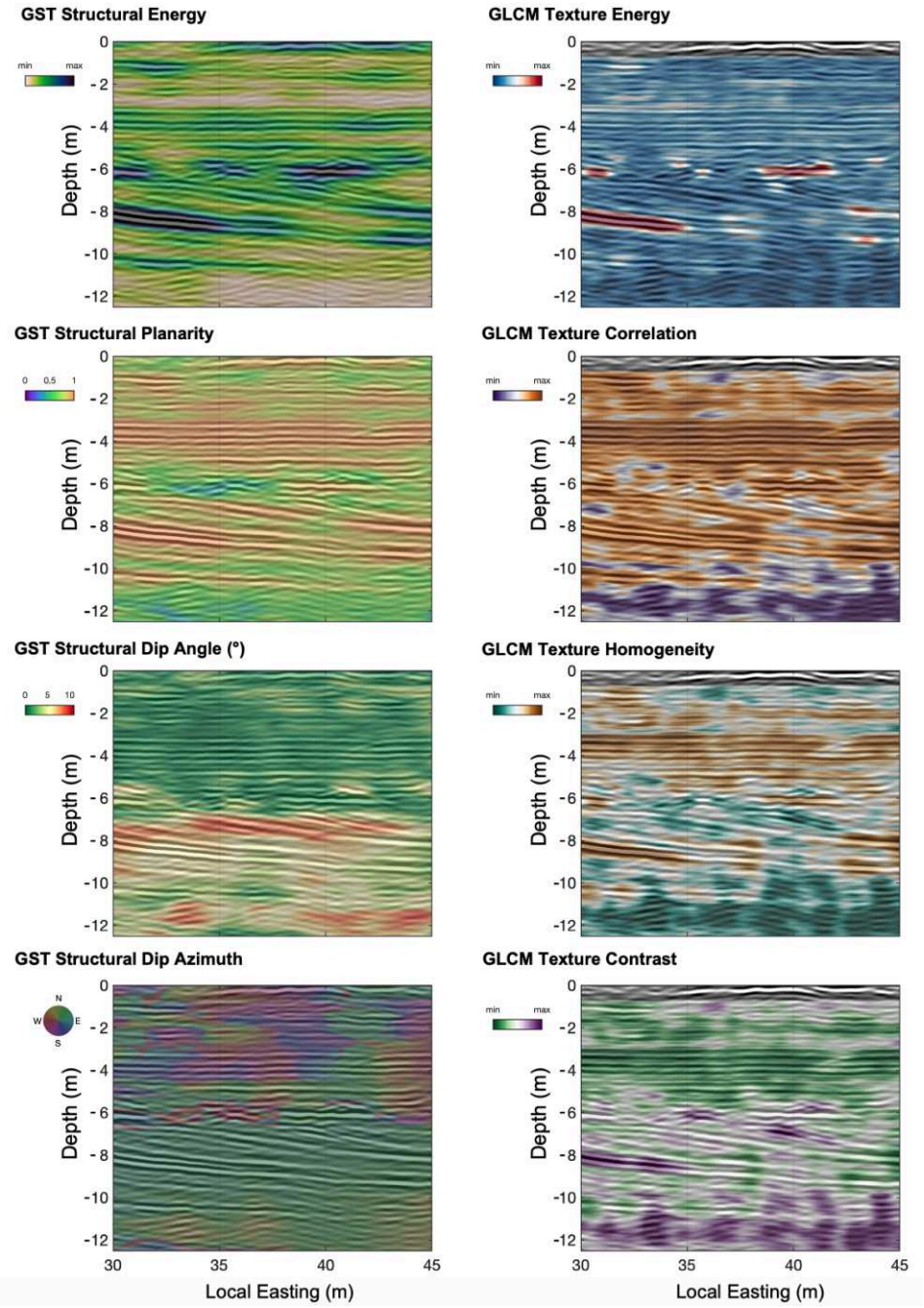

Figure 7.2.: Typical GPR slice extracted from Figure 7.1b and four prominent 3D structure attributes calculated using a GST approach (left column) and four prominent 3D texture attributes calculated using a GLCM approach (right column) shown as transparent overlays.

characterize diverse features and patterns in the corresponding GPR data. However, if an even more comprehensive and in-depth characterization of a GPR data set and a sedimentary environment is of interest, the combination of both structure and texture attributes has proven to be a reliable approach to produce classified GPR facies models at different spatial scales in a reproducible and objective fashion.

In this thesis, I focus on the use of structure and texture attributes to generate classified (single- or multi-scale) 3D facies models from (single- or multi-frequency) GPR volumes. In the presented studies, the obtained facies models are employed in a rather qualitative fashion. This is, for example, after the resulting facies models have been evaluated by qualitative visual comparison to petrophysical borehole logging data (Figure 7.1a) or 1D GPR velocity profiles, the depositional history is reconstructed by integrated interpretation of these facies models, the GPR data set, and geological background information (Figure 7.1b). In future studies, the obtained facies models can be used as an excellent starting point to further extend the presented interpretation strategies by including petrophysical properties into the workflow thus extending the so far standard (reflection-based) definition of GPR facies. To do so, petrophysical properties (such as porosity, hydraulic conductivity, grain-size distribution, or GPR velocity measured at a few locations of the investigated field site; Figure 7.1a) could be incorporated into the workflow by direct correlations to the facies models, or by establishing links relying on advanced non-parametric statistical tools or suitable machine learning techniques. Thus, future GPR facies models could be used to predict and interpolate sparse point information in 2D and 3D as they comprise both petrophysical characteristics and structural information (in terms of classical GPR facies).

The studies presented in this thesis comprise various applications using 3D field and synthetic data sets imaging various complex sedimentary scenarios at different spatial scales, thus highlighting the potential of attribute analysis and classification in general and the potential and adaptability of the proposed workflow in particular. Although unveiling the full potential of 3D attribute-based facies classification requires further investigation, the presented methods and observations are considered an important step towards a more efficient, reproducible, and comprehensive interpretation of 3D GPR data sets imaging complex sedimentary environments.

Cumulative Bibliography

Aaltonen, J., Nissen, J., 2002. Geological mapping using GPR and differential GPS positioning — A case study, in: Proceedings of the 9th Conference on Ground-penetrating radar, pp. 207–210. doi:10.1117/12.462245.

Adams, S., Payne, J., Boppana, R., 2007. Finite difference time domain (fdtd) simulations using graphics processors, in: 2007 DoD High Performance Computing Modernization Program Users Group Conference, pp. 334–338. doi:10.1109/HPCMP-UGC.2007.34.

Al-Dossary, S., 2015. Preconditioning seismic data for channel detection. Interpretation 3(1), T1–T4. doi:10.1190/INT-2014-0031.1.

Al-Dossary, S., Marfurt, K.J., 2006. 3D volumetric multispectral estimates of reflector curvature and rotation. Geophysics 71(5), P41–P51. doi:10.1190/1.2242449.

Alaudah, Y., Michałowicz, P., Alfarraj, M., AlRegib, G., 2019. A machine learning benchmark for facies classification. Interpretation 7(3), SE175–SE187. doi:10.1190/int-2018-0249.1.

Allen, L., O'Connell, A., Kiermer, V., 2019. How can we ensure visibility and diversity in research contributions? How the Contributor Role Taxonomy (CRediT) is helping the shift from authorship to contributorship. Learned Publishing 32, 71–74. doi:10.1002/leap.1210.

Allroggen, N., Heincke, B.H., Koyan, P., Wheeler, W., Rønning, J.S., 2022. 3D ground-penetrating radar attribute classification: A case study from a paleokarst breccia pipe in the Billefjorden area on Spitsbergen, Svalbard. Geophysics 87(4), WB19–WB30. doi:10.1190/GEO2021-0651.1.

Allroggen, N., Tronicke, J., 2016. Attribute-based analysis of time-lapse ground-penetrating radar data. Geophysics 81(1), H1–H8. doi:10.1190/geo2015-0171.1.

Allroggen, N., Tronicke, J., Delock, M., Böniger, U., 2015. Topographic migration of 2D and 3D ground-penetrating radar data considering variable velocities. Near Surface Geophysics 13(3), 253–259. doi:10.3997/1873-0604.2014037.

Aminzadeh, F., Brac, J., Kunz, T., 1997. 3D Salt and Overthrust models, in: SEG/EAGE Modeling Series, No 1: Distribution CD of Salt and Overthrust models.

Annan, A.P., 2002. GPR-History, trends, and future developments. Subsurface Sensing Technologies and Applications 3, 253–270. doi:10.1023/A:1020657129590.

Annan, A.P., 2005a. GPR methods for hydrogeological studies, in: Rubin, Y., Hubbard, S.S. (Eds.), Hydrogeophysics. Springer Netherlands, Dordrecht. Water Science and Technology Library, pp. 185–213.

Annan, A.P., 2005b. Ground-penetrating radar, in: Butler, D. (Ed.), Near-surface geophysics. SEG, pp. 357–438.

Archie, G.E., 1942. The electrical resistivity log as an aid in determining some reservoir characteristics. Transactions of the AIME 146(01), 54–62. doi:10.2118/942054-G.

Bakker, P., 2002. Image structure analysis for seismic interpretation. PhD thesis, Delft University for Technology.

Barnes, A.E., 2000. Attributes for automating seismic facies analysis, in: SEG Technical Program Expanded Abstracts 2000, pp. 553–556. doi:10.1190/1.1816121.

Barnes, A.E., 2001. Seismic attributes in your facies. CSEG Recorder 27.

Barnes, A.E., 2016. Handbook of poststack seismic attributes. SEG.

Bayer, P., 2000. Aquifer-Analog-Studie in grobklastischen "braided-river" Ablagerungen: Sedimentäre/hydrogeologische Wandkartierung und Kalibrierung von Georadarmessungen. Diploma mapping campaign. Universität Tübingen.

Bayer, P., Huggenberger, P., Renard, P., Comunian, A., 2011. Three-dimensional high resolution fluvio-glacial aquifer analog: Part 1: Field study. Journal of Hydrology 405(1–2), 1–9. doi:10.1016/j.jhydrol.2011.03.038.

Behura, J., 2022. Geophysics bright spots. The Leading Edge 41, 62–64. doi:10.1190/tle41010062.1.

Belina, F., Dafflon, B., Tronicke, J., Holliger, K., 2009. Enhancing the vertical resolution of surface georadar data. Journal of Applied Geophysics 68, 26–35. doi:10.1016/j.jappgeo.2008.08.011.

Benedetto, A., Pajewski, L., 2015. Civil engineering applications of ground penetrating radar. Springer, Berlin.

Beres, M., Green, A., Huggenberger, P., Horstmeyer, H., 1995. Mapping the architecture of glaciofluvial sediments with three-dimensional georadar. Geology 23(12), 1087–1090. doi:10.1130/0091-7613(1995)023<1087:MTAOGS>2.3.CO;2.

Beres, M., Haeni, F.P., 1991. Application of ground penetrating radar methods in hydrogeologic studies. Groundwater 29, 375–386. doi:10.1111/j.1745-6584.1991.tb00528.x.

Bergmann, T., Robertsson, J.O., Holliger, K., 1998. Finite-difference modeling of electromagnetic wave propagation in dispersive and attenuating media. Geophysics 63, 856–867. doi:10.1190/1.1444396.

Bezdek, J.C., 1981. Pattern recognition with fuzzy objective function algorithms. Advanced Applications in Pattern Recognition, Springer US.

Bezdek, J.C., Ehrlich, R., Full, W., 1984. FCM: The fuzzy c-means clustering algorithm. Computers and Geosciences 10(2–3), 191–203. doi:10.1016/0098-3004(84)90020-7.

Bitri, A., Grandjean, G., 1998. Frequency-wavenumber modelling and migration of 2D GPR data in moderately heterogeneous dispersive media. Geophysical Prospecting 46(3), 287–301. doi:10.1046/j.1365-2478.1998.00091.x.

Boehm, C., Hanzich, M., de la Puente, J., Fichtner, A., 2016. Wavefield compression for adjoint methods in full-waveform inversion. Geophysics 81(6), R385–R397. doi:10.1190/GEO2015-0653.1.

Böniger, U., Tronicke, J., 2010a. Improving the interpretability of 3D GPR data using target-specific attributes: Application to tomb detection. Journal of Archaeological Science 37(4), 672–679. doi:10.1016/j.jas.2009.09.049.

Böniger, U., Tronicke, J., 2010b. Integrated data analysis at an archaeological site: A case study using 3D GPR, magnetic, and high-resolution topographic data. Geophysics 75(4), B169–B176. doi:10.1190/1.3460432.

Böniger, U., Tronicke, J., 2010c. On the potential of kinematic GPR surveying using a self-tracking total station: Evaluating system crosstalk and latency. IEEE Transactions on Geoscience and Remote Sensing 48(10), 3792–3798. doi:10.1109/TGRS.2010.2048332.

Bowling, R.D., Laya, J.C., Everett, M.E., 2018. Resolving carbonate platform geometries on the Island of Bonaire, Caribbean Netherlands through semi-automatic GPR facies classification. Geophysical Journal International 214, 687–703. doi:10.1093/gji/ggy175.

Bricheva, S.S., Dubrovin, I.O., Lunina, O.V., Denisenko, I.A., Matasov, V.M., Turova, I.V., Entin, A.L., Panin, A.V., Deev, E.V., 2021. Numerical simulation of ground-penetrating radar data for studying the geometry of fault zone. Near Surface Geophysics 19, 261–277. doi:10.1002/nsg.12153.

Bristow, C.S., Jol, H.M. (Eds.), 2003. Ground Penetrating Radar in Sediments. Geological Society, Special Publications, 211, London.

Burke, M.J., Woodward, J., Russell, A.J., Fleisher, P.J., Bailey, P.K., 2010. The sedimentary architecture of outburst flood eskers: A comparison of ground-penetrating radar data from Bering Glacier, Alaska and Skeiarárjökull, Iceland. Bulletin of the Geological Society of America 122(9–10), 1637–1645. doi:10.1130/B30008.1.

Cassidy, N., 2009. Ground-penetrating radar data processing, modeling and analysis, in: Jol, H.M. (Ed.), Ground-Penetrating Radar: Theory and Applications. Elsevier, pp. 141–172.

Cassidy, N.J., 2007. A review of practical numerical modelling methods for the advanced interpretation of ground-penetrating radar in near-surface environments. Near Surface Geophysics 5, 5–21. doi:10.3997/1873-0604.2006014.

Cassidy, N.J., 2008. GPR attenuation and scattering in a mature hydrocarbon spill: A modeling study. Vadose Zone Journal 7, 140–159. doi:10.2136/vzj2006.0142.

Cassidy, N.J., Millington, T.M., 2009. The application of finite-difference time-domain modelling for the assessment of GPR in magnetically lossy materials. Journal of Applied Geophysics 67, 296–308. doi:10.1016/j.jappgeo.2008.09.009.

Cassidy, N.J., Murdie, R.E., 2000. Application of mathematical modeling in the interpretation of near-surface ground penetrating radar sections, in: Noon, D.A., Stickley, G.F., Longstaff, D. (Eds.), Eighth International Conference on Ground Penetrating Radar, International Society for Optics and Photonics. SPIE. pp. 842 – 847. doi:10.1117/12.383526.

Chopra, S., Marfurt, K.J., 2005. Seismic attributes – A historical perspective. Geophysics 70(5), 3SO–28SO. doi:10.1190/1.2098670.

Chopra, S., Marfurt, K.J., 2006. Seismic attributes – A promising aid for geologic prediction. CSEG Recorder 2006 Special Edition.

Chopra, S., Marfurt, K.J., 2007. Seismic attributes for prospect identification and reservoir characterization. Geophysical development series, SEG.

Chopra, S., Marfurt, K.J., 2008. Emerging and future trends in seismic attributes. The Leading Edge 27(3), 298–318. doi:10.1190/1.2896620.

Coléou, T., Poupon, M., Azbel, K., 2003. Unsupervised seismic facies classification: A review and comparison of techniques and implementation. The Leading Edge 22, 942–953. doi:10.1190/1.1623635.

Comunian, A., Renard, P., Straubhaar, J., Bayer, P., 2011. Three-dimensional high resolution fluvio-glacial aquifer analog - Part 2: Geostatistical modeling. Journal of Hydrology 405(1–2), 10–23. doi:10.1016/j.jhydrol.2011.03.037.

Conyers, L.B., 2023. Ground-Penetrating Radar for Archaeology. Rowman & Littlefield.

Corbeanu, R.M., Soegaard, K., Szerbiak, R.B., Thurmond, J.B., McMechan, G.A., Wang, D., Snelgrove, S., Forster, C.B., Menitove, A., 2001. Detailed internal architecture of a fluvial channel sandstone determined from outcrop, cores, and 3-D ground-penetrating radar: Example from the Middle Cretaceous Ferron Sandstone, East-Central Utah. AAPG Bulletin 85, 1583–1608. doi:10.1306/8626CCCB-173B-11D7-8645000102C1865D.

Corbeanu, R.M., Wizevich, M.C., Bhattacharya, J.P., Zeng, X., McMechan, G.A., 2004. 3-D Architecture of ancient lower delta plain point bars using ground-penetrating radar, Cretaceous Ferron Sandstone, Utah. AAPG Studies in Geology 50, 427–449.

Daniels, D.J., 2004. Ground penetrating radar. Radar, sonar, navigation, and avionics series, Institution of Electrical Engineers.

Davis, J.L., Annan, A.P., 1989. Ground-penetrating radar for high-resolution mapping of soil and rock stratigraphy. Geophysical Prospecting 37, 531–551. doi:10.1111/j.1365-2478.1989.tb02221.x.

Delf, R., Giannopoulos, A., Bingham, R.G., Curtis, A., 2021. A sliced-3D approach to finite-difference time-domain modeling by optimizing perfectly matched layers. Geophysics 86(6), H43–H52. doi:10.1190/geo2020-0222.1.

Delf, R., Giannopoulos, A., Bingham, R.G., Hulton, N.R., Curtis, A., 2017. A sliced-3D FDTD approach as an alternative to 2D Ground Penetrating Radar modelling, in: 2017 9th International Workshop on Advanced Ground Penetrating Radar (IWAGPR), IEEE, Edinburgh, United Kingdom. pp. 1–5. doi:10.1109/IWAGPR.2017.7996038.

Delock, M., 2013. Hochauflösende Erkundung sedimentärer Strukturen mittels 2D und 3D Georadarmessungen. Diploma Thesis. Universität Potsdam.

Desbarats, A.J., Bachu, S., 1994. Geostatistical analysis of aquifer heterogeneity from the core scale to the basin scale: A case study. Water Resources Research 30(3), 673–684. doi:10.1029/93WR02980.

dGB Earth Sciences, 2023. OpendTect Pro and Plugins User Documentation v6.6, Chapter 4, Dip steering. Accessed 14-Nov-2023. URL: https://doc.opendtect.org/6.6.0/doc/dgb_userdoc/content/dip-steering.htm?tocpath=4%20Dip-Steering%7C_____0.

Dix, C.H., 1955. Seismic velocities from surface measurements. Geophysics 20, 68–86. doi:10.1190/1.1438126.

Dossi, M., Forte, E., Pipan, M., 2015. Automated reflection picking and polarity assessment through attribute analysis: Theory and application to synthetic and real ground-penetrating radar data. Geophysics 80(5), 23–35. doi:10.1190/geo2015-0098.1.

Economou, N., Vafidis, A., 2012. GPR data time varying deconvolution by Kurtosis maximization. Journal of Applied Geophysics 81, 117–121. doi:10.1109/ICGPR.2010.5550132.

Eichkitz, C.G., Amtmann, J., 2018. GLCM-based anisotropy estimation – The influence of computation parameters on the results. First Break 36(5), 47–52. doi:10.3997/1365-2397.n0091.

Eichkitz, C.G., Amtmann, J., Schreilechner, M.G., 2013. Calculation of grey level co-occurrence matrix-based seismic attributes in three dimensions. Computers and Geosciences 60, 176–183. doi:10.1016/j.cageo.2013.07.006.

Eichkitz, C.G., Schreilechner, M.G., de Groot, P., Amtmann, J., 2015. Mapping directional variations in seismic character using gray-level co-occurrence matrix-based attributes. Interpretation 3(1), T13–T23. doi:10.1190/INT-2014-0099.1.

Elseicy, A., Alonso-Díaz, A., Solla, M., Rasol, M., Santos-Assunçao, S., 2022. Combined use of GPR and other NDTs for road pavement assessment: An overview. Remote Sensing 14, 4336. doi:10.3390/rs14174336.

Emery, X., Lantuéjoul, C., 2006. TBSIM: A computer program for conditional simulation of three-dimensional Gaussian random fields via the turning bands method. Computers and Geosciences 32(10), 1615–1628. doi:10.1016/j.cageo.2006.03.001.

Ernst, J.R., Green, A.G., Maurer, H., Holliger, K., 2007. Application of a new 2D time-domain full-waveform inversion scheme to model crosshole radar data. Geophysics 72(5), J53–J64. doi:10.1190/1.2761848.

Fang, G.Y., Zhou, B., Ji, Y.C., Zhang, Q.Y., Shen, S.X., Li, Y.X., Guan, H.F., Tang, C.J., Gao, Y.Z., Lu, W., Ye, S.B., Han, H.D., Zheng, J., Wang, S.Z., 2014. Lunar penetrating radar onboard the Chang'e-3 mission. Research in Astronomy and Astrophysics 14, 1607–1622. doi:10.1088/1674-4527/14/12/009.

Faraklioti, M., Petrou, M., 2005. The use of structure tensors in the analysis of seismic data, in: Iske, A., Randen, T. (Eds.), Mathematical Methods and Modelling in Hydrocarbon Exploration and Production. Springer, pp. 47–88.

Fehmers, G.C., Höcker, C.F.W., 2003. Fast structural interpretation with structure-oriented filtering. Geophysics 68, 1286–1293. doi:10.1190/1.1598121.

Forte, E., Mocnik, A., Basso, P., Casagrande, G., Martinucci, D., Pillon, S., Possamai, M., Zambrini, R., 2021a. Optimised extraction of archaeological features from full 3-D GPR data. Applied Sciences 11, 8517. doi:10.3390/app11188517.

Forte, E., Pipan, M., 2017. Review of multi-offset GPR applications: Data acquisition, processing and analysis. Signal Processing 132, 210–220. doi:10.1016/j.sigpro.2016.04.011.

Forte, E., Pipan, M., Casabianca, D., Di Cuia, R., Riva, A., 2012. Imaging and characterization of a carbonate hydrocarbon reservoir analogue using GPR attributes. Journal of Applied Geophysics 81, 76–87. doi:10.1016/j.jappgeo.2011.09.009.

Forte, E., Santin, I., Ponti, S., Colucci, R.R., Gutgesell, P., Guglielmin, M., 2021b. New insights in glaciers characterization by differential diagnosis integrating GPR and remote sensing techniques: A case study for the Eastern Gran Zebrù Glacier (Central Alps). Remote Sensing of Environment 267, 112715. doi:10.1016/j.rse.2021.112715.

Gao, D., 2003. Volume texture extraction for 3D seismic visualization and interpretation. Geophysics 68, 1294–1302. doi:10.1190/1.1598122.

Gao, D., 2004. Texture model regression for effective feature discrimination: Application to seismic facies visualization and interpretation. Geophysics 69, 958–967. doi:10.1190/1.1778239.

Gao, D., 2011. Latest developments in seismic texture analysis for subsurface structure, facies, and reservoir characterization: A review. Geophysics 76(2), W1–W13. doi:10.1190/1.3553479.

Garrison, James R., J., Williams, J., Potter Miller, S., Weber, Egon T., I., McMechan, G., Zeng, X., 2010. Ground-penetrating radar study of North Padre Island: Implications for barrier island internal architecture, model for growth of progradational microtidal barrier islands, and Gulf of Mexico sea-level cyclicity. Journal of Sedimentary Research 80, 303–319. doi:10.2110/jsr.2010.034.

Gelhar, L.W., 1993. Stochastic subsurface hydrology. Prentice-Hall.

Giannakis, I., Giannopoulos, A., Warren, C., 2016. A realistic FDTD numerical modeling framework of ground penetrating radar for landmine detection. IEEE Journal of Selected Topics in Applied Earth Observations and Remote Sensing 9(1), 37–51. doi:10.1109/JSTARS.2015.2468597.

Giannakis, I., Giannopoulos, A., Warren, C., 2019. Realistic FDTD GPR antenna models optimized using a novel linear/nonlinear full-waveform inversion. IEEE Transactions on Geoscience and Remote Sensing 57, 1768–1778. doi:10.1109/TGRS.2018.2869027.

Giannakis, I., Martin-Torres, J., Su, Y., Feng, J., Zhou, F., Zorzano, M.P., Warren, C., Giannopoulos, A., 2024. Evidence of shallow basaltic lava layers in Von Kármán crater from Yutu-2 Lunar Penetrating Radar. Icarus 408, 115837. doi:doi.org/10.1016/j.icarus.2023.115837.

Goodman, D., Piro, S., 2013. GPR Remote Sensing in Archaeology. Springer, Berlin, Heidelberg. doi:10.1007/978-3-642-31857-3.

Grandjean, G., Gourry, J.C., 1996. GPR data processing for 3D fracture mapping in a marble quarry (Thassos, Greece). Journal of Applied Geophysics 36, 19–30. doi:10.1016/S0926-9851(96)00029-8.

Grasmueck, M., 1996. 3-D ground-penetrating radar applied to fracture imaging in gneiss. Geophysics 61, 1050–1064. doi:10.1190/1.1444026.

Grasmueck, M., Weger, R., Horstmeyer, H., 2004. Three-dimensional ground-penetrating radar imaging of sedimentary structures, fractures, and archaeological features at submeter resolution. Geology 32(11), 933–936. doi:10.1130/G20776.1.

Grasmueck, M., Weger, R., Horstmeyer, H., 2005. Full-resolution 3D GPR imaging. Geophysics 70(1), 12–19. doi:10.1190/1.1852780.

Hale, D., 2009. Structure-oriented smoothing and semblance. Colorado School of Mines, CWP Report 635, 261–270.

Hamann, G., Tronicke, J., 2014. Global inversion of GPR traveltimes to assess uncertainties in CMP velocity models. Near Surface Geophysics 12(4), 505–514. doi:10.3997/1873-0604.2014005.

Hamann, G., Tronicke, J., Steelman, C.M., Endres, A.L., 2013. Spectral velocity analysis for the determination of ground-wave velocities and their uncertainties in multi-offset GPR data. Near Surface Geophysics 11(2), 167–176. doi:10.3997/1873-0604.2012038.

Haralick, R.M., Shanmugam, K., Dinstein, I., 1973. Textural features for image classification. IEEE Transactions on Systems, Man and Cybernetics SMC-3(6), 610–621. doi:10.1109/TSMC.1973.4309314.

Harris, C.G., Stephens, M., 1988. A combined corner and edge detector, in: Proceedings of the Fourth Alvey Vision Conference, pp. 147–152. doi:10.5244/C.2.23.

Hartley, J., Giannopoulos, A., Warren, C., 2018. A Huygens subgridding approach for efficient modelling of Ground Penetrating Radar using the Finite-Difference Time-Domain method, in: 17th International Conference on Ground Penetrating Radar (GPR). doi:10.1109/ICGPR.2018.8441677.

Heinz, J., Aigner, T., 2003. Hierarchical dynamic stratigraphy in various Quaternary gravel deposits, Rhine glacier area (SW Germany): Implications for hydrostratigraphy. International Journal of Earth Sciences 92, 923–938. doi:10.1007/s00531-003-0359-2.

Henderson, J., Purves, S.J., Fisher, G., Leppard, C., 2008. Delineation of geological elements from RGB color blending of seismic attribute volumes. The Leading Edge 27(3), 342–350. doi:10.1190/1.2896625.

Hladuvka, J., Gröller, E., 2001. Direction-driven shape-based interpolation of volume data, in: Proceedings of the Vision Modeling and Visualization Conference, pp. 113–120.

Holliger, K., Bergmann, T., 2002. Numerical modeling of borehole georadar data. Geophysics 67, 1249–1257. doi:10.1190/1.1500387.

Hubbard, S.S., Chen, J., Williams, K., Peterson, J., Rubin, Y., 2005. Environmental and agricultural applications of GPR. Lawrence Berkeley National Laboratory Report '05.

Huisman, J.A., Hubbard, S.S., Redman, J.D., Annan, A.P., 2003. Measuring soil water content with ground penetrating radar: A review. Vadose Zone Journal 2, 476–491. doi:10.2113/2.4.476.

Irving, J., Knight, R., 2003. Removal of wavelet dispersion from ground-penetrating radar data. Geophysics 68, 960–970. doi:10.1190/1.1581068.

Irving, J., Knight, R., 2006. Numerical modeling of ground-penetrating radar in 2-D using MATLAB. Computers and Geosciences 32(9), 1247–1258. doi:10.1016/j.cageo.2005.11.006.

Jol, H.M., 2009. Ground penetrating radar: Theory and applications. Elsevier Science.

Kass, M., Witkin, A., 1987. Analyzing oriented patterns. Computer Vision, Graphics and Image Processing 37, 362–385. doi:10.1016/0734-189X(87)90043-0.

Kaur, H., Pham, N., Fomel, S., Geng, Z., Decker, L., Gremillion, B., Jervis, M., Abma, R., Gao, S., 2023. A deep learning framework for seismic facies classification. Interpretation 11, T107–T116. doi:10.1190/INT-2022-0048.1.

Keller, B., 1996. Lithofazies-Codes für die Klassifikation von Lockergesteinen. Mitteilungen der Schweizerischen Gesellschaft für Boden- und Felsmechanik 132, 5–12.

van Kempen, G.M.P., van den Brink, N., van Vliet, L.J., van Ginkel, M., Verbeek, P.W., 1999. The application of a local dimensionality estimator to the analysis of 3D

microscopic network structures, in: Proceedings of the 11th Scandinavian Conference on Image Analysis, pp. 447–455.

Khan, A.R., Cornea, A., Leigland, L.A., Kohama, S.G., Jespersen, S.N., Kroenke, C.D., 2015. 3D Structure tensor analysis of light microscopy data for validating diffusion MRI. Neuroimage 111, 192–203. doi:10.1016/j.neuroimage.2015.01.061.

Kim, J.H., Cho, S.J., Yi, M.J., 2007. Removal of ringing noise in GPR data by signal processing. Geoscience Journal 11, 75–81. doi:10.1007/BF02910382.

Klotzsche, A., van der Kruk, J., Meles, G.A., Doetsch, J., Maurer, H., Linde, N., 2010. Full-waveform inversion of cross-hole ground-penetrating radar data to characterize a gravel aquifer close to the Thur River, Switzerland. Near Surface Geophysics 8(6), 635–649. doi:10.3997/1873-0604.2010054.

Knight, R., 2001. Ground-penetrating radar for environmental applications. Annual Review of Earth and Planetary Sciences 29, 229–255. doi:10.1146/annurev.earth.29.1.229.

Knutsson, H., 1989. Representing local structure using tensors, in: Proceedings of the 6th Scandinavian Conference on Image Analysis, pp. 244–251.

Kostic, B., Aigner, T., 2007. Sedimentary architecture and 3D ground-penetrating radar analysis of gravelly meandering river deposits (Neckar Valley, SW Germany). Sedimentology 54(4), 789–808. doi:10.1111/j.1365-3091.2007.00860.x.

Kowalsky, M.B., Dietrich, P., Teutsch, G., Rubin, Y., 2001. Forward modeling of ground-penetrating radar data using digitized outcrop images and multiple scenarios of water saturation. Water Resources Research 37(6), 1615–1625. doi:10.1029/2001WR900015.

Koyan, P., Tronicke, J., 2019. [dataset] A synthetic 3D ground-penetrating radar (GPR) data set across a realistic sedimentary model. Mendeley Data. doi:10.17632/by3yh79hx4.1.

Koyan, P., Tronicke, J., 2020a. 3D modeling of ground-penetrating radar data across a realistic sedimentary model. Computers and Geosciences 137, 104422. doi:10.1016/j.cageo.2020.104422.

Koyan, P., Tronicke, J., 2020b. Analyzing 3D multi-frequency ground-penetrating radar (GPR) data simulated across a realistic sedimentary model, in: 18th International Conference on Ground Penetrating Radar, SEG, Global Meeting Abstracts, pp. 275–278. doi:10.1190/gpr2020-073.1.

Koyan, P., Tronicke, J., 2022. 3D classified GPR facies models from multi-frequency data volumes: A synthetic study, in: 19th International Confererence on Ground Penetrating Radar (GPR), SEG, Global Meeting Abstracts, pp. 139–142. doi:10.1190/gpr2022-042.1.

Koyan, P., Tronicke, J., 2023a. 3D ground-penetrating radar data analysis and interpretation using attributes based on the gradient structure tensor. Geophysics (submitted).

Koyan, P., Tronicke, J., 2023b. The gradient structure tensor (GST): An efficient tool to analyze 3D GPR data for archaeological prospection, in: 15th International Conference of Archaeological Prospection, pp. 423–425. doi:10.38072/978-3-928794-83-1/p86.

Koyan, P., Tronicke, J., Allroggen, N., 2021. 3D GPR attributes to generate classified facies models: A case study from a dune island. Geophysics 86(6), B335–B347. doi:10.1190/geo2021-0204.1.

Koyan, P., Tronicke, J., Klose, T., Guillemoteau, J., 2023. 3D GPR to explore peat deposits: Strategies for data acquisition, processing, and interpretation, in: 12th International Workshop on Advanced Ground Penetrating Radar (IWAGPR). doi:10.1109/IWAGPR57138.2023.10329077.

van der Kruk, J., Liu, T., Mozaffari, A., Gueting, N., Klotzsche, A., Vereecken, H., Warren, C., Giannopoulos, A., 2018. GPR full-waveform inversion, recent developments, and future opportunities, in: 17th International Conference on Ground Penetrating Radar (GPR), IEEE, Rapperswil, Switzerland. doi:10.1109/ICGPR.2018.8441667.

Kunz, K.S., Luebbers, R.J., 1993. Finite Difference Time Domain Method for Electromagnetics. CRC Press.

Lai, W.W.L., Dérobert, X., Annan, P., 2018. A review of ground penetrating radar application in civil engineering: A 30-year journey from locating and testing to imaging and diagnosis. NDT & E International 96, 58–78. doi:10.1016/j.ndteint.2017.04.002.

Lang, J., Sievers, J., Loewer, M., Igel, J., Winsemann, J., 2017. 3D architecture of cyclic-step and antidune deposits in glacigenic subaqueous fan and delta settings: Integrating outcrop and ground-penetrating radar data. Sedimentary Geology 362, 83–100. doi:10.1016/j.sedgeo.2017.10.011.

Leblanc, M.W., 2001. Denoising of aeromagnetic data via the wavelet transform. Geophysics 66, 1793–1804. doi:10.1190/1.1487121.

Leckebusch, J., 2003. Ground-penetrating radar: A modern three-dimensional prospection method. Archaeological Prospection 240, 213–240. doi:10.1002/arp.211.

Leckebusch, J., 2005. Use of antenna arrays for GPR surveying in archaeology. Near Surface Geophysics 3, 111–115. doi:10.3997/1873-0604.2005006.

Lee, K., Gani, M.R., McMechan, G.A., Bhattacharya, J.P., Nyman, S.L., Zeng, X., 2007a. Three-dimensional facies architecture and three-dimensional calcite concretion distributions in a tide-influenced delta front, Wall Creek Member, Frontier Formation, Wyoming. AAPG Bulletin 91, 191–214. doi:10.1306/08310605114.

Lee, K., McMechan, G.A., Gani, M.R., Bhattacharya, J.P., Zeng, X., Howell, Charles D., J., 2007b. 3-D architecture and sequence stratigraphic evolution of a forced regressive top-truncated mixed-influenced delta, Cretaceous Wall Creek Sandstone, Wyoming, U.S.A. Journal of Sedimentary Research 77, 303–323. doi:10.2110/jsr.2007.031.

Lehmann, F., Green, A.G., 1999. Semiautomated georadar data acquisition in three dimensions. Geophysics 64, 719–731. doi:10.1190/1.1444581.

Lindeberg, T., 1993. Scale-space theory in Computer Vision. Springer.

Linder, S., Paasche, H., Tronicke, J., Niederleithinger, E., Vienken, T., 2010. Zonal cooperative inversion of crosshole P-wave, S-wave, and georadar traveltime data sets. Journal of Applied Geophysics 72(4), 254–262. doi:10.1016/j.jappgeo.2010.10.003.

Liu, B., Zhang, C., Xu, S., Zhang, Q., Li, S., Li, Y., Zhang, F., Nie, L., 2018. Forward modelling and imaging of ground-penetrating radar in tunnel ahead geological prospecting. Geophysical Prospecting 66(4), 784–797. doi:10.1111/1365-2478.12613.

Loewer, M., Igel, J., 2016. FDTD simulation of GPR with a realistic multi-pole debye description of lossy and dispersive media, in: 16th International Conference on Ground Penetrating Radar (GPR), IEEE, Hong Kong, China. doi:10.1109/ICGPR.2016.7572599.

Long, Z., Alaudah, Y., Qureshi, M.A., Hu, Y., Wang, Z., Alfarraj, M., AlRegib, G., Amin, A., Deriche, M., Al-Dharrab, S., Di, H., 2018. A comparative study of texture attributes for characterizing subsurface structures in seismic volumes. Interpretation 6(4), T1055–T1066. doi:10.1190/int-2017-0181.1.

Lu, G., Zhao, W., Forte, E., Tian, G., Li, Y., Pipan, M., 2020. Multi-frequency and multi-attribute GPR data fusion based on 2-D wavelet transform. Measurement 166, 108243. doi:10.1016/j.measurement.2020.108243.

Luo, Y., Higgs, W.G., Kowalik, W.S., 1996. Edge detection and stratigraphic analysis using 3D seismic data, in: SEG Technical Program Expanded Abstracts 1996, pp. 324–327. doi:10.1190/1.1826632.

Manataki, M., Vafidis, A., Sarris, A., 2021. GPR data interpretation approaches in archaeological prospection. Applied Sciences 11, 7531. doi:10.3390/app11167531.

Marfurt, K.J., 2006. Robust estimates of 3D reflector dip and azimuth. Geophysics 71(4), P29–P40. doi:10.1190/1.2213049.

Marfurt, K.J., Kirlin, R.L., 2000. 3-D broad-band estimates of reflector dip and amplitude. Geophysics 65, 304–320. doi:10.1190/1.1444721.

Marfurt, K.J., Sudhaker, V., Gersztenkorn, A., Crawford, K.D., Nissen, S.E., 1999. Coherency calculations in the presence of structural dip. Geophysics 64, 104–111. doi:10.1190/1.1444508.

de Matos, M.C., Yenugu, M.M., Angelo, S.M., Marfurt, K.J., 2011. Integrated seismic texture segmentation and cluster analysis applied to channel delineation and chert reservoir characterization. Geophysics 76(5), P11–P21. doi:10.1190/geo2010-0150.1.

McClymont, A.F., Green, A.G., Streich, R., Horstmeyer, H., Tronicke, J., Nobes, D.C., Pettinga, J., Campbell, J., Langridge, R., 2008. Visualization of active faults using geometric attributes of 3D GPR data: An example from the Alpine Fault Zone, New Zealand. Geophysics 73(2), B11–B23. doi:10.1190/1.2825408.

McMechan, G.A., Gaynor, G.C., Szerbiak, R.B., 1997. Use of ground-penetrating radar for 3-D sedimentological characterization of clastic reservoir analogs. Geophysics 62, 786–796. doi:10.1190/1.1444188.

Mellett, J.S., 1995. Ground penetrating radar applications in engineering, environmental management, and geology. Journal of Applied Geophysics 33, 157–166. doi:10.1016/0926-9851(95)90038-1.

Métivier, L., Brossier, R., Mérigot, Q., Oudet, E., Virieux, J., 2016. An optimal transport approach for seismic tomography: Application to 3D full waveform inversion. Inverse Problems 32(11), 115008. doi:10.1088/0266-5611/32/11/115008.

Millington, T.M., Cassidy, N.J., 2010. Optimising GPR modelling: A practical, multi-threaded approach to 3D FDTD numerical modelling. Computers and Geosciences 36(9), 1135–1144. doi:10.1016/j.cageo.2009.12.006.

Moysey, S., Knight, R.J., Jol, H.M., 2006. Texture-based classification of ground-penetrating radar images. Geophysics 71(6), K111–K118. doi:10.1190/1.2356114.

Narayan, S., Konka, S., Chandra, A., Abdelrahman, K., Andráš, P., Eldosouky, A.M., 2023. Accuracy assessment of various supervised machine learning algorithms in lithofacies classification from seismic data in the Penobscot field, Scotian Basin. Frontiers in Earth Science 11. doi:10.3389/feart.2023.1150954.

Neal, A., 2004. Ground-penetrating radar and its use in sedimentology: Principles, problems and progress. Earth-Science Reviews 66(3–4), 261–330. doi:10.1016/j.earscirev.2004.01.004.

Neal, A., Roberts, C.L., 2000. Applications of ground-penetrating radar (GPR) to sedimentological, geomorphological and geoarchaeological studies in coastal environments. Geological Society, London, Special Publications 175, 139–171. doi:10.1144/GSL.SP.2000.175.01.12.

Nuzzo, L., Leucci, G., Negri, S., Carrozzo, M.T., Quarta, T., 2002. Application of 3D visualization techniques in the analysis of GPR data for archaeology. Annals of Geophysics 45, 321–337.

Nuzzo, L., Quarta, T., 2004. Improvement in GPR coherent noise attenuation using τ-p and wavelet transforms. Geophysics 69, 789–802. doi:10.1190/1.1759465.

Olhoeft, G.R., 2000. Maximizing the information return from ground penetrating radar. Journal of Applied Geophysics 43, 175–187. doi:10.1016/S0926-9851(99)00057-9.

Paasche, H., Tronicke, J., 2007. Cooperative inversion of 2D geophysical data sets: A zonal approach based on fuzzy c-means cluster analysis. Geophysics 72(3), A35–A39. doi:10.1190/1.2670341.

Paasche, H., Tronicke, J., Holliger, K., Green, A.G., Maurer, H., 2006. Integration of diverse physical-property models: Subsurface zonation and petrophysical parameter estimation based on fuzzy c-means cluster analyses. Geophysics 71(3), H33–H44. doi:10.1190/1.2192927.

Pascucci, V., Martini, I.P., Endres, A.L., 2009. Facies and ground-penetrating radar characteristics of coarse-grained beach deposits of the uppermost Pleistocene glacial Lake Algonquin, Ontario, Canada. Sedimentology 56(2), 529–545. doi:10.1111/j.1365-3091.2008.00984.x.

Patsia, O., Giannopoulos, A., Giannakis, I., 2023. Developing a realistic numerical equivalent of a GPR antenna transducer using global optimizers. Near Surface Geophysics xx, preprint, 1–12. doi:10.1002/nsg.12280.

Payton, C.E., 1977. Seismic Stratigraphy - Applications to Hydrocarbon Exploration. American Association of Petroleum Geologists. doi:10.1306/M26490.

Peters, L., Daniels, J., Young, J., 1994. Ground penetrating radar as a subsurface environmental sensing tool. Proceedings of the IEEE 82, 1802–1822. doi:10.1109/5.338072.

Prasad, S., Li, W., Fowler, J.E., Bruce, L.M., 2012. Information fusion in the redundant-wavelet-transform domain for noise-robust hyperspectral classification. IEEE Transactions on Geoscience and Remote Sensing 50(9), 3474–3486. doi:10.1109/TGRS.2012.2185053.

Robertson, J.D., Fisher, D.A., 1988. Complex seismic trace attributes. The Leading Edge 7, 22–26. doi:10.1190/1.1439517.

Robertson, J.D., Nogami, H.H., 1984. Complex seismic trace analysis of thin beds. Geophysics 49, 344–352. doi:10.1190/1.1441670.

Roksandić, M.M., 1978. Seismic facies analysis concepts. Geophysical Prospecting 26, 383–398. doi:10.1111/j.1365-2478.1978.tb01600.x.

Roncoroni, G., Forte, E., Pipan, M., 2023. Merging gated frequency-modulated continuous-wave Mars2020 RIMFAX ground-penetrating radar data. Geophysics 88(2), A7–A12. doi:10.1190/geo2022-0466.1.

Röper, T., Kröger, K.F., Meyer, H., Sültenfuss, J., Greskowiak, J., Massmann, G., 2012. Groundwater ages, recharge conditions and hydrochemical evolution of a barrier island freshwater lens (Spiekeroog, Northern Germany). Journal of Hydrology 454-455, 173–186. doi:10.1016/j.jhydrol.2012.06.011.

Roth, K., Schulin, R., Flühler, H., Attinger, W., 1990. Calibration of time domain reflectometry for water content measurement using a composite dielectric approach. Water Resources Research 26(10), 2267–2273. doi:10.1029/WR026i010p02267.

Samet, R., Celik, E., Tural, S., Sengönül, E., Özkan, M., Damci, E., 2017. Using interpolation techniques to determine the optimal profile interval in ground-penetrating radar applications. Journal of Applied Geophysics 140, 154–167. doi:10.1016/j.jappgeo.2017.04.003.

Saraswat, P., Sen, M.K., 2012. Artificial immune-based self-organizing maps for seismic-facies analysis. Geophysics 77(4), O45–O53. doi:10.1190/geo2011-0203.1.

Sato, M., Hamada, Y., Feng, X., Kong, F.N., Zeng, Z., Fang, G., 2004. GPR using an array antenna for landmine detection. Near Surface Geophysics 2, 7–13. doi:10.3997/1873-0604.2003011.

Schennen, S., Tronicke, J., Wetterich, S., Allroggen, N., Schwamborn, G., Schirrmeister, L., 2016. 3D ground-penetrating radar imaging of ice complex deposits in northern East Siberia. Geophysics 81(1), WA195–WA202. doi:10.1190/geo2015-0129.1.

Schennen, S., Wetterich, S., Schirrmeister, L., Schwamborn, G., Tronicke, J., 2022. Seasonal impact on 3D GPR performance for surveying Yedoma Ice Complex deposits. Frontiers in Earth Science 10. doi:10.3389/feart.2022.741524.

Schmelzbach, C., Tronicke, J., Dietrich, P., 2011. Three-dimensional hydrostratigraphic models from ground-penetrating radar and direct-push data. Journal of Hydrology 398, 235–345. doi:10.1016/j.jhydrol.2010.12.023.

Schön, J.H., 1998. Physical Properties of Rocks. Pergamon.

Sénéchal, P., Perroud, H., Sénéchal, G., 2000. Interpretation of reflection attributes in a 3-D GPR survey at Vallée d'Ossau, Western Pyrenees, France. Geophysics 65, 1435–1445. doi:10.1190/1.1444832.

Shensa, M.J., 1992. The discrete wavelet transform: Wedding the à trous and Mallat algorithms. IEEE Transactions on Signal Processing 40(10), 2464–2482. doi:10.1109/78.157290.

Sindowski, K.H., 1973. Das ostfriesische Küstengebiet. Inseln, Watten und Marschen. Gebrüder Borntraeger.

Slob, E., Sato, M., Olhoeft, G., 2010. Surface and borehole ground-penetrating-radar developments. Geophysics 75(5), A103–A120. doi:10.1190/1.3480619.

Soh, L.K., Tsatsoulis, C., 1999. Texture analysis of SAR sea ice imagery using gray level co-occurrence matrices. IEEE Transactions on Geoscience and Remote Sensing 37(2), 780–795. doi:10.1109/36.752194.

Stadler, S., Igel, J., 2022. Developing realistic FDTD GPR antenna surrogates by means of particle swarm optimization. IEEE Transactions on Antennas and Propagation 70, 4259–4272. doi:10.1109/TAP.2022.3142335.

Stadler, S., Schennen, S., Hiller, T., Igel, J., 2023. Realistic simulation of GPR for landmine and IED detection including antenna models, soil dispersion and heterogeneity. Near Surface Geophysics xx, preprint. doi:10.1002/nsg.12282.

Starck, J.L., Murtagh, F., Fadili, J., 2015. Sparse image and signal processing: Wavelets and related geometric multiscale analysis. 2 ed., Cambridge University Press. doi:10.1017/CBO9781316104514.

Stephan, S.M., Allroggen, N., Tronicke, J., 2023. Adding realistic noise models to synthetic ground-penetrating radar data. Near Surface Geophysics xx, preprint. doi:10.1002/nsg.12273.

Streif, H., 1990. Das ostfriesische Küstengebiet. Nordsee, Inseln, Watten und Marschen. Gebrüder Borntraeger.

Streif, H., 2002. The Pleistocene and Holocene development of the southeastern North Sea Basin and adjacent coastal areas, in: Wefer, G., Berger, W.H., Behre, K.E., Jansen, E. (Eds.), Climate Development and History of the North Atlantic Realm. Springer Berlin Heidelberg, pp. 387–397. doi:10.1007/978-3-662-04965-5_25.

Svendsen, E.B., Nielsen, L., Nilsson, B., Kjær, K.H., Looms, M.C., 2023. Crosshole ground-penetrating radar in clay-rich Quaternary deposits: Toward characterization of high-loss media. Journal of Geophysical Research: Solid Earth 128, e2022JB025909. doi:10.1029/2022JB025909.

Switzer, A.D., Gouramanis, C., Bristow, C.S., Simms, A.R., 2020. Chapter 8 - Ground-penetrating radar (GPR) in coastal hazard studies, in: Engel, M., Pilarczyk, J., May, S.M., Brill, D., Garrett, E. (Eds.), Geological Records of Tsunamis and Other Extreme Waves. Elsevier, pp. 143–168. doi:10.1016/B978-0-12-815686-5.00008-0.

Szerbiak, R.B., McMechan, G.A., Corbeanu, R., Forster, C., Snelgrove, S.H., 2001. 3-D characterization of a clastic reservoir analog: From 3-D GPR data to a 3-D fluid permeability model. Geophysics 66, 1026–1037. doi:10.1190/1.1487050.

Taflove, A., Hagness, S.C., Piket-May, M., 2005. Computational electromagnetics: The finite-difference time-domain method. The Electrical Engineering Handbook 3.

Taner, M.T., Sheriff, R.E., 1977. Application of amplitude, frequency, and other attributes to stratigraphic and hydrocarbon determination, in: Payton, C.E. (Ed.), Seismic Stratigraphy: Applications to Hydrocarbon Exploration. American Association of Petroleum Geologists. doi:10.1306/M26490C17.

Tingdahl, K., Hemstra, N., 2003. Estimating fault-attribute orientation with gradient analysis, principal component analysis and the localized Hough-transform, in: SEG Technical Program Expanded Abstracts 2003, pp. 358–361. doi:10.1190/1.1817920.

Trinks, I., Hinterleitner, A., 2020. Beyond amplitudes: Multi-trace coherence analysis for ground-penetrating radar data imaging. Remote Sensing 12, 1583. doi:10.3390/rs12101583.

Trinks, I., Johansson, B., Gustafsson, J., Emilsson, J., Friborg, J., Gustafsson, C., Nissen, J., Hinterleitner, A., 2010. Efficient, large-scale archaeological prospection using a true three-dimensional ground-penetrating radar array system. Archaeological Prospection 17, 175–186. doi:10.1002/arp.381.

Tronicke, J., Allroggen, N., 2015. Toward automated delineation of ground-penetrating radar facies in clastic sediments: An example from stratified glaciofluvial deposits. Geophysics 80(4), A89–A94. doi:10.1190/geo2015-0188.1.

Tronicke, J., Allroggen, N., Biermann, F., Fanselow, F., Guillemoteau, J., Krauskopf, C., Lück, E., 2020a. Rapid multi-scale analysis of near-surface geophysical anomaly maps: Application to an archaeo-geophysical data set. Geophysics 85(4), B109–B118. doi:10.1190/geo2019-0564.1.

Tronicke, J., Blindow, N., Groß, R., Lange, M.A., 1999. Joint application of surface electrical resistivity- and GPR-measurements for groundwater exploration on the island of Spiekeroog–northern Germany. Journal of Hydrology 223(1–2), 44–53. doi:10.1016/S0022-1694(99)00111-0.

Tronicke, J., Böniger, U., 2013. GPR attribute analysis: There is more than amplitudes. First Break 31, 103–108. doi:10.3997/1365-2397.31.8.70636.

Tronicke, J., Holliger, K., 2005. Quantitative integration of hydrogeophysical data: Conditional geostatistical simulation for characterizing heterogeneous alluvial aquifers. Geophysics 70(3), H1–H10. doi:10.1190/1.1925744.

Tronicke, J., Koyan, P., Allroggen, N., 2020b. The redundant wavelet transform to process and interpret GPR data, in: 18th International Conference on Ground Penetrating Radar, SEG, Global Meeting Abstracts, pp. 400–403. doi:10.1190/gpr2020-104.1.

Tronicke, J., Villamor, P., Green, A.G., 2006. Detailed shallow geometry and vertical displacement estimates of the Maleme Fault Zone, New Zealand, using 2D and 3D georadar. Near Surface Geophysics 4, 155–161. doi:10.3997/1873-0604.2005041.

Ursin, B., 1983. Review of elastic and electromagnetic wave propagation in horizontally layered media. Geophysics 48, 1063–1081. doi:10.1190/1.1441529.

Vail, P.R., Mitchum, Jr., R.M., Thompson, III, S., 1977. Seismic stratigraphy and global changes of sea level, Part 4: Global cycles of relative changes of sea level, in: Payton, C.E. (Ed.), Seismic Stratigraphy: Applications to Hydrocarbon Exploration. American Association of Petroleum Geologists. doi:10.1306/M26490C6.

Van Overmeeren, R.A., 1998. Radar facies of unconsolidated sediments in The Netherlands: A radar stratigraphy interpretation method for hydrogeology. Journal of Applied Geophysics 40(1–3), 1–18. doi:10.1016/S0926-9851(97)00033-5.

Vaughan, C.J., 1986. Ground-penetrating radar surveys used in archaeological investigations. Geophysics 51, 595–604. doi:10.1190/1.1442114.

Versteeg, R., 1994. The Marmousi experience: Velocity model determination on a synthetic complex data set. The Leading Edge 13(9), 927–936. doi:10.1190/1.1437051.

Villamor, P., Berryman, K., 2001. A late Quaternary extension rate in the Taupo Volcanic Zone, New Zealand, derived from fault slip data. New Zealand Journal of Geology and Geophysics 44, 243–269. doi:10.1080/00288306.2001.9514937.

Vinther, R., Mosegaard, K., Kierkegaard, K., Abatzis, I., Andersen, C., Vejbaek, O.V., If, F., Nielsen, P.H., 1995. Seismic texture classification: A computer-aided approach to stratigraphic analysis, in: SEG Technical Program Expanded Abstracts 1995, pp. 153–155. doi:10.1190/1.1887260.

van Vliet, L.J., Verbeek, P.W., 1995. Estimators for orientation and anisotropy in digitized images, in: Proceedings of the First Annual Conference of the Advanced School for Computing and Imaging, pp. 442–450.

Walden, A.T., Hosken, J.W.J., 1985. An investigation of the spectral properties of primary reflection coefficients. Geophysical Prospecting 33(3), 400–435. doi:10.1111/j.1365-2478.1985.tb00443.x.

Wang, X., Liu, S., 2017. Noise suppressing and direct wave arrivals removal in GPR data based on shearlet transform. Signal Processing 132, 227–242. doi:10.1016/j.sigpro.2016.05.007.

Wang, Z., Yin, C., Lei, X., Gu, F., Gao, J., 2015. Joint rough sets and Karhunen-Loève transform approach to seismic attribute selection for porosity prediction in a Chinese sandstone reservoir. Interpretation 3(4), SAE19–SAE28. doi:10.1190/INT-2014-0268.1.

Warren, C., Giannopoulos, A., Giannakis, I., 2016. gprMax: Open source software to simulate electromagnetic wave propagation for Ground Penetrating Radar. Computer Physics Communications 209, 163–170. doi:10.1016/j.cpc.2016.08.020.

Warren, C., Wetter, L., Giannakis, I., Gray, A., Giannopoulos, A., Hamrah, A., Patterson, A., 2018. A CUDA-based GPU engine for gprMax: Open source FDTD electromagnetic simulation software. Computer Physics Communications 237, 208–218. doi:10.1016/j.cpc.2018.11.007.

West, B.P., May, S.R., Eastwood, J.E., Rossen, C., 2002. Interactive seismic facies classification using textural attributes and neural networks. The Leading Edge 21, 1042–1049. doi:10.1190/1.1518444.

Westin, C.F., Bhalerao, A., Knutsson, H., Kikinis, R., 1997. Using local 3D structure for segmentation of bone from computer tomography images, in: Proceedings of the IEEE Computer Society Conference on Computer Vision and Pattern Recognition, pp. 794–800. doi:10.1109/CVPR.1997.609418.

Westin, C.F., Wigstroem, L., Loock, T., Sjoeqvist, L., Kikinis, R., Knutsson, H., 2001. Three-dimensional adaptive filtering in magnetic resonance angiography. Journal of Magnetic Resonance Imaging 14, 63–71. doi:10.1002/jmri.1152.

White, R.E., 1991. Properties of instantaneous seismic attributes. The Leading Edge 10, 26–32. doi:10.1190/1.1436827.

Winsemann, J., Lang, J., Polom, U., Loewer, M., Igel, J., Pollok, L., Brandes, C., 2018. Ice-marginal forced regressive deltas in glacial lake basins: Geomorphology, facies variability and large-scale depositional architecture. Boreas 47, 973–1002. doi:doi.org/10.1111/bor.12317.

Wright, J., Pless, R., 2005. Analysis of persistent motion patterns using the 3D structure tensor, in: Proceedings of the Seventh IEEE Workshops on Motion and Video Computing (WACV/MOTION'05), pp. 14–19. doi:10.1109/ACVMOT.2005.21.

Wrona, T., Pan, I., Gawthorpe, R.L., Fossen, H., 2018. Seismic facies analysis using machine learning. Geophysics 83(5), O83–O95. doi:10.1190/geo2017-0595.1.

Wu, X., 2017. Directional structure-tensor-based coherence to detect seismic faults and channels. Geophysics 82(2), A13–A17. doi:10.1190/geo2016-0473.1.

Xing, S.G., Su, Y., Feng, J.Q., Dai, S., Xiao, Y., Ding, C.Y., Li, C.L., 2017. The penetrating depth analysis of Lunar Penetrating Radar onboard Chang'e-3 rover. Research in Astronomy and Astrophysics 17, 46–58. doi:10.1088/1674-4527/17/5/46.

Xu, T., McMechan, G.A., 1997. GPR attenuation and its numerical simulation in 2.5 dimensions. Geophysics 62, 403–414. doi:10.1190/1.1444151.

Yang, P., Gao, J., Wang, B., 2014. RTM using effective boundary saving: A staggered grid GPU implementation. Computers and Geosciences 68, 64–72. doi:10.1016/j.cageo.2014.04.004.

Yee, K., 1966. Numerical solution of initial boundary value problems involving maxwell's equations in isotropic media. IEEE Transactions on Antennas and Propagation 14, 302–307. doi:10.1109/TAP.1966.1138693.

Yenugu, M.M., Marfurt, K.J., Matson, S., 2010. Seismic texture analysis for reservoir prediction and characterization. The Leading Edge 29, 1116–1121. doi:10.1190/1.3485772.

Yılmaz, Ö., 2001. Seismic data analysis: Processing, inversion and interpretation of seismic data. SEG Investigations in Geophysics No. 10. doi:10.1190/1.9781560801580.

Young, R.A., Deng, Z., Marfurt, K.J., Nissen, S.E., 1997. 3-D dip filtering and coherence applied to GPR data: A study. The Leading Edge 16, 921–928. doi:10.1190/1.1437699.

Zakri, T., Laurent, J.P., Vauclin, M., 1998. Theoretical evidence for 'Lichtenecker's mixture formulae' based on the effective medium theory. Journal of Physics D: Applied Physics 31(13), 1589–1594. doi:10.1088/0022-3727/31/13/013.

Zhao, T., Jayaram, V., Roy, A., Marfurt, K.J., 2015. A comparison of classification techniques for seismic facies recognition. Interpretation 3(4), SAE29–SAE58. doi:10.1190/INT-2015-0044.1.

Zhao, T., Li, F., Marfurt, K.J., 2017. Constraining self-organizing map facies analysis with stratigraphy: An approach to increase the credibility in automatic seismic facies classification. Interpretation 5, T163–T171. doi:10.1190/INT-2016-0132.1.

Zhao, W., Forte, E., Fontolan, G., Pipan, M., 2018. Advanced GPR imaging of sedimentary features: Integrated attribute analysis applied to sand dunes. Geophysical Journal International 213, 147–156. doi:10.1093/gji/ggx541.

Zhao, W., Forte, E., Pipan, M., 2016. Texture attribute analysis of GPR data for archaeological prospection. Pure and Applied Geophysics 173(8), 2737–2751. doi:10.1007/s00024-016-1355-3.

Zhao, W., Forte, E., Pipan, M., Tian, G., 2013. Ground penetrating radar (GPR) attribute analysis for archaeological prospection. Journal of Applied Geophysics 97, 107–117. doi:10.1016/j.jappgeo.2013.04.010.

Zhu, D., Shi, Z., Wang, X., Chen, W., 2021. A high-resolution GPR horizon extraction method based on local reflection and global correlation. IOP Conference Series: Earth and Environmental Science 660, 012025. doi:10.1088/1755-1315/660/1/012025.

Appendix

For better readability, the following Figures and Tables are not shown in List of Figures and List of Tables. In the following, references are given seperately for each article and thus might be duplicates of those identified in the main part of this thesis.

A. The redundant wavelet transform to process and interpret GPR data

Jens Tronicke, Philipp Koyan and Niklas Allroggen*

Summary

To analyze ground-penetrating radar (GPR) data, we propose a multi-scale decomposition approach based on a redundant wavelet transform (RWT). Our RWT is based on B_3-spline filters and the à trous algorithm, which allows to efficiently decompose 1D, 2D, and 3D data with a series of 1D convolutions. Using different examples, we demonstrate potential applications of this approach for data processing and interpretation. Our results show that the RWT is a powerful and computationally efficient tool to improve GPR data analysis.

Introduction

Today, densely sampled 2D and 3D GPR data sets are routinely acquired in various archaeological, engineering, environmental, and geological applications (e.g., Jol, 2009). To ease the interpretation of such data sets, there is a growing need for efficient data processing and analysis tools. We investigate a multi-scale decomposition approach and its potential for different tasks within a typical GPR processing and interpretation flow.

The basic idea of multi-scale analysis is to decompose a given data set into several subsets representing the data at different spatial or temporal scales. This allows to visualize the data at various resolutions and, thus, to separate and analyze signal or image components appearing at specific scales. For such a decomposition, the most popular tools rely on the wavelet transform including its variants and further developments (Starck et al., 2015). For decomposing GPR data, we use the discrete redundant wavelet transform (RWT; Shensa, 1992; Starck et al., 2015). After presenting the methodological basics, we apply the RWT to analyze field and synthetic GPR data, and evaluate its potential for rapid multi-scale processing. Our examples include 1D temporal denoising of GPR traces, 2D spatial decomposition of time slices, and 3D spatial filtering of attribute volumes.

*A reviewed expanded abstract of the same title is published as Tronicke et al. (2020b) in the proceedings of 18th International Conference on Ground Penetrating Radar, SEG, Global Meeting Abstracts, 400–403.

Methodology

Our decomposition relies on a discrete RWT (Shensa, 1992) implemented using the à trous algorithm (Holschneider et al., 1989). In astronomy, this transform is known as the starlet transform (Starck and Murtagh, 2006) and, more recently, it has also been used to analyze geophysical data. While Al-Dossary (2015) uses the RWT to enhance channel patterns in time slices of 3D reflection seismic data, Tronicke et al. (2020) apply it to magnetic mapping data to ease the interpretation of archaeologically relevant anomalies.

Using Figure A.1, we present the basic concepts of the RWT following Starck et al. (2015). In the shown example, a given data set a_0 is decomposed up to a scale level $n = 3$ using a series of low-pass filters L_j into three wavelet planes w_1, w_2, and w_3, and a final approximation a_3. At each scale level j (with $j = 1, \ldots, n$), the wavelet plane w_j is calculated as the difference between the approximations a_{j-1} and a_j, where a_j is obtained after applying L_j to a_{j-1}.

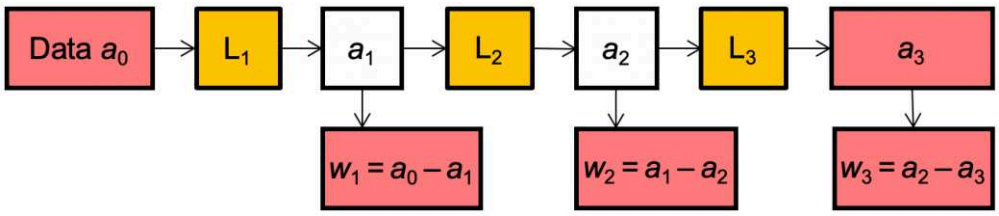

Figure A.1.: The basic concept of RWT-based decomposition. In the shown example, the input data a_0 are decomposed up to three scale levels resulting in three wavelet planes w_1, w_2, and w_3, and the final approximation a_3.

The most popular approach to set up L_j relies on B_3-splines which, for 1D data (e.g., a time series) and $j = 1$, results in $L_j = 1/16$ (1, 4, 6, 4, 1). For $j > 1$, the filters L_j are set up by extending L_1 via inserting $2^j - 1$ zero elements between the individual non-zero filter coefficients of L_1. Selecting B_3-spline-based filters results in separable 2D and 3D filters; i.e., the corresponding 2D and 3D filter processes can be implemented by two and three successive 1D convolutions, respectively. This is computationally more efficient than performing 2D or 3D convolutions using full 2D or 3D filter kernels. More details regarding the algorithm are given, for example, by Starck et al. (2015).

The result of applying the series of filters L_j to a data set is a redundant undecimated decomposition, where all w_j and a_j are of the same size. If we are interested in some kind of data reconstruction, such an undecimated decomposition is often preferred. For example, if the data are decomposed up to level n, the original data a_0 can be completely reconstructed by summing up a_n and all w_j (with $j = 1, \ldots, n$). For filtering and denoising applications, we may use only selected scales for reconstruction and/or manipulate individual planes before reconstruction by, for example, thresholding (e.g., Donoho and Johnston, 1995) or different normalization strategies (e.g., Tronicke et al., 2020) to generate a filtered and scale-balanced data set.

Example 1: 1D trace denoising

To demonstrate the basic ideas of decomposing and reconstructing GPR data using the RWT, we apply it to a noisy transmitter gather from a crosshole experiment performed in a sand and gravel-dominated environment for aquifer characterization (Figure A.2a). The horizontal distance between the two ~25 m deep vertical boreholes is ~15 m. The data have been recorded using 100 MHz antennas, a fixed transmitter depth of $z_{tra} = 10.75$ m, and a receiver station spacing of $\Delta z = 0.25$ m. Further details regarding this data set are given by Rumpf and Tronicke (2014).

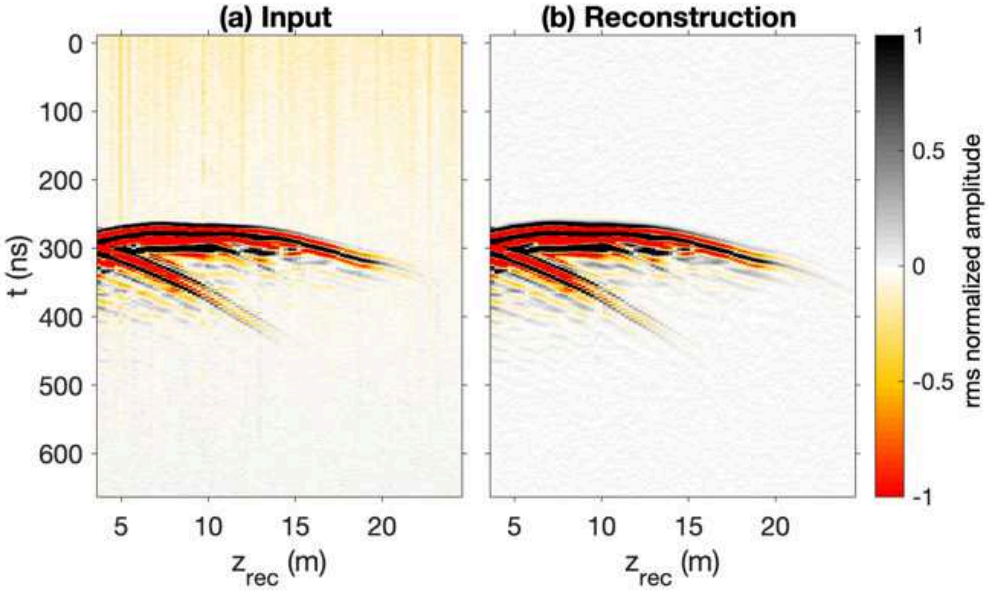

Figure A.2.: (a) Raw GPR transmitter gather, (b) same data after trace-based (1D) denoising. For visualization, the amplitudes of each image are normalized to their individual rms amplitude values.

In the raw data (Figure A.2a), we recognize the first-arriving direct events and some secondary arrivals such as the down-going reflected event originating at the groundwater table at a depth of ~3 m. The data are characterized by high and low frequency noise and a decreasing signal-to-noise ratio with increasing receiver depth z_{rec}. Thus, the direct arrivals are not clearly identifiable for $z_{rec} \gtrsim 20$ m. In Figure A.3, we show the result of a trace-based 1D decomposition of the raw data gather calculated up to $n = 9$ scale levels. This spectral decomposition allows us to analyze different signal and noise components in more detail. For example, w_1 is dominated by high-frequency noise while w_7 to w_9 are capturing mainly different low-frequency noise components. We also realize that most of the signal is found in w_3 to w_5 and, thus, we use these three planes to calculate the reconstruction shown in Figure A.2b, which is the sum of w_3 to w_5 shown in Figure A.3. When comparing Figures A.2a and A.2b, it is evident that our reconstruction (Figure

A.2b) represents a denoised, band-pass filtered version of the input data, where high and low-frequency noise is successfully suppressed.

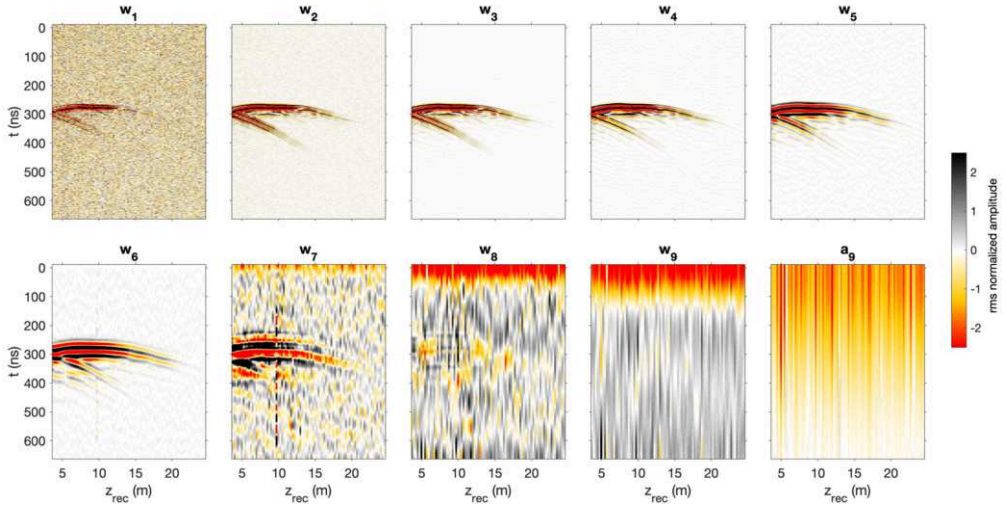

Figure A.3.: Decomposing the crosshole transmitter gather from Figure A.2a up to $n = 9$ scale levels resulting in wavelet planes w_1 to w_9 and the final approximation a_9. For visualization, all shown images are normalized to their individual rms amplitude values.

Example 2: 2D image decomposition

To illustrate the potential of the RWT approach for a 2D decomposition, we apply it to a time slice extracted from a migrated 3D GPR data volume at $t = 195$ ns. The data have been recorded using 100 MHz antennas across volcanic sediments to image near-surface faults in a graben system in New Zealand. Further details regarding this data set and the field site are given by Tronicke et al. (2006).

In Figure A.4a, we show the extracted time slice characterized by patterns at various spatial scales. This includes high-wavenumber noise features and low-wavenumber patterns related to sub-horizontal reflection events. We decompose this image using a 2D RWT up to $n = 9$ scale levels. The rms amplitudes of the resulting wavelet planes w_1 to w_9 and the final approximation a_9 are shown in Figure A.5 demonstrating that scale levels two to six comprise most of the energy of the input image. For the reconstructions, we use planes two to five to highlight image details including high-wavenumber patterns as expected for discontinuities related to faults. In Figure A.4b, we show the reconstruction calculated by summing up w_2 to w_5. In Figure A.4c, we illustrate an image reconstructed using the same planes but where each plane has been scaled before summation. Here, we apply a scaling strategy relying on rms-amplitude normalization; i.e., we divide each plane by its rms amplitude value (Figure A.5) to balance the contribution of each scale in the reconstruction. When comparing all slices in Figure A.4, we see that high- and

low-wavenumber noise is successfully suppressed in both reconstructions, while Figure A.4c further highlights low-scale structures as intended by the applied scaling strategy.

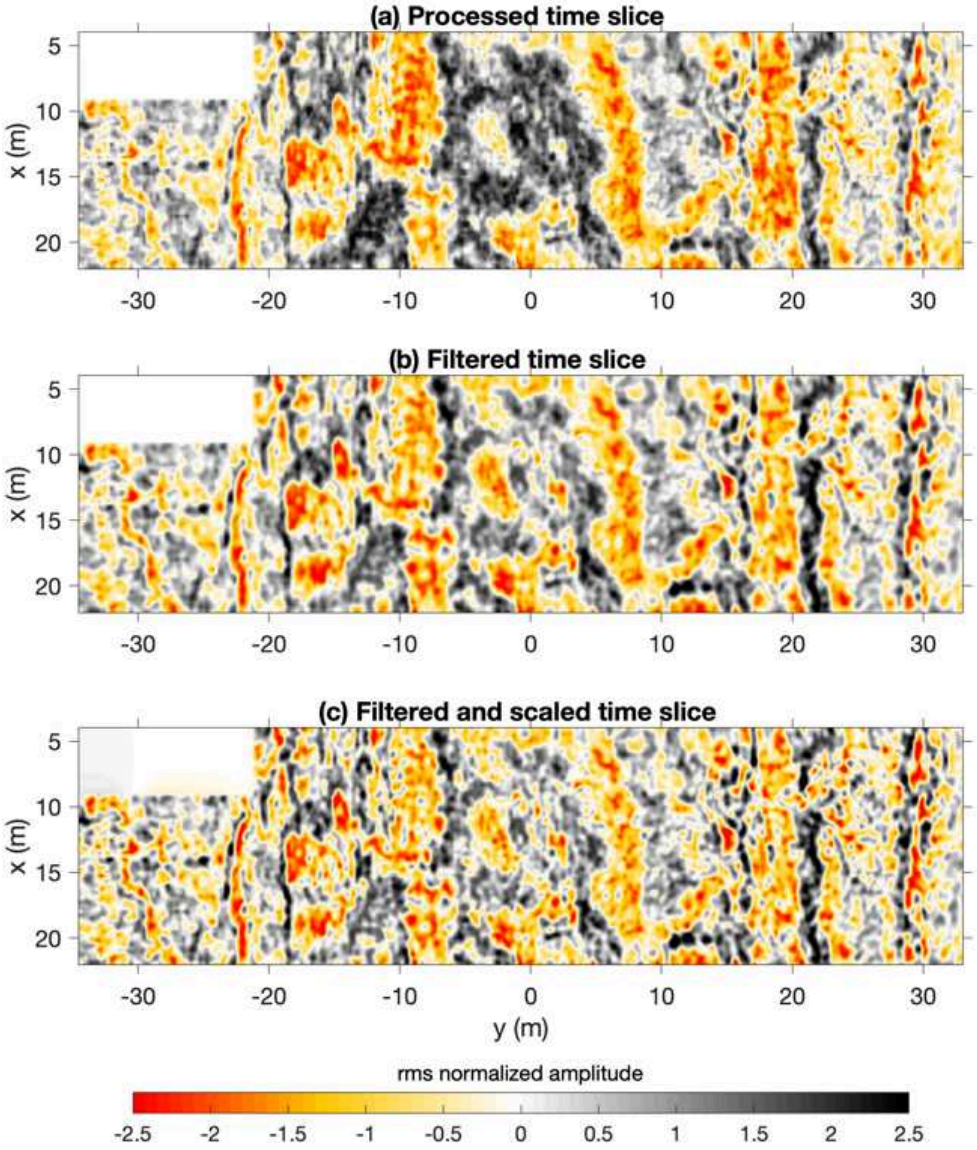

Figure A.4.: (a) Input time slice and reconstructions calculated by summing up w_2 to w_5 (b) without normalization and (c) with normalizing each w_j by its rms amplitude. All images are normalized to their individual rms values.

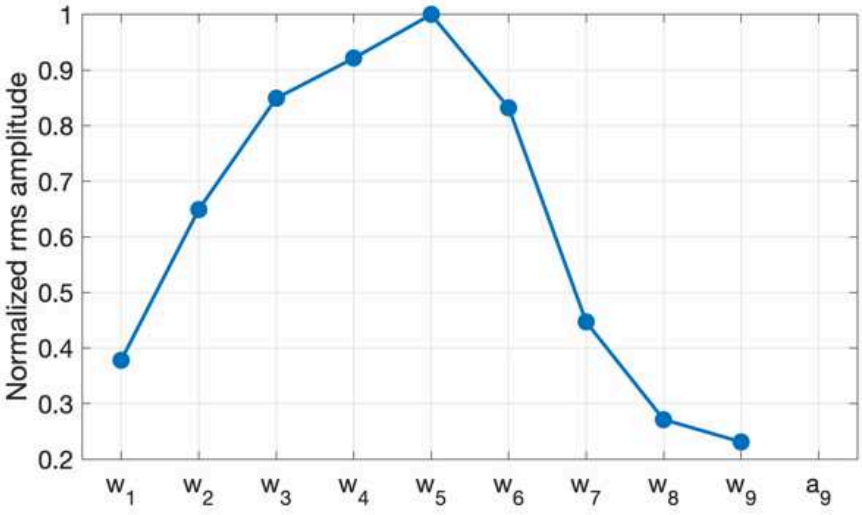

Figure A.5.: Normalized rms amplitude values of the wavelet planes w_1 to w_9 and the final approximation a_9 calculated from the decomposition result of the time slice shown in Figure A.4a.

Example 3: 3D volume filtering

As a 3D example of RWT-based processing, we use it to filter a 3D GPR attribute volume. Here, we analyze a synthetic 3D data set simulated across a realistic sedimentary model using a source wavelet with a center frequency of 100 MHz. The model comprises heterogeneities at different spatial scales and extends 16 m, 10 m, and 7 m in x-, y-, and z-direction, respectively. In Figure A.6a, we show an inline profile extracted from this 3D data set at $y = 6$ m after applying a typical processing flow including migration and time-to-depth conversion. Without providing a detailed interpretation, this profile shows reflection patterns as typically observed in sedimentary environments including (semi-)continuous horizontal and dipping reflections. Further details regarding this publicly available data set and the underlying model are given in Koyan and Tronicke (2019, 2020).

For a detailed interpretation of GPR data sets recorded in sedimentary environments, attribute analyses including different textural attributes are increasingly used (e.g., Tronicke and Allroggen, 2015). To analyze our synthetic 3D data, we calculate a textural attribute known as homogeneity from the gray-level co-occurrence matrix (GLCM), which is a well-known statistical concept to describe texture in 2D and 3D data (Chopra and Marfurt, 2007; Eichkitz et al., 2013).

In Figure A.6b, we illustrate the homogeneity attribute at an inline profile extracted from the 3D homogeneity cube calculated from the 3D GPR data volume using a 3D GLCM approach with a window size of 0.8 m in x-, y-, and z- direction. Without providing a detailed sedimentological interpretation of Figure A.6b, we realize artifacts

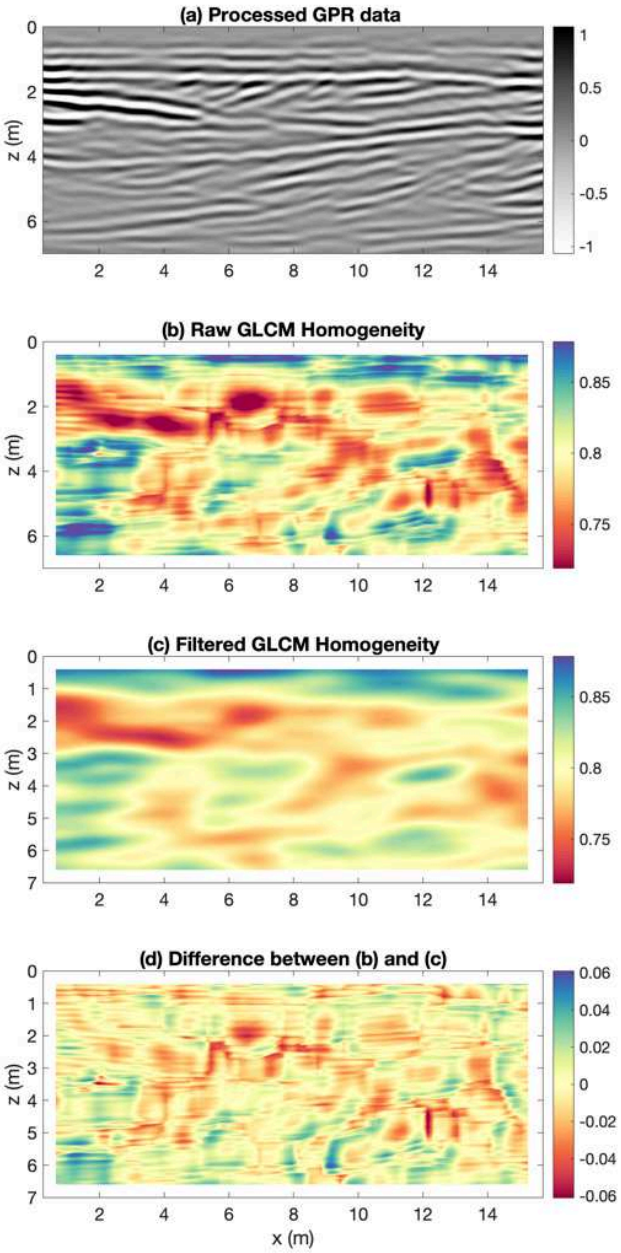

Figure A.6.: (a) Inline profile extracted from a 3D synthetic data set, (b) same profile extracted from a raw GLCM homogeneity cube, (c) same as (b) after 3D RWT-based filtering, and (d) difference between raw and filtered data cubes as illustrated in (b) and (c).

such as some isolated near-vertical features or the overall remaining wavelet character of the attribute image. To suppress these artifacts, we decompose the attribute volume using a 3D RWT up to $n = 9$ scale levels. After analyzing the 3D decomposition result, we reconstruct a filtered attribute volume by summing up w_4 to w_7. In Figure A.6c, we show an inline profile extracted from this filtered attribute volume at the same position as the input GPR and the raw attribute data shown in Figure A.6a and A.6b, respectively. Comparing Figure A.6a-A.6c and, in addition, considering the difference between the raw and the filtered attribute data (Figure A.6d), we conclude that our 3D filtering strategy has successfully removed the above discussed artifacts and results in a clear attribute image which can form the basis for further sedimentological interpretations.

Conclusions

We present a multi-scale decomposition approach based on a RWT to analyze GPR data. Our implementation based on B_3-spline filters and the à trous algorithm allows us to efficiently compute the decomposition of 1D, 2D, and 3D data using a series of 1D convolutions. We present different examples on how such an RWT can be used in a typical GPR processing flow including 1D denoising of GPR time series, 2D decomposition of GPR time-slice images, and 3D filtering of GPR attribute volumes. For practical use, we highlight the computational efficiency and the possibility of an almost parameter-free implementation. Considering the amount of data as provided by modern multi-channel GPR systems, we believe that RWT-based approaches and related methods are powerful tools to improve the processing and interpretation of such data sets.

References

Al-Dossary, S., 2015. Preconditioning seismic data for channel detection. Interpretation 3(1), T1–T4. doi:10.1190/INT-2014-0031.1.

Chopra, S., Marfurt, K.J., 2007. Seismic attributes for prospect identification and reservoir characterization. Geophysical development series, SEG.

Donoho, D. L., Johnstone, I.M., 1995. Adapting to unknown smoothness via wavelet shrinkage. Journal of the American Statistical Association 90(432), 1200–1224. doi:10-.2307/2291512.

Eichkitz, C. G., Amtmann, J., Schreilechner, M.G, 2013. Calculation of grey level co-occurrence matrix-based seismic attributes in three dimensions. Computers & Geosciences 60, 176–183. doi:10.1016/j.cageo.2013.07.006.

Holschneider, M., Kronland-Martinet, R., Morlet, J., Tchamitchian, P., 1989. A real-time algorithm for signal analysis with the help of the wavelet transform, in: Combes, J.M., Grossman, A., Tchmitchian, P. (Eds.), Wavelets: Time-Frequency Methods and Phase Space, Springer Berlin Heidelberg, pp. 286–297. doi:10.1007/978-3-642-75988-8_28.

Jol, H. M., 2009. Ground Penetrating Radar: Theory and Applications. Elsevier.

Koyan, P., Tronicke, J., 2019. [dataset] A synthetic 3D ground-penetrating radar (GPR) data set across a realistic sedimentary model. Mendeley Data. doi:10.17632/by3yh-79hx4.1.

Koyan, P., Tronicke, J., 2020. 3D modeling of ground-penetrating radar data across a realistic sedimentary model. Computers and Geosciences 137, 104422. doi:10-.1016/j.cageo.2020.104422.

Rumpf, M., Tronicke, J., 2014. Predicting 2D geotechnical parameter fields in near-surface sedimentary environments. Journal of Applied Geophysics 101, 95–107. doi:1-0.1016/j.jappgeo.2013.12.002.

Shensa, M. J., 1992. Discrete Wavelet Transforms: Wedding the à trous and Mallat algorithms. IEEE Transactions on Signal Processing 40(10), 2464–2482. doi:10.1109/-78.157290.

Starck, J. L., Murtagh, F., Fadili, J. M., 2015. Sparse Image and Signal Processing: Wavelets and related geometric multiscale analysis. Cambridge University Press.

Tronicke, J., Allroggen, N., 2015. Toward automated delineation of ground-penetrating radar facies in clastic sediments: An example from stratified glaciofluvial deposits. Geophysics 80(4), A89–A94. doi:10.1190/geo2015-0188.1.

Tronicke, J., Villamor, P., Green, A.G., 2006. Detailed shallow geometry and vertical displacement estimates of the Maleme Fault Zone, New Zealand, using 2D and 3D georadar. Near Surface Geophysics 4(3), 155–161. doi:10.3997/1873-0604.2005041.

Tronicke, J, Allroggen, N., Biermann, F., Fanselow, F., Guillemoteau, G., Krauskopf, C., Lück, E., 2020. Rapid multi-scale analysis of near-surface geophysical anomaly maps: Application to an archaeo-geophysical data set. Geophysics 85(4), B109–B118. doi:10.1190/geo2019-0564.1.

B. 3D GPR to explore peat deposits: Strategies for data acquisition, processing, and interpretation

Philipp Koyan, Jens Tronicke, Tim Klose and Julien Guillemoteau *

Abstract

In soil sciences and geology, ground- penetrating radar (GPR) reflection data are routinely used to explore the shallow subsurface. Recognizing that peatlands represent an important part of the global climate system, there is an increasing need to investigate and characterize peat deposits in more detail. Up to today, the application of GPR in peatland studies focuses on collecting 2D data along selected lines to develop models of peat thickness and stratigraphy. We present a 3D GPR case study from a peatland in northeastern Germany where we develop a detailed 3D model of the investigated peat body. Our results show significant variations in peat thickness including a prominent circular depression structure. We conclude that such structures could not be reliably imaged using 2D GPR surveying strategies. Thus, our results highlight the benefit of 3D GPR surveying to develop a more profound understanding of peat deposits and their characteristics.

Introduction

For decades, ground-penetrating radar (GPR) has been successfully used to investigate peatlands (e.g., Ulriksen, 1982; Hänninen et al., 1992; Jol and Smith, 1995). Typically, GPR data are used to estimate peat thickness, develop a stratigraphic model of the peat body, and characterize the underlying mineral deposits (Proulx-McInnis et al., 2013). Often, point data provided by drillings and push soundings complement such GPR data sets; e.g., to develop and calibrate a GPR velocity model or to interpret internal peat layering in more detail. More recently, especially because peatlands are considered to be a crucial part of the global climate system, there is a growing interest in using near-surface geophysical methods, including GPR, to characterize peatlands and their carbon storage capabilities in more detail (e.g., Walter et al., 2016; Comas et al., 2017).

If the goal of a GPR survey is to develop a detailed and reliable model of subsurface architecture from the recorded GPR data, the benefits of 3D surveying strategies are well known. Especially, in environments characterized by complex subsurface geometries

*A reviewed expanded abstract of the same title is published as Koyan et al. (2023) in the proceedings of 12th International Workshop on Advanced Ground Penetrating Radar.

or numerous point diffractors, a densely spaced acquisition grid is needed to properly reconstruct subsurface structures (Grasmueck et al., 2005). Up to today, most published GPR data sets collected across peatlands rely on a 2D surveying strategy; i.e., GPR data are collected along selected profile lines where the spacing between individual lines is much larger than the in-line trace spacing. In such 2D data sets, reflections and diffractions originating from structures off the surveyed profiles may result in distorted reflection images and, thus, may lead to misinterpretations.

Here, we present a case study to illustrate the benefits of a 3D GPR surveying strategy. Our data have been collected across a peat body in northeastern Germany where a 3D subsurface architecture is expected. In the following, we first present more details regarding our field site and data acquisition. After presenting our GPR processing flow, we interpret our 3D data volume and, considering available point data, develop a 3D model of the surveyed peat body.

Materials and Methods

Field Size and data acquisition

Following a dry summer season in 2022, we collected 3D GPR, electromagnetic induction (EMI), and 2D electrical resistivity tomography (ERT) data to characterize a peat body near the city of Kremmen (Brandenburg, Germany). Considering the resolution of our GPR survey in all three spatial dimensions, we expect a two-layer peat body at our field site, consisting of a poorly saturated (almost dry) peat layer (with a thickness in the order of a few decimeters) on top of a more water-saturated peat layer (with a variable thickness up to a few meters). As known from available geological background information, we expect sand and mud deposits underneath the peat body.

Here, we focus on a 3D GPR data set recorded using a pair of 100 MHz antennas to image both the interface between unsaturated and saturated peat, and the base of the peat body, which, in turn, allows us to infer characteristics of the peat body such as thickness, or volume. Our GPR survey includes a 3D common-offset data set covering an area of approximately 6000 m^2 (50 m x 120 m). This data set has been acquired using an in- and crossline trace spacing of approximately 0.2 m and 0.5 m, respectively. Furthermore, we collected collocated positioning and topographic information as recorded by a tracking total station (TTS) during GPR data acquisition (Böniger and Tronicke, 2010) and common- midpoint (CMP) data gathers at selected locations.

For ground-truthing and in-depth characterization of the peat body, we complement our geophysical survey with manual push soundings. Pushing a metal rod down until it strikes the hardened mineral deposits allows us to obtain information on the peat-base depth up to several meters. When deploying these soundings, we focus on selected profiles and regions where we expect the thickest parts of the peat body whose location can be inferred, for example, from preliminary results of the collocated EMI survey in form of apparent conductivity maps, aerial photography, local vegetation, and topography.

Data processing

To produce a ready-to-interpret GPR volume allowing us to pick and map the target interfaces, we apply a state-of- the-art 3D processing flow to our common-offset data set (e.g., Koyan et al., 2021). This workflow includes DC-shift and time-zero corrections as well as 1D frequency-domain bandpass filtering, spectral balancing (Tronicke et al., 2015), and 3D spatial filtering using a wavelet-based strategy (Tronicke et al., 2020) to suppress noise and reconstruct higher signal frequencies. Furthermore, we use f-k filtering to remove wavefield components and noise related to, for example, direct arrivals, varying antenna coupling, or the remains of out-of-plane reflections and diffractions. In addition, our processing flow includes 3D topographic migration (Allroggen et al., 2015), topographic correction, and time-to-depth conversion relying on a digital terrain model (DTM) derived from our TTS-based topographic data, and a root-mean-square (rms) velocity model obtained from reflection-based analysis of the CMP gathers (not shown here). Here, we refer to local depth with respect to the maximum topographic elevation as inferred from our DTM. In Figure B.1, we show a selected inline (a) and depth slice (b) extracted from the ready-to-interpret GPR data volume. Analyzing Figure B.1a in more detail reveals a largely horizontal and continuous reflection structure with medium amplitudes at depths around 0.5 m. In the deeper parts (at depths between approximately 1 m and 2 m), we observe a reflection structure that shows high amplitudes and high continuity in the southern part of the field site, whereas in the northern part both the amplitudes and the continuity of this reflection decrease. As indicated by Figure B.1b, this reflection forms a nearly circular depression structure located in the central part of our survey area (centered around local x/y coordinates of 40/115 m).

Results and Discussion

GPR interpretation

To analyze our GPR volume in more detail, we interpret the two prominent reflection structures (as already identified above) in terms of GPR horizons. We use the open-source software package OpendTect to pick and map two distinct horizons using a combination of both manual and automated horizon tracking. In Figure B.2, we visualize these two horizons together with selected inline, crossline, and depth slices extracted from our processed data volume.

The shallow horizon at depths around 0.5 m can be tracked across the entire survey area and shows a largely continuous, horizontal character. Thus, we show this horizon in Figure B.2 as a dotted line plotted only onto the selected inline and crossline slices. Considering the results from our CMP velocity analysis, EMI mapping as well as geological information, we interpret this horizon as the interface between a poorly saturated, almost dry peat, and a more saturated variant underneath. Here, the contrast in water saturation results in an abrupt change of electromagnetic properties subdividing the peat body. In terms of GPR velocities, this results in a thin, near-surface high-velocity zone (GPR

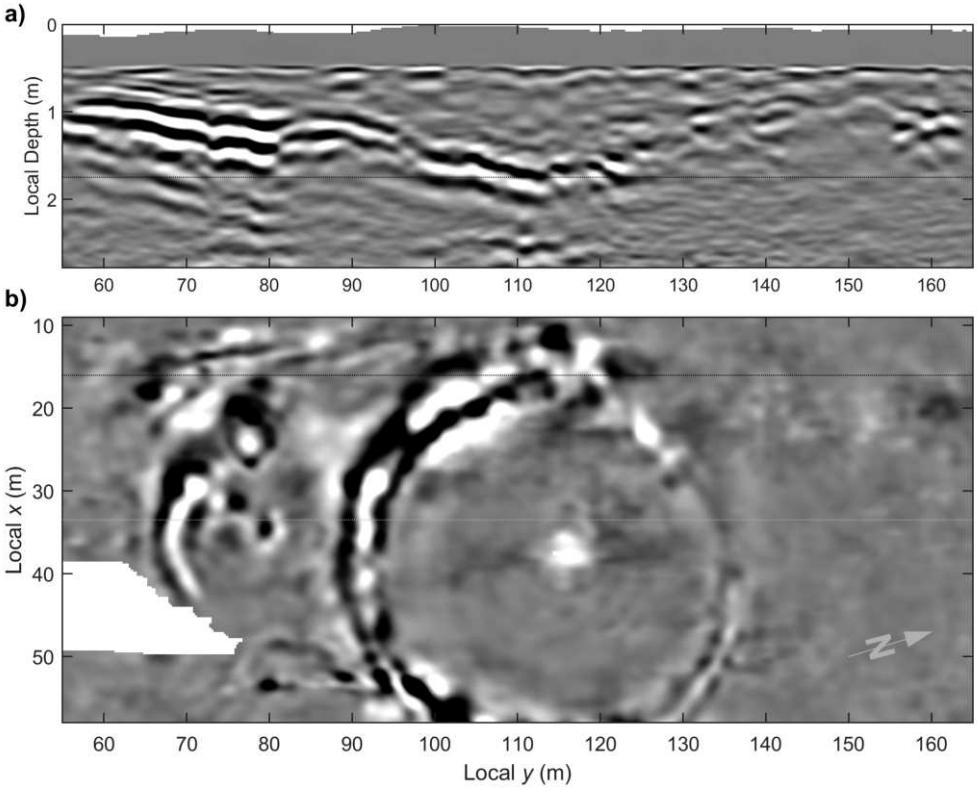

Figure B.1.: Selected, representative **a** inline and **b** depth slices extracted from our ready-to-interpret GPR volume. In **a** and **b**, the black dotted lines show the location of depth slice **b** and inline slice **a**, respectively. In **b**, the gray dotted line illustrates the location of the central inline slice shown in Figure B.3.

velocities around v 1 = 0.2 m/ns) underlain by a low-velocity zone (GPR velocities around v 2 = 0.035 m/ns).

At depths between 0.8 m and 2.2 m, we observe a horizon that corresponds to the priorly identified circular structures. We interpret this horizon as the base of the peat body that is characterized by a circular depression structure in its central part where we observe rather steeply dipping flanks and, consequently, a rapid increase in peat thickness. In regions, where the thickness of the peat body significantly exceeds two meters, the reflections are highly attenuated and no longer reliably trackable. Thus, the corresponding GPR horizon shows gaps, especially, in the central part of the circular depression.

Integrated Interpretation

To further characterize and interpret the peat body (especially in terms of its thickness and volume), we consider the results from GPR horizon tracking and manual push soundings. Integrating depth information inferred from the GPR survey and the manual

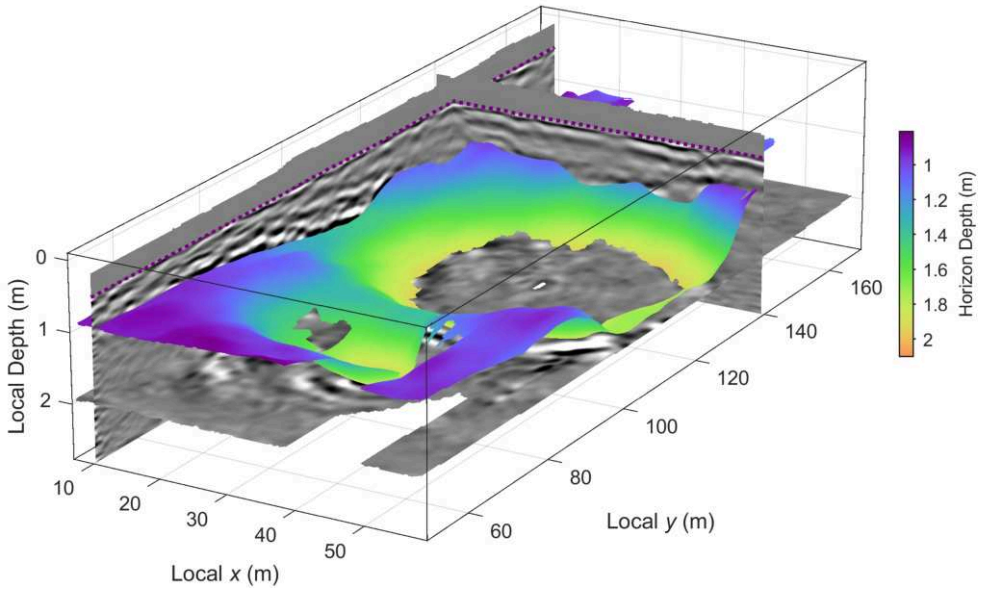

Figure B.2.: Results of a horizon-based interpretation visualized together with selected slices extracted from our processed GPR volume. The dotted lines at depths around 0.5 m indicate a largely continuous, horizontal horizon while the color-coded surface represents a discontinuous horizon undulating between depths of 0.8 m and 2.2 m.

push soundings allows us to estimate a closed interface corresponding to the peat base across the entire field site. This results in a model representation of the peat body that we show in Figure B.3 together with the push soundings along an inline slice crossing the central part of the prominent circular structure (location indicated by the gray line in Figure B.1b).

The model illustrated in Figure B.3 subdivides the peat body into an almost dry top layer characterized by high GPR velocities and a thickness up to 0.5 m, and a layer of more saturated peat showing considerably low GPR velocities (ratio of approximately 1:6 with respect to the top layer). The interpolated base of the peat body as inferred from integrated analysis of the corresponding GPR horizon (Figure B.2) and data from push soundings shows a maximum peat thickness of more than 4.5 m. Having at hand the top (i.e., the local topography), the internal interface between almost dry and more saturated peat variants, and the base of the peat body allows us to estimate the total peat volume at our field site (approximately 8600 m^3) as well as the volumetric fractions of both dry (approximately 2300 m^3, i.e., 25 % of the total peat volume) and more saturated peat (approximately 4200 m^3, i. e., 75 % of the total peat volume). For a detailed characterization of peat bodies also in view of carbon storage, such data represent important information for evaluating peatlands with respect to their role in the climate system.

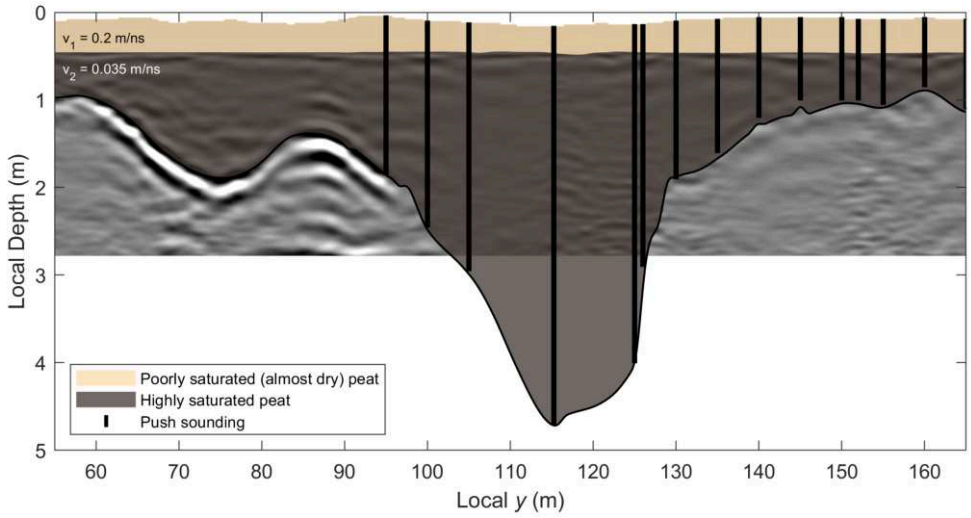

Figure B.3.: Selected central inline slice extracted from the processed GPR volume (for location see Figure B.1) overlain by our final subsurface model of the peat body as inferred from integrating the results of GPR interpretation and several push soundings.

Conclusion

Using a 3D GPR data set (100 MHz), we characterize a peat body in terms of its shape, internal structuring, and composition. Using state-of-the-art GPR acquisition, processing, and interpretation techniques (also integrating topographic information and manual push data), we infer two closed horizons characterizing the base of the peat body and an internal interface between poorly saturated (almost dry) and more saturated peat variants.

Our interpretation approach reveals that the peat body is characterized by a circular depression with steep flanks and a maximum peat thickness of more than 4.5 m resulting in a total peat volume of approximately 8500 m^3 (of which 25% are almost dry and 75% are more saturated). Such a detailed characterization in terms of subsurface structures and properties would not be possible using 2D acquisition and interpretation strategies. In fact, for complex peat bodies such as the one investigated in our study, a pure 2D strategy bears the potential of distorted imaging and, in turn, provokes misinterpretations.

Our results can be considered as a starting point for a more in-depth pedological characterization and can provide crucial prior information to constrain interpretations of other geophysical data sets such as inversions of collocated EMI or ERT surveys.

References

Allroggen, N., Tronicke, J., Delock, M., Böniger, U., 2015. Topographic migration of 2D and 3D ground-penetrating radar data considering variable velocities. Near Surface Geophysics 13, 253–259. doi: 10.3997/1873-0604.2014037.

Böniger, U., Tronicke, J., 2010. On the potential of kinematic GPR surveying using a self-tracking total station: Evaluating system cross-talk and latency. IEEE Transactions on Geoscience and Remote Sensing 48, 3792–3798. doi: 10.1109/TGRS.2010.2048332.

Comas, X., Terry, N., Hribljan, J. A., Lilleskov, E. A., Suarez, E., Chimner, R. A., Kolka, R. K., 2017. Estimating belowground carbon stocks in peatlands of the Ecuadorian páramo using ground-penetrating radar (GPR). Journal of Geophysical Research: Biogeosciences 122, 370–386. doi: 10.1002/2016JG003550.

Grasmueck, M., Weger, R., Horstmeyer, H., 2005. Full-resolution 3D GPR imaging. Geophysics 70(1), K12–K19. doi: 10.1190/1.1852780.

Hänninen, P., Geological Survey of Finland, 1992. Application of ground penetrating radar techniques to peatland investigations: 4th International Conference on Ground Penetrating Radar, EAGE, 217-221. doi: 10.3997/2214-4609-pdb.303.28.

Jol, H. M., Smith, D. G., 1995. Ground penetrating radar surveys of peatlands for oilfield pipelines in Canada. Journal of Applied Geophysics 34, 109–123. doi: 10.1016/0926-9851(95)00018-6.

Koyan, P., Tronicke, J., Allroggen, N., 2021. 3D ground-penetrating radar attributes to generate classified facies models: A case study from a dune island. Geophysics 86(6), B335–B347. doi: 10.1190/geo2021-0204.1.

Proulx-McInnis, S., St-Hilaire, A., Rousseau, A. N., Jutras, S., 2013. A review of ground-penetrating radar studies related to peatland stratigraphy with a case study on the determination of peat thickness in a northern boreal fen in Quebec, Canada. Progress in Physical Geography: Earth and Environment 37, 767–786. doi: 10.1177/0309133313501106.

Tronicke, J., Schennen, S., Allroggen, N., 2015. Spectral enhancement of GPR data: Some practical considerations: 8th International Workshop on Advanced Ground Penetrating Radar, IEEE. doi: 10.1109/IWAGPR.2015.7292692.

Tronicke, J., Allroggen, N., Biermann, F., Fanselow, F., Guileemoteau, J., Krauskopf, C., Lück, E., 2020. Rapid multiscale analysis of near-surface geophysical anomaly maps: Application to an archaeogeophysical data set. Geophysics 85(4), B109–B118. doi: 10.1190/geo2019-0564.1.

Ulriksen, C. P. F, 1982. Application of impulse radar to civil engineering. Doctoral Thesis, Lund University of Technology.

Walter, J., Hamann, G., Lück, E., Klingenfuss, C., Zeitz, J., 2016. Stratigraphy and soil properties of fens: Geophysical case studies from northeastern Germany. CATENA 142, 112–125. doi: 10.1016/j.catena.2016.02.028.

C. The gradient structure tensor (GST): An efficient tool to analyze 3D GPR data for archaeological prospection

Philipp Koyan and Jens Tronicke*

Introduction

Ground-penetrating radar (GPR) is a well-established near-surface geophysical tool commonly applied in archaeological prospection. Thanks to steady developments in system design and surveying strategies, the acquisition of 3D GPR data sets densely covering thousands of square meters has become common practice. However, developing GPR interpretation strategies has not kept pace with technological novelties. Today, the ever-growing amount of GPR data is still typically interpreted in a manual fashion which makes interpretation a time- consuming and rather subjective process. Recently, the application of 3D attributes has shown to be a helpful strategy in GPR data analysis to concise the interpretation processes and make interpretation a less subjective and more reproducible task. Attributes enhancing and quantifying structure information such as dip and continuity are prone to deliver reliable results when incorporated into the interpretation process (Koyan et al., 2021). The gradient structure tensor (GST) is well known as a tool to describe structure in 2D/3D/4D image and video processing including medical applications. GST-based strategies have also been successfully used to interpret reflection seismic data (e.g., Bakker, 2002) but to our knowledge no examples for the application to 3D GPR data sets can be found in the literature.

Theory and Method

In 3D, the gradient structure tensor N of an image I is defined by smoothed outer products of the image gradients:

$$\mathrm{N}(x,y,z) = \begin{pmatrix} \langle I_x^2 \rangle & \langle I_x I_y \rangle & \langle I_x I_z \rangle \\ \langle I_y I_x \rangle & \langle I_y^2 \rangle & \langle I_y I_z \rangle \\ \langle I_z I_x \rangle & \langle I_z I_y \rangle & \langle I_z^2 \rangle \end{pmatrix}. \tag{C.1}$$

*A reviewed expanded abstract of the same title is published as Koyan and Tronicke (2023b) in the proceedings of 15th International Conference of Archaeological Prospection.

Here, the indices x, y, z denote the derivatives with respect to the three spatial dimensions and $\langle\cdot\rangle$ denotes a Gaussian smoothing operation applied to produce stable results at the target spatial scale characterized by a standard deviation $\sigma_T(x, y, z)$. Relevant information from this tensor can be obtained by calculating its three eigenvalues ($\lambda_1 \geq \lambda_2 \geq \lambda_3 \geq 0$) and the corresponding eigenvectors $\hat{e_i}$ with $i = 1,2,3$. From the orientation of the eigenvectors, local structure, for example, within locally stratified environments can be quantified by calculating the dip angle and dip azimuth. In contrast, to detect and map archaeological targets, we analyze the tensor eigenvalues in terms of planarity C_{plane} calculated by

$$C_{plane} = \frac{\lambda_1 - \lambda_2}{\lambda_1 + \lambda_2}. \tag{C.2}$$

In general, planarity describes the local structure in terms of continuous regions ($C_{plane} \approx 1$) such as layers in stratified sediments and discontinuous regions ($C_{plane} \ll 1$) such as debris. Compared to other relevant attribute calculation strategies, the GST procedure (1) can be considered as computationally efficient (calculation times in the order of seconds for typical 3D data sets), (2) delivers a wide range of diverse attributes highlighting different structural characteristics, and (3) enables an intuitive parameter selection because its output mainly depends on the target-specific parameter $\sigma_T(x, y, z)$.

Results and Discussion

To detect the remains of ancient architectural elements in the Palace Garden of Paretz, Brandenburg (Germany), Böniger and Tronicke (2010) collected densely-sampled 3D GPR data using a common-offset pair of unshielded 200 MHz antennas covering an area of approximately 35x40 m. In Figure C.1a, we show selected slices of the GPR amplitude volume after applying a typical 3D processing sequence including migration, topographic correction, and time-to-depth conversion. By performing extensive attribute-based analyses of this GPR volume also considering collocated magnetic and topographic surveys, the authors identified several anomalies that they interpret using a historical sketch of the garden from the early 19th century (Figure C.1b). To demonstrate the potential of our GST-based method, we focus on structure A, where the historical sketch reports an ancient grotto with rectangular walls underneath a teahouse.

To calculate the GST, we set $\sigma_T(x, y, z)$ to 0.35 m such that the Gaussian smoothing kernels operate in the order of a dominant GPR wavelength. In Figure C.2a, we show a selected x-y slice of the GPR amplitude volume shown in Figure C.1a at a depth of approximately 3 m. We observe mainly chaotic reflection patterns appearing to lack a preferential direction which makes it hard to interpret the GPR data alone in terms of archaeologically relevant structures. Mainly the same holds for GPR energy, a common attribute in archaeological GPR prospection, that we show along the same slice in Figure C.2b. Here, we calculate planarity across the GPR amplitude volume following Equations C.1 and C.2, and show the result as transparent overlay on the corresponding GPR data

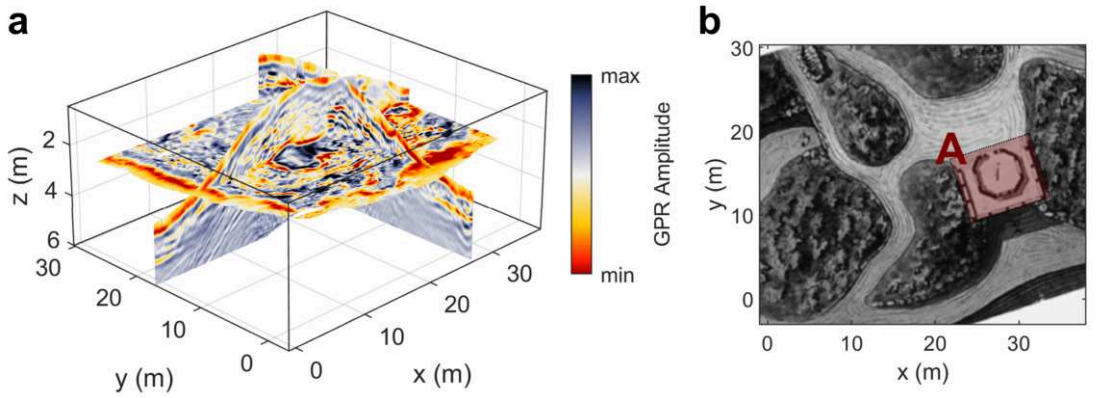

Figure C.1.: (a) Example slices of the processed data set in terms of GPR amplitude (vertical exaggeration is 3). (b) Historical sketch of the Paretz Palace Garden highlighting structure A, a historical grotto located beneath a teahouse (redrawn after Böniger and Tronicke, 2010).

slice shown in Figure C.2a. Comparing Figures C.1b and C.2c reveals that discontinuous areas (highlighted by lower planarity values) nearly perfectly trace the apparently well-preserved walls of the grotto. Additionally, we calculate planarity for the GPR energy volume and show the result in Figure C.2d as transparent overlay on the corresponding GPR energy slice shown in Figure C.2b. Comparing Figure C.2b and C.2d shows that the energy-based planarity highlights the inner part of structure A and thus indirectly images the outer boundaries of the grotto. Taking also Figure C.1b into consideration implies that the low energy-based planarity values in the central part of structure A are caused by discontinuous energy patterns that, in turn, indicate debris originating from the formerly overlying teahouse.

Conclusion

Analyzing GPR attributes aids the interpretation of the underlying data sets. However, calculating and selecting an appropriate set of attributes can be a cumbersome procedure. We apply the 3D gradient structure tensor (GST), a time-efficient, flexible, and comparatively objective tool that runs with only a few (target-specific) parameters. Additionally, applying the GST strategy delivers a selection of attributes to outline diverse structures in the underlying 3D data sets. Here, by calculating the planarity attribute based on the GST across a GPR amplitude and a GPR energy volume, we show that GST-based analysis is a useful mean to detect and highlight a grotto and remains of an associated teahouse in the ancient Palace Garden in Paretz, Brandenburg (Germany).

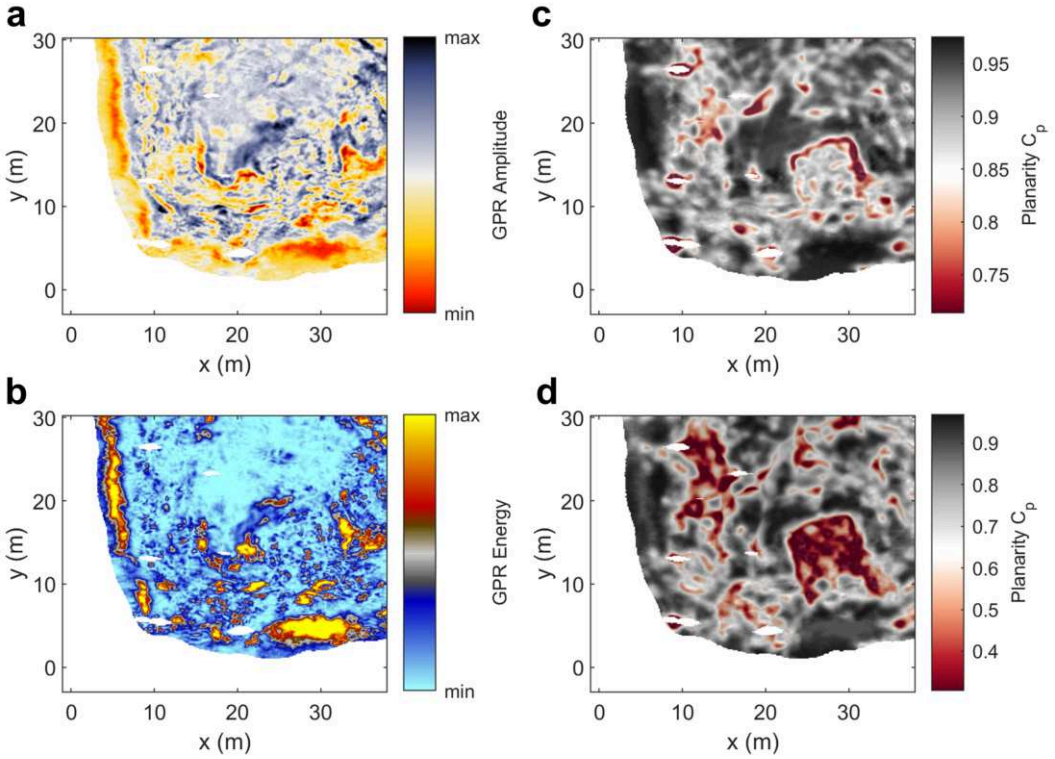

Figure C.2.: Example x-y slices at a depth of approximately 3 m of (a) GPR amplitude, (b) GPR energy, (c) GST-based planarity calculated across GPR amplitude, and (d) GST-based planarity calculated across GPR energy.

References

Bakker, P., 2002. Image structure analysis for seismic interpretation. Doctoral Thesis. Delft University of Technology. Link:f3f60507-5b08-43cb-a309-c3446c972395.

Böniger, U., Tronicke, J., 2010. Integrated data analysis at an archaeological size: A case study using GPR, magnetic, and high-resolution topographic data. Geophysics 75(4), B169-B176. doi:10.1190/1.3460432.

Koyan, P., Tronicke, J., Allroggen, N., 2021. 3D ground-penetrating radar attributes to generate classified facies models: A case study from a dune island. Geophysics 86(6), B335-B347. doi:10.1190/geo2021-0204.1.

D. 3D ground-penetrating radar attribute classification: A case study from a paleokarst breccia pipe in the Billefjorden area on Spitsbergen, Svalbard

Niklas Allroggen, Björn H. Heincke, Philipp Koyan, Walter Wheeler and Jan S. Rønning*

Abstract

Ground-penetrating radar (GPR) is a method that can provide detailed information about the near subsurface in sedimentary and carbonate environments. The classical interpretation of GPR data (e.g., based on manual feature selection) often is labor-intensive and limited by the experience of the interpreter. Novel attribute-based classification approaches, typically used for seismic interpretation, can provide faster, more repeatable, and less biased interpretations. We have recorded a 3D GPR data set collected across a paleokarst breccia pipe in the Billefjorden area on Spitsbergen, Svalbard. After performing advanced processing, we compare the results of a classical GPR interpretation to the results of an attribute-based classification. Our attribute classification incorporates a selection of dip and textural attributes as the input for a k-means clustering approach. Similar to the results of the classical interpretation, the resulting classes differentiate between undisturbed strata and breccias or fault zones. The classes also reveal details inside the breccia pipe that are not discerned in the classical interpretation. Using nearby outcropping breccia pipes, we infer that the intrapipe GPR facies result from subtle differences, such as breccia lithology, clast size, or pore-space filling.

Introduction

Carbonate and evaporite formations often are subject to dissolution processes, commonly summarized as karstification. Due to the complexity of karst structures and features (e.g., sinkholes, caves, collapse pipes, and underground drainage systems), karst environments

*A peer-reviewed journal article of the same title is published as Allroggen et al. (2022) in Geophysics 87(4), WB19–WB30. This article has been awarded from the SEG with *Honorable Mention* in the selection of *the Best Paper in Geophysics in 2022.*

are challenging targets for groundwater exploration, geothermal investigations, pollution remediation, and other environmental and engineering applications; therefore, they are the subject of a variety of geologic, morphological, geotechnical, and environmental studies (e.g., Ford and Williams 2007; White 2007). After collapse and burial, karst features are preserved as local heterogeneities (paleokarst), which are typically connected to vertically extending transstratal collapse structures (chimneys), often filled with porous and permeable brecciated material (breccia pipes) cutting tens to hundreds of meters through the overlaying strata (Eliassen and Talbot, 2005). Such paleokarst breccias and the associated faults form potential fluid pathways for economically relevant hydrocarbon, geothermal, and hydrologic reservoirs (Mazzullo and Chilingarian, 1996; Loucks, 1999; Goldscheider et al., 2010; Lonoy et al., 2021). However, the modeling of paleokarst systems is generally restricted by a lack of detailed knowledge on the volume, spatial distribution, and connectivity of karst features, which are typically below the resolution limit of exploration seismic surveys (Borghi et al., 2012; Lonoy et al., 2021). Therefore, a better understanding of paleokarst environments and their collapse processes requires detailed geophysical imaging to derive information on the structural extent and on the physical parameters of these subsurface features. Consequently, a range of geophysical methods has been applied to map karstified areas and the associated subsurface structures (Kruse et al., 2006; Chalikakis et al., 2011; Carrière et al., 2013).

Due to its fast data acquisition and its ability to image structures with high resolution, ground-penetrating radar (GPR) is a method particularly suited for detecting subsurface karst features. Especially in areas without electrically conductive soil cover, GPR is known to provide detailed information on the shape and extent of karst features (e.g., McMechan et al., 2002; Chalikakis et al., 2011). However, the complex shape and often large extent of such karstified areas pose challenges for GPR surveying and interpretation. Despite the increasing availability of fast and efficient GPR data acquisition strategies (e.g., Trinks et al., 2018), classical GPR data interpretation still relies on manual workflows making the interpretation labor-intensive and largely depending on the experience of the interpreter. After recording and applying an appropriate processing scheme, the data are typically loaded in an interpretation software application. During the classical interpretation process, reflection and diffraction patterns are assigned to geologic structures and tracked as horizons in the presence of continuous reflectors. Areas of similar patterns are typically summarized as GPR facies that map sedimentary structures as, for example, different types of karst features (McMechan et al., 2002). More advanced interpretation strategies incorporate attribute-based workflows. Such workflows rely on attributes that are typically derived from seismic imaging (e.g., McClymont et al., 2008) or from attributes that are specifically developed for GPR applications (Böniger and Tronicke, 2010; Tronicke and Böniger, 2013; Allroggen and Tronicke, 2016) and highlight features and discontinuities that can potentially be missed when following classical layer-based interpretation strategies.

The basic idea of GPR attribute analysis is to highlight specific characteristics or features in the data, thereby easing the interpretation of a GPR data set. From this perspective, an attribute represents a subset of information extracted from the original

data (Chopra and Marfurt, 2005). In the past decades, numerous attributes have been suggested, each highlighting a different type of information in the data. Typically, an attribute highlights a specific property at a specific trace and sample location (e.g., instantaneous frequency) or, in the case of multitrace attributes, the relation of a sample to its surrounding samples (e.g., semblance) in two or more dimensions. Although attributes can aid classical interpretation, selecting relevant attributes can be time-consuming, as a compilation of different attributes (attribute database) often is necessary to image different data characteristics. Furthermore, an attribute is not necessarily tied to a designated stratigraphic unit, and an individual attribute database might be necessary for different geologic settings or depositional environments (Van Heteren et al., 1998). Therefore, interpretation of attributes, and in particular attribute databases, remains a labor-intensive task.

Interpretation of such attribute databases can be simplified by attribute classification approaches. Applications of such approaches are known from GPR data collected in sedimentary (Tronicke and Allroggen, 2015; Koyan et al., 2021) and particularly in carbonate environments (Forte et al., 2012; Bowling et al., 2018). These classification approaches rely on dividing an attribute database into discrete groups (classes) that represent different reflection patterns or geometries (GPR facies). Although interpreting and validating an attribute database still requires manual interaction, an attribute classification provides a first step toward a workflow to interpret attribute databases in a repeatable and objective manner. In the following, we apply an attribute classification approach to a 3D GPR data set acquired across a single paleokarst breccia pipe located in the Billefjorden area on Spitsbergen, Svalbard. After processing the 3D GPR data, including topographic compensation, we interpret the data following a classical horizon-based strategy and compare this interpretation with the results of an attribute-based classification. Although GPR attribute classifications have already been used in a few GPR case studies (Forte et al., 2012; Tronicke and Allroggen, 2015; Bowling et al., 2018; Koyan et al., 2021), their application on 3D GPR data to date has been limited and requires further examples and applications.

Methods

Geologic site description

The study site is located on the mesa-like Wordiekammen plateau in the Billefjorden Basin on Spitsbergen (Figure D.1). The Billefjorden Basin, with its well-exposed strata, breccias, and half-graben structure, is considered a textbook example for basin development (Braathen et al., 2011; Smyrak-Sikora et al., 2019, 2021). Furthermore, it is considered an analog for the Paleozoic and Mesozoic strata on the Barents Sea shelf hydrocarbon province in part because breccias also have been found there (e.g., Sayago et al., 2012; Ahlborn et al., 2014; Matapour et al., 2019); because of their crosscutting nature, they can affect fluid-flow characteristics on a meter- to hundred-meter scale (Simpson, 1988). Outcrops along the cliffs of the steep mountains along the basin expose late-Carboniferous

strata that are punctuated by numerous breccia pipes (Dallmann, 1999; Eliassen and Talbot, 2005; Braathen et al., 2011; Smyrak-Sikora et al., 2019). The 3D GPR data presented in this study cover one of the breccia pipes, as well as its surrounding wall rock of the Wordiekammen plateau.

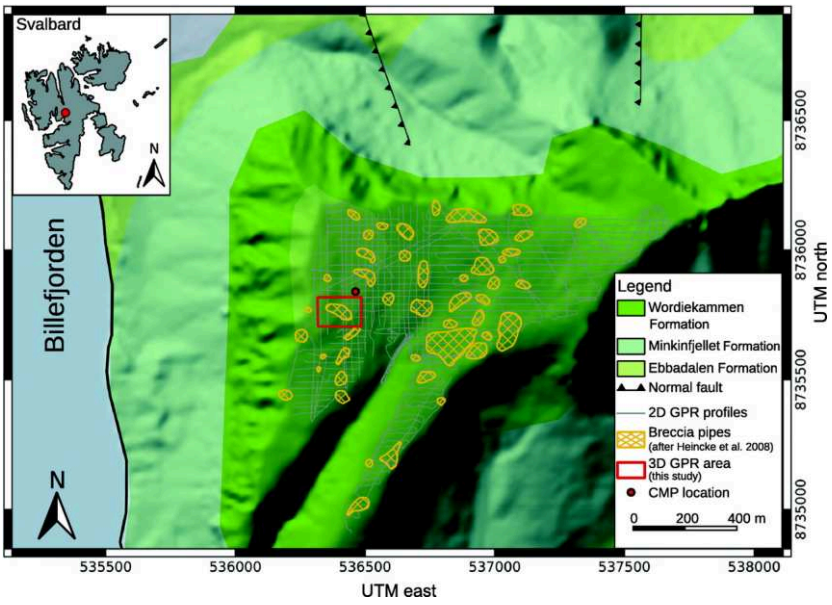

Figure D.1.: Geologic map (Norwegian Polar Institute, 2014) of the field site located on the Wordiekammen plateau on Spitsbergen, Svalbard. It includes the location of the GPR survey presented in this study and the 2D GPR lines used to derive an overview of the distribution of breccia pipes, as shown by Heincke et al. (2008) and Wheeler et al. (2011).

The Wordiekammen plateau lies at a height of approximately 470 m.a.s.l near the stratigraphic top of the late-Carboniferous to early Permian Wordiekammen Formation limestone. The overlying eroded strata would be the Permian-aged gipsiferous Gipshuken Formation. The Wordiekammen Formation is composed nearly entirely of the Black Crag Beds (BCB) member, composed of alternating thick (5–20 m) layers of micrite and wackestone-packstone, dipping approximately 15° west-southwest. They form a series of cliffs approximately 170 m high. The base of the BCB and Wordiekammen Formation is marked by a 20 m thick micrite layer and the beginning of a talus slope. This slope is formed by the underlying late-Carboniferous Minkinfjellet Formation, which consists of alternating layers of dolostone and gypsum (Dallmann, 1999; Eliassen and Talbot, 2005). Two blind west-dipping normal faults cut the plateau, forming west-vergent monoclines in the BCB, each with stratal thickening on the downthrown side (see Figure D.1; Braathen et al., 2011; Smyrak-Sikora et al., 2019, 2021).

The cliff-forming BCB strata are cut in numerous places by subvertical pipe-like bodies of limestone breccia, 30–60 m in exposed width, some of which are clearly continuous for more than 50 m in height (Eliassen and Talbot, 2005). The BCB layers adjacent to the

pipes are in places displaced by small-offset (>3 m) normal faults. No clear paleocave passages have been recognized in the BCB, although breccias at the base of the lowest BCB layer have cavern-roof characteristics (e.g., Loucks, 1999, 2007). Holocene-aged taphoni caverns exist in the lower BCB sections. The lithology of the breccias is similar to the BCB, although one pipe outcropping at the north side of the plateau exhibits 0.3–0.6 m diameter subangular clasts similar to the Gipshuken Formation. In the lower half of the BCB, the breccia-pipe clasts range in size from a millimeter to several meters and in shape from tabular to rounded. In the few exposures at the upper levels of the BCB, large clasts (>0.6 m) are rare. The breccia pipes are interpreted to have resulted from karstification in the Minkinfjellet Formation, recognized widely in the basin by Eliassen and Talbot (2005), and studied using GPR at the southwestern base of Wordiekammen plateau by Janocha et al. (2021). That is, dissolution in the Minkinfjellet Formation formed caverns; the collapse of the cavern roofs continued upward into and through the BCB as the collapse breccia dissolved and was transported away.

On top of the Wordiekammen plateau, the BCB and the breccias are covered by an approximately 1 m thick layer of regolith, consisting of 0.01–0.1 m sized clasts of carbonate. Although the area is almost free of vegetation, such a debris layer effectively prevents mapping the breccia pipes by conventional geologic field surveying from the surface. Cliff side outcrops, and exposures in gullies crossing the plateau, expose micritic layers 2–4 m in thickness with greater porous-limestone thicknesses (>6 m, Figure D.2a).

The BCB micrite layers (carbonate mudstones) have extremely low porosity (<1%), whereas the wackestone and packstone layers are porous (approximately 5%). These layers and bodies differ in physical parameters, such as electrical conductivity and permittivity creating reflections shown in the GPR data (see subsequent sections). The breccias in the pipes have a similar lithology but a much greater porosity, which (including the poor sorting) creates GPR reflections distinct from the BCB. Therefore, breccia pipes are detectable by GPR. For example, Heincke et al. (2008) and Wheeler et al. (2011) describe a 2D GPR survey covering most of the plateau (approximately 25 m line spacing) and a similar, though not as extensive, grid of electrical resistivity tomography (ERT) profiles. By the means of reflection characteristics in these 2D GPR data and their correspondence to outcropping examples (Figure D.2), the authors identified the breccia pipes (shown in Figure D.1), including the site for the 3D GPR field study described herein. In total, 47 distinct pipe-like breccia bodies were interpreted from the 2D GPR data. The shapes were better constrained for large pipes than small pipes. Pipe area ranged from 160 m² to 16,000 m² with most pipes in the range of 1000–4000 m² (major diameter 50–100 m and aspect ratios 1.0–3.0). Half of the pipes were relatively round (aspect ratios 1.0–1.3). Pipes, on average, tended to be 43 m apart measured between walls and 109 m apart measured between centers. The distribution of pipe azimuths and clustering can be deduced from the map (Figure D.1).

For the field study described herein, the objective is to investigate the detailed geometry and internal characteristics of a single large breccia pipe near the western edge of the plateau (Figures D.1 and D.2). Therefore, we selected a breccia pipe using the interpreted 2D GPR profiles collected in the winters of 2007 and 2008 (Heincke et al., 2008; Wheeler

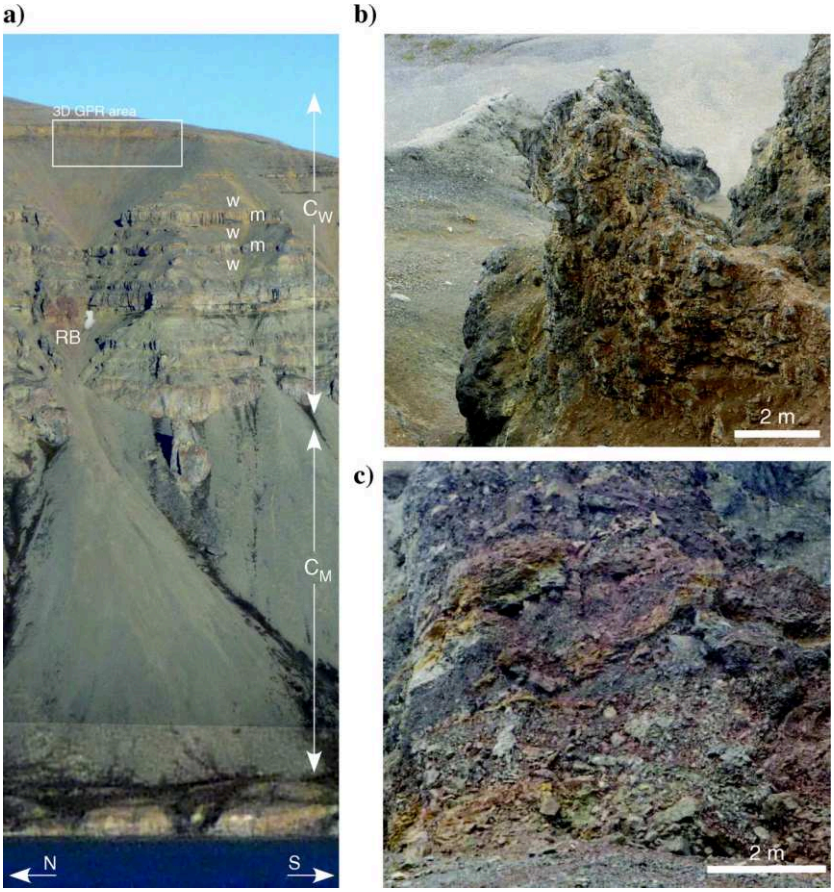

Figure D.2.: (a) Photo of the outcrops at the west face of the Wordiekammen plateau with the location 3D GPR survey with a size of approximately 80 m × 30 m and 60 m behind the cliff (CW, Wordiekammen Formation; CM, Minkinfjellet Formation; w, wackestonepackstone layers; m, micritic layers; and RB, red breccia). (b) Photo looking down from clifftop at the eroded top of a pipe breccia with clast sizes up to the meter scale. (c) "Red breccia" at RB in (a) revealing coarse local stratification within an otherwise chaotic deposit.

et al., 2011). This pipe, based on the 2D lines, was determined to have an area of 3650 m^2, a major axis of 108 m to 153°, and an aspect ratio 2.4. We determined that an approximately 180 m × 80 m area would cover the indications of breccia on the 2D profiles, plus a significant amount of wall rock. The coordinates of the southwest corner of the survey area are 8,735,715 m N, 536,310 m E (UTM 33N, WGS84) with an ellipsoidal elevation of 473 m.

3D GPR data acquisition and processing

Collecting the 3D GPR data followed parallel lines oriented east–west. As with previous GPR surveys (Heincke et al., 2008), we used a PulseEKKO 100 system with unshielded 50MHz antennas. GPR test surveys (not shown here) suggest that these antennas provide a good compromise between penetration depth (up to 40 m) and acceptable vertical resolution (estimated to be 1 m, considering a wavelength λ of 2 m corresponding to a velocity of 0.1 m/ns) and postmigration horizontal resolution corresponding to $\lambda/2 \approx 1$ m (Sandring et al., 2017). The receiving and the transmitting antenna were mounted on a cart at a distance of 2 m from each other in a parallel broadside configuration (Figure D.3). A trigger wheel was used to realize a trace spacing of approximately 0.4 m in the inline direction. To avoid spatial aliasing in our 50MHz GPR data set, which is expected to appear at trace spacings $> \lambda/4 \approx 0.5$ m, Lehmann and Green, 1999), we chose a rather dense trace spacing of 0.4 m (see Table D.1). The coordinates of each trace were determined using a differential, postprocessed global navigation satellite system (using the GPS and GLONASS L1–L2 band) with one antenna located on top of a 2 m high mast in the center of the acquisition cart (Figure D.3) and another antenna as a local reference station at approximately 500 m distance at the northwestern edge of the plateau. The output signal from the trigger also served to mark the trace recordings in the global positioning system (GPS) memory (resulting in trace positions with an accuracy of approximately 6 cm). Data collection was hampered by hummocks and permafrost polygons with diameters of 1– 3 m and heights of 0.3–0.4 m across the central part of the study site causing severe variations in microtopography. Therefore, GPR surveying took five full days during summertime (August 2008).

Table D.1.: Table summarizing the 3D GPR acquisition parameters.

Acquisition parameter	Value
Nominal center frequency	50 MHz
Recording window length	1129 ns
Sampling interval	1.59 ns
Crossline trace spacing	~0.40 m
Inline trace spacing	~0.40 m
Survey size	~180 m x 80 m
Antenna offset	2 m

Figure D.3.: A photo showing the GPR antenna cart on a relatively even section of the field site on top of the Wordiekammen plateau (view toward south). We used additional wooden constructions to stabilize the GPR antennas and the differential GPS antenna, given the harsh field conditions.

In Figure D.4, we present a flowchart summarizing the GPR data processing. Our data processing starts with assigning the measured coordinates to each trace and correcting for the mast inclination and length (Lehmann and Green, 1999). We apply a microleveling routine from Mauring and Kihle (2006), originally developed to remove leveling artifacts in airborne magnetic data, on the topography data to reduce discrepancies associated with inaccuracies of the GPS height and move all traces onto the same topographic reference level. After processing the coordinates, we apply a dewow filter and remove spikes from the GPR data using a crosscorrelation criterion. We align the first arrival times using the Akaike information criterion (Zhang et al., 2003). Next, we interpolate the data on a regular grid with a trace spacing of 0.4 m × 0.4 m using a natural neighbor gridding routine (Sambridge et al., 1995). To further reduce incoherent noise, we apply a trapezoidal Ormsby band-pass filter (10–20–100–200 MHz) followed by 2D f-k filtering in the inline and crossline directions.

After performing this standard GPR processing, we apply a topographic 3D Kirchhoff migration scheme (Lehmann and Green, 2000) using a constant velocity of 0.1 m/ns and a constant aperture radius of 35 m. This velocity estimate originates from a reflection-based velocity spectrum, as shown in Figure D.5a (using semblance as a coherence measure) that is calculated from a common-midpoint (CMP) survey (Figure D.5b) collected close to the 3D survey site in a nonbrecciated area of the Wordiekammen plateau (see Figure D.1). This CMP survey reveals reflected energy at traveltimes <600 ns, with two strong reflection events at traveltimes of approximately 200 ns and 520 ns. Both events align in the velocity spectrum with a constant stacking velocity of approximately 0.1 m/ns. Such a constant velocity is in agreement with hardrock conditions ignoring the approximately

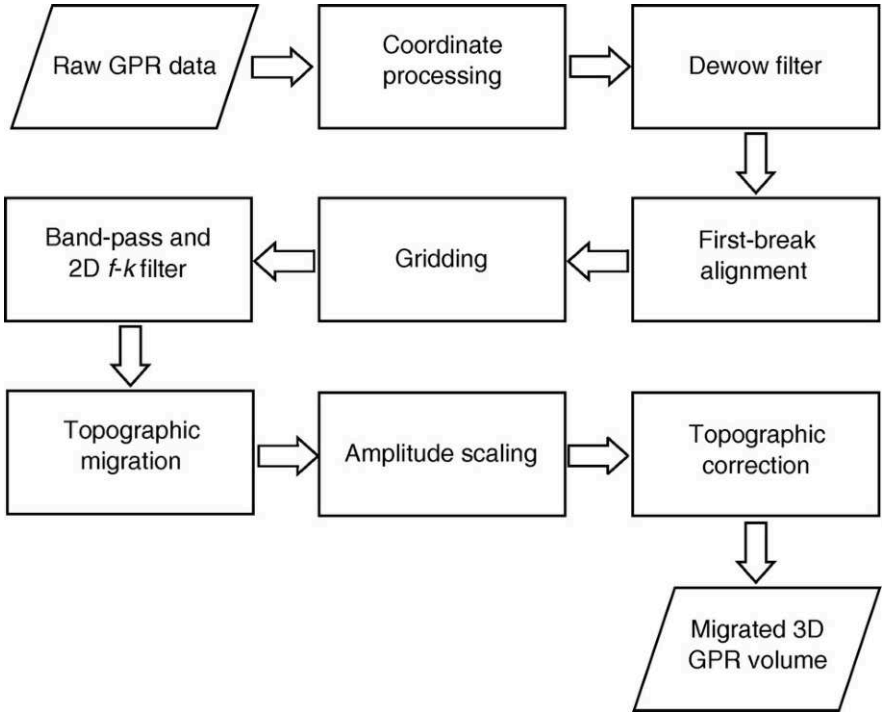

Figure D.4.: Flowchart showing the processing of our 3D GPR data, including full topographic compensation.

0.5–1.0 m deep active layer with lower surface velocities and potential velocity variations associated with different conditions inside the breccia pipe.

After migrating the data, we apply a tracewise amplitude gain using a low-pass-filtered version of the inverse amplitude envelope (Gross et al., 2003) and shift all traces to a constant topographic reference level (topographic correction) using the same subsurface velocity (0.1 m/ns) as for the migration. We regard this processing flow (including full compensation of surface topographic variations) to be essential to place reflections in the 3D data cube as close as possible to the real positions of the related structures in the subsurface and, consequently, to obtain reliable attributes. The resulting data pose a densely sampled and high-resolution 3D GPR volume imaging the breccia pipe in its central area and revealing the regular westward dipping strata outside the breccia pipe down to a traveltime of 600 ns (approximately 30 m).

To summarize our data processing results and emphasize the importance of migrating the data, we present an exemplary inline profile (33.2 m crossline distance) after standard processing (Figure D.6a) and after applying topographic migration and correction (Figure D.6b). After applying the standard processing, we observe a series of continuous reflectors that are interrupted by chaotic reflection patterns. After migration, these patterns collapse to reveal a narrower fault zone (highlighted in green) and a broader zone with chaotic reflections and point scatterers in the central area (highlighted in blue). Due to limitations of our constant velocity assumption, some diffraction hyperbolas seem not to collapse

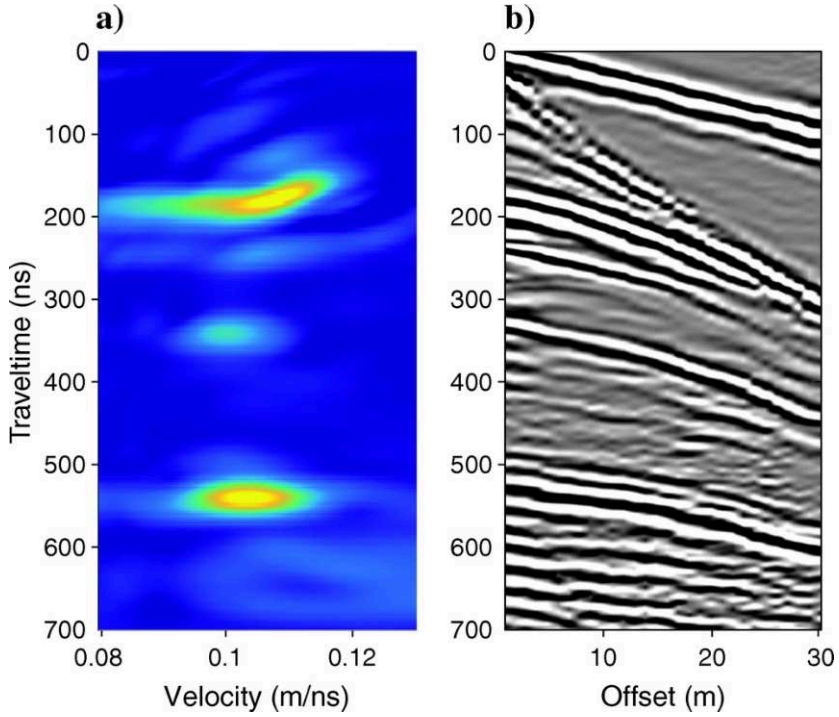

Figure D.5.: (a) Reflection velocity semblance spectrum indicating a constant subsurface velocity of 0.1 m/ns (the blue colors indicate low and the yellow colors high semblance values) derived from (b), a CMP gather collected next to the investigated breccia pipe (see Figure D.1).

completely during the migration causing artifacts that affect the classical interpretation and the attribute classification.

Results

Classical data interpretation

Interpretation of GPR data often relies on the manual identification of targets and tracking selected horizons. The migrated GPR data (Figures D.6b and D.7) reveal several piece-wise continuous reflectors surrounding the central brecciated area. We track the maximum peak amplitude of these reflections using a standard 3D semiautomatic picking routine relying on manually placed seed points (implemented in the OpendTect software package). This picking routine provides reliable estimates for continuous horizons, but it requires manual interactions in the presence of small-offset faults, in which samples of neighboring traces have low correlation values or significant amplitude differences. Therefore, the use of such a classical data interpretation is labor-intensive due to setting appropriate seed points for each horizon and between each fault segment, especially when determining phase offsets across small-offset faults. In approximately one week of

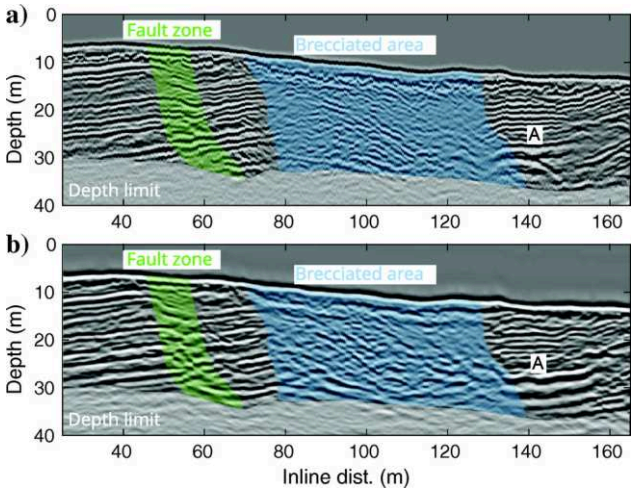

Figure D.6.: (a) Inline profile extracted from the 3D GPR volume at 33.2 m crossline distance after (a) applying a standard processing (and additional topographic correction) and (b) the same profile after applying topographic migration and correction using a constant velocity of 0.1 m/ns superimposed by a manual GPR interpretation (green and blue colors). Position A highlights the apex of a diffraction hyperbola that collapsed during the migration process indicating the successful application of the migration.

working time, we picked 10 distinct horizons within the undisturbed sedimentary strata. These horizons surround the central chaotic reflection patterns of the breccia pipe and indirectly outline its extent and shape in the 3D GPR volume. In Figure D.7, we present a 3D view with the picked horizons superimposed on an inline and crossline profile of the 3D GPR volume intersecting with the chaotic reflection and diffraction patterns in the central brecciated area. The shape of the breccia pipe can be estimated from the central gap in the horizons caused by heavily fragmented and brecciated rocks. Further classical interpretation could include the picking and mapping of all fragmented reflections and faults in the data volume and interpret them in terms of GPR facies. However, for these 3D GPR data, such a procedure is a labor-intensive task and, given the spatial resolution and extent, becomes impractical for this data set. Furthermore, such an interpretation depends on the individual geologic and geophysical expertise of the interpreter. Therefore, we develop and apply an attribute- based classification approach for this study.

Attribute calculation and classification

To provide a repeatable and more objective interpretation approach, we develop and apply an attribute-based GPR facies classification. To perform such an attribute-based interpretation, we calculate an attribute database focusing on multitrace attributes with calculations based on more than one GPR trace and highlight the relations of a sample at one trace to its surrounding samples. From a broad selection of multitrace attributes, we manually select only those with a normalized correlation coefficient smaller than 0.8

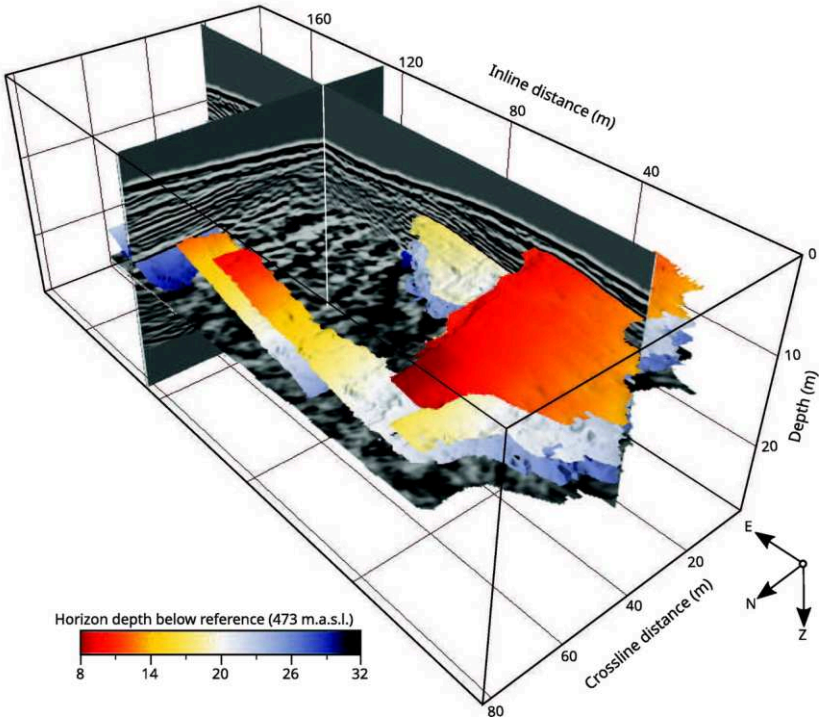

Figure D.7.: View to the southeast showing the picked horizons together with an inline profile (at 22 m crossline distance) and a crossline profile (at 130 m inline distance) extracted from the 3D GPR volume. The lack of continuous horizons in the central area indirectly outlines the breccia pipe that is characterized by chaotic reflection and diffraction patterns. For calculating the depth conversion, we use a constant velocity of 0.1 m/ns.

with all other selected attributes. Therefore, we limit the number of attributes, reduce redundant information, and simplify the classification process (Zhao et al., 2016).

Our attribute database contains dip attributes, directional semblance, and a set of gray-level co-occurrence matrix (GLCM) attributes that highlight textural features (e.g., roughness) of the data (Haralick et al., 1973; Eichkitz et al., 2013). In Table D.2, we provide an overview on our attribute database and summarize their potential interpretation. All attributes are calculated within the OpendTect Software package. In Figure D.8, we present a time slice at a traveltime of 380 ns and the corresponding attributes (Figure D.8b–D.8h) that will be described in more detail in the following. In this field example, the presence of surface topography, slightly dipping strata, and dislocated (i.e., translated or rotated) blocks within the breccia affects multitrace attributes. Therefore, it is essential for this geologic setting to include attributes with directional information to obtain meaningful attributes and classification results. To do so, we calculate a dip volume from the data by applying an fast Fourier transform (FFT) algorithm (Tingdahl and De Groot, 2003) onto volumes of 1.2 m × 1.2 m × 6 ns and smooth the resulting dips using a step out of four horizontal and six vertical

Table D.2.: Overview and interpretation of the seven attributes forming our attribute database that we use in the classification approach.

Attribute	Description and interpretation
Dip azimuth	• Direction of dip • Distinguishes stratified regions (westward dipping) from brecciated areas (more heterogeneous values)
Curvature gradient	• Variation rate of local curvature • Large absolute values indicate large variations of the local dip angle (e.g., in brecciated areas)
Directional semblance	• Measure of weighted similarity between neighboring traces • Low values indicate significant trace-to-trace variations found in brecciated areas, medium values can be explained with faulted regions, and high values correspond to parallel stratified regions
GLCM energy	• Measure of homogeneity in the GLCM • Distinguishes regions of equally distributed amplitudes showing high-energy values from regions with more chaotic amplitude distributions
GLCM entropy	• Measure of entropy/randomness in the GLCM • The inverse of GLCM entropy has a meaning similar to GLCM energy but different weightings, such that small-scale amplitude variations are more precisely distinguishable (compare Figure B.8e and B.8f)
GLCM entropy gradient	• Measure of GLCM entropy change • Distinguishes regions of constant GLCM levels (high values) from small-scale amplitude variations, as found in brecciated regions
GLCM standard derivation (stdw)	• Measure of variability in the GLCM • High values correspond to variable GLCM values, such that chaotic amplitude variations are similarly imaged to GLCM entropy but differently weighted

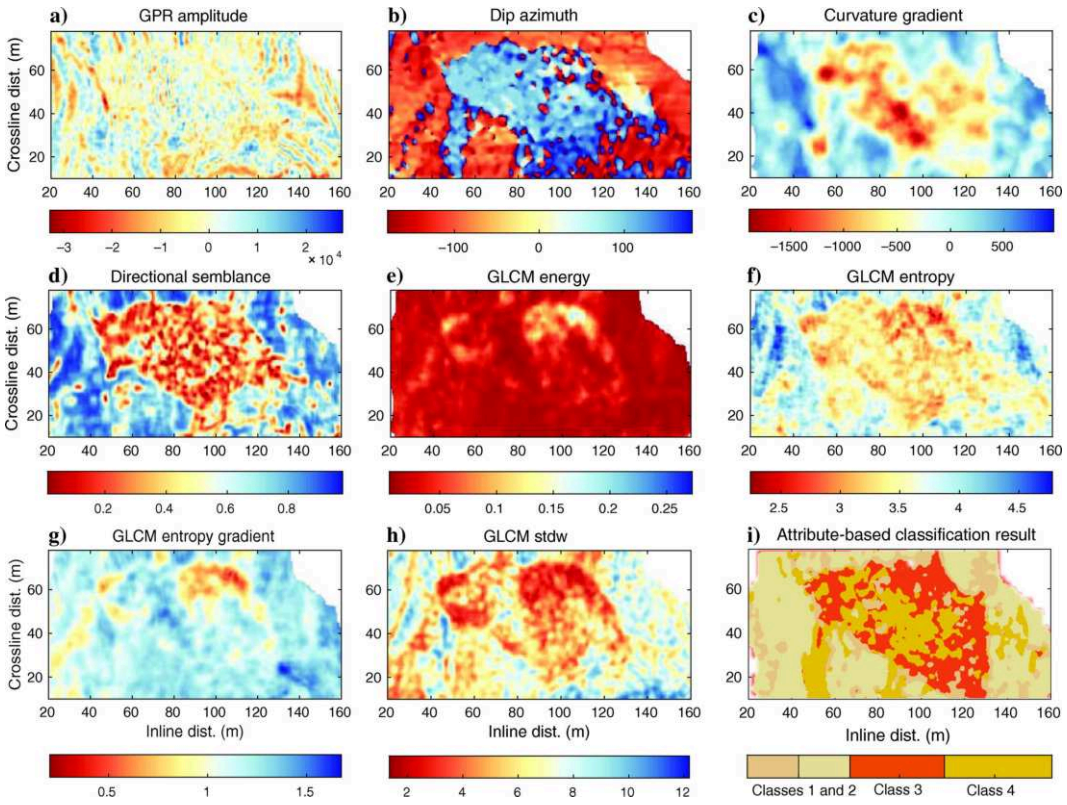

Figure D.8.: Example time slice extracted at 380 ns (approximately 19 m) showing (a) the migrated GPR data and (b–h) the attributes in our attribute database. (i) The resulting attribute-based classification result along the corresponding time slice.

samples (corresponding to 1.6 m in the horizontal and approximately 0.5 m in the vertical direction). This dip volume contains information about the dominant local dip in the GPR data. In undisturbed areas, it indicates the dip of the strata, whereas in faulted and brecciated areas, the dip direction points in multiple directions. For our attribute database, we extract the azimuth (no additional smoothing) and the curvature gradient (second derivative) after applying additional horizontal smoothing more than 8 m from this dip volume and add them to our attribute database (Figure D.8 and D.8c). Furthermore, we use the dip volume to calculate directional multitrace attributes that compensate for the general dip of the strata. In contrast to nondirectional attributes that are calculated within symmetric sliding windows, directional attributes are calculated in local windows that are warped using the local dip volume (Roberts, 2001; Tingdahl and De Groot, 2003). Therefore, the shape of the local windows follows the local dip of the strata, such that these attributes highlight data properties that are mostly independent of local dip variations. In our attribute database, we include the directional semblance (with 6 ns time window, Figure D.8d) and a set of four directional GLCM attributes. These attributes (Figure D.8e–D.8h) are calculated from the GLCM, which contains information on the distribution of co-occurring samples in a selected window. Our GLCM

attributes are calculated from a GLCM with 32 gray levels in local windows of 6 ns and seven traces in the inline and crossline direction, followed by a horizontal smoothing using a running average with a window size of 2 m in the inline and crossline direction. Although such textural attributes have no direct physical meaning, they are shown to be useful to classify seismic and GPR data (Eichkitz et al., 2013; Tronicke and Allroggen, 2015; Zhao et al., 2016; Koyan et al., 2021). In Table D.2, we provide an overview and detailed description of the seven attributes forming our attribute database that we use for further interpretation.

Ideally, such an attribute database comprises independent representations of properties of the processed GPR data. To investigate the correlation of the individual attributes, we present histograms of all seven attributes and the corresponding crossplots (Figure D.9). In contrast to previous studies (Tronicke and Allroggen, 2015; Koyan et al., 2021), we observe rather complex distributions for the different attributes. Most attributes show a bimodal or even multimodal distribution indicating a clear segmentation of the attributes in two (e.g., semblance and GLCM standard deviation) or more classes (e.g., dip azimuth and GLCM entropy gradient). Such complicated distributions suggest largely different characteristics for reflection and diffraction patterns across the data volume. For example, the histogram of the semblance attribute (on the top left shown in Figure D.9) has two maxima. One maximum at relatively low semblance values indicates the brecciated area, and the other one at high semblance values indicates high semblance values in the regular sedimentary strata (Figure D.8d). Other attributes, such as the dip azimuth, GLCM standard deviation, and GLCM entropy, reveal similar complex distributions but slightly different spatial patterns (Figure D.8). Therefore, they are considered to highlight different details in the data. For this data set, it seems that the bimodal distributions mainly represent the undisturbed sedimentary strata on the one hand and the disturbed strata within the breccia pipe on the other hand. From analyzing the attribute crossplots and correlation coefficients, we obtain an overview on the relation of the attributes within our attribute database and can identify attributes carrying uncorrelated information that can be used in the classification. Many of the crossplots show two maxima and thus confirm that there are predominately two types of data characteristics associated with undisturbed strata and brecciated rocks. However, the crossplots of the dip azimuth and curvature gradient (Figure D.9) show a spike in their distribution, which is likely caused by near-zero dip values in the chaotic area of the breccia pipe, making the calculation of these attributes inaccurate in these regions.

To integrate these characteristics of our attribute database, we apply a k-means classification algorithm (de Rooij and Tingdahl, 2002; Coléou et al., 2003). The k-means algorithm distributes multiparameter data into classes (clusters) of similar values. As input for the classification, attribute samples are arranged in vectors. Each vector corresponds to a sample in the GPR data set containing all attribute values at that sample location. In an iterative process, the distances of a given number of random initial class centers and their nearby attribute vectors are minimized by updating the locations of the class centers. Within this process, each attribute vector is assigned to the class for which the distance to its class center is the smallest. To speed up the classification, we

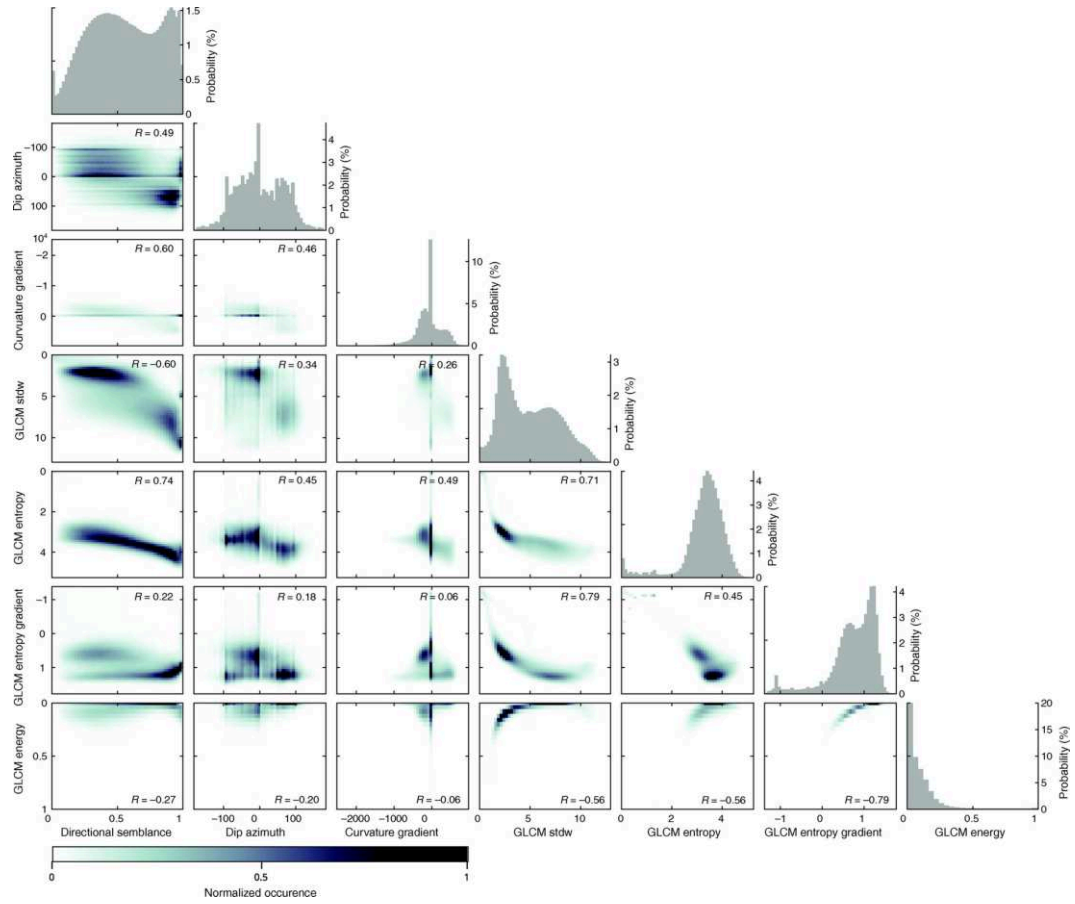

Figure D.9.: Histograms and crossplots of each attribute in our attribute database. The normalized correlation coefficient (R) between the attributes is shown on the right side of the corresponding crossplot.

select 20,000 (approximately 10% of all data samples) randomly distributed locations within the 3D GPR data and use the corresponding attribute vectors at these locations to find four class centers from the attribute distribution. We found that using less than four class centers is insufficient to explain the variability in the data (high final distance values). In contrast, more classes are not required to explain the specific geologic features and do not reduce the final distance values significantly. After identifying the appropriate class centers, we classify the full data set by calculating the distance of each center to each attribute vector and assign the closest class for each vector. The result of this classification algorithm is a 3D volume with each sample being assigned to one class. From the classification result (Figure D.8i), we observe that the breccia and the regular strata are generally separated into different classes. However, nonunique reflection patterns (e.g., originating from processing artifacts) create a rather complex classification result that requires further manual interpretation to derive a 3D GPR facies model.

Discussion and interpretation

We interpret the classification result in terms of the 3D GPR facies model shown in Figure D.10. Our GPR facies interpretation is in close agreement with the GPR facies derived from GPR data collected across breccias within the Minkinfjellet Formation at the base of the Wordiekammen plateau (Janocha et al., 2021). Based on our classification result, we interpret three distinct GPR facies.

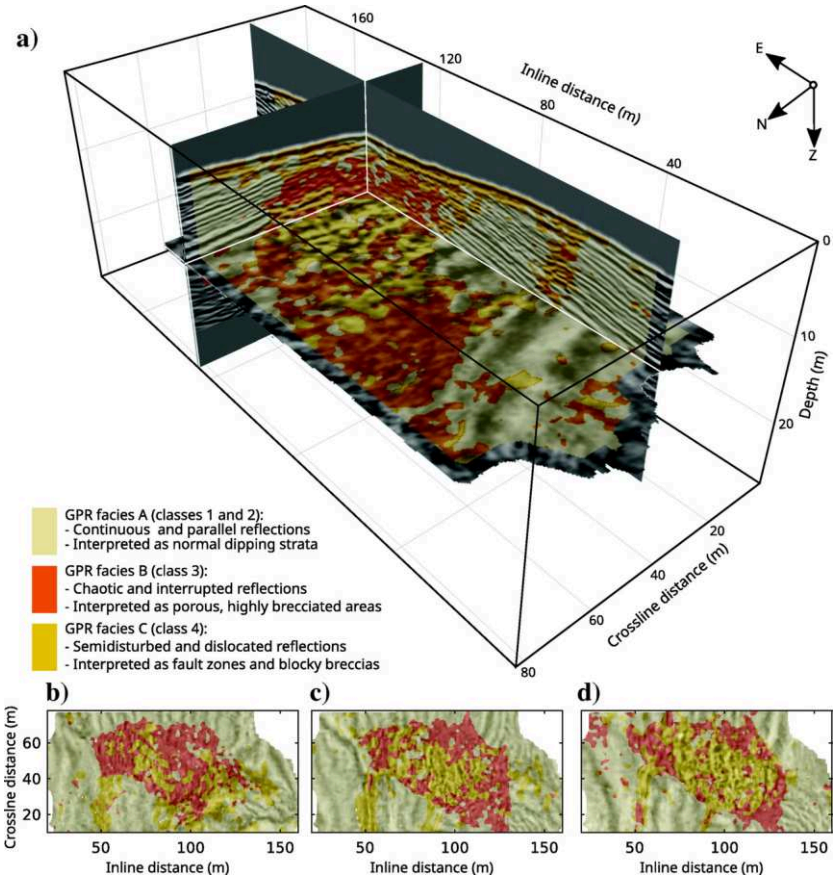

Figure D.10.: (a) View to the southeast (same as in Figure D.7) on a visualization of the 3D GPR facies model facies model superimposed on an inline profile (at 22 m crossline distance), a crossline profile (at 130 m inline distance), and a depth slice (at 14 m). To visualize the complexity of our 3D facies model, we show additional depth slices at (b) 15 m depth, (c) 19 m depth, and (d) 23 m depth.

(A) GPR facies A: Comprising classes 1 and 2. This GPR facies is characterized by continuous and parallel reflections that are slightly dipping, mainly in the direction of the undisturbed strata of the Wordiekammen Formation. The frequency and amplitude of the patterns in this GPR facies vary with depth. This GPR facies is similar to GPR facies A in Janocha et al. (2021).

(B) GPR facies B: Comprising class 3. This GPR facies is characterized by chaotic reflection patterns that are inconsistent over short distances (partly below the GPR resolution) and have low amplitudes, including numerous poorly collapsed diffraction hyperbolas. This GPR facies is similar to GPR facies B in Janocha et al. (2021).

(C) GPR facies C: Comprising class 4. This GPR facies is characterized by reflection patterns that are semidisturbed and associated with, for example, dislocated blocks and fragments (translated and rotated), thus having a similar architecture but different amplitude, dip azimuth, and angle relative to the adjacent strata. This GPR facies has not been described by Janocha et al. (2021).

GPR facies A surrounds the other GPR facies in large parts of our data set and represents 54% of the data volume. This GPR facies is characterized by continuous, mainly gentle southwest-dipping, parallel reflections that are at some locations offset by small faults. In position and geometry, it matches the outcropping limestone strata exposed in the cliffside approximately 60 m west of the study area (BCB member of the Wordiekammen Formation at this stratigraphic level). Hence, we infer GPR facies A to represent the typical GPR reflection patterns originating from the undisturbed BCB.

GPR facies B is mainly located in the central part of the survey and occupies 16% of the 3D GPR volume. This GPR facies is characterized by occasional local reflections that are horizontally consistent over only a few meters and in cases stacked vertically over several meters. They intersperse with chaotic zones with no obvious reflections, and it is likely that it contains material with clast sizes below the resolution limit of our GPR survey. Nearby cliffside breccia-pipe exposures (Figure D.2) are characterized by a large range of grain sizes (millimeters to several meters), occasional layering and large blocks, and areas where fragments with various clast sizes are chaotically distributed. The patterns of this facies (Figure D.7) are similar to the ones observed in the 2D GPR profiles across features that are identified as breccia pipes by Heincke et al. (2008) and Wheeler et al. (2011). Hence, we infer GPR facies B to represent the typical GPR characteristics of collapse breccias on the Wordiekammen plateau.

GPR facies C occurs locally in the central area (GPR facies B) and in the surrounding area (GPR facies A). It represents the remaining 30% of the data volume. In the central area, it presents local reflections that are horizontally consistent (Figure D.10b–D.10d) as narrow zones patchy to continuous for 20–40 m and in lumpy contact with GPR facies B. We note that the trends of facies C are partly subparallel to the strike of the layering, as shown in the crossline profile in Figure D.10a. Furthermore, GPR facies C is associated with small-offset, steeply dipping, north–south-striking faults (e.g., at an inline distance of approximately 52 m shown in Figure D.6 and on the inline profile shown in Figure D.10a). Facies C also is found locally in the uppermost several meters and, thus, in the regolith and permafrost active layer. We interpret this GPR facies to represent larger, translated, and rotated features that are related to local small-offset faults or, when located within GPR facies B (brecciated area), massive blocks of the size of several meters (Figure D.2b) or sorted materials within the breccia pipe (Figure D.2c). Facies C also could arise from

dissolution or diagenetic processes related to water ingress along the faults that cut the breccia bodies. These areas in facies C are intuitively identified based on shape and location when performing a geologic interpretation of the classification result, and they require further analysis, including reference data and verification of our classification result by local borehole data or complementary geophysical and petrophysical information (e.g., porosity and grain-size measurements). However, with the current classification approach, we are not able to further distinguish small-offset fault zones from features associated with larger fragments because they belong to the same class and therefore originate from similar patterns in our attribute database. Although facies C seems not entirely consisting of brecciated material, its larger volume compared with facies B (ratio: 1:2) supports outcrop observations of a coarse breccia material at the altitude level of our survey (Eliassen and Talbot, 2005). However, a detailed analysis of a coarsening upward trend needs more information because our GPR data do not provide enough penetration depth and thus require analyzing data from different stratigraphic levels.

In summary, we identify a breccia pipe and image its complex 3D shape and internal variation within a depth of 25 m below the ground surface (see Figure D.10). Our results generally agree with the estimated pipe size and area of the 2D GPR data, although we resolve much more detail regarding the shape and internal variations of the breccia pipe (compare Figures D.1 and D.10b–D.10d). The direction of the north–south-striking faults that cut through the breccia pipe generally agrees with the dominant fault direction in this area. Such detailed observations are generally not possible with other geophysical and geologic methods because they do not provide the same resolution (seismic and ERT) or, even given the excellent outcrops situation at the Wordiekammen plateau, can only provide an incomplete image limited to analyzing exposed features.

Conclusion

We present a 3D GPR data set collected across a paleokarst breccia pipe within the Billefjorden area on Spitsbergen. After applying a standard processing workflow followed by a topographic migration and correction, we perform classical horizon picking and compare this interpretation to the results of an attribute classification approach. Results of the classical interpretation propose several distinct horizons that are associated with the slightly dipping strata of the carbonate rocks. These horizons surround chaotic reflections and diffraction patterns, thus indirectly imaging the shape of the central breccia pipe. By performing an attribute calculation and subsequent classification, we identify three distinct GPR facies, revealing details on the shape of the brecciated area and its inner architecture.

Comparing this classification result with the classical interpretation reveals that both methods are able to determine the outer margin of the brecciated area. However, in a classical interpretation, the boundaries of the brecciated areas can only be inferred from the extent of the picked horizons. This procedure requires a highly labor-intensive picking procedure depending on the geologic expertise of the interpreter. Contrarily, after performing an attribute classification, the boundary of the breccia pipe is (with

some exceptions) directly assigned by the class boundaries. Furthermore, by performing the attribute classification, we are able to distinguish internal details of the breccia pipe. As such, we observe 16% of the data volume to belong to fine-grained breccias (facies B) and 30%of the data volume to belong to coarser collapse breccias and faulted areas (facies C). Thus, we estimate the ratio of fine material (below the resolution of the GPR method) and coarse collapse material to be 1:2. Such observations might be relevant for understanding the collapse processes and for determining the pipe's hydrologic and mechanical properties. However, we emphasize that it was not possible to discriminate certain intrapipe GPR features from those associated with small-offset faults outside the pipes because both show similar characteristics in our GPR attributes, such that they are not distinguished by different classes in the classification. A more detailed analysis, for example, by verification of the attribute classification, requires independent ground-truth information originating from boreholes, geologic, or complementary geophysical methods (e.g., ERT or seismic measurements).

Nevertheless, we demonstrate the successful application of an attribute classification to image a breccia pipe using 3D GPR data. In contrast to a manual interpretation, our approach provides repeatable results that require a limited number of manual decisions (e.g., choosing the number of classes and assigning the classes to geologic features), thus aiding the interpretation of extensive 3D GPR data. Although our attribute classification approach does not allow for a fully automated data interpretation, it provides the possibility to analyze GPR data from complex geologic settings in a semiautomated manner, revealing details that otherwise require labor- and time-consuming manual interpretation.

Acknowledgments

We thank UNIS for logistical team support for during the measurements. We also thank dGB Earth Sciences for the OpendTect open source software package. Furthermore, we thank Kim Senger and three anonymous reviewers for providing thoughtful and useful suggestions. This work is supported by a Petromaks grant from the Norwegian Research Council, and by StatoilHydro and Det norske Oljeselskapet.

Data and materials availability

Data associated with this research are available and can be obtained by contacting the corresponding author.

References

Ahlborn, M., Stemmerik, L., Kalstø, T.-K., 2014. 3D seismic analysis of karstified interbedded carbonates and evaporites, Lower Permian Gipsdalen Group, Loppa

High, southwestern Barents Sea. Marine and Petroleum Geology, 56, 16–33, doi: 10.1016/j.marpetgeo.2014.02.015.

Allroggen, N., Tronicke, J., 2016. Attribute-based analysis of time-lapse ground-penetrating radar data. Geophysics, 81(1), H1–H8, doi: 10.1190/geo2015-0171.1.

Böniger, U., Tronicke, J., 2010. Improving the interpretability of 3D GPR data using target-specific attributes: Application to tomb detection. Journal of Archaeological Science, 37, 672–679, doi: 10.1016/j.jas.2010.01.013.

Borghi, A., Renard, P., Jenni, S., 2012. A pseudo-genetic stochastic model to generate karstic networks. Journal of Hydrology, 414, 516–529, doi: 10.1016/j.jhydrol.-2011.11.032.

Bowling, R. D., Laya, J. C., Everett, M. E., 2018. Resolving carbonate platform geometries on the island of Bonaire, Caribbean Netherlands through semi-automatic GPR facies classification. Geophysical Journal International, 214, 687–703, doi: 10.1093/gji/ggy175.

Braathen, A., Bælum, K., Maher, H., Buckley, S. J., 2011. Growth of extensional faults and folds during deposition of an evaporite-dominated half-graben basin; the Carboniferous Billefjorden Trough, Svalbard. Norsk Geologisk Tidsskrift, 91, 137–161.

Carrière, S. D., Chalikakis, K., Sénéchal, G., Danquigny, C., Emblanch, C., 2013. Combining electrical resistivity tomography and ground penetrating radar to study geological structuring of karst unsaturated zone. Journal of Applied Geophysics, 94, 31–41, doi: 10.1016/j.jappgeo.2013.03.014.

Chalikakis, K., Plagnes, V., Guerin, R., Valois, R., Bosch, F. P., 2011. Contribution of geophysical methods to karst-system exploration: An overview. Hydrogeology Journal, 19, 1169–1180, doi: 10.1007/s10040-011-0746-x.

Chopra, S., Marfurt, K. J., 2005. Seismic attributes — A historical perspective. Geophysics, 70(5), 3SO–28SO, doi: 10.1190/1.2098670.

Coléou, T., Poupon, M., Azbel, K., 2003. Unsupervised seismic facies classification: A review and comparison of techniques and implementation. The Leading Edge, 22, 942–953, doi: 10.1190/1.1623635.

Dallmann, W. K., 1999, Lithostratigraphic lexicon of Svalbard: Review and recommendations for nomenclature use: Upper Palaeozoic to Quaternary bedrock. Norsk Polarinstitutt.

de Rooij, M., Tingdahl, K., 2002. Meta-attributes — The key to multivolume, multiattribute interpretation. The Leading Edge, 21, 1050–1053, doi: 10.1190/1.1518445.

Eichkitz, C. G., Amtmann, J., Schreilechner, M. G., 2013. Calculation of grey level co-occurrence matrix-based seismic attributes in three dimensions. Computers & Geosciences, 60, 176–183, doi: 10.1016/j.cageo.2013.07.006.

Eliassen, A., Talbot, M. R., 2005. Solution-collapse breccias of the Minkinfjellet and Wordiekammen Formations, Central Spitsbergen, Svalbard: A large gypsum palaeokarst system. Sedimentology, 52, 775–794, doi: 10.1111/j.1365-3091.2005.00731.x.

Ford, D., Williams, P., 2007. Karst hydrogeology and geomorphology. John Wiley & Sons.

Forte, E., Pipan, M., Casabianca, D., Di Cuia, R., Riva, A., 2012. Imaging and characterization of a carbonate hydrocarbon reservoir analogue using GPR attributes. Journal of Applied Geophysics, 81, 76–87, doi: 10.1016/j.jappgeo.2011.09.009.

Goldscheider, N., Mádl-Szőnyi, J., Erőss, A., Schill, E., 2010. Review: Thermal water resources in carbonate rock aquifers. Hydrogeology Journal, 18, 1303–1318, doi: 10.1007/s10040-010-0611-3.

Gross, R., Green, A., Horstmeyer, H., Holliger, K., Baldwin, J., 2003. 3-D georadar images of an active fault: Efficient data acquisition, processing and interpretation strategies. Subsurface Sensing Technologies and Applications, 4, 19–40, doi: 10.1023/A:1023059329899.

Haralick, R. M., Shanmugam, K., Dinstein, I., 1973. Textural features for image classification. IEEE Transactions on Systems, Man, and Cybernetics, SMC-3, 610–621, doi: 10.1109/TSMC.1973.4309314.

Heincke, B. H., Rønning, J. S., Dalsegg, E., Bælum, K., Wheeler, W., Nordeide, H. C., 2008. Using 2-D and 3-D georadar to characterize karst collapse as a basis for high-resolution reservoir-analogue models, in: Proceedings of the 12th International Conference on Ground Penetrating Radar.

Janocha, J., Smyrak-Sikora, A., Senger, K., Birchall, T., 2021. Seeing beyond the outcrop: Integration of ground-penetrating radar with digital outcrop models of a paleokarst system. Marine and Petroleum Geology, 125, 104833, doi: 10.1016/j.marpetgeo.2020.104833.

Koyan, P., Tronicke, J., Allroggen, N., 2021. 3D ground-penetrating radar attributes to generate classified facies models: A case study from a dune island. Geophysics, 86(6), B335–B347, doi: 10.1190/geo2021-0204.1.

Kruse, S., Grasmueck, M., Weiss, M., D. Viggiano, D., 2006. Sinkhole structure imaging in covered karst terrain. Geophysical Research Letters, 33, L16405, doi: 10.1029/2006GL026975.

Lehmann, F., Green, A. G., 1999. Semiautomated georadar data acquisition in three dimensions. Geophysics, 64, 719–731, doi: 10.1190/1.1444581.

Lehmann, F., Green, A. G., 2000. Topographic migration of georadar data: Implications for acquisition and processing. Geophysics, 65, 836–848, doi: 10.1190/1.1444781.

Lonoy, B., Pennos, C., Tveranger, J., Fikos, I., Vargemezis, G., Lauritzen, S.-E., 2021. Delimiting morphological and volumetric elements of cave surveys as analogues for paleokarst reservoir modelling — A case study from the Maaras cave system, northern Greece. Marine and Petroleum Geology, 129, 105091, doi: 10.1016/j.marpetgeo.2021.-105091.

Loucks, R. G., 1999. Paleocave carbonate reservoirs: Origins, burial-depth modifications, spatial complexity, and reservoir implications. AAPG Bulletin, 83, 1795–1834, doi: 10.1306/E4FD426F-1732-11D7-8645000102C1865D.

Loucks, R. G., 2007. A review of coalesced, collapsed paleocave systems and associated suprastratal deformation. Acta Carsologica, 36, 121–132, doi: 10.3986/ac.v36i1.214.

Matapour, Z., Karlsen, D. A., Lerch, B., Backer-Owe, K., 2019. Petroleum occurrences in the carbonate lithologies of the Gohta and Alta discoveries in the Barents Sea, Arctic Norway. Petroleum Geoscience, 25, 50–70, doi: 10.1144/petgeo2017-085.

Mauring, E., Kihle, O., 2006. Leveling aerogeophysical data using a moving differential median filter. Geophysics, 71(1), L5–Z15, doi: 10.1190/1.2163912.

Mazzullo, S. J., Chilingarian, G. V., 1996. Chapter 9: Hydrocarbon reservoirs in karsted carbonate rocks, in: Dominguez, G. C., Samaniego, F. (Eds.), Developments in petroleum science. Elsevier, Volume 44 of Carbonate Reservoir Characterization: A Geologic-Engineering Analysis, 797–865.

McClymont, A. F., Green, A. G., Streich, R., Horstmeyer, H., Tronicke, J., Nobes, D. C., Pettinga, J., Campbell, J., Langridge, R., 2008. Visualization of active faults using geometric attributes of 3D GPR data: An example from the Alpine Fault Zone, New Zealand. Geophysics, 73(2), B11– B23, doi: 10.1190/1.2825408.

McMechan, G. A., Loucks, R. G., Mescher, P., Zeng, X., 2002. Characterization of a coalesced, collapsed paleocave reservoir analog using GPR and well-core data. Geophysics, 67, 1148–1158, doi: 10.1190/1.1500376.

Norwegian Polar Institute, 2014. Kartdata Svalbard 1:100 000 (S100 Kartdata)/ Map Data [Data set]. Norwegian Polar Institute, 10.21334/npolar.2014.645336c7 (accessed 25 Sep 2021).

Roberts, A., 2001. Curvature attributes and their application to 3D interpreted horizons. First Break, 19, 85–100, doi: 10.1046/j.0263-5046.2001.00142.x.

Sambridge, M., Braun, J., McQueen, H., 1995. Geophysical parametrization and interpolation of irregular data using natural neighbours. Geophysical Journal International, 122, 837–857, doi: 10.1111/j.1365-246X.1995.tb06841.x.

Sandring, F., Allroggen, N., Tronicke, J., 2017. A physical modeling study to analyze the horizontal resolution limits of GPR reflection imaging, in: Proceedings of the 9th International Workshop on Advanced Ground Penetrating Radar.

Sayago, J., Di Lucia, M., Mutti, M., Cotti, A., Sitta, A., Broberg, K., Przybylo, A., Buonaguro, R., Zimina, O., 2012. Characterization of a deeply buried paleokarst terrain in the Loppa High using core data and multiattribute seismic fades classification. AAPG Bulletin, 96, 1843–1866, doi: 10.1306/02271211137.

Simpson, F., 1988. Solution-generated collapse (SGC) structures associated with bedded evaporites: Significance to base-metal and hydro-carbon localization. Geoscience Canada, 15, 89–93.

Smyrak-Sikora, A., Johannessen, E. P., Olaussen, S., Sandal, G., Braathen, A., 2019. Sedimentary architecture during Carboniferous rift initiation— The arid Billefjorden Trough, Svalbard. Journal of the Geological Society, 176, 225–252, doi: 10.1144/jgs2018-100.

Smyrak-Sikora, A., Nicolaisen, J. B., Braathen, A., Johannessen, E. P., Olaussen, S., Stemmerik, L., 2021. Impact of growth faults on mixed siliciclastic- carbonate-evaporite deposits during rift climax and reorganisation — Billefjorden Trough, Svalbard, Norway. Basin Research, 33, 2643–2674, doi: 10.1111/bre.12578.

Tingdahl, K. M., De Groot, P. F., 2003. Post-stack-dip-and azimuth processing. Journal of Seismic Exploration, 12, 113–126.

Trinks, I., Hinterleitner, A., Neubauer, W., Nau, E., Löcker, K., Wallner, M., Gabler, M., Filzwieser, R., Wilding, J., Schiel, H., Jansa, V., Schneidhofer, P., Trausmuth, T., Sandici, V., Ruß, D., Flöry, S., Kainz, J., Kucera, M., Vonkilch, A., Tencer, T., Gustavsen, L., Kristiansen, M., Bye-Johansen, L. M., Tonning, C., Zitz, T., Paasche, K., Gansum, T., Seren, S., 2018. Large-area high-resolution ground-penetrating radar measurements for archaeological prospection. Archaeological Prospection, 25, 171–195, doi: 10.1002/arp.1599.

Tronicke, J., Allroggen, N., 2015. Toward automated delineation of ground-penetrating radar facies in clastic sediments: An example from stratified glaciofluvial deposits. Geophysics, 80(4), A89–A94, doi: 10.1190/geo2015-0188.1.

Tronicke, J., Böniger, U., 2013. GPR attribute analysis: There is more than amplitudes. First Break, 31, 103–108, doi: 10.3997/1365-2397.31.8.70636.

Van Heteren, S., Fitzgerald, D. M., Mckinlay, P. A., Buynevich, I. V., 1998. Radar facies of paraglacial barrier systems: Coastal New England, USA. Sedimentology, 45, 181–200, doi: 10.1046/j.1365-3091.1998.00150.x.

Wheeler, W., Tveranger, J., Heincke, B., Stemmerik, L., Breesch, L., Braathen, A., Maher, H., Rossi, G., Buckley, S., 2011. Paleokarst breccia-pipe reservoir analogue, Carboniferous, Svalbard. International Conference and Exhibition, AAPG.

White, W. B., 2007. A brief history of karts hydrogeology: Contributions of the NSS. Journal of Cave and Karst Studies, 69, 13–26.

Zhang, H., Thurber, C., Rowe, C., 2003. Automatic P-wave arrival detection and picking with multiscale wavelet analysis for single-component recordings. Bulletin of the Seismological Society of America, 93, 1904–1912, doi: 10.1785/0120020241.

Zhao, W., Forte, E., Pipan, M., 2016. Texture attribute analysis of GPR data for archaeological prospection. Pure and Applied Geophysics, 173, 2737–2751, doi: 10.1007/s00024-016-1355-3.

E. Publications and Conference Contributions

My individual contributions to the journal articles listed below follow the Contributor Roles Taxonomy (CRediT; Allen et al., 2019).

Peer-Reviewed Journal Articles

- **Koyan, P.**, Tronicke, J., 2020. 3D modeling of ground-penetrating radar data across a realistic sedimentary model. Computers and Geosciences 137, 104422. doi: 10.1016/j.cageo.2020.104422.
  - Candidate's contributions (CRediT): Conceptualization, Methodology, Software, Validation, Formal analysis, Investigation, Data Curation, Writing - Original Draft, Writing - Review & Editing, Visualization
- **Koyan, P.**, Tronicke, J., Allroggen, N., 2021. 3D GPR attributes to generate classified facies models: A case study from a dune island. Geophysics 86(6), B335–B347. doi: 10.1190/geo2021-0204.1.
  - Candidate's contributions (CRediT): Conceptualization, Methodology, Software, Validation, Formal analysis, Investigation, Data Curation, Writing - Original Draft, Writing - Review & Editing, Visualization
- **Koyan, P.**, Tronicke, J., 2023. 3D ground-penetrating radar data analysis and interpretation using attributes based on the gradient structure tensor. Submitted to Geophysics.
  - Candidate's contributions (CRediT): Conceptualization, Methodology, Software, Validation, Formal analysis, Investigation, Data Curation, Writing - Original Draft, Writing - Review & Editing, Visualization
- Allroggen, N., Meincke, B. H., **Koyan, P.**, Wheeler, W., Rønning, J. S., 2022: 3D ground- penetrating radar attribute classification: A case study from a paleokarst breccia pipe in the Billefjorden area on Spitsbergen, Svalbard. Geophysics 87(4), WB19–WB30. doi: 10.1190/GEO2021-0651.1.
  - Candidate's contributions (CRediT): Validation, Investigation, Writing - Review & Editing

Reviewed Expanded Abstracts

- Guillemoteau, J., **Koyan, P.**, Tronicke, J., 2017: Processing of Densely Sampled Electromagnetic Induction Data Collected across Peat Deposits, in: 23rd European Meeting of Environmental and Engineering Geophysics, EAGE. doi: 10.3997/2214-4609.201701983.
- **Koyan, P.**, Tronicke, J., Allroggen, N., Kathage, A., Willmes, M., 2018. Estimating moisture changes in concrete using GPR velocity analysis: potential and limitations, in: 17th International Conference On Ground Penetrating Radar (GPR), IEEE. doi: 10.1109/ICGPR.2018.8441572.
- Tronicke, J., **Koyan, P.**, Allroggen, N., 2020. The redundant wavelet transform to process and interpret GPR data, in: 18th International Conference On Ground Penetrating Radar (GPR), SEG Global Meeting Abstracts, 400-403. doi: 10.1190/gpr2020-104.1.
- **Koyan, P.**, Tronicke, J., 2020: Analyzing 3D multi-frequency ground-penetrating radar (GPR) data simulated across a realistic sedimentary model, in: 18th International Conference On Ground Penetrating Radar (GPR), SEG Global Meeting Abstracts, 275-278. doi: 10.1190/gpr2020-073.1.
- **Koyan, P.**, Tronicke, J., 2022: 3D Classified GPR Facies Models from Multi-frequency Data Volumes: A Synthetic Study, in: 19th International Conference On Ground Penetrating Radar (GPR), SEG Global Meeting Abstracts, 139-142. doi: 10.1190/gpr2022-042.1.
- **Koyan, P.**, Tronicke, J., 2023: The gradient structure tensor (GST): An efficient tool to analyze 3D GPR data for archaeological prospection, in: 15th International Conference of Archaeological Prospection, Universitätsverlag Kiel | Kiel University Publishing, 423-425. doi: 10.38072/978-3-928794-83-1/p86.
- Klose, T., Guillemoteau, J., Vignoli, G., **Koyan, P.**, Walter, J., Herrmann, A., Tronicke, J., 2023: Structurally-constrained FD-EMI data inversion using a Minimum Gradient Support (MGS) regularization, in: EGU General Assembly 2023. doi: 10.5194/egusphere-egu23-7067.
- **Koyan, P.**, Tronicke, J., Klose, T., Guillemoteau, J., 2023: 3D GPR to explore peat deposits: Strategies for data acquisition, processing, and interpretation, in: 12th International Workshop on Advanced Ground Penetrating Radar, IEEE. doi: 10.1109/IWAGPR57138.2023.10329077.

Data sets

- **Koyan, P.**, Tronicke, J., 2019. A synthetic 3D ground-penetrating radar (GPR) data set across a realistic sedimentary model. Mendeley Data. doi: 10.17632-/by3yh79hx4.1.

Conference Contributions

- Poster presentation at 17th International Conference On Ground Penetrating Radar (GPR), Rapperswil/CH (2018): Estimating moisture changes in concrete using GPR velocity analysis: potential and limitations. doi: 10.23689/fidgeo-5747.
- Poster presentation at 79th Jahrestagung der Deutschen Geophysikalischen Gesellschaft (DGG), Braunschweig/GER (2019): Realistische 3D-Simulation von Georadar-Daten im sedimentologischen Kontext. doi: 10.23689/fidgeo-5745.
- Conference talk at 13th Georadar Rundtischgespräch, Aachen/GER (2019): Modellierung realitätsnaher 3D-Georadar-Daten im sedimentologischen Kontext.
- Poster presentation at NSGG/BGA New Advances in Geophysics meeting - "Geophysics in the Critical Zone: Modern Approaches to Characterising Near Surface Materials", London/GB (2019): Simulation of 3D Ground-Penetrating Radar (GPR) Data Across a Realistic Sedimentary Model.
- Invited conference talk at 1st Online Workshop on Ground-Penetrating Radar Modelling Using gprMax, Newcastle Upon Tyne/GB (2020): 3D GPR Data Simulated Across a Realistic Sedimentary Model: Modelling, Analyses and Applications. Link: https://www.youtube.com/watch?v=sw5zncmyKU0
- Poster presentation at 19th International Conference On Ground Penetrating Radar (GPR), Golden (CO)/USA (2022): 3D Classified GPR Facies Models from Multi-frequency Data Volumes: A Synthetic Study. doi: 10.23689/fidgeo-5746.
- Conference talk at 14th Georadar Rundtischgespräch, Aachen/GER (2022): The gradient structure tensor (GST): An efficient tool for 3D GPR data analysis.
- Poster presentation at 83rd Jahrestagung der Deutschen Geophysikalischen Gesellschaft (DGG), Bremen/GER (2023): 3D GPR zur Erkundung von Torfvorkommen: Strategien zur Datenaufzeichnung, -bearbeitung und -interpretation. doi: 10.23689-/fidgeo-5744.
- Conference talk at 15th International Conference of Archaeological Prospection, Kiel/GER (2023): The gradient structure tensor (GST): An efficient tool to analyze 3D GPR data for archaeological prospection.
- Conference talk at 12th International Workshop on Advanced Ground Penetrating Radar, Lisbon/POR (2023): 3D GPR to explore peat deposits: Strategies for data acquisition, processing, and interpretation.

We live on an island surrounded by ignorance.
As our island of knowledge grows, so does the shore of our ignorance.

John Archibald Wheeler (1911-2008)

PHILIPP KOYAN

was born in 1994 in Eberswalde, Germany, where he attended primary and secondary school. He holds a Bachelor's degree in Geosciences (2015) and a Master's degree in Geosciences/Geophysics (2018) from the University of Potsdam. Since 2018, he works on GPR and near-surface imaging techniques in the Applied Geophysics Group at the University of Potsdam.

Universität Potsdam

GROUND-PENETRATING-RADAR

(GPR) is widely used for characterizing near-surface sedimentary systems in three dimensions. However, manual interpretations of the resulting 3D data sets, as typically performed today, are time-consuming and often incomplete. They commonly rely on the interpreter's expertise and yield non-reproducible results.

PHILIPP KOYAN

advances manual interpretation techniques in this doctoral thesis by employing GPR attribute analysis and classification. Through field and synthetic data sets, this thesis identifies suitable attributes and demonstrates their use in creating 3D facies models. This attribute-based approach enables partially automated, more comprehensive, and reproducible interpretation results compared to what has typically been achieved through traditional manual methods.